UAB
Universitat Autònoma de Barcelona

MHD atmospheric simulations of Hot Jupiters to study non-ideals effects and turbulence

Clàudia SORIANO-GUERRERO

UNIVERSITAT AUTÒNOMA DE BARCELONA
DEPARTAMENT DE FÍSICA

UAB
Universitat Autònoma
de Barcelona

MHD atmospheric simulations of Hot Jupiters to study non-ideals effects and turbulence

By
Clàudia SORIANO-GUERRERO

ADVISORS:
Dr. Daniele Viganò
Dr. Rosalba Perna

TUTOR:
Prof. Lluis Font Guiteras

Astrophysics Department
Institute of Space Sciences, ICE-CSIC/IEEC

A thesis submitted for the degree of
Doctor of Philosophy in Physics

Barcelona
October 10th, 2025

Institute of Space Sciences
EXCELENCIA MARÍA DE MAEZTU
CSIC
CONSEJO SUPERIOR DE INVESTIGACIONES CIENTÍFICAS
erc
European Research Council
Established by the European Commission

COMMITTEE MEMBERS

Dr. Ludmila Carone
Ludmila.Carone@oeaw.ac.at
Institut für Weltraumforschung (Österreichische Akademie der Wissenschaften), Austria

Dr. Juan Carlos Morales
morales@ice.csic.es
Institut de Ciències de l'Espai (ICE-CSIC), Spain.

Dr. Vivien Parmentier
vivien.parmentier@oca.eu
Observatoire de la Côte d'Azur, France

Jabata, hacia las estrellas . . .

ACKNOWLEDGEMENTS

This thesis would not have been possible without the support and help of many people, probably many more than the ones I will mention in the following lines.

First of all, I would like to thank my two supervisors Daniele Viganò and Rosalba Perna for their continuous guidance, advice, and encouragement throughout this journey. Their support has been essential in helping me grow and learn scientifically. Grazie mille! At different stages of my PhD I was fortunate to receive help from many researchers. In particular, I am grateful to Borja Miñano and Carlos Palenzuela for solving all my doubts about Simflowny and his team for kindly hosting me during my visit to Mallorca.

I would also like to thank Juan Carlos Morales, Vivien Parmentier, and Ludmila Carone for kindly accepting to be members of my thesis committee.

A very special thanks goes to my fellow PhD colleagues and now friends, Albert and Simran, for all the discussions in the office, the countless lunches, and the many conferences we shared together. I am sure we still have much more to experience, both scientifically and in friendship. I also want to thank Pedro Díaz, my fellow PhD representative and friend, for sharing all those meetings, co-organizing the retreats, and for the endless hours we spent together. I am also grateful to Elena, Víctor, and Maider, who I am sure will continue the work of PhD representatives with enthusiasm. And, of course, to the rest of the PhD candidates with whom I shared these years: Dani, Michele, Clara, Antía, Pau, Simone, Gisela, Guille, Pablo, Rebeca, Andrés, Cristina, Carline, Celsa, José, Carlos, and many more, thank you for making this experience richer, and for all the dinners and retreats shared.

I am also grateful for the experiences and people I met along the way in the Collserola PhD Meetings, SG Spain, WIA, and the various scientific conferences. These encounters enriched my journey and broadened my perspective.

Més enllà de la part acadèmica, vull agrair als meus amics, que han tingut la paciència d'escoltar hores i hores d'audios sobre els 1001 dilemes que he viscut durant aquests quatre anys. Gràcies a la gent de Vilafranca, a Los Ángeles de Nadie, al grup de Sants i a molts més. Una menció especial per a l'Adina, la Selene, la Miriam i el Tomàs, però també per a tots els meus amics que, més d'una vegada, han hagut de suportar els meus intents d'explicar com funciona realment la ciència i el sistema de recerca i per què haig de marxar a l'estranger.

Però sobretot, el meu agraïment més profund és per a la meva família: la Montse, en Rami, l'Alejandra, l'Alina, la Marina, l'Ariadna, l'Andreu, el Nil i tots aquells que ja no hi són, per permetre'm ser qui sóc i donar-me la llibertat d'escollir el meu propi camí a la vida. No tothom té aquest privilegi, i n'estic molt agraïda.

These four years have been a journey full of challenges, joys, and lessons, both in science and in life. Every step, every person, and every moment, bright or dark, has left a mark that I carry with me. This thesis is, in many ways, also a part of them.

Gràcies

PARTICIPATION IN JOURNAL ARTICLES DURING THE PHD

The present manuscript not only summarizes but also frames within a broader scientific context the main results obtained during my doctoral research. These outcomes are directly connected with several peer–reviewed journal articles, which are outlined below according to their degree of integration in the thesis.

Papers that fully appear in the thesis:

- C. Soriano-Guerrero, D. Viganò, R. Perna, T. Akgün & C. Palenzuela: 2023 **Magnetic winding and turbulence in ultra-hot Jupiters**, *Monthly Notices of the Royal Astronomical Society,*, 525, 626-641 (arXiv:2304.07066, ADS, DOI).
- C. Soriano-Guerrero, D. Viganò, R. Perna, A. López-Elias & H. Beltz: 2025 **Non-ideal MHD simulations of hot Jupiter atmospheres**, *Monthly Notices of the Royal Astronomical Society,*, 540, 1827-1843 (arXiv:2505.14342, ADS, DOI).
- C. Soriano-Guerrero, D. Viganò, R. Perna, A. López-Elias & H. Beltz: 2025 **Influence of turbulent perturbations in the magnetised atmospheres of Hot Jupiters**, submitted to *Astronomy & Astrophysics* (arXiv pending, ADS pending, DOI pending).

Papers that partially appear in the thesis:

- D. Viganò, S. Sengupta, C. Soriano-Guerrero, R. Perna, A. Elias-López, S. Kumar & T. Akgün: 2025 **Inflated hot Jupiters: Inferring average atmospheric velocity via Ohmic models coupled with internal dynamo evolution**, *Astronomy & Astrophysics*, 701, A8 (arXiv:2507.13991, ADS, DOI).

Papers that do not appear in the thesis:

- A. Elias-López, F. Del Sordo, D. Viganò, C. Soriano-Guerrero, T. Akgün, A. Reboul-Salze & M. Cantiello: 2025 **Planetary Dynamos in Evolving Cold Gas Giants**, *Astronomy & Astrophysics*, 696, A161 (arXiv:2412.07551, ADS, DOI).
- A. Elias-López, M. Cantiello, D. Viganò, F. Del Sordo, S. Kaur & C. Soriano-Guerrero: 2025 **Rossby number regime, convection suppression, and dynamo-generated magnetism in inflated hot Jupiters**, *The Astrophysical Journal*, 990, 38 (arXiv:2507.05202, ADS, DOI).

The computational resources listed below correspond to the simulations that were carried out and directly contributed to the results presented in the three main papers of this thesis.

List of related computing resources:

1. BSC, RES, AECT-2023-2-0013, 1721 khr, **MHD simulations of Hot Jupiters atmospheres: winding and turbulence**, D. Viganò (PI), C. Soriano-Guerrero, C. Palenzuela, T. Akgün
2. BSC, RES, AECT-2024-2-0026, 1756 khr, **MHD simulations of Hot Jupiters atmospheres, part II: winding and local turbulence with background profiles from state-of-the-art global circulation models**, C. Soriano-Guerrero (PI), D. Viganò, A. Elias-López, C. Palenzuela, R. Perna
3. Hidra, local cluster at ICE–CSIC: $\sim$ 2000 khr

ABSTRACT

Hot Jupiters (HJs), a particular class of gas giant exoplanets orbiting very close to their host stars, with equilibrium temperatures that surpass 1000 K, are among the most extreme planetary environments known. Their thermal properties, especially due to the strong stellar irradiation they receive, their chemical composition with a diversity of atmospheric species, and their dynamical conditions driven by powerful atmospheric winds, make them unique laboratories for understanding the interplay between irradiation, atmospheric dynamics, and magnetic effects. While the hydrodynamical scenario has been extensively studied thorough both local and global simulations, the role of magnetic fields in HJs atmospheres has received comparatively less attention. Particularly, here I face the magnetohydrodynamical (MHD) study of HJs atmospheres from a complementary angle to previous studies: a quantitative assessment of the local MHD induction in the non-linear regime, i.e. when the induced magnetic fields are comparable or larger than the internal ones. For the first time, I present local MHD simulations of a narrow atmospheric column in the dayside radiative layers of a HJ upper atmosphere. The aim is to have a first assessment of the combined effects of winding and MHD turbulence as well as to explore non-ideal effects. Yet, those magnetic interactions are expected to significantly affect wind circulation and energy dissipation, which could be a key ingredient in explaining their large inflated radii and, ultimately, the long-term evolution of these planets.

In the first part of this thesis, I present local MHD simulations suitable for ultra-HJs with very high local temperatures ($T \gtrsim 3000$ K). This initial study aims to provide a first assessment of two key processes: the winding of magnetic fields driven by strong zonal winds, and the generation of small-scale MHD turbulence. I include parametrized velocity profiles that mimic the steepest wind structures predicted by global circulation models, under an isothermal scenario. Moreover, this study focuses exclusively on the ideal regime, with dissipation arising only from the numerical scheme. In this regime, the high conductivity allows the zonal winds to strongly wind up the magnetic field, generating intense toroidal fields confined within a thin shear layer around ~ 1 bar. These fields, reaching up to kilogauss strengths, are supported by meridional currents and are largely independent of any internal dynamo. By adding random perturbations, which could favour the development of turbulence, we study its potential role in producing additional, though weaker, magnetic field amplification. An a posteriori estimation of the Ohmic dissipation associated with these currents suggests a potential contribution to the observed radius inflation of HJs.

Building upon this, the second study focuses on the inclusion of non-ideal MHD effects; Ohmic diffusion, Hall drift, and ambipolar diffusion, in one-dimensional plane-parallel atmospheric models. Here, I take a step forward in complexity, leaving the isothermal scenario and using wind and thermodynamic profiles derived from global circulation models for simulations representative of WASP 76b, WASP 18b, WASP 121b, HD 209458b and HD 1189733b. The dominant mechanism remains the nonlinear winding of the magnetic field. However the Hall and ambipolar terms introduce noticeable modifications in the induced fields at low pressures ($p \lesssim 1$ bar), especially in the hottest planets, by shaping and twisting the magnetic field. Although the geometry is limited by construction to plane-parallel columns and the setup cannot fully capture the magnetic drag on the winds, these results assess the nonlinearity and complexity of magnetic induction in HJ atmospheres, and highlight the necessity of self-consistently including MHD effects in Ohmic dissipation

studies and circulation models, beyond the often-assumed perturbative regime.

Finally, in the third part of this thesis, I extend the study to local three-dimensional, non-ideal MHD simulations. Starting from the 1D equilibrium state between winding and Ohmic dissipation, I include random small-scale 3D perturbations in the forcing term. These perturbations lead to the formation of coherent magnetic structures superimposed on the dominant azimuthal field, with characteristic length scales of tens to hundreds of kilometres. Furthermore, meridional magnetic components are generated, in some cases reaching amplitudes comparable to the expected intrinsic planetary field. I also find that the amplitude of the perturbations and the vertical extent of the atmosphere significantly influence both the spatial distribution and intensity of the induced magnetic fields. These results highlight the necessity of fully 3D treatments of atmospheric dynamics to accurately capture magnetic effects and assess their potential contribution to radius inflation in HJs.

Overall, this thesis provides a first detailed exploration of the complexity of magnetic effects in HJs atmospheres at the local level. The results obtained show that these effects are nonlinear, strongly coupled, and significantly more complex than often assumed. From idealized models to non-ideal and three-dimensional treatments, this work offers new insights into the mechanisms of magnetic induction, the role of MHD turbulence, and the resulting energy dissipation in strongly irradiated planetary atmospheres. These contributions call for a systematic incorporation of MHD effects into global circulation and evolutionary models of HJs, as they may hold the key to explaining some of their most puzzling properties.

ABSTRACT

Los Júpiter calientes (HJ), son una clase particular de exoplanetas gigantes gaseosos que orbitan muy cerca de sus estrellas anfitrionas, con temperaturas de equilibrio que superan los 1000 K, se encuentran entre los entornos planetarios más extremos que se pueden conocer. Sus propiedades térmicas, especialmente debido a la fuerte irradiación estelar que reciben, su composición química con una gran diversidad de especies en la atmósfera, y sus condiciones dinámicas impulsadas por intensos vientos atmosféricos, los convierten en laboratorios únicos para estudiar la interacción entre irradiación, dinámica atmosférica y efectos magnéticos. Mientras que la hidrodinámica se ha sido estudiado extensamente mediante simulaciones locales y globales, el papel de los campos magnéticos en las atmósferas de los HJs ha recibido una atención comparativamente menor. En particular, en esta tesis abordo el estudio magnetohidrodinámico (MHD) de las atmósferas de los HJs desde un ángulo complementario a estudios previos: una evaluación cuantitativa de la inducción MHD local en el régimen no lineal, es decir, cuando los campos magnéticos inducidos son comparables o mayores que los internos. Por primera vez, presento simulaciones MHD locales de una columna atmosférica estrecha en las capas radiativas del lado diurno de la atmósfera superior de un HJ. El objetivo es realizar una primera evaluación de los efectos combinados del *winding* del campo magnético y de la turbulencia MHD, así como explorar los efectos no ideales. Dichas interacciones magnéticas se espera que afecten de forma significativa la circulación de los vientos y la disipación de energía, lo que podría ser un ingrediente clave para explicar sus grandes radios hinchados y, en última instancia, la evolución a largo plazo de estos planetas.

En la primera parte de esta tesis, presento simulaciones MHD locales adecuadas para Júpiters ultracalientes con temperaturas locales muy elevadas ($T \gtrsim 3000$ K). Este estudio inicial tiene como objetivo ofrecer una primera evaluación de dos procesos clave: el *winding* de los campos magnéticos impulsado por intensos vientos y la generación de turbulencia a pequeña escala. Incluyo perfiles de velocidad parametrizados que reproducen las estructuras de viento más abruptas predichas por los modelos de circulación global, bajo un escenario isotermo. Además, este estudio se centra exclusivamente en el régimen ideal, con la disipación originada únicamente por el esquema numérico. En este régimen, la alta conductividad permite que los vientos combinados con el campo magnético interno, generen intensos campos toroidales confinados en una fina capa de cizalla alrededor de ~ 1 bar. Estos campos, que alcanzan intensidades de hasta kiloGauss, se sostienen mediante corrientes meridionales y son en gran medida independientes de cualquier dinamo interno. Añadiendo perturbaciones aleatorias, que pueden favorecer el desarrollo de turbulencia, estudiamos como ésta última se desarrolla y cual es su efecto adicional, aunque más débil, en la aplificación magnética. Una estimación a posteriori de la disipación óhmica asociada a estas corrientes sugiere una posible contribución al fenómeno de inflación de radio observado en los HJs.

Sobre esta base, el segundo estudio se centra en la inclusión de efectos MHD no ideales: difusión óhmica, efecto Hall y difusión ambipolar, en modelos atmosféricos unidimensionales plano-paralelos. Aquí doy un paso adelante en complejidad, dejando atrás el escenario isotermo y empleando perfiles de viento y termodinámicos derivados de modelos de circulación global para simulaciones representativas de la población de Júpiters calientes, concretamente se estudian modelos correspondientes a WASP 76b, WASP 18b, WASP 121b, HD 209458b y HD 1189733b. El mecanismo dominante sigue siendo el *winding* no lineal del campo magnético. Sin embargo, los términos de Hall y ambipolar introducen modificaciones notables en los

campos inducidos a bajas presiones ($p \lesssim 1$ bar), especialmente en los planetas más calientes, moldeando y retorciendo el campo magnético. Aunque la geometría está limitada por construcción a columnas plano-paralelas y el diseño no puede capturar por completo el frenado magnético sobre los vientos, estos resultados evalúan la no linealidad y complejidad de la inducción magnética en las atmósferas de los HJs, y resaltan la necesidad de incluir de forma autoconsistente los efectos MHD en estudios de disipación óhmica y modelos de circulación, más allá del régimen perturbativo que a menudo se asume.

Finalmente, en la tercera parte de esta tesis, extiendo el estudio a simulaciones locales MHD tridimensionales y no ideales. Partiendo del estado de equilibrio unidimensional entre el *winding* y la disipación óhmica, incluyo perturbaciones tridimensionales aleatorias a pequeña escala en el término de forzamiento. Estas perturbaciones conducen a la formación de estructuras magnéticas coherentes superpuestas al campo azimutal dominante, con escalas características de decenas a cientos de kilómetros. Además, se generan componentes magnéticas meridionales que, en algunos casos, alcanzan amplitudes comparables a las del campo planetario intrínseco. También encuentro que la amplitud de las perturbaciones y la extensión vertical de la atmósfera influyen significativamente tanto en la distribución espacial como en la intensidad de los campos magnéticos inducidos. Estos resultados ponen de relieve la necesidad de tratamientos tridimensionales completos de la dinámica atmosférica para capturar con precisión los efectos magnéticos y evaluar su posible contribución a la inflación de radio en los HJs.

En conjunto, esta tesis proporciona una primera exploración detallada de la complejidad de los efectos magnéticos en las atmósferas de los HJs a nivel local. Los resultados obtenidos muestran que estos efectos son no lineales, fuertemente acoplados y significativamente más complejos de lo que se suele suponer. Desde modelos idealizados hasta tratamientos no ideales y tridimensionales, este trabajo ofrece nuevas perspectivas sobre los mecanismos de inducción magnética, el papel de la turbulencia y la disipación de energía resultante en atmósferas planetarias fuertemente irradiadas. Estas contribuciones llaman a una incorporación sistemática de los efectos MHD en los modelos de circulación global y evolución de los HJs, ya que podrían ser la clave para explicar algunas de sus propiedades más enigmáticas.

ABSTRACT

Els Júpiter calents (HJs), són una classe particular d'exoplanetes gegants gasosos que orbiten molt a prop de les seves estrelles, amb temperatures d'equilibri que superen els 1000 K, es troben entre els entorns planetaris més extrems que es coneixen. Les seves propietats tèrmiques, especialment a causa de la forta irradiació estel·lar que reben, la seva composició química amb una gran diversitat d'espècies a l'atmosfera, i les seves condicions dinàmiques impulsades per intensos vents atmosfèrics, els converteixen en laboratoris únics per entendre la interacció entre irradiació, dinàmica atmosfèrica i efectes magnètics. Mentre que l'escenari hidrodinàmic ha estat àmpliament estudiat mitjançant simulacions locals i globals, el paper dels camps magnètics en les atmosferes dels HJs ha rebut una atenció comparativament menor. En particular, en aquesta tesi abordo l'estudi magnetohidrodinàmic (MHD) de les atmosferes de HJs des d'un angle complementari als estudis previs: una avaluació quantitativa de la inducció MHD local en el règim no lineal, és a dir, quan els camps magnètics induïts són comparables o més grans que els interns. Per primera vegada, presento simulacions MHD locals d'una columna atmosfèrica estreta en les capes radiatives del costat diürn de l'atmosfera superior d'un HJ. L'objectiu és realitzar una primera avaluació dels efectes combinats del *winding* del camp magnètic i de la turbulència MHD, així com explorar els efectes no ideals. Es preveu que aquestes interaccions magnètiques afectin de manera significativa la circulació dels vents i la dissipació d'energia, cosa que podria ser un ingredient clau per explicar els seus grans radis inflats i, en última instància, l'evolució a llarg termini d'aquests planetes.

A la primera part d'aquesta tesi, presento simulacions MHD locals adequades per a HJs ultracalents amb temperatures locals molt elevades ($T \gtrsim 3000$ K). Aquest estudi inicial té com a objectiu oferir una primera avaluació de dos processos clau: el *winding* dels camps magnètics impulsat per intensos vents i la generació de turbulència MHD a petita escala. Incloc perfils de velocitat parametritzats que reprodueixen les estructures de vent més abruptes predites pels models de circulació global, sota un escenari isoterm. A més, aquest estudi se centra exclusivament en el règim ideal, amb la dissipació originada únicament per l'esquema numèric. En aquest règim, l'alta conductivitat permet que els vents zonals es combinin amb el camp magnètic, generant intensos camps toroidals confinats en una fina capa de cisalla al voltant d'~ 1 bar. Aquests camps, que arriben a intensitats de fins a quilogauss, es mantenen mitjançant corrents meridionals i són, en gran mesura, independents de qualsevol dinamo interna. Afegint pertorbacions aleatòries, també s'estudia la generació de la turbulència, que produeix una amplificació magnètica addicional, encara que més feble. Una estimació a posteriori de la dissipació òhmica associada a aquestes corrents suggereix una possible contribució al fenomen d'inflació del radi observat als HJs.

Sobre aquesta base, el segon estudi se centra en la inclusió d'efectes MHD no ideals: difusió òhmica, efecte Hall i difusió ambipolar, en models atmosfèrics unidimensionals pla-paral·lels. Aquí faig un pas endavant en complexitat, deixant enrere l'escenari isoterm i utilitzant perfils de vent i termodinàmics derivats de models de circulació global per a simulacions representatives de WASP 76b, WASP 18b, WASP 121b, HD 209458b i HD 1189733b. El mecanisme dominant continua sent el *winding* del camp magnètic. No obstant això, els termes de Hall i ambipolar introdueixen modificacions notables en els camps induïts a baixes pressions ($p \lesssim 1$ bar), especialment en els planetes més calents, modificant i torçant el camp magnètic. Tot i que la geometria està limitada per construcció a columnes pla-paral·leles i el la simulació no pot capturar completament l'efecte magnètic de frenada sobre els vents, aquests

resultats avaluen la no linealitat i complexitat de la inducció magnètica en les atmosferes dels HJs, i remarquen la necessitat d'incloure de manera autoconsistent els efectes MHD en estudis de dissipació òhmica i models de circulació, més enllà del règim pertorbatiu que sovint s'assumeix.

Finalment, a la tercera part d'aquesta tesi, amplio l'estudi a simulacions MHD tridimensionals locals i no ideals. Partint de l'estat d'equilibri unidimensional entre el *winding* i la dissipació òhmica, incloc pertorbacions tridimensionals aleatòries a petita escala en el terme de forçament. Aquestes pertorbacions condueixen a la formació d'estructures magnètiques coherents superposades al camp azimutal dominant, amb escales característiques de desenes a centenars de quilòmetres. A més, es generen components magnètiques meridionals que, en alguns casos, arriben a amplituds comparables a les del camp planetari intrínsec. També trobo que l'amplitud de les pertorbacions i l'extensió vertical de l'atmosfera influeixen significativament tant en la distribució espacial com en la intensitat dels camps magnètics induïts. Aquests resultats posen de manifest la necessitat de tractaments tridimensionals complets de la dinàmica atmosfèrica per capturar amb precisió els efectes magnètics i avaluar la seva possible contribució a la inflació del radi als HJs.

En conjunt, aquesta tesi proporciona una primera exploració detallada de la complexitat dels efectes magnètics en les atmosferes dels HJs a escala local. Els resultats obtinguts mostren que aquests efectes són no lineals, fortament acoblats i significativament més complexos del que sovint es pressuposa. Des de models idealitzats fins a tractaments no ideals i tridimensionals, aquest treball ofereix noves perspectives sobre els mecanismes d'inducció magnètica, el paper de la turbulència i la dissipació d'energia resultant en atmosferes planetàries fortament irradiades. Aquestes contribucions posen en manifest la necessitat de la incorporació sistemàtica dels efectes MHD en els models de circulació global i evolució dels HJs, ja que podrien ser la clau per explicar algunes de les seves propietats més enigmàtiques.

LIST OF ABBREVIATIONS

AMR	**A**daptive **M**esh **R**efinement
ANDES	**A**rmazo**N**es high **D**ispersion **E**chelle **S**pectrograph
ARIEL	**A**tmospheric **R**emote sensing **I**nfrared **E**xoplanet **L**arge survey
BC	**B**oundary **C**ondition
CARMENES	**C**alar **A**lto high-**R**esolution search for **M** dwarfs with **E**xoearths with **N**ear-infrared and optical **É**chelle **S**pectrographs
CHEOPS	**Ch**aracteraizing **Ex****op**lanets **S**atellite
CFL	**C**ourant-**F**riedrichs-**L**ewy
COROT	**CO**nvection **RO**tation et **T**ransits planétaires
CRIES	**CR**yogenic high-resolution **I**nfra**R**ed **E**chelle **S**pectrograph
ELT	**E**xtremely **L**arge **Telescope**
EOS	**E**quation **O**f **S**tate
ESA	**E**uropean **S**pace **A**gency
ESPRESSO	**E**chelle **S**pectrograph for **R**ocky **E**xoplanet- and **S**table **S**pectroscopic **O**bservations
FMR	**F**ixed **M**esh **R**efinement
GCM	**G**lobal **C**irculation **M**odel
HARPS	**H**igh **A**ccuracy **R**adial velocity **P**lanet **S**earcher
HZ	**H**abitable **Z**one
Hiparcos	**Hi**gh Precision **Par**allax **C**ollecting **S**atellite
JWST	**J**ames **W**ebb **S**pace **T**elescope
HJ	**H**ot **J**upiter
HPC	**H**igh **P**erformance **C**omputing
HST	**H**ubble **S**pace **T**elescope
KHI	**K**elvin **H**elmholtz **I**nstability
MAROON-X	**M**-dwarf **A**dvanced **R**adial velocity **O**bserver Of **N**eighboring e**X**oplanets
MHD	**M**agneto**H**ydro**D**ynamics
MOST	**M**icrovariability and **O**scillations of **St**ars
MP5	**5**th order accurate **M**onotonicity **P**reserving scheme
NASA	**N**ational **A**eronautics and **S**pace **A**dministration
PLATO	**Pla**netary **T**ransits and **O**scillations of Stars
PDE	**P**artial **D**ifferential **E**quation
RCB	**R**adiative-**C**onvective-**B**oundary
SAMRAI	**S**tructured **A**daptive **M**esh **R**efinement **A**pplication **I**nfrastructure
RK4	**R**unge **K**utta **4**th order
SPI	**S**tar **P**lanet **I**nteraction
SST	**S**pitzer **S**pace **T**elescope
TESS	**T**ransiting **E**xoplanet **S**urvey **S**atellite
uHJ	**u**ltra **H**ot **J**upiter
UV	**U**ltra-**v**iolet **r**adiation
XUV	**X**-ray and Extreme **U**ltra**v**iolet radiation

TABLE OF CONTENTS

1

Introduction

1.1 History and methods of exoplanetary discoveries

The idea that other worlds might exist beyond our own has been part of human thought for thousands of years. Philosophers in ancient civilizations, such as Greece, imagined a universe filled with millions of exo bodies. However, these concepts remained untested until the late 20th century. The discovery of the first planets orbiting pulsars in the early 1990s (Wolszczan and Frail, 1992), followed by the detection of 51 Pegasi b (Mayor and Queloz, 1995), a gas giant orbiting a main-sequence star, in 1995, marked a turning point in modern astronomy. This latter discovery is widely regarded as the formal beginning of exoplanetary science. Since then the exoplanetary science has grown significantly over the past three decades. Around 6000[1] exoplanets have been found so far, thanks to the efforts of thousands of scientists and engineers, as well as the significant advancements in theoretical and observational methods. We now have progressively detailed information regarding the physical characteristics, internal structures, and atmospheric compositions of a significant number of these planets (Seager and Deming, 2010).

The roots of contemporary exoplanetary science can be found in a number of missions that were initially intended for other different purposes but contributed to the development of this new area of study. One of them was the *HIgh Precision PARallax COllecting Satellite (Hipparcos)*, which was held between 1989 and 1993, a mission that provided the first accurate measurements of stellar positions and proper motions (Perryman et al., 1997). The data obtained were later used to place constraints on planetary masses derived through radial velocity methods (Reffert, S. and Quirrenbach, A., 2011). Similarly, the *Hubble Space Telescope (HST)*, launched in 1990, also made relevant contributions to exoplanet research. In 2001, *HST* made the first detection of an exoplanetary atmosphere by detecting sodium (Na) in the atmosphere of HD 209458b (Charbonneau et al., 2002). Several other early missions also played an important role. The *Canadian satellite Microvariability and Oscillations*

[1]See the NASA exoplanets archive: https://exoplanetarchive.ipac.caltech.edu/

of STars (MOST), launched in 2003, was one of the first space telescopes to detect planetary transits. Although its main focus was the study of stellar seismology, it also helped refine our understanding of known exoplanetary systems. In parallel, the *Spitzer Space Telescope (SST)*, launched by the *National Aeronautics and Space Administration (NASA)* in 2003, was designed for infrared observatory but made major contributions to exoplanet science that included thermal emission measurements of the hottest gas giants, detection of exoplanetary atmospheres, and the first infrared light curve of an exoplanet (Charbonneau et al., 2005; Deming et al., 2005).

The first space mission explicitly dedicated to exoplanet detection was the *COnvection ROtation et Transits planétaires (CoRoT)*, operative from 2006, which systematically employed the transit method to detect several exoplanets. Among its achievements was the discovery of CoRoT 7b, the first confirmed rocky exoplanet outside the Solar System, (Léger et al., 2009).

After the first dedicated mission, following space missions have made significant contributions to the field. These efforts have not only increased the number of discovered exoplanets but also significantly advanced their physical and atmospheric characterization. Among the more relevant missions was *Kepler*, launched in 2009. It detected thousands of exoplanet candidates and offered a statistical perspective on the frequency and diversity of planets in the Milky Way (Batalha et al., 2013; Borucki et al., 2010). Following *Kepler*, the *Transiting Exoplanet Survey Satellite (TESS*) was launched into space in 2018. The focus shifted to finding exoplanets around bright, nearby stars, which are excellent targets for detailed follow-up studies, both from the ground and from space (Ricker et al., 2015). Similarly, the *European Space Agency (ESA)* mission, *CHaracterizing ExOPlanets Satellite (CHEOPS)*, launched in 2019, was designed to measure with high precision the radii of known exoplanets, leading to improved estimates of their densities and sizes (Benz et al., 2020).

It is relevant to note that, apart from the previously mentioned space-based missions, ground-based facilities also play a crucial role in advancing our understanding of exoplanetary atmospheres. High-resolution spectrographs such as *M-dwarf Advanced Radial velocity Observer Of Neighboring eXoplanets (MAROON-X)* (Seifahrt et al., 2022), *Echelle Spectrograph for Rocky Exoplanet- and Stable Spectroscopic Observations (ESPRESSO)* (Pepe et al., 2021) and *CRyogenic high-resolution InfraRed Echelle Spectrograph (CRIRES)* (Holmberg and Madhusudhan, 2022) have enabled the detection of molecular species and the direct measurement of atmospheric wind speeds through Doppler-resolved line profiles. Instruments like *High Accuracy Radial velocity Planet Searcher (HARPS)* (Mayor et al., 2003) and *Calar Alto high-Resolution search for M dwarfs with Exoearths with Near-infrared and optical Échelle Spectrographs (CARMENES)* (Quirrenbach et al., 2018) have also contributed significantly to detecting and characterizing exoplanets and their orbital properties.

Despite these successes, exoplanetary science still has many fundamental questions to answer. Scientists are working to understand how planets are formed and develop, particularly in cases like those gas giants that are located exceptionally close to their host stars (Showman, Lewis, and Fortney, 2015; Fortney, Dawson, and Komacek, 2021). As such, these do not easily fit the traditional models of planetary formation. Another central question pertains to the frequency of Earth-like planets. Although many rocky exoplanets have been identified, only a small fraction are located within the habitable zones of their stars, where conditions might be right for complex chemistry and stable climates.

Atmospheric characterization remains a major frontier in exoplanetary science. The detection and spectral analysis of atmospheric constituents, such as water vapor (H_2O), carbon dioxide (CO_2), and methane (CH_4), are crucial for understanding

planetary environments, energy balance, and potential surface conditions. These observations can reveal key physical and chemical processes occurring in distant worlds.

Beyond those challenges, the existence of moons or rings around exoplanets (e.g., Kipping et al. 2012; Kipping et al. 2013; Heller et al. 2014) is still a question waiting to be answered. Although no exomoon has been confirmed so far, such bodies might also provide valuable insights into planetary system formation and evolution.

Looking ahead, the *PLAnetary Transits and Oscillations of stars mission (PLATO)* by ESA, scheduled for launch in 2026, aims to detect Earth-sized planets in the habitable zones of solar-type stars. By combining transit photometry with asteroseismology, *PLATO* will enhance our understanding of both exoplanets and their host stars. Meanwhile, the *James Webb Space Telescope (JWST)*, now operational, represents a transformative step in exoplanet research. Its unprecedented infrared sensitivity allows scientists to study exoplanetary atmospheres in extraordinary detail. Complementing *JWST, ESA's Atmospheric Remote-sensing Infrared Exoplanet Large-survey (ARIEL)* mission, planned for launch in 2029, will systematically observe the atmospheres of hundreds of exoplanets to characterize their chemical composition, thermal structures, and cloud properties.

Moreover, the new generation of high-resolution spectrographs, such as *ArmazoNes high Dispersion Echelle Spectrograph (ANDES)* on the *Extremely Large Telescope (ELT)*, will deliver even higher precision and sensitivity. These instruments will enable the detection of fainter atmospheric features and improve our ability to constrain wind structures and temperature distributions in exoplanetary atmospheres.

Together, this set of missions (see Fig. 1.1 for an overview sketch of the space-based missions) is launching a new era in exploration. By studying distant worlds, characterizing their atmospheres, and looking for signs of life, humanity is gradually moving closer to answering one of its oldest and most profound questions: Are we alone in the universe?

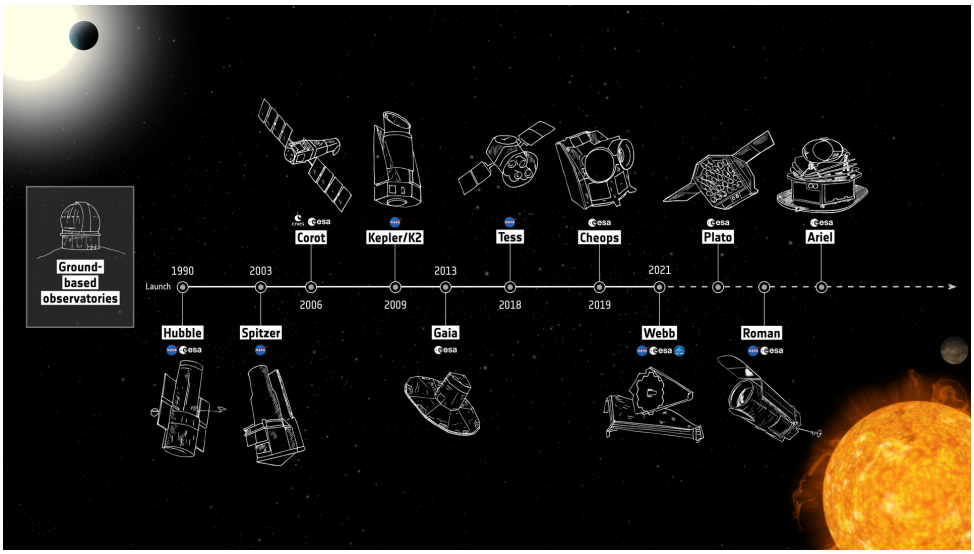

FIGURE 1.1: Timeline of key space-based missions that have contributed or will contribute to the discovery and characterization of exoplanets. From early observatories such as *Hubble* and *Spitzer* to current and future missions like *JWST, PLATO* and *ARIEL*, these facilities have progressively expanded our knowledge of planetary diversity and atmospheric properties. Note that ground-based observatories have operated in parallel, providing complementary observations and discoveries. Credit: *ESA*.

1.2 Exoplanet diversity

Although it is predicted that there are millions of exoplanets in our galaxy (Fressin et al., 2013; Zhu et al., 2018; Kunimoto and Matthews, 2020) and potentially many more in other galaxies, the number of confirmed detections as of October 14th, 2025 is around 6000. We only need to look at our own solar system to appreciate the diversity of planetary properties. Even within a sample of just eight planets, we observe a wide variety of sizes, compositions, structures, and other characteristics. This suggests that the diversity among the known exoplanets may be even more extensive than we currently observe.

To make sense of this growing and diverse population, scientists have developed classification schemes based on physical properties. One of the most widely used criteria for classifying exoplanets is based on their mass. According to this approach, exoplanets can be categorized as terrestrial planets (with radii of 0.8–1.25 $R_\oplus$ and masses of 0.5–2 $M_\oplus$ [2] (Buchhave et al., 2014)), super-Earths (radii of 1.25–2 $R_\oplus$ and masses of 2–10 $M_\oplus$ (Valencia, Sasselov, and O'Connell, 2007)), Neptune-like planets (radii of 2–6 $R_\oplus$ and masses up to $\sim$ 20 $M_\oplus$ (Rogers et al., 2011; Müller et al., 2024)), or gas giants (radii > 0.5 R_J[3], and masses above $\sim$0.3 M_J (Hatzes and Rauer, 2015; Winn and Fabrycky, 2015; Müller et al., 2024)). While this classification offers a useful first approximation, it inevitably oversimplifies the true diversity of planetary types. In particular, many exoplanets fall into transitional categories, such as sub-Neptunes, gas dwarfs, lava worlds and water-rich worlds, that do not fit neatly into the standard four-group scheme. These intermediate types often exhibit a wide range of compositions and atmospheric characteristics, challenging the sharp boundaries implied by basic mass-based classification.

Fig. 1.2 illustrates this diversity by showing the distribution of known exoplanets in terms of their radius (relative to Earth) and orbital period (in days). It also highlights several of the populations mentioned above, such as rocky planets, ocean worlds, cold and hot gas giants. It is important to note that most detection methods are intrinsically biased toward large planets with short-period orbits, which produce stronger signals. As a result, the currently known population does not necessarily reflect the real underlying distribution of planets in the Galaxy.

Many active research lines remain across the exoplanet population, including studies of formation and migration pathways, atmospheric chemistry and dynamics, interior structure and thermal evolution, and planetary habitability, among others. The latter is of particular interest to the community, given its implications not only for science but also for humanity. For this reason, the detection and characterization of terrestrial planets remains a major goal, as some may currently host, or may once have hosted, conditions suitable for life (Seager, 2013). However, this topic lies outside the scope of this thesis; instead, we now turn to the study of gas giants which cointain the exoplanets analyzed in this thesis.

1.3 Gas giants

Gas giant exoplanets are among the most commonly detected beyond the solar system, about 1900 confirmed to date, with Jupiter and Saturn as the local benchmarks.

[2] $R_\oplus$ corresponds to the Earth's radius ($R_\oplus = 6.371 \times 10^6$ m), while $M_\oplus$ denotes the Earth's mass ($M_\oplus = 5.972 \times 10^{24}$ kg).

[3] R_J corresponds to Jupiter's radius ($R_J = 7.1492 \times 10^7$ m) while M_J to Jupiter's mass ($M_J = 1.898 \times 10^{27}$ kg).

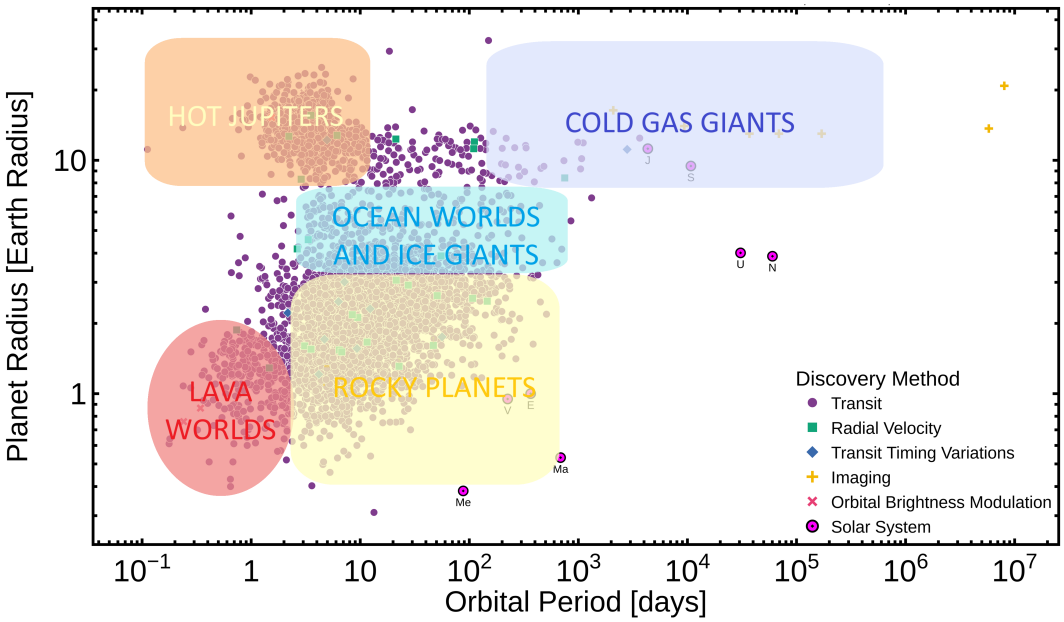

FIGURE 1.2: Distribution of the confirmed exoplanets as a function of their radius (relative to Earth) and orbital period. Distinct populations such as lava worlds, rocky planets, ocean worlds and ice giants, hot Jupiters, and cold gas giants are indicated. The data points are color-coded according to the detection method used. This plot has been obtained from the NASA exoplanet archive and modified to represent different population groups.

In terms of composition, gas giants are dominated by hydrogen and helium, but they are not all alike. Prior to *Juno* mission for Jupiter, interior models for gas giants exoplanets, based on measurements from previous Jovian missions and theoretical models from solar system's gas giants, typically invoked a compact heavy-element core beneath a largely homogeneous H/He envelope made of two layers: an external one dominated by molecular hydrogen and depleted in helium and in internal layer, where hydrogen was in a metallic form combined with enriched helium, (Fortney and Nettelmann, 2010). The new data, however, show that this classical picture is incomplete. The gravity harmonics measured by *Juno* are best explained by a *dilute (fuzzy) core*, a heavy element enriched region extending over a substantial fraction of the radius, in which the core material is partially mixed into the overlying H/He envelope, yielding deep heavy element gradients and an inhomogeneous interior (Helled et al., 2022; Miguel and Vazan, 2023), see Fig. 1.3. However, some studies, such as Helled and Stevenson (2024), question the existence of a small compact core beneath this fuzzy region. Although several interior models allow for the presence of such a dense central core of a few Earth masses, its detection remains extremely challenging because its gravitational signature is negligible and cannot be constrained by current gravity data. Therefore, both scenarios, with or without a compact core, are still considered plausible within present interior models, although the compact core, if it exists, is expected to be much lighter than originally predicted. Note that internal structures also vary with planetary mass, age, and irradiation.

Close-in gas giants are excellent laboratories for atmospheric physics under extreme irradiation. Many exhibit anomalously large radii, as will be described in more detail in the next sections. Moreover, some planets present atmospheric escape in the form of hydrogen tails (Guillot, 1999; Vidal-Madjar et al., 2003). Detection and atmospheric studies have benefited greatly from their size. Gas giants were the first

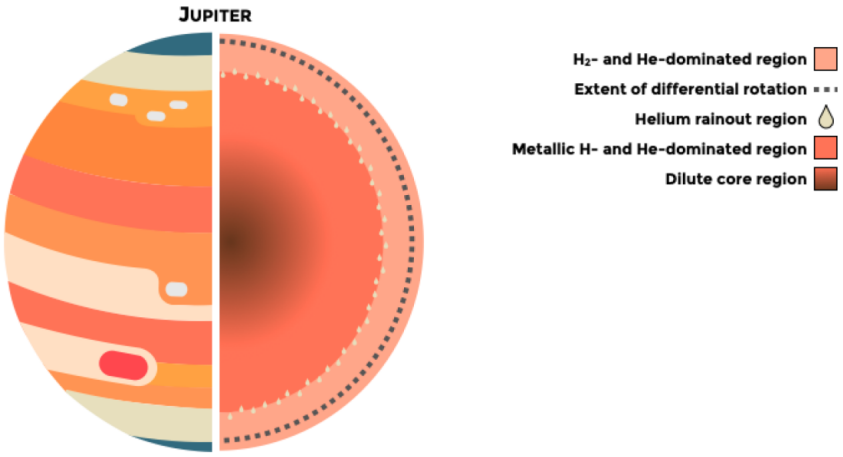

FIGURE 1.3: Schematic figure showing the interior structure of Jupiter. From Miguel et al., 2022.

.

exoplanets found because they produce strong radial velocity signals (Mayor and Queloz, 1995) and deep transits, the latter enabling atmospheric characterization via transmission spectroscopy (Charbonneau et al., 2002). Spectroscopy from missions like *HST, SST*, and now *JWST* has allowed researchers to know the chemistry of their atmospheres. The upcoming *ARIEL* mission will expand these efforts further (Tinetti et al., 2018). Up to now we know that the atmospheres of gas giants are dominated by H_2 and He, but also contain trace amounts of heavier molecules like CH_4 (Bell et al., 2023), NH_3 (Mâlin et al., 2025), H_2O (Tinetti et al., 2007; Deming et al., 2013; Alderson et al., 2023), and carbon monoxide (CO) (Kok et al., 2013). Depending on temperature and pressure, these species condense to form cloud decks at different altitudes. In cold gas giants like Jupiter and Saturn, ammonia and water clouds are observed, while in hotter gas giants, clouds consist of silicates (Grant et al., 2023), and may contain iron, and other metal oxides (Parmentier et al., 2016). Photochemical hazes produced by stellar ultra-violet (UV) irradiation can also form at high altitudes, particularly in strongly irradiated planets.

While gas giants are unlikely to be habitable, their diversity offers valuable insights into how planetary systems evolve. Just as not all rocky or Neptune-like planets are the same, gas giants too display a wide range of physical and orbital characteristics, this makes that no single model can fully capture their variety.

In our solar system, gas giants are located far from the Sun. However, many discovered in other systems orbit extremely close to their stars, often completing an orbit in just a few days. These so-called Hot Jupiters (HJs), gaseous planets orbiting within 0.1 au (astronomical units), are markedly different from the gas giants we are familiar with, residing much closer to their stars than Mercury or Venus is to the Sun. Their proximity exposes them to intense stellar irradiation, driving strong atmospheric dynamics and magnetic interactions. These characteristics make them excellent laboratories for testing theories of planetary structure, energy transport, and, in particular, magnetism under extreme conditions. For these reasons, HJs are the primary focus of this thesis, which specifically investigates their magnetic effects and will examine them in more detail in the following section.

1.4 Hot and ultra Hot Jupiters

As previously mentioned, the first exoplanet discovered orbiting a main-sequence star was a HJ: 51 Pegasi b. This planet presented a four-day orbital period and was detected by Mayor and Queloz, 1995 via radial velocity.

Two years after this discovery, Butler et al., 1997 detected a new giant planet located very close to its host star. This finding marked the emergence of a new class of gas giants, now known as HJs, which increase in the following year up to several hundreds confirmed up to the date. Due to their large sizes and short orbital periods, these planets proved relatively easy to detect, and a growing number of candidates began to appear, mainly, via transit and radial velocity methods. Due to their ease of detection, these planets are over-represented in the exoplanet detected sample, leading to a biased view of the overall exoplanet population. Several studies estimate the occurrence rate of this group to range from 0.3 to 1.2 planets per 100 stars (Wright et al., 2012; Zhou et al., 2019; Temmink and Snellen, 2023; Gan et al., 2023).

HJs exhibit several extreme properties that distinguish them from other giant planets (see Fortney, Dawson, and Komacek, 2021 for a full review). They orbit very close to their host stars, typically within 0.1 au, which results in extremely short orbital periods (few days), always less than 10 days (Cumming et al., 2008; Dawson and Johnson, 2018). This proximity leads to intense stellar irradiation, causing their atmospheric temperatures to exceed 1000 K. When the equilibrium temperature, T_{eq}, exceeds $\sim$2200 K, such planets are usually referred to as ultra-hot Jupiters (uHJs) (Tan and Komacek, 2019). Note that the T_{eq} for a full day-night redistribution is defined as:

$$T_{\rm eq} = T_* \left(\frac{R_*}{2a}\right)^{1/2} \left(1 - A_B\right)^{1/4}, \tag{1.1}$$

where A_B is the Bond albedo (fraction of incident stellar power reflected to space), a is the star–planet separation, and R_* and T_* are the stellar radius and effective temperature, respectively.

However, their existence raised a series of questions, as their properties differed significantly from the giant planets in our own solar system. Did these planets form close to their stars, or did they originate farther out and migrate inward? If migration occurred, did it happen shortly after their formation, or billions of years later (Malhotra, 1993; Thommes, Duncan, and Levison, 1999; Walsh et al., 2011; Madhusudhan, Amin, and Kennedy, 2014)? What are the atmospheres of these highly irradiated planets like (Crossfield, 2015)? And, perhaps one of the most puzzling questions: why are so many of them inflated (Guillot and Showman, 2002; Bodenheimer, Laughlin, and Lin, 2003; Fortney, Marley, and Barnes, 2007; Sestović, Demory, and Queloz, 2018)? This question, while not the central focus of this thesis, is among the major open problems in exoplanetary science and remains linked to the local magnetic and physical processes addressed here. Before discussing possible explanations for their inflated radii, we will first explore the main physical characteristics of HJs, including the formation mechanisms, their internal structure and atmospheric conditions, which will be key to understand physical processes produced in the simulations presented in this thesis.

1.4.1 Formation mechanisms

Over the past decades, the origin of HJs has been one of the central questions in exoplanetary science. Three main formation pathways have been proposed: in situ

formation, disk migration, and high-eccentricity tidal migration, see Fig. 1.4.

In situ formation suggests that HJs form or assemble their cores and accrete gaseous envelopes close to their current locations. However, this scenario faces major difficulties. Core accretion can operate close to the star (Lee, Chiang, and Ormel, 2014; Batygin, Bodenheimer, and Laughlin, 2016), but building a sufficiently large core ($\sim 10\,M_{\oplus}$) is challenging because the feeding zones near the star contain limited solid material (Schlichting, 2014). In addition, mergers of multiple smaller cores are prevented by the surrounding disk (Lee and Chiang, 2016), and pebble accretion becomes inefficient at small orbital distances (Johansen and Lambrechts, 2017).

In the disk migration model, giant planets form farther out, where conditions for core accretion or gravitational instability are favorable (Pollack et al., 1996; Boss, 1997), and subsequently migrate inward due to torques from the gaseous disk (Lin and Papaloizou, 1986; Baruteau et al., 2014). The migration rate depends strongly on the disk's structure (Paardekooper and Mellema, 2006; Duffell et al., 2014). If the planet reaches a short orbital period before the disk dissipates, it could be tidally disrupted or engulfed by the star. However, tidal interactions with the star (Trilling et al., 1998; Valsecchi, Rasio, and Steffen, 2014) or stalling by a magnetospheric cavity in the innermost disk (Rice, Armitage, and Hogg, 2008; Chang, Gu, and Bodenheimer, 2010) may preserve the HJ in a stable close-in orbit.

Finally, high-eccentricity tidal migration occurs after disk dispersal, when a planet is excited to a highly eccentric orbit through planet–planet scattering (Rasio et al., 1996; Weidenschilling and Marzari, 1996), cyclic secular interactions (Kozai, 1962; Lidov, 1962; Wu and Murray, 2003; Fabrycky and Tremaine, 2007), or chaotic secular interactions (Wu and Lithwick, 2011). Once the planet approaches the star, tides raised on the planet by the host star shrink and circularize its orbit (Eggleton, Kiseleva, and Hut, 1998).

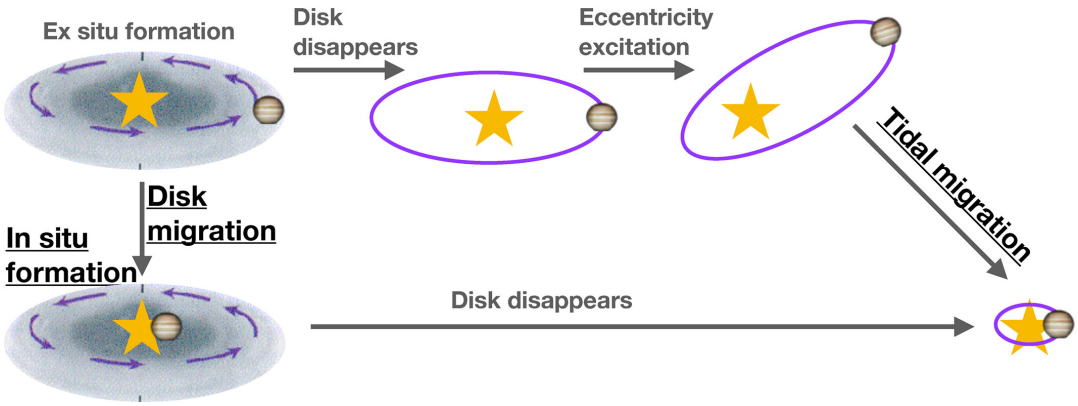

FIGURE 1.4: Origins hypotheses for hot Jupiters: in-situ formation, disk migration, and high eccentricity tidal migration. From Fortney, Dawson, and Komacek, 2021

.

There are several observational constraints help to test these different hypotheses, including orbital properties, stellar and companion characteristics, and atmospheric composition.

Obital properties provide key tests for these mechanisms. Most HJs have orbital periods of ∼3 days, shorter than predicted by in situ formation (∼10 days; Lee and Chiang 2016). HJs could arrive through disk migration to roughly half the stellar corotation period, which is more consistent with the observed values. On the other hand, high-eccentricity tidal migration predicts that surviving planets should

remain at or beyond twice the Roche limit ($a \gtrsim 2a_{\rm Roche}$). However many HJs are indeed beyond this distance, several are located between 1–2 $a_{\rm Roche}$, which high-eccentricity migration alone cannot easily explain (Jackson, Greenberg, and Barnes, 2008; Valsecchi, Rasio, and Steffen, 2014). Moreover, the observed mix of circular and moderately eccentric ($0.2 < e < 0.6$) orbits supports a combination of migration channels (Hut, 1981).

On the other hand, spin–orbit misalignments also provide insights into formation histories. While in situ and disk migration are expected to preserve alignment, many HJs are strongly misaligned (Albrecht et al., 2012), consistent with dynamical excitation (Fabrycky and Tremaine, 2007; Chatterjee et al., 2008). However, tidal interactions may realign the system (Albrecht et al., 2012), potentially erasing evidence of high-eccentricity migration. Moreover, stellar spin axes can become misaligned with the protoplanetary disk through other processes (Batygin, 2012; Rogers, Lin, and Lau, 2012; Storch, Anderson, and Lai, 2014), meaning that the use of only the spin–orbit alignment is not necessarily diagnostic of a specific formation channel.

Host-star and companion properties offer additional constraints. HJ occurrence increases with host-star metallicity (Gonzalez, 1997; Fischer and Valenti, 2005; Jenkins et al., 2017), supporting core accretion and in situ growth in metal-rich disks. Their general absence around young stars and the scarcity of close small planets (Steffen et al., 2012) favor tidal migration, although exceptions such as WASP-47 b (Becker et al., 2015) imply multiple channels. Distant planetary companions consistent with secular excitation (Knutson et al., 2014; Bryan et al., 2016) further support the high-eccentricity migration pathway.

A complementary diagnostic arises from atmospheric composition, particularly the C/O ratio (Öberg, Murray-Clay, and Bergin, 2011; Madhusudhan, Amin, and Kennedy, 2014). The chemical environment during formation leaves imprints on the gas accreted by the planet. Planets formed beyond the water ice line and later migrated inward are expected to exhibit super-stellar C/O ratios, as they accrete carbon-rich, oxygen-poor gas (Öberg, Murray-Clay, and Bergin, 2011; Madhusudhan, Amin, and Kennedy, 2014). In contrast, in situ formation or migration within the inner disk should reflect the local composition of the inner disk, yield stellar-like or sub-stellar C/O ratios, reflecting enrichment by oxygen-bearing refractory materials. Hence, measured atmospheric C/O ratios provide a powerful constraint on the formation location and migration history of HJs. While the atmospheric C/O ratio has long been considered a tracer of the formation environment, recent studies indicate that giant planets can also actively modify the local disk chemistry during their formation. As they accrete solids and open gaps, they can alter the distribution of volatiles such as H_2O, CO_2, and CH_4, potentially enriching their atmospheres in oxygen while rendering the surrounding disk regions carbon-rich (Jiang et al., 2023). Hence, deviations in measured C/O ratios may reflect both the birth location and the chemical feedback between the forming planet and its natal disk. Moreover, while the atmospheric C/O ratio was initially considered a direct diagnostic of planetary formation and migration pathways, recent observations and modelling indicate that this parameter can be substantially modified not only by the location where the planets where formed but also by the planet accretion history, the chemical structure of the formation environment and other post-formation processes such as solid accretion, chemical disequilibrium, and condensation (Cridland, Eistrup, and van Dishoeck, 2019; Pacetti et al., 2022). As a result, the C/O ratio should be interpreted in combination other indicators, rather than as a standalone signal of formation location.

In summary, no single mechanism can explain the full diversity of observed HJ

properties. High-eccentricity tidal migration, often triggered by planet–planet interactions, likely accounts for eccentric and misaligned systems, whereas disk migration and in situ formation better explain close-in planets around metal-rich or young stars. The inclusion of new tools to determine their origin can help us better understand their formation and evolution.

1.4.2 Internal structure

HJs are generally thought to share a broadly similar internal structure to that proposed for Jupiter and Saturn: a diluted core, surrounded by a layer of hydrogen and helium, with metallic hydrogen in the deeper regions and molecular hydrogen in the outer envelope. However, even for the solar system's giant planets, where direct measurements can be made, their internal structure still presents open questions. For exoplanets, unlike the solar system giants, there are no seismology or gravity measurements that can directly constrain such structures. As a result, current models rely heavily on extrapolations from Jupiter and Saturn, using indirect observables such as the average density, derived from the measured mass and radius, as the main indicator of internal composition. In the case of HJs, their proximity to the host star can further modify the outer structure through irradiation-driven effects, as will be discussed in the next section.

Before the diluted-core scenario was introduced, interior models assumed a compact, dense central core. These models predicted a core radius of approximately $\sim 1{-}2\,R_\oplus$ and a mass of $\sim 5{-}20\,M_\oplus$, accounting for about 5%–30% of the planet's total mass (Guillot, 2005; Fortney, Marley, and Barnes, 2007; Thorngren et al., 2016). In cases of strong enrichment in heavy elements, cores as massive as $\sim 60\,M_\oplus$ were proposed for any gas giant (Thorngren et al., 2016). Such a core would likely be composed of silicates and iron (Guillot, 2005). Alternatively, heavy elements could be mixed throughout the interior (Ikoma et al., 2006; Fortney and Nettelmann, 2010). Note that if a dense core is present in those planets, heat transfer within it would occur primarily by conduction if solid, or by convection if partially molten.

Surrounding the core, there is the dominant metallic hydrogen layer. In this region hydrogen exists in a metallic state due to the extreme pressures in this region, ranging from roughly $\sim$ 1 Mbar near the top of the layer to $\sim 30{-}40$ Mbar at its base (Saumon and Chabrier, 1991; French et al., 2012; Bonitz et al., 2024). Under such conditions, hydrogen becomes ionized and behaves as an electrically conductive fluid. This metallic nature enables the generation of electric currents, which, combined with large-scale convection and planetary rotation, is believed to sustain the dynamo mechanism responsible for the global magnetic field (Stevenson, 1983; Stevenson, 2010). It is important to mention that convection is the dominant transport of heat mechanism in this region.

Above the metallic layer lies the dominant molecular hydrogen (H_2) envelope in a dense fluid state, extending from pressures of $\sim 10^3$ bar down to the metallic transition at $\sim 1{-}2$ Mbar. Some equation of state (EOS) models support that the hydrogen in this envelope behaves as a compressed fluid, with properties intermediate between a gas and a liquid, facilitating efficient convective heat transport of this nearly adiabatic layer (Nettelmann et al., 2008). This dense H_2 layer is critical for constraining the internal thermal structure and evolutionary models of close-in giant planets (Guillot, 2005; Fortney and Nettelmann, 2010). However, some interior models (Komacek and Youdin, 2017; Viganò et al., 2025; Elias-López et al., 2025) demonstrate that internal heat deposited at depths of $\sim 100{-}10^5$ bar, even at modest rates ($\gtrsim$ 1% of the incident stellar power), can locally suppress convection and

form deep, secondary radiative zones embedded within the convective envelope. This leads to a stratified structure with alternating convective and radiative layers, potentially affecting the planet's cooling, size evolution, and magnetic field generation. The upper limit of this deep convective region is set by the radiative–convective boundary (RCB), the interface where the temperature gradient becomes shallower than the adiabatic value and radiative transfer overtakes convection as the dominant energy transport mechanism. The location of the RCB, which in HJs can occur at much greater depths than in Jupiter due to intense stellar irradiation, effectively separates the convective interior from the stably stratified outer radiative envelope discussed in the next section.

In addition to their compositional structure, HJs are expected to exhibit a high internal heat content, often parameterized by the internal temperature $T_{\rm int}$ as:

$$T_{\rm int} = \left(\frac{F_{\rm int}}{\sigma_B} \right)^{1/4}, \tag{1.2}$$

where $F_{\rm int}$ is the outward energy flux from the planet's interior (in $\mathrm{W\,m^{-2}}$) in the absence of stellar irradiation, and $\sigma_B = 5.6704 \times 10^{-8}\ \mathrm{W\,m^{-2}\,K^{-4}}$ is the Stefan-Boltzmann constant. Although $T_{\rm int}$ cannot be directly measured, it is inferred through interior structure models that reproduce the observed mass and radius of the planet. $T_{\rm int}$ therefore serves as a proxy for the planet's internal energy budget and for the efficiency of internal heating mechanisms. Classical evolutionary models predicted that giant planets should gradually cool over time to internal temperatures comparable to Jupiter's (~ 100 K). However, to reproduce the inflated radii of HJs, which will be described in detail in following subsections, interior models require significantly higher $T_{\rm int}$ values, typically in the range of $\sim 300-1000$ K (Thorngren, Gao, and Fortney, 2019), suggesting the presence of additional heat sources beyond long-term cooling. In the deep interior, adiabatic models for Jupiter estimate central temperatures of about 20000 K. The presence of heavy-element gradients in Jupiter's interior may, however, increase the local metallicity and produce a superadiabatic temperature profile, yielding higher central values of up to ~ 35000 K (Debras and Chabrier, 2019; Militzer et al., 2022). For HJs, interior temperatures may reach similar or even greater magnitudes depending on their mass and internal heating mechanisms.

Magnetic fields in hot Jupiters

To date, no magnetic field has been directly measured for any HJ. Observational estimates of magnetic fields in HJs remain scarce and highly uncertain, relying exclusively on indirect tracers such as information obtained using star-planet interaction (SPI) models, some of them used to interpret the observed trends of X-ray luminosities versus the presence of short-orbit planets (Scharf, 2010) while others to study the modulation of Ca II K line with HJ orbital periods (Cauley et al., 2019). However the inference of planetary magnetic fields in this case remains strongly model dependent. On the other hand, low-frequency radio searches offer a promising avenue, in analogy with the coherent emission seen in magnetised solar planets, yet so far they have provided only upper limite and one tentative signals (Turner et al., 2021), not confirmed by follow-up observations (Turner et al., 2024). In the absence of observational evidence, estimates of HJ magnetic fields currently rely on dynamo scaling laws. These scaling laws, linking key dimensionless parameters, have been derived from self-sustained dynamo simulations (e.g, Christensen and Aubert 2006; Yadav et al. 2013), and validated by comparison with the magnetic fields observed in

Earth, Jupiter, and fast-rotating low-mass stars (Christensen, Holzwarth, and Reiners, 2009; Reiners and Christensen, 2010). These scaling laws predict that, in the fast-rotator regime, the magnetic field strength is controlled by the convective heat flux. Applied to the HJ context, such heat-flux scaling relations typically yield magnetic fields up to an order of magnitude stronger than those on Jupiter (4.3 G for Jupiter), depending on the planet's interior structure, heat flux, age and rotation (Yadav and Thorngren, 2017; Kilmetis et al., 2024). However, the break down of the convective layer (Elias-López et al., 2025; Viganò et al., 2025), previously described, makes that the derived surface magnetic fields can be greatly reduced to or below Jovian values, contrary to what is commonly assumed, thus negatively affecting estimates for coherent radio emission, and possibly explaining the failure in detecting it so far. These different results highlight the need for observational constraints in order to shed some light on HJ magnetism.

1.4.3 Atmospheric properties

The atmospheres of HJs are excellent laboratories for studying planetary climate and chemistry, as they exhibit very distinctive thermal, chemical, and dynamical conditions (Seager and Deming, 2010). Unlike the atmospheres of solar system gas giants such as Jupiter and Saturn, those of HJs are shaped by their extreme proximity to their host stars. These planets receive stellar fluxes up to four orders of magnitude greater than Jupiter (Fortney, Dawson, and Komacek, 2021), which dramatically alters their atmospheric energy budgets and thermal structures (Fortney et al., 2008; Showman et al., 2009).

In the context of this work, the term *atmosphere* includes not only the observable layers probed by spectroscopy, typically spanning from upper limits of about 10^{-6}–10^{-5} bar to lower limits around 10^{-1} bar, depending on wavelength, instrument, and cloud coverage (Heng, 2017), but also the deep outer radiative zone produced by intense stellar irradiation. In HJs, this stably stratified radiative region can extend from the photosphere (pressures of order $\lesssim 1$ bar) down to depths of $\sim 10^3$–10^4 bar (Guillot and Showman, 2002; Thorngren, Gao, and Fortney, 2019), far deeper than in Jupiter, which this regions reaches up to, at most, a few tens to a few hundred bars, before convection becomes the dominant energy transport mechanism (Guillot, 2005).

In this section, we first examine the atmospheric composition of HJs and the methods used to characterise it from observations. We then discuss their thermal and dynamical structures, including the role of extreme stellar irradiation and the modelization of these atmospheres via local and global simulations to analyse the complex atmospheric dynamics.

Composition and atmospheric characterization

On the observational side, HJs are among the most accessible exoplanets for atmospheric characterisation due to their large radii and short orbital periods, which produce deep, frequent transits and eclipses. Transmission and emission spectroscopy are the primary techniques for characterizing their atmospheres. As seen in Fig. 1.5, in transmission, starlight passes through the planet's atmospheric limb during transit, imprinting wavelength-dependent absorption features that reveal its chemical composition (Brown, 2001; Hubbard et al., 2001). In emission spectroscopy, the planet's thermal infrared signal is measured during secondary eclipse, providing complementary information on composition and vertical temperature structure at

different depths and across various regions of the planet's dayside (Charbonneau et al., 2005; Deming et al., 2005; Knutson et al., 2008).

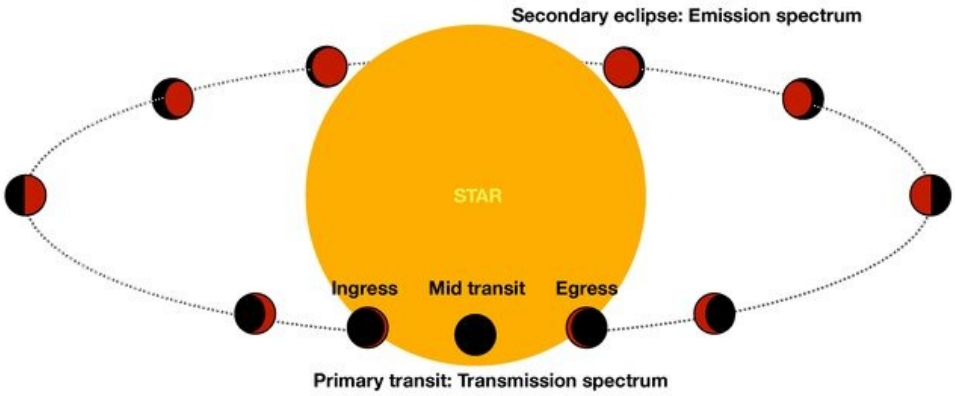

FIGURE 1.5: Example of a transiting planet phase curve. During the primary transit, the starlight passes through the planet's atmospheric limb, allowing the measurement of a transmission spectrum. During the secondary eclipse, when the planet passes behind the star, the planet's dayside thermal emission is blocked, enabling the extraction of the emission spectrum. Adapted from Pluriel, 2023.

Combining transmission and emission spectroscopy with other approaches such as high-resolution Doppler spectroscopy and phase curve observations has enabled the detection of a diverse array of chemical species in HJs atmospheres (Cont et al., 2022; Ramkumar et al., 2023). Current observations indicate that HJ atmospheres are generally hydrogen–helium dominated, with varying degrees of heavy-element enrichment (Seager and Sasselov, 2000; Madhusudhan, Amin, and Kennedy, 2014). In the most extreme cases, such as uHJs, there is the hypothesis that molecular hydrogen undergoes thermal dissociation and recombination: on the dayside, hydrogen dissociation acts as an endothermic process that cools the local atmosphere, while strong winds advect the resulting atomic hydrogen to the cooler nightside, where recombination releases heat and effectively warms the atmosphere (Bell and Cowan, 2018). Although this mechanism provides a plausible explanation for the day–night thermal redistribution, it remains a hypothesis that has not yet been observationally confirmed. Subsequent studies, such as Tan and Komacek, 2019; Baeyens et al., 2024, have explored this process, the latter investigating its potential observational implications. However, the efficiency of this mechanism likely depends on the structure of the horizontal wind flow which is shaped with magnetic coupling and moreover the intense stellar irradiation might also alter the heat advection. Thus, significant uncertainties remain regarding the actual temperature structure of the dayside.

On top of this dominant H/He composition, a number of molecular and atomic species has been detected. H_2O is often the dominant infrared absorber, though its abundance can vary strongly with atmospheric temperature, C/O ratio, and cloud coverage. CO and CO_2 are prevalent in the hottest atmospheres, while CH_4 becomes more abundant in cooler HJs, broadly consistent with chemical equilibrium. In some cases, enhanced HCN and C_2H_2 features have been interpreted as signatures of non-equilibrium chemistry and moderately elevated C/O ratios (as the high C/O scenarios of Madhusudhan et al. 2011), however these have been challenged by recent JWST observations showing CH_4 depletion even at moderate temperatures; e.g. Deming et al. 2013; Line et al. 2016; Sing et al. 2016; Stevenson et al. 2017). In the optical, atomic Na and potassium (K) have been frequently observed in relatively

clear atmospheres (Charbonneau et al., 2002; Redfield et al., 2008; Nikolov et al., 2015; Sing et al., 2015; Wyttenbach et al., 2015), while their absence is often attributed to high altitude hazes or clouds. High-resolution spectroscopy has further revealed numerous neutral and ionised metals, including iron (Fe, Fe^+), calcium (Ca^+), magnesium (Mg), manganese (Mn), lithium (Li), titanium (Ti), and vanadium (V), in several HJs and uHJs (Hoeijmakers et al., 2018; Ehrenreich et al., 2020; Costa Silva et al., 2024). At the highest atmospheric temperatures, molecular metal oxides such as titanium monoxide (TiO) and vanadium monoxide (VO) have been proposed as potential contributors to thermal inversions in the upper atmosphere. Although chemically and dynamically plausible, their observational detection has proven extremely challenging. In particular, several studies such as Evans et al., 2016 have reported evidence consistent with TiO/VO absorption rather than unambiguous detections, noting that alternative explanations such as high-altitude haze scattering cannot yet be ruled out. This difficulty arises because TiO/VO opacity features are broad and located in the optical, where low-resolution spectra lack distinctive signatures, and observations are further complicated by stellar activity, clouds, and limited data quality. However, recent high-resolution observations have provided the first unambiguous detection of TiO in the atmosphere of the ultra-hot Jupiter WASP-189b (Prinoth et al., 2022), confirming its presence with a 14σ significance. Regarding VO, its detection remains more uncertain, although recent analyses have reported strong evidence of VO in the atmospheres of WASP-76b (Maguire et al., 2024) and TOI-1518b (Simonnin et al., 2025), pending independent confirmation with different instruments and line lists. Thus, while TiO is now confirmed as a key absorber in some ultra-hot Jupiters, VO detections are still tentative and require further validation.

Clouds are a key modulator of observed spectra in HJs. Recent studies indicate that the role of clouds and hazes changes substantially between the HJ and uHJs regimes. Roman et al., 2021 explored cloud coverage across a range of irradiation temperatures and found that for uHJs, clouds are essentially non-existent on the dayside and, if present at all, would likely be confined to nightside upper latitudes (Parmentier, Showman, and Lian, 2013). By contrast, HJs can sustain clouds throughout much of their atmospheres, with significant radiative feedback on the thermal structure through either heating or cooling depending on cloud extent and local conditions (Harada et al., 2021).

Atmospheric thermal structure and dynamics

The thermal structure and dynamical behaviour of HJ atmospheres are fundamental to understanding their climate and energy transport. Due to their proximity to the host star, HJs experience strong tidal interactions that have brought them into a state of synchronous rotation, in which the same hemisphere permanently faces the star (Rasio et al., 1996; Lubow, Tout, and Livio, 1997; Showman and Guillot, 2002). This configuration leads to permanent dayside (the star-facing hemisphere) and nightside (the dark hemisphere facing away from the star), producing extreme temperature contrasts, as proved also by direct observations (Knutson et al., 2007). The temperature gradients drive powerful atmospheric circulation (Showman et al., 2009; Heng and Showman, 2015; Tan and Komacek, 2019). These atmospheric dynamics are usually studied with exoplanetary climate simulations, also known as General Circulation Models (GCMs), which provide the framework to investigate heat transport and wind patterns under such extreme conditions by solving a set of

fluid dynamical equations known as the *primitive equations of meteorology* to simulate a planet's atmosphere, as done in most GCMs for HJs, as in Showman et al., 2009.

The thermal structure of HJs atmospheres is primarily governed by two energy sources: intense stellar irradiation and internal heat flux originating from the planet's deep interior. The stellar flux, deposited at the top of the atmosphere on the dayside, is generally the dominant driver of the upper atmospheric temperature profile, while the internal heat may significantly influence the deeper layers, at pressure $p \sim 100 - 1000$ bars, (Guillot and Showman, 2002; Fortney, Marley, and Barnes, 2007; Showman et al., 2009; Komacek and Youdin, 2017; Thorngren, Gao, and Fortney, 2019). On long evolutionary timescales, stellar luminosity changes as the host star ages, and stellar activity, such as flares and rotational modulation, can introduce short-term variability in the incident flux. Nevertheless, when modelling the present-day atmospheric state of a given planet, stellar irradiation is generally treated as constant in time for simplicity, as such variability is usually small compared to the mean flux and does not strongly affect the large-scale thermal structure in most HJs.

In planetary atmospheres, temperature typically varies with pressure, as illustrated by the blue line in Fig. 1.6, as a representative model. The temperature–pressure profile is shaped by the absorption of stellar radiation as a function of wavelength and altitude, the re-emission of both absorbed and intrinsic fluxes, and the redistribution of energy by horizontal and vertical advection, that is, the transport of heat by winds either across the planet's surface (horizontal) or between atmospheric layers (vertical) (Hubeny, Burrows, and Sudarsky, 2003; Heng, Menou, and Phillipps, 2011; Parmentier et al., 2018). At low pressures ($\sim$ mbar-bar), the radiative timescale, i.e, the characteristic time it takes for the atmosphere to change its temperature through radiation, is short ($\sim$ hours). This means that temperatures respond quickly to the local balance between stellar heating and radiative cooling. At higher pressures ($\sim$ 10-100 bar), the atmosphere is denser, and photons take much longer to escape, so the radiative timescale becomes longer ($\sim$ weeks-months). In this regime, radiative processes adjust the temperature slowly, and the movement of the gas itself (advection) becomes increasingly important in setting the temperature structure. This means that in the upper atmosphere temperature is mainly determined by the instantaneous balance between heating and cooling, whereas in deeper layers, winds and circulation patterns play a greater role in distributing heat. Thermal inversions (see red line in Fig. 1.6) are now observationally confirmed in several uHJs, such as WASP-121b and WASP-18b, where HST and JWST emission spectra reveal molecular features like H_2O and CO in emission rather than absorption (Evans et al., 2017; Arcangeli et al., 2018; Coulombe et al., 2023). However, thermal inversions are not ubiquitous: cooler or moderately irradiated planets such as HD 189733b and HD 209458b lack inversions in their dayside spectra (Crouzet et al., 2014; Line et al., 2016). Current interpretations favour a competition between strong optical and near-UV absorption in the upper atmosphere, mainly by H^- continuum and atomic metals, and infrared cooling by molecules such as H_2O, which becomes inefficient once water is thermally dissociated at high temperatures (Arcangeli et al., 2018; Coulombe et al., 2023). Consequently, recent data indicate that inversions can arise without TiO/VO, especially in the ultra–hot regime where H^- opacity and metal lines could dominate the stellar energy deposition (Arcangeli et al., 2018).

Beyond the vertical direction, temperature also varies significantly with longitude and latitude, as illustrated in Fig. 1.7 for a model designed to reproduce HD 189733b, shown here as a representative example of this variability at three different pressure levels. In typical HJs, the dayside can be heated to $\sim$1500–3000 K, while the

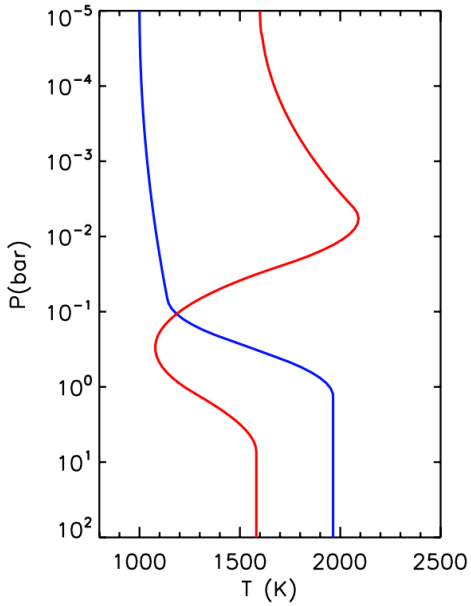

FIGURE 1.6: Illustration of P–T profiles from simulations produced by (Madhusudhan and Seager, 2010). The red and blue curves show P–T profiles with and without a thermal inversion, respectively.

nightside remains much cooler, typically ∼800–1500 K (Showman and Guillot, 2002; Zhang and Showman, 2017). These large day–night temperature differences are one of the main drivers of global atmospheric circulation, which will be described in the upcoming paragraphs. It is relevant to note that winds in HJs are in any case not fast enough to move the absorbed heat to the night side before it is radiated away, so the two hemispheres maintain a certain temperature difference (Showman and Guillot, 2002; Cooper and Showman, 2005; Pérez-Becker and Showman, 2013). This incomplete redistribution leads to significant horizontal variations not only in temperature, but also in atmospheric composition and cloud coverage (Knutson et al., 2007; Parmentier et al., 2018; Helling et al., 2019; Parmentier et al., 2021).

Furthermore, intense stellar XUV irradiation in the upper atmosphere can heat those layers (the thermosphere) to temperatures of order 10^4 K, driving hydrodynamic outflows and atmospheric escape. This process, known as hydrodynamic blow-off, can lead to substantial mass loss over gigayear timescales (Lammer et al., 2003; Murray-Clay, Chiang, and Murray, 2009; Owen, 2019). Observational evidence includes detections of extended hydrogen envelopes in Lyman-α and Balmer lines (Vidal-Madjar et al., 2003; Etangs et al., 2010), as well as neutral helium at 1083 nm (Oklopčić and Hirata, 2018; Spake et al., 2018). The efficiency of escape depends on factors such as the level of stellar irradiation, planetary gravity, and magnetic interactions (Muñoz, 2007; Owen, 2019). Escape is particularly effective during the first few hundred million years of a planet's lifetime, when the host star is most active and emits intense XUV radiation (Ribas et al., 2005). As the star ages and its high-energy emission (dictated by magnetic activity) decreases, escape rates typically decrease; however, planets in extremely close orbits or with low surface gravities can continue losing significant mass for billions of years. Over long timescales, such escape can reshape a planet's mass, radius, and atmospheric composition, potentially altering its bulk density and even its classification within the exoplanet population. Therefore, atmospheric escape is not merely a transient process but a fundamental

driver of planetary evolution, influencing the thermal structure, atmospheric dynamics, and observable characteristics of HJs (Owen, 2019).

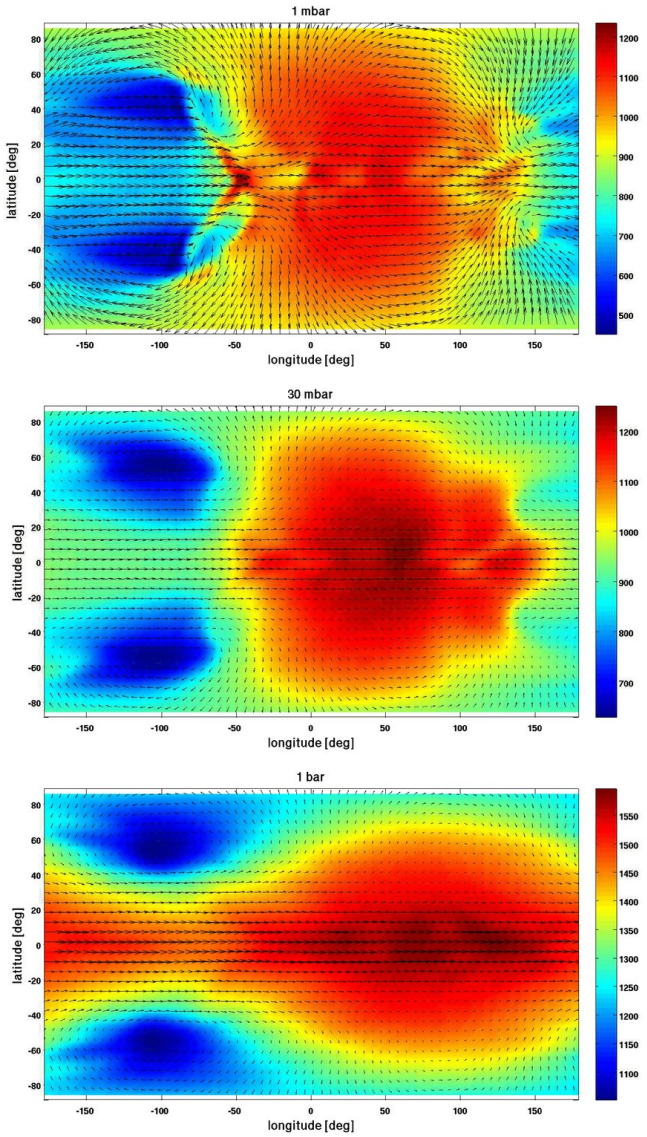

FIGURE 1.7: Temperature (color scale, in K) and winds (arrows) for a model suitable to HD 189733b with solar abundances and no TiO/VO. Panels show the flow at 1 mbar (top); 30 mbar, corresponding to an approximate photosphere level in the mid-IR (middle); and 1 bar (bottom). The substellar point is at longitude and latitude $(0°, 0°)$. The dayside corresponds to the region between longitudes $-90°$ and $90°$, while the nightside is at longitudes $-180°$ to $-90°$ and $90°$ to $180°$. From Showman et al., 2009.

As noted earlier, horizontal temperature contrasts in HJ atmospheres drive powerful winds and large-scale circulation. One of the most prominent dynamical features predicted by theory and confirmed by numerical simulations is the presence of a broad, fast, eastward super-rotating equatorial jet. This jet can extend over a wide range of pressures, from millibars to several bars, with speeds reaching a few km s^{-1} in the upper atmosphere, as inferred from radial velocity spectral shifts (Showman and Guillot, 2002; Cooper and Showman, 2005; Heng and Showman, 2015) and by observationally eastward advection of the hottest point in HD 189733b (Knutson

et al., 2007; Knutson, Lewis, and Fortney, 2012). The superrotation arises from the interaction between planetary-scale waves, primarily equatorial Kelvin and Rossby waves, and the mean flow, which transport angular momentum toward the equator (Showman and Polvani, 2011). Slower flows in the opposite direction are usually present at larger depths. Nevertheless, the opposite trend has been proposded with outer retrograde equatorial flows and inner superrotational flows (Carone et al., 2020). On the other hand there also exist a second feature which is the high-latitude ($\sim$ mbar-$\sim$0.1 bar) day-to-night flow which is dominant in atmospheres with short radiative timescales and strong drag forces[4] (Showman and Polvani, 2011; Komacek and Showman, 2016). These circulation patterns transport heat toward the nightside, partially reducing the temperature contrast and affecting the thermal emission observed from the planet (Cho et al., 2008; Showman et al., 2009; Heng, Menou, and Phillipps, 2011; Rauscher and Menou, 2013; Perna, Menou, and Rauscher, 2010a; Perna, Heng, and Pont, 2012; Pérez-Becker and Showman, 2013; Parmentier, Showman, and Lian, 2013; Showman, Lewis, and Fortney, 2015; Kataria et al., 2015; Koll and Komacek, 2018; Beltz et al., 2022; Komacek, Gao, and Fortney, 2022).

The representative GCM results from Showman et al., 2009 are shown in Fig. 1.7, at three different pressure levels. The circulation varies noticeably with depth. At low pressures ($\sim$1 mbar), the strong eastward equatorial jet shifts the hottest regions eastward of the substellar point by about 50°, producing a warm local *chevron-shaped* pattern west of the substellar point. This feature should not be confused with the global *Matsuno–Gill* pattern, sometimes also referred to as a "chevron-shaped" structure, which results from the interaction of planetary-scale Kelvin and Rossby waves and is responsible for driving the equatorial superrotation (Showman and Polvani, 2011). The patter seen here arises from adiabatic heating: as air parcels descend, they are compressed by the higher ambient pressure, and in the absence of significant radiative exchange this compression increases their temperature. At intermediate pressures ($\sim$ 30 mbar), the hotspot shift remains but the chevron structure is less distinct, and temperature contrasts between day and night are reduced. At deeper layers ($\sim$ 1 bar), horizontal temperature variations are smoother and the flow is dominated by the broad superrotating jet with weaker high-latitude structures. At higher latitudes ($\gtrsim$ 40°), in all three cases, broad, cold nightside regions appear, with the coldest areas displaced off the equator.

Wind speeds also vary significantly with pressure. Near the photosphere, where radiative timescales are short, horizontal flows respond rapidly to thermal forcing and can achieve the highest velocities. Deeper in the atmosphere, where radiative timescales are long, winds tend to be slower primarily because thermal contrasts are reduced and the thermal forcing is weaker (Showman and Guillot, 2002; Showman, Menou, and Cho, 2008; Heng and Showman, 2015). Additional drag mechanisms (Perna, Menou, and Rauscher, 2010a; Menou, 2012) can also contribute to a decrease of the wind, particularly in the upper, low-density atmosphere where the fluid has lower inertia. This vertical wind shear can influence the efficiency of heat redistribution and the observed day–night temperature contrast.

Fig. 1.8 illustrates the zonally averaged zonal wind for a representative model, from Rauscher and Menou, 2013, highlighting the prominent equatorial superrotating jet that is a characteristic feature of HJ circulation (Showman and Polvani, 2011). This eastward jet extends vertically from the uppermost layers down to nearly the

[4] In HJs atmospheres, drag can arise from several processes, including magnetic (Lorentz) forces acting on ionized winds, dissipation by shocks and turbulence, and momentum deposition by breaking atmospheric waves.

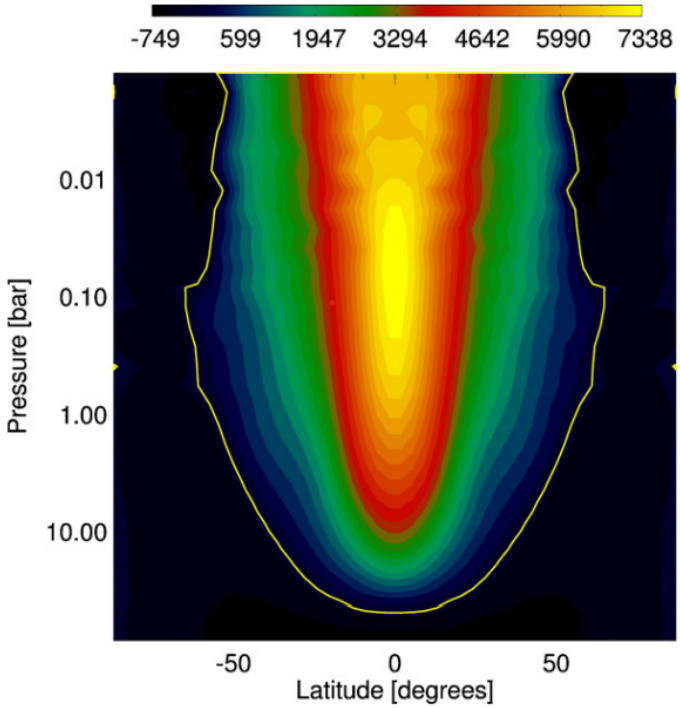

FIGURE 1.8: Zonal average of the zonal (east–west) wind (color scale in m/s) as a function of latitude and pressure obtained from simulations. The yellow line separates eastward (positive) flow from westward (negative) flow. An equatorial super-rotating jet extends throughout most of the atmosphere, typical of HJ circulation. From Rauscher and Menou, 2013.

deepest modelled levels, with only the lowest layers exhibiting westward equatorial flow. At high altitudes (pressures $\lesssim$1 mbar), the flow is strongly supersonic, several times the local sound speed, and includes intense meridional components driving day-to-night transport across the terminator (the boundary between the permanently irradiated dayside and the dark nightside). At intermediate pressures, the flow becomes transonic, while at $\gtrsim$10 bar, winds are subsonic and dominated by weaker zonal motions.

Circulation patterns also depend strongly on latitude. At low latitudes, the superrotating equatorial jet efficiently advects heat eastward, shifting the dayside hotspot away from the substellar point. At higher latitudes, the circulation tends to transport heat more directly from the dayside to the nightside, with less longitudinal deflection than at the equator (Showman et al., 2009; Showman and Polvani, 2011). In these regions the winds are weaker and exhibit greater variability, both spatially (less organized flow structures) and temporally (fluctuating patterns driven by waves and instabilities) (Cho et al., 2008; Tan and Komacek, 2019). While the strongest sustained velocities are typically zonal (east–west) within the equatorial jet, intense localized meridional (north–south) winds can occur, particularly near the day–night terminators where converging flows also drive significant vertical motion. Such wind structures are crucial for understanding both heat transport and the spatial distribution of chemical species.

Magnetic effects can further modify the dynamics. In atmospheres hot enough to have non-negligible electrical conductivity due to the presence of partially ionized alkali metals, magnetic induction (the focus of this thesis) and the associated

Lorentz forces can act as a drag on the flow, reducing wind speeds and altering the jet structure (Perna, Menou, and Rauscher, 2010a; Rogers and Komacek, 2014; Hindle, Bushby, and Rogers, 2021). The strength of this magnetic drag depends on temperature, ionization fraction, and the background magnetic field strength. In extreme cases, strong drag can suppress the formation of a coherent superrotating jet, leading to predominantly day-to-night flow (Arcangeli et al., 2019; Showman, Tan, and Parmentier, 2020).

Recent advances in high-resolution spectroscopy have enabled direct measurements of atmospheric dynamics in several HJs. Using instruments such as ESPRESSO on the VLT and MAROON-X on the Magellan Clay telescope, it is now possible to resolve Doppler shifts in atomic and molecular lines during transit, providing direct constraints on wind velocities at the planetary limbs and at different atmospheric pressures. For instance, ESPRESSO observations of WASP-76b revealed asymmetric iron absorption at the morning and evening terminators, interpreted as evidence for day-to-night winds and condensation processes, with wind speeds increasing toward lower pressures (Seidel et al., 2021). Similarly, *MAROON-X* observations of TOI-1518b detected phase-dependent Doppler shifts in the transmission signal, which, when compared with GCM predictions, are consistent with longitudinal wind flows in the observable atmosphere during transit. The modelling indicates that a strong atmospheric drag is required to reproduce the observed line broadening and reduced velocity amplitudes, suggesting that magnetic or other frictional processes significantly slow the winds in this uHJs (Simonnin et al., 2025).

In addition to large-scale jets, small-scale dynamical processes may contribute to shaping the atmospheric flow in HJs. Local instabilities, such as baroclinic or shear instabilities, can generate turbulence, redistributing momentum and heat on shorter spatial and temporal scales. Such perturbations are a well-known feature of gas giant atmospheres in the solar system: high-resolution observations of Jupiter from *Voyager*, *Hubble*, and *Juno* have revealed mesoscale structures including baroclinic waves, equatorially trapped gravity waves, and compact vortices embedded in zonal jets (Simon, Wong, and Orton, 2015; Orton et al., 2020). These structures interact with the background flow and can help sustain turbulence via inverse energy cascades (Ingersoll et al., 2004; Young and Read, 2017). Similar features may arise in the atmospheres of HJs, caused from processes such as Kelvin–Helmholtz instabilities (KHI), vertical shear instabilities (Fromang, Leconte, and Heng, 2016), baroclinic instabilities (Polichtchouk and Cho, 2011; Showman, Tan, and Parmentier, 2020; Tan and Showman, 2020), inertial instabilities, convective overshooting, and gravity wave breaking (Freytag et al., 2010; Medvedev and Yiğit, 2019; Borchert and Zängl, 2022). Supersonic flows and shock-driven transitions near the day–night terminator have also been proposed as potential sources of perturbations (Heng, 2012).

The circulation patterns and wind structures described above are not merely theoretical concepts as they have been both predicted by numerical simulations (Cooper and Showman, 2005; Menou and Rauscher, 2009; Heng, Menou, and Phillipps, 2011; Rauscher and Menou, 2013; Perna, Heng, and Pont, 2012; Dobbs-Dixon and Agol, 2013; Showman, Lewis, and Fortney, 2015; Tan and Komacek, 2019) and inferred from observations (Cowan, Agol, and Charbonneau, 2007; Snellen et al., 2010; Louden and Wheatley, 2015; Brogi et al., 2016; Seidel et al., 2020). Observational techniques such as thermal phase curves and high-resolution spectroscopy provide key constraints on wind speeds, heat redistribution efficiency, and the spatial distribution of atmospheric temperatures. Interpreting these measurements requires a detailed understanding of the coupling between thermal structure and dynamics, and this is

where atmospheric models play a central role. Atmospheric models vary from the simplest to the most complex: from simplified one-dimensional radiative–convective profiles, through two-dimensional frameworks capturing longitudinal or latitudinal variability, to fully three-dimensional GCM, as seen in the previous paragraphs, most of them which couple radiative transfer, fluid dynamics, and chemistry. In addition, local high-resolution simulations are often used to study small-scale processes such as instabilities, shocks, or cloud formation in much more physical detail. Together, these tools aim to reproduce, with varying degrees of complexity and physical fidelity, the rich and extreme atmospheric environments of HJs and to link the observations with the real physical processes in the atmosphere.

However, most atmospheric models remain under the hydrodynamic scenario without explicitly including magnetic effects, despite their potential importance in the hottest, partially ionized atmospheres. In many GCM studies, magnetic Lorentz forces are either neglected or represented through a simple Rayleigh-drag parametrization, which cannot capture the full spatial and temporal variability of magnetic interactions or via estimates of magnetic drag within hydrodynamical models (Rauscher and Menou, 2013; Beltz et al., 2022), see Chapter 4 for an example of how it is implemented. A few 3D models have begun to incorporate magnetohydrodynamic (MHD) effects self-consistently (Batygin, Stanley, and Stevenson, 2013; Rogers and Komacek, 2014; Rogers and Showman, 2014; Rogers and McElwaine, 2017; Hindle, Bushby, and Rogers, 2021), allowing for a more realistic treatment of magnetic drag, and its impact on wind patterns, jet structure, and heat redistribution. In possibly the most advanced work in this respect so far, Rogers and McElwaine (2017) demonstrated that a self-sustaining atmospheric dynamo can operate within the thin, stably stratified atmosphere of a HJ, driven by spatial variations in electrical conductivity arising from the strong day–night temperature contrast. These works show that magnetic coupling can significantly slow the equatorial jet, alter global circulation patterns, and deposit energy into the deep atmosphere through ohmic heating mechanism, which will be discussed in the next section.

On the other hand, such global simulations cannot resolve small-scale turbulence atmospheric effects due to the intrinsic computational limitations (i.e., the achievable resolution) in capturing all relevant scales. Turbulence in HJ atmospheres has been investigated separately in a number of works, but with little explicit focus on magnetic effects. For example, Li and Goodman (2010) analysed the generation of turbulence in circulation models via a linear analysis and 2D hydrodynamical simulations with laminar horizontal forcing, finding that turbulent and vertical mixing dominate the dissipation through recurrent KHI triggered by the zonal winds. Youdin and Mitchell (2010) assumed turbulent flows and studied, in a semi-analytical framework, how turbulent diffusion and energy deposition modify the radiative equilibrium profile, proposing a so-called mechanical greenhouse effect whereby turbulence transports heat into deeper atmospheric layers. Ryu, Zingale, and Perna (2018) employed box simulations to examine turbulence generation via the shear layer associated with strong upper-atmosphere zonal winds, although their purely hydrodynamic setup precluded any treatment of magnetic field induction. Complementary to these studies, other works (Liu, Goldreich, and Stevenson, 2008; Batygin and Stevenson, 2010; Batygin, Stevenson, and Bodenheimer, 2011; Knierim, Batygin, and Bitsch, 2022; Viganò et al., 2025) have provided semi-analytical estimates of the magnetic field induced by atmospheric winds, whose mechanism will be described in Chapter 2. However, there is still a lack of dedicated local MHD simulations exploring the non-ideal effects that are essential for understanding local magnetism, as well as how small-scale turbulence interacts with magnetic fields under the wide

range of ionization conditions expected in HJs atmospheres.

1.4.4 Inflated radii

Despite the remarkable progress in both observational capabilities and theoretical modelling, HJs still present open questions. Their thermal structures and atmospheric dynamics are now relatively well-characterised for a growing sample, and key processes such as heat redistribution, chemical composition, and atmospheric escape have been explored in detail. However, one of the most intriguing open questions concerning HJs is the physical origin of their inflated radii, which remains a matter of active debate within the scientific community.

Many of them exhibit sizes significantly larger, up to $R \sim 2R_J$, than predicted by standard cooling and contraction models for their measured masses and estimated ages (Showman and Guillot, 2002). This radius anomaly has been well documented in previous works, see Fig. 1.9. In this plot, the red dashed line represents an evolutionary model for a 1 M_J (Jovian mass), purely made of H/He, including stellar irradiation as the only external heating source, at an age of 4.5 Gyr. Most observed planets lie above this curve, indicating that additional physical processes, a part from irradiation, must be acting to slow planetary contraction and maintain higher radii values over gigayear timescales. Those planets falling below the red dashed curve are likely enriched in heavy elements which increase their bulk density and lead to smaller radii (Burrows et al., 2007; Fortney, Marley, and Barnes, 2007).

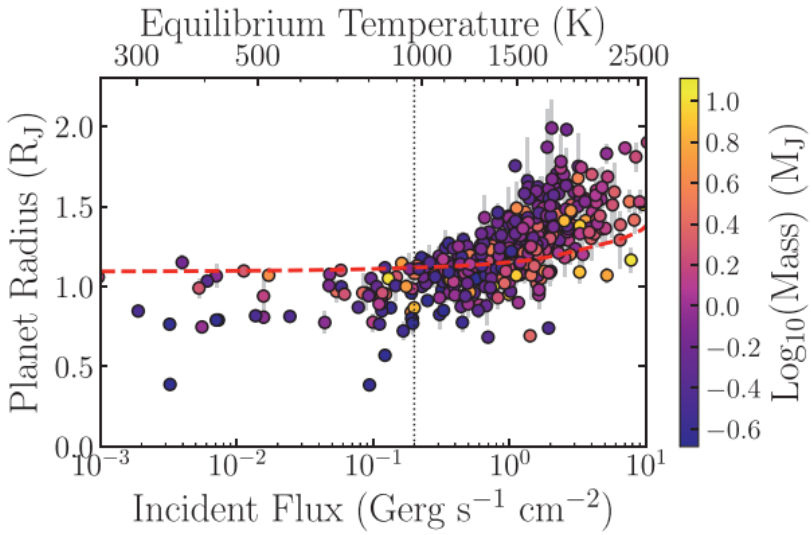

FIGURE 1.9: Radius of giant exoplanets plotted against their incident flux (and equilibrium temperature) and coloured by mass on the log scale. The red dashed line shows an evolutionary model for a Jupiter-mass pure H/He planet without any additional inflation effects at an age of 4.5 Gyr. The vertical dashed line marks the approximate flux threshold below which no radius inflation is observed, from Thorngren and Fortney, 2018a.

The discrepancy is seen for highly irradiated planets, $T_{eq} \gtrsim 1000$ K, whereas cooler gas giants do not show such inflation (Miller and Fortney, 2011; Brice-Olivier and Seagers, 2011; Laughlin et al., 2011). The clear trend between radii and irradiation suggests that the mechanisms responsible for radius inflation are strongly linked to the intense stellar flux received from the host star, or equivalently to T_{eq}

(Laughlin et al., 2011). Notably, Thorngren and Fortney (2018b) showed that the fraction of incident stellar flux that must be transformed into deep interior heating to reproduce the observed radii reaches a maximum for planets with intermediate equilibrium temperatures, around $T_{\rm eq} \approx 1600$ K. This indicates a continuous deposition of heat, corresponding to up to a few percent of the irradiation flux (Komacek and Youdin, 2017), that slows down their long-term cooling, or even re-inflates them (Lopez and Fortney, 2016; Komacek et al., 2020).

In order to update this picture, we performed a new population analysis using the latest exoplanetary parameters from NASA Exoplanet Archive. This study has been part of the paper Viganò et al., 2025. As of June 1$^{\rm st}$, 2025, there were a total of 1899 confirmed gas giants with known masses in the range considered here, $M \in [0.5,13]\ M_J$. The upper limit of the range is simply the Deuterium-burning boundary with brown dwarfs. The lower limit is conservatively in agreement with other studies, e.g. Sestović, Demory, and Queloz, 2018, who excluded the lightest planets whose masses and radii might be affected by mass loss.

Among that sample, only 470 planets have available information on the quantities we are interested: mass M, radius R, age t, and equilibrium temperature T_{eq}. Since the radius is our main observable to compare with, we have excluded data with high errors in radius, and only selected those planets with errors less than 25%. Moreover, we have discarded those planets with only upper limits on the mass and without associated mass uncertainties. We also excluded 7 planets younger than 100 Myr, since at those ages the planet shrinking has some memory of the initial entropy and the very early ages, which is unknown, therefore introducing additional free parameters in the problem.

These selection criteria yield a data set of 424 gas giants. Figs. 1.10 and 1.11 show the measured values of R versus T_{eq} and the distribution of radii for different planets grouped by different ranges of temperature with 250 K-wide bins centered around values in the range $T_{eq} = [1000, 2500]$ K, with the associated mean and standard deviation values, $\bar{R}$ and σ_R represented by grey boxes. As mentioned before, the radii of the planets increase as the equilibrium temperature rises (e.g., Menou 2012), for planets with $T_{\rm eq} \gtrsim 1000$ K. The average radius increases up to $\bar{R} = 1.48 \pm 0.18\ R_J$ for the $T_{eq} \in [1875, 2125]$ K sample, and up to $\bar{R} = 1.53 \pm 0.19\ R_j$ for the $T_{eq} \in [2125, 2375]$ K sample (which is, however, sparsely populated). The colored lines in the figure show the best-fitting trends of the form $R/R_j = C + A \log(F_{\rm irr}/F_s)$, where we fix $F_s = 0.227$ MW m^{-2}, i.e. the irradiation flux corresponding to $T_{\rm eq} = 1000$ K. The fit is performed for planets with $T_{\rm eq} \gtrsim 1000$ K, across different mass ranges, as reported in Table 1.1. Such fits are comparable to the values provided by Sestović, Demory, and Queloz, 2018, who fitted the same functional form for planets with $F \geq F_s$, but they let F_s to vary. Other older studies (Laughlin et al., 2011; Enoch, Cameron, and Horne, 2012) use different functional forms, all non-linear with T_{eq} as well, with a sample a few times smaller. Considering the differences in samples and functional forms, our results can be considered overall consistent with previous works but with an updated sample of the HJs detected.

These trends show that lighter HJs ($M \sim 0.5 - 1.5\ M_J$) have a statistically significant steeper dependence with irradiation ($A \sim 0.5$), compared to the heavier ones. The extremely massive HJs, $M \gtrsim 8\ M_J$ (close to the border with brown dwarfs) barely show signs of inflation. Such trend with mass is well known, (e.g. Sestović, Demory, and Queloz 2018; Thorngren 2024 and references within), and, at first level, can be understood by the gravity counteracting inflation, for a given rate of deposited heat (see also e.g. Lopez and Fortney 2016 for a brief discussion).

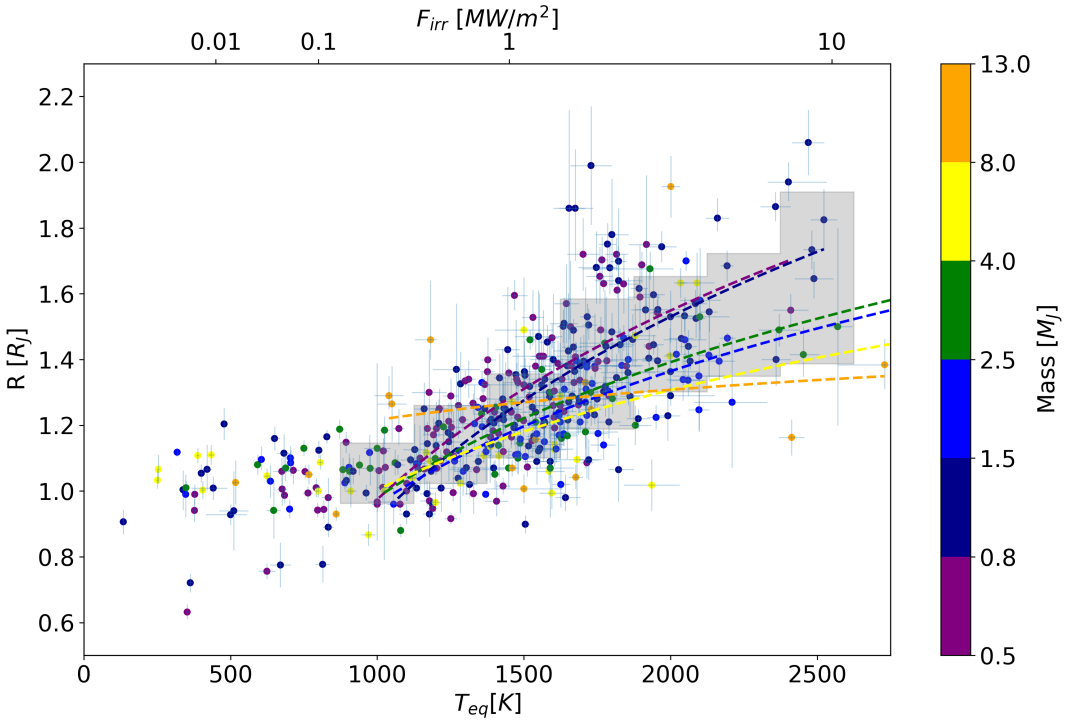

FIGURE 1.10: Planetary radius R versus T_{eq} or, equivalently, irradiated flux $F_{\rm irr} = 4\sigma_{\rm sb}T_{\rm eq}^4$.. Colors indicate the mass range: purple [0.5,0.8) M_J, dark blue [0.8,1.5) M_J, blue [1.5,2.5) M_J, green [2.5,4) M_J, yellow [4,8) M_J and orange [8,13] M_J. Lines show the best fits reported in Table 1.1 for planets within each mass range and with $T_{\rm eq} > 1000$ K. Grey boxes indicate the mean and standard deviation of the observed radius $\bar{R} \pm \delta_R$ for all HJs within 250 K-wide $T_{\rm eq}$ bins where radius inflation starts to appear and enough planets are available. For clarity, three uHJs with $T_{\rm eq} > 3300$ K are excluded from the plot but included in the statistics. The dataset corresponds to 424 Jupiter-like exoplanets from our restricted selection (see text), excluding seven planets younger than 100 Myr. Taken from our recent HJ evolutionary study Viganò et al., 2025.

In Viganò et al., 2025 we assessed this dispersion in terms of the most important factors intervening in the planetary long-term cooling, considering the dependence of the modelled radius evolution on observables (T_{eq}, M) and on the deposition of heat, as a mechanism which will be explained later to inflate the planet. Factors like composition, mass core can also contribute to the dispersion of the sample.

Although the correlation between irradiation and radii is evident, the effects of irradiation alone are not quantitatively sufficient to explain the large radii inflation, given the shallowness of the absorbing layer of irradiation: the blanketing effect of the shallow radiation-absorbing layers (above a few bars typically) can keep the planet relatively warm, slowing down the shrinking (i.e., cooling), but can only explain the inflation of up to typically $\sim 1.2 - 1.3\ R_J$, (Thorngren and Fortney, 2018a). For this reason, in the following subsection, we review the leading hypotheses proposed to explain this radius anomaly (see Thorngren, 2024 for a deep review), focusing on the physical mechanisms that could introduce the extra energy required and the observational evidence that supports or challenges each scenario.

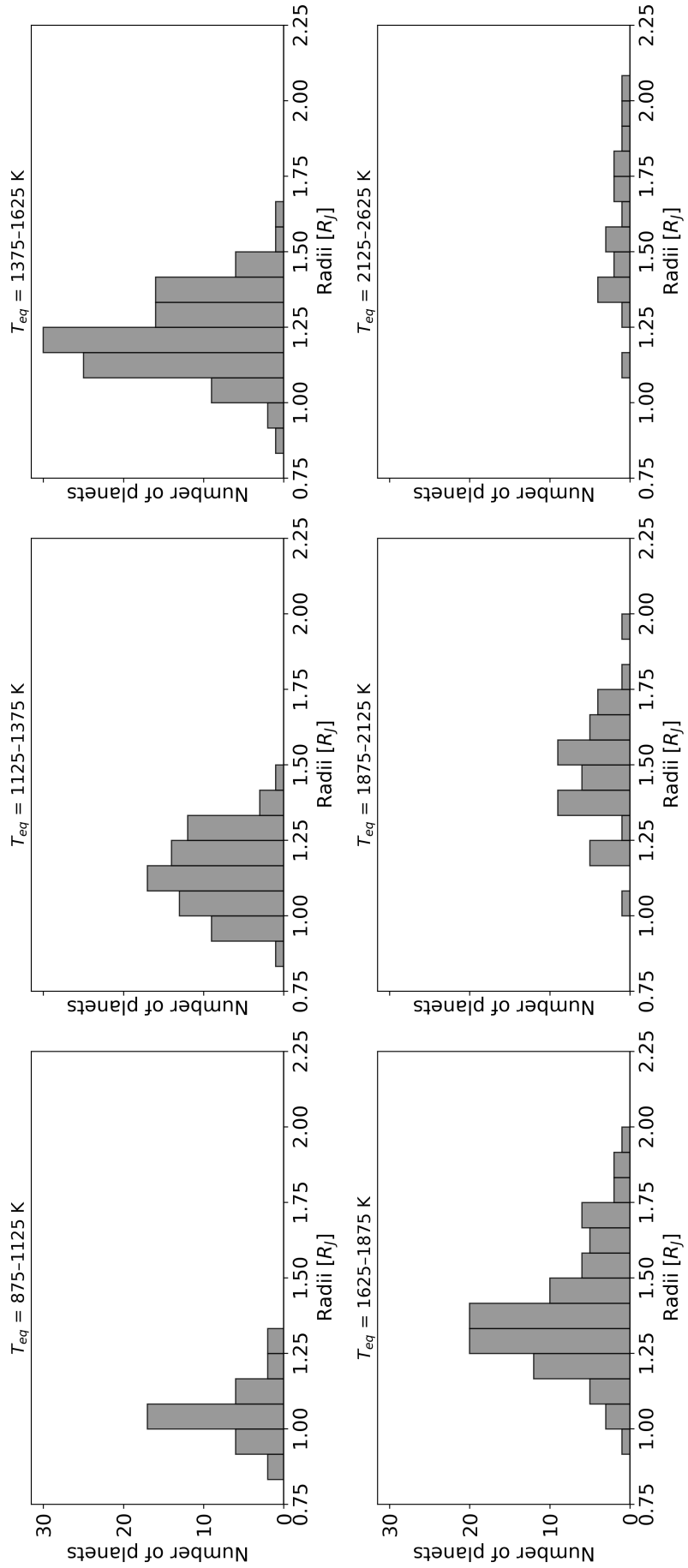

FIGURE 1.11: Histograms of the observed radii for the same T_{eq} ranges indicated by the grey boxes in Fig. 1.10. For the hottest HJs, the two highest-T_{eq} bins are combined due to the small number of planets in these ranges. The dataset corresponds to 424 Jupiter-like exoplanets from our restricted selection (see text), excluding seven planets younger than 100 Myr. From Viganò et al., 2025.

Mass [M_J]	Number	A	C
0.5-0.8	118	0.48 ± 0.04	0.97 ± 0.03
0.8-1.5	150	0.51 ± 0.04	0.92 ± 0.04
1.5-2.5	65	0.34 ± 0.04	0.96 ± 0.04
2.5-4	41	0.34 ± 0.05	0.98 ± 0.05
4-8	33	0.25 ± 0.08	1.00 ± 0.07
8-13	15	0.08 ± 0.15	1.22 ± 0.14

TABLE 1.1: Observed HJs trends as a function of mass range: number of objects with $T_{eq} \geq 1000$ K and best-fit parameters of the functional form $R/R_j = C + A \log(F/F_s)$, where F_s corresponds to the irradiation flux of $T_{eq} = 1000$ K.

Possible mechanisms

Several mechanisms have been proposed throughout the years to explain the inflated radii of HJ, which fall in two general categories: those that reduce the planet's rate of internal cooling, and those that deposit additional heat into the deep interior.

In their early stages, gas giants form in a hot, expanded state with large radii, then gradually contract as their interiors cool. Any process that slows this cooling will help maintain a higher internal temperature for longer. As gas giant's radius is directly tied to its internal temperature (Burrows et al., 1997; Guillot, 2005; Arras and Bildsten, 2006), slowing the cooling rate also slows its contraction over time. Without such a slowdown, HJs would cool and shrink to Jupiter-like radii within less than a gigayear (Guillot and Showman, 2002). Two main types of mechanisms have been proposed to limit this internal cooling. The first is increased atmospheric opacity, which elevates the radiative timescale in the planet's stably stratified envelope, trapping heat more effectively (Burrows et al., 2007). While this can slightly increase planetary radii, detailed models show that the effect is insufficient to explain the full range of observed inflation. The second is double-diffusive layered convection, a process that occurs when the mean molecular weight of the gas increases with depth. This compositional gradient acts as a stabilizing force that suppresses large-scale convective motions, even if the deeper layers are hotter. Instead of a single, well-mixed convective zone, the interior develops a series of thin convective layers separated by stably stratified regions, which transport heat much less efficiently. This reduced convective transport slows the escape of heat from the deep interior (Chabrier and Baraffe, 2007; Kurokawa and Inutsuka, 2015). Both mechanisms above struggle to explain the observed dependence of radius on incident flux for HJs, since they look to be quite independent to it.

The second class of mechanisms focuses on the active deposition of heat into the planetary interior. If enough energy is delivered deep within the convective layers, it can slow, or even counteract, the loss of internal energy, maintaining an inflated radius. The efficiency of this process depends on both the amount and depth of the deposited energy (Gu, Bodenheimer, and Lin, 2004; Spiegel and Burrows, 2013; Komacek and Youdin, 2017). There are two more studied categories of such heating mechanisms: tidal dissipation and the conversion of incident stellar flux into interior heat.

Tidal dissipation was the first internal heating mechanism proposed for HJs (Bodenheimer, Lin, and Mardling, 2001). In general, tidal dissipation occurs when the gravitational pull from the host star distorts the planet, creating a tidal deformation.

If this deformation is misaligned with the star–planet axis, internal friction develops as the planet's material is periodically stretched and compressed, converting orbital or rotational energy into heat. One form of tidal dissipation is eccentricity tides, which operate when the planet's orbit is not perfectly circular, note that this is not common in HJs due to the strong tidal damping. Variations in the planet–star distance along the orbit cause the tidal forces to change in strength and orientation, generating repeated flexing of the planet's interior. This flexing dissipates energy as heat while gradually circularizing the orbit (Ogilvie and Gu, 2003; Jackson, Greenberg, and Barnes, 2008; Ibgui and Burrows, 2009), and can explain radius anomalies in certain systems (Miller, Fortney, and Jackson, 2009; Leconte et al., 2010). Another form is thermal tides, where asymmetries in atmospheric mass due to heating generate torques that spin up the planet and cause dissipation via gravitational tides (Arras and Socrates, 2010; Socrates, 2013; Gu, Peng, and Yen, 2019). Thermal tides have been shown to provide a sufficient rotational perturbation and resulting dissipation to explain the radius anomaly (Arras and Socrates, 2010; Socrates, 2013) but the depth at which thermal tides deposit heat is uncertain (Gu, Peng, and Yen, 2019). However, thermal tides alone cannot robustly reproduce the observed flux–radius correlation across the whole sample of HJs.

The second type of deposited heating mechanism involves those mechanisms which convert incident stellar energy into interior heating. One of the first proposed mechanisms in this category involves shear instabilities in the deep atmosphere, which can deposit heat by dissipating the powerful $\sim$km s^{-1} winds of HJs (Guillot and Showman, 2002; Bodenheimer, Laughlin, and Lin, 2003). These fluid instabilities developed at regions where wind speeds drop sharply, convert kinetic energy into heat. Another related mechanism is large-scale vertical mixing in the deep atmosphere, which can drive a downward heat flux, transporting a fraction of the absorbed stellar energy to higher pressure regions. There, the energy can influence the planet's thermal evolution and slow its contraction or inflate the planet (Youdin and Mitchell, 2010; Tremblin et al., 2017; Sainsbury-Martinez et al., 2019; Sainsbury-Martinez et al., 2023). Finally, Ohmic dissipation, arising from the interaction between ionized atmospheric winds and the planetary magnetic field, has been widely discussed as an efficient way to deposit stellar energy at depth. Given its importance, it will be discussed in more detail in the next subsection. Finally, some works support the idea that several of these heating mechanisms can be at play within the observed sample (Sarkis, Mollière, and Mordasini, 2021).

1.4.5 Ohmic dissipation

Among the proposed mechanisms for HJ radius inflation, Ohmic dissipation is often considered one of the most promising, largely because it has been explored in greater quantitative detail than most alternatives. At the high temperatures of HJs, metals such as Na and K become partially ionized (Parmentier et al., 2018; Kumar et al., 2021; Dietrich et al., 2022), producing a weakly ionized atmosphere. The presence of strong charged winds, under a non-ideal environment, make the currents to dissipate as heat through the finite resistivity of the gas. The depth of the resulting dissipation depends on the atmospheric conductivity and wind structure: when conductivity is low, resistive damping confines currents to the upper radiative atmosphere, whereas at higher conductivity can close at higher pressures, potentially reaching the convective interior where the deposited energy has a stronger impact on the planet's long-term thermal evolution (Liu, Goldreich, and Stevenson, 2008; Batygin and Stevenson, 2010; Komacek and Youdin, 2017).

Moreover Ohmic dissipation efficiency changes with temperature as there are two competing effects that modify it: higher $T_{\rm eq}$ strengthens the winds and therefore the induced magnetic fields are stronger (the underlygin physics will be presented in Chapter 2), but also increases magnetic drag (Perna, Menou, and Rauscher, 2010a; Rogers and Komacek, 2014; Kumar et al., 2021; Benavides et al., 2022). The latter arises because HJs are expected to possess strong intrinsic magnetic fields (Cauley et al., 2019; Yadav and Thorngren, 2017), which couple with the atmospheric currents. This interaction generates induced magnetic forces that act against the circulation (see Fig. 1.12) and thereby reduce the Ohmic heating rate. Quantifying this coupling is crucial for determining the efficiency of Ohmic dissipation as possible mechanism for radius inflation.

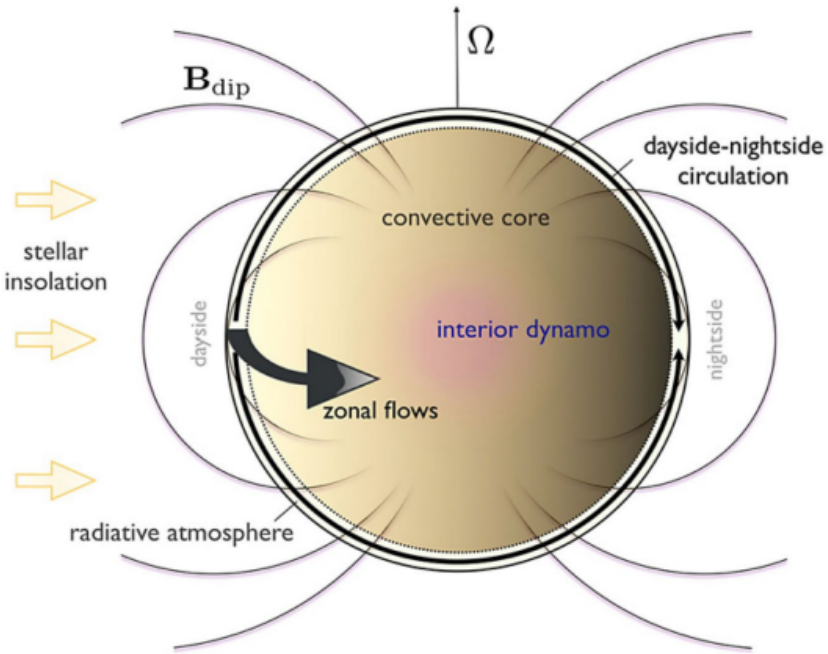

FIGURE 1.12: Schematic diagram showing the coupling between atmospheric circulation and the interior magnetic field of a HJ. Strong zonal winds in the atmosphere distort the planet's dipolar magnetic field ($B_{\rm dip}$), inducing electric currents. These currents can dissipate as heat either in the atmosphere or after penetrating into the convective interior. The magnetic field is generated by a dynamo in the deep convective core. Adapted from Batygin, Stanley, and Stevenson (2013).

Quantifying Ohmic dissipation requires prescriptions for both the radial conductivity profile and the distribution of electric currents and Ohmic dissipation is given by:

$$Q_j = \frac{J^2}{\sigma} \tag{1.3}$$

where Q_j corresponds to the energy dissipated via Ohmic dissipation per unit volume, σ to the electric conductivity and J is the modulus of the current density vector, calculated as: $\mathbf{J} = (\nabla \times \mathbf{B})/\mu_0$, where $\mathbf{B}$ is the magnetic field and μ_0 is the vacuum magnetic permeability defined as $\mu_0 = 4\pi \times 10^{-7} \mathrm{H\,m^{-1}} \approx 1.257 \times 10^{-6}\ \mathrm{N\,A^{-2}}$.

The ability of the atmosphere to sustain such currents is set by its electrical conductivity, which depends on the degree of ionization. Fig. 1.13 shows how the conductivity of key atmospheric species varies with temperature: K, with low ionization potential, dominate the ionization fraction for temperatures T ∼1000–2200 K. For even hotter regions, sodium, calcium and even iron, in some extreme cases, may contribute to the conductivity. Once ionized, these species allow the atmospheric flow to maintain electric currents in the presence of the planetary magnetic field, with the magnitude and depth of Ohmic dissipation determined by the conductivity profile, itself dependent on both local temperature and pressure, as will be presented in the next chapter.

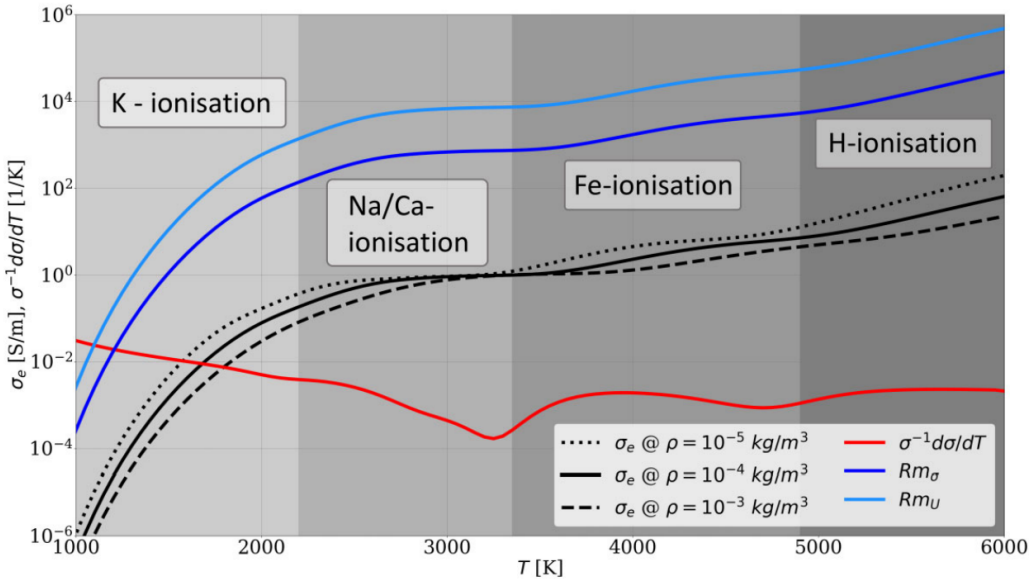

FIGURE 1.13: Electrical conductivity as a function of temperature for different species relevant in HJs atmospheres along three isochores with density, ρ= 10^{-3}-10^{-5} km/m^3 (black solid, dashed and dotted line). The grey shaded areas indicate the main donors of electrons. The red profile shows the temperature variability of the electrical conductivity. The blue profiles show two magnetic Reynolds numbers based on the solid conductivity profile (see 4.3.1 for a full description onf the magnitude), a flow velocity of U = 2×10^3 m/s (Snellen et al., 2010) and d_U = 3×10^6 m (Wicht, Gastine, and Duarte, 2019) as length scale. Both curves cross unity around 1300 or 1500 K, suggesting that the linear estimate of induction is not valid at temperatures higher than that. K, with low ionization potential, dominate the ionization fraction above ∼ 1000–1200 K, enabling the formation of atmospheric currents when coupled with strong winds and magnetic fields. This conductivity is a key factor controlling the efficiency of Ohmic dissipation. From Dietrich et al., 2022.

Numerous studies have explored the viability of Ohmic dissipation as a driver of radius inflation from different perspectives. Evolutionary and analytical works have examined whether Ohmic dissipation can provide sufficient interior heating to explain inflated radii (Batygin and Stevenson, 2010; Huang and Cumming, 2012; Menou, 2012; Wu and Lithwick, 2013; Ginzburg and Sari, 2016; Knierim, Batygin, and Bitsch, 2022; Viganò et al., 2025). In parallel, atmospheric and circulation studies have focused on how magnetic drag and induced currents operate in HJs atmospheres and how they affect the magnitude and distribution of Ohmic dissipation

heating (Perna, Menou, and Rauscher, 2010a; Perna, Menou, and Rauscher, 2010b; Rogers and Komacek, 2014; Rogers and Showman, 2014; Rogers and McElwaine, 2017; Hardy, Cumming, and Charbonneau, 2022; Beltz et al., 2022). One of the most recent studies addressing Ohmic dissipation in this context is presented by Viganò et al., 2025 (related to this thesis), who coupled the atmospheric induction to the internal dynamo evolution, via the afore-mentioned convective heat flux scaling laws for the internal fields (Christensen, Holzwarth, and Reiners, 2009). Our results highlight the role of electrical conductivity profiles shaped by both thermal and pressure ionization, and show how the interplay between wind speeds and magnetic field evolution can modulate Ohmic dissipation efficiency over gigayear timescales.

Most atmospheric and circulation studies have adopted simplifying assumptions to model magnetic effects. They usually rely on the perturbative induction regime (sometimes called linear, e.g. Dietrich et al. 2022), where the magnetic field induced by the winds is a small perturbation to the intrinsic planetary field, and neglects some non-ideal effects such as Hall currents, ambipolar diffusion. These approximations are useful for cooler HJs (Batygin, Stanley, and Stevenson, 2013; Dietrich et al., 2022; Soriano-Guerrero et al., 2023), but they break down when the induced field becomes comparable to the background one or when non-ideal processes influence the coupling between winds and magnetic fields. In this thesis, I investigate non-ideal MHD effects, considering the effect of an imposed, stable atmospheric wind, together with small-scale perturbations. I explicitly explore the non-linear regime where the induced field is comparable or larger than the planetary one. This approach allows to evaluate how local magnetic effects are shaped by atmospheric dynamics and how this affects efficiency of Ohmic dissipation locally for both HJs and uHJs.

1.5 Dissertation overview

This thesis explores the role of magnetic effects at the atmospheric level for HJs and uHJs. The work presents local three-dimensional MHD simulations, together with analytic theory and numerical tools, to study how large-scale winds and small-scale perturbation can combine locally.

Chapter 2 develops a general numerical framework to generate 3D MHD local simulations of HJ atmospheric magnetised columns. It introduces the governing physical equations (EOS, ideal gas law, and MHD equations), as well as the numerical setup, providing the basis for a systematic investigation of how wind and small-scale perturbations interact under magnetic influence in a non-linear regime, and how they contribute to Ohmic dissipation at the local level.

Chapter 3 applies this framework to the first local MHD study of uHJ atmospheres in the non-linear regime. We focus on two key processes: the winding of magnetic fields by strong zonal winds and the generation of small-scale turbulence. Using simplified ideal MHD simulations under an isothermal setup with analytical wind profiles, we explore how currents are induced and toroidal fields amplified at the very high temperatures ($T \gtrsim 3000$ K) characteristic of uHJs. This chapter provides a first quantitative assessment of the combined effects in shaping local magnetic induction.

Chapter 4 extends this work by incorporating non-ideal MHD effects, Ohmic, Hall, and ambipolar diffusion, into the analysis. Building on the idealised models of Chapter 3, we use thermodynamical and wind profiles from GCM simulations (performed by collaborators) to solve the induction equations in a plane-parallel

framework. Focusing on the substellar point, we evaluate how conductivity affects the efficiency of magnetic induction. This study bridges idealised simulations with more realistic atmospheric conditions, obtaining winding effects and, local Ohmic dissipation for a representative sample of HJs of different temperatures as well as the effect of other non-magnetic terms.

Chapter 5 presents the first fully three-dimensional non-ideal MHD simulations of HJ atmospheres, combining both large-scale wind shear and small-scale perturbations. By comparing these results with one-dimensional models, we quantify the relative role of perturbations in magnetic induction and dissipation.

Chapter 6 summarises the main results of the thesis and discusses their implications for the study of HJs.

In summary, this thesis contributes to the field of HJs science in three main ways. First, it provides a methodology to quantify local magnetic effects in 3D exoplanetary atmospheres through systematic local simulations. Second, it investigates the impact of non-ideal magnetic effects at the atmospheric level. Finally, it evaluates how small-scale perturbations influence magnetic induction, thereby advancing our understanding of the coupling between atmospheric dynamics and magnetism in irradiated gas giants.

2

Modeling magnetised atmospheric columns of hot Jupiters

In what follows, we provide all the ingredients to perform local, narrow ($\sim 1^\circ \times 1^\circ$) atmospheric simulations at the substellar point of the radiative region of HJ atmospheres, covering pressure ranges from 10–1000 bar, depending on the simulation, down to 0.01–0.0005 bar. These numerical box simulations are designed to investigate both ideal and non-ideal MHD effects, as well as to examine how winds and small-scale perturbations interact under magnetic influence, ultimately affecting the amount of Ohmic dissipation generated at the local level in HJs. This setup constitutes the common basis for the main studies of this thesis, Soriano-Guerrero et al., 2023; Soriano-Guerrero et al., 2025b; Soriano-Guerrero et al., 2025a, presented in the subsequent chapters of this thesis. Note that the input parameters are characteristic of each specific model and will be presented in detail in the following chapters.

2.1 Physical equations

2.1.1 Equation of state and hydrostatic equilibrium

We consider the gas to follow the ideal gas EOS:

$$p = \rho R_\mu T = (\gamma - 1)\rho e \,, \tag{2.1}$$

where p is the gas pressure, ρ the mass density, e the specific internal energy, T the temperature, γ the ideal gas index here fixed at $\gamma = 1.4$, $R_\mu = k_b/\bar{m} = (8.254/\mu) \times 10^3$ J/(kg K) the specific gas constant, with k_b the Boltzmann constant, $\bar{m} = \mu m_u$ the mean molecular mass of the gas and m_u the atomic mass unit. The mean molecular weight μ depends on the chemical composition and on the degree of ionization. As commented in the last chapter, HJ atmospheres are arguably dominated by H/He and traces of heavier atoms and molecules; as a reference, in the Solar System, atmospheres of ice and gas giants have $\mu \sim (2 - 2.7)$. However, such values are possibly

lower in HJs due to partial ionization and dissociation of molecules, H_2 in particular (see e.g. Fig. 1 of Parmentier et al. 2018). For simplicity, hereafter we consider a homogeneous value $\mu = 2$, keeping in mind that the results of our MHD models depend very little on μ (compared to other parameters).

Under the presence of gravity directed downwards in the z direction, $\mathbf{g} = -g\hat{z}$, the equation of hydrostatic equilibrium reads

$$\frac{dp}{dz} = -\rho g \,. \tag{2.2}$$

Note that the gravity can be calculated as:

$$g = \frac{GM_P}{R_P^2} \,, \tag{2.3}$$

where M_P is the mass of the planet, R_P the radii of the planet and G is the gravitational constant. We assume the gravitational acceleration to be constant throughout the atmospheric column, as its mass and thickness are negligible compared to the planet's enclosed mass and radius. We consider values of g from the total planetary mass and radius. Considering the enclosed values (instead of total), g would vary by at most $\sim$ 10% across the range of pressures considered. Eq. 2.2 is solved accordingly to the setup of the simulated column. This equation is solved according to the specific g as well as the p, T and ρ profiles for each simulation, which will be described in each specific case.

2.1.2 MHD equations and magnetic effects on the atmosphere

The fluid in the atmosphere of HJs is partially ionized, mainly thanks to the presence of Na^+ and K^+ due to the high local temperatures, which typically range between 1000 and 3000 K (see §1.4.5 for details). To describe the dynamics of these electrically conducting fluids in the presence of the planetary magnetic field, we use the MHD framework, which couples fluid dynamics with Maxwell's equations. In the following, we present and explain in detail the full set of MHD equations, which are defined as:

$$\frac{\partial \rho}{\partial t} + \nabla \cdot (\rho \mathbf{v}) = 0 \,, \tag{2.4}$$

$$\frac{\partial \mathbf{S}}{\partial t} + \nabla \cdot \left[\rho \mathbf{v}\mathbf{v} + \left(p + \frac{B^2}{2\mu_0} \right) \mathbf{I} - \frac{\mathbf{B}\mathbf{B}}{\mu_0} \right] = \rho \mathbf{g} + \mathbf{F}, \tag{2.5}$$

$$\frac{\partial U}{\partial t} + \nabla \cdot \left[\left(U + p + \frac{B^2}{2\mu_0} \right) \mathbf{v} - (\mathbf{v} \cdot \mathbf{B}) \frac{\mathbf{B}}{\mu_0} \right] = \rho \mathbf{v} \cdot \mathbf{g} + \mathbf{v} \cdot \mathbf{F} - \frac{p - p_0}{\tau_{\text{cool}}} + Q_j, \tag{2.6}$$

$$\frac{\partial \mathbf{B}}{\partial t} = -\nabla \times \mathbf{E} \tag{2.7}$$

which correspond to the continuity, momentum, energy and induction equations, respectively.

In the continuity equation (eq. 2.4), the first term, $\partial\rho/\partial t$, represents how the density ρ changes over time at a fixed point in space. The second term, $\nabla \cdot (\rho \mathbf{v})$, where $\mathbf{v}$ is the velocity of the fluid, corresponds to the divergence of the mass flux; this

term measures the net amount of mass flowing out of (if positive) or into (if negative) a small volume. Physically, this equation states that the rate of change of mass within a given volume is balanced by the net mass flow across its boundaries. In other words, mass cannot be created or destroyed: it can only move and redistribute within the system.

The second equation is the momentum equation (eq. 2.5). On its left-hand side, the first term, $\partial_t \mathbf{S}$, where $\mathbf{S} = \rho\mathbf{v}$ is the momentum density, represents the temporal change of momentum in the fluid. The second term, $\nabla \cdot (\rho\mathbf{v}\mathbf{v})$, describes the advection of momentum, i.e., how the bulk flow transports momentum from one place to another. The third term, $\nabla \cdot \left(p + \frac{B^2}{2\mu_0}\right)\mathbf{I}$, is the pressure gradient term where $\mathbf{I}$ corresponds to the identity tensor. This term represents the isotropic forces acting on the fluid due to thermal pressure and the magnetic pressure. The fourth term, $\nabla \cdot \left(\frac{\mathbf{BB}}{\mu_0}\right)$, corresponds to the magnetic tension term, which accounts for the directional forces arising from the curvature and orientation of magnetic field lines.

On the right-hand side, the term $\rho\mathbf{g}$ represents the gravitational force density, i.e., the force per unit volume from the planet's gravity; and $\mathbf{F}$ corresponds to any external forcing, which will be described in detail in the following section. Overall, the physical interpretation of the momentum equation is that it describes the conservation of momentum density for a magnetized fluid, stating that the rate of change of momentum density in a fluid element is balanced by the sum of forces acting on it.

The third equation, eq. 2.6, is the energy equation, where U corresponds to the total energy density, defined as

$$U = \rho e + \frac{1}{2}\left(\rho v^2 + \frac{B^2}{\mu_0}\right) = \frac{p}{\gamma - 1} + \frac{1}{2}\left(\rho v^2 + \frac{B^2}{\mu_0}\right). \tag{2.8}$$

In this expression, the first term, $\frac{p}{\gamma-1}$, is the internal energy density, $\frac{1}{2}\rho v^2$ is the kinetic energy density, and $\frac{B^2}{2\mu_0}$ is the magnetic energy density. In eq. 2.6, the term $\frac{\partial U}{\partial t}$ on the left-hand side represents the local time derivative of the total energy density, while the divergence term $\nabla \cdot \left(U + p + \frac{B^2}{2\mu_0}\right)$ accounts for the advection of total energy by the fluid flow, including the transport of kinetic, thermal, and magnetic energy, along with the work done by pressure and magnetic pressure. The final divergence term, $\nabla \cdot \left[(\mathbf{v} \cdot \mathbf{B})\frac{\mathbf{B}}{\mu_0}\right]$, corresponds to the Poynting flux from magnetic tension, representing the transport of electromagnetic energy due to the motion of the plasma through the magnetic field. On the right-hand side, the term $\rho\mathbf{v} \cdot \mathbf{g}$ represents the work done by gravity, while $\mathbf{v} \cdot \mathbf{F}$ corresponds to the work done by external forces. In the cooling term, $\frac{p-p_0}{\tau_{\rm cool}}$, p_0 corresponds to the background pressure, as explained below. This cooling term is implemented in the code through its inverse, $\nu_{\rm cool} = \tau_{\rm cool}^{-1}$, and acts to prevent an unphysical increase of internal energy, which would otherwise raise the temperature and sound speed. This effective cooling term, inspired by several other studies, e.g. Batygin, Stanley, and Stevenson (2013), Rogers and Komacek (2014), Rogers and Showman (2014), and Rogers and McElwaine (2017)[1], allows us to regulate thermal buildup. Here we set it to $\nu_{\rm cool} = 0.1\ \nu_{\rm cool*}$ (see details in § 2.2.2 for the * definition). The cooling timescale is chosen to be short enough

[1] In the anelastic approximation, where temperature rather than energy is evolved, the term is usually written as $\partial_t T + \cdots = \cdots - T_1/\tau_{\rm cool}$ where in this case $\nu_{cool} = [(\gamma - 1)\tau_{cool}]^{-1}$.

to avoid excessive heating, yet long enough to preserve finite perturbations in temperature and pressure. Moreover it maintains hydrostatic stability for our setup and numerical method (see Appendix C.1). Finally, the term Q_j accounts for Ohmic heating, as defined in § 1.4.5, representing the dissipation of currents in resistive regions. Altogether, this equation expresses the conservation and redistribution of energy in a magnetized plasma, accounting for mechanical work, magnetic transport, energy losses, and dissipative heating.

The fourth is the induction equation, eq. 2.7, in which **E** corresponds to the electric field. This equation will be discussed below, as it involves several aspects of particular importance for this thesis.

Induction equation

In the atmospheres of HJs, the motion of an electrically conducting fluid in the presence of a planetary magnetic field gives rise relevant local magnetic induction processes as well as other minor effects. To accurately capture these effects, the magnetic field evolution must be described by the induction equation (eq. 2.7), in which the electric field **E** is defined as:

$$\mathbf{E} = -\mathbf{v} \times \mathbf{B} + \frac{\mathbf{J}}{\sigma} + \frac{\mathbf{J} \times \mathbf{B}}{e n_e} - \frac{(\mathbf{J} \times \mathbf{B}) \times \mathbf{B}}{\nu_{in} \rho_i} \tag{2.9}$$

which follows from Faraday's law combined with a generalized Ohm's law including non-ideal terms. The first contribution on the right-hand side, the so-called ideal term, accounts for the advection, while the additional non-ideal terms represent Ohmic, Hall effect, and ambipolar diffusion, respectively, each modifying the field through dissipation, reorientation, or redistribution mechanisms.

First, the term $\mathbf{v} \times \mathbf{B}$ corresponds to the advective part of the electromotive force, arising from the transport and distortion of the magnetic field by the moving plasma. When only this term is retained in the induction equation, the system is refered to as *ideal MHD*. In HJs, where the large-scale background magnetic field is expected to be of the order of a few gauss, the presence of strong atmospheric winds can locally induce a substantial magnetic component in the wind direction through winding, the stretching and reorientation of the background field by velocity shear. This process can amplify the magnetic field well above its background value. When such amplification occurs, the system enters the non-linear regime (as used in Dietrich et al., 2022), in which the induced field is comparable to or larger than the original one, and the magnetic Reynolds number, $\mathcal{R}m$ is high (see 4.3.1 for a full description of the magnitude):

$$\mathcal{R}m = \mu_0 \sigma v_l L_l \gg 1, \tag{2.10}$$

where v_l and L_l are the characteristic velocity and length scale of the flow.

The second term $\frac{\mathbf{J}}{\sigma} = \mu_0 \eta \mathbf{J}$, where $\eta = 1/\sigma$ is the magnetic resistivity, corresponds to the Ohmic diffusion or dissipation. This term represents the resistive dissipation of magnetic fields due to finite conductivity of the atmosphere caused by the presence of ionised particles. This currents under a non ideal environment converts magnetic energy into thermal energy via Ohmic heating. The electrical conductivity, which regulates the Ohmic term, is calculated locally along the whole vertical column considering the classical formula, e.g. Draine, Roberge, and Dalgarno, 1983:

$$\sigma(T, p) = \frac{x_e(T, P)}{\langle \sigma_c v_{en} \rangle (T)} \frac{q^2}{m_e}, \tag{2.11}$$

where q is the elementary charge, m_e is the electron mass, $\langle \sigma_c v_{en} \rangle$ is the momentum transfer rate coefficient (average of the product between the momentum-transfer cross section σ_c and the relative speed v_{en}) between electrons and neutrals (the dominant channel), which depends on the temperature:

$$\langle \sigma_c v_{en} \rangle (T) = 10^{-19} \left(\frac{128 k_B T}{9\pi m_e} \right)^{1/2} \mathrm{m^3\,s^{-1}}\,. \tag{2.12}$$

As explained before, several species can contribute to the conductivity of the atmospheric fluid. However, for simplicity, we only consider the dominant contribution, K^+, to the electron fraction x_e, and evaluate the latter via the following expression as in Balbus and Hawley, 2000:

$$x_e = \frac{n_e}{n_n} = 6.47 \times 10^{-13} \left(\frac{a_K}{10^{-7}} \right)^{1/2} \left(\frac{T}{10^3} \right)^{3/4} \left(\frac{2.4 \times 10^{15}}{n_n(T,P)} \right)^{1/2} \frac{\exp\left(-\frac{25188}{T}\right)}{1.15 \times 10^{-11}}, \tag{2.13}$$

where $n_n \simeq \rho/(\mu m_u)$ is the neutral particle density, n_e is the number density of electrons and a_K is the potassium mass fraction ($\sim 10^{-7}$ in the Sun).

Eq. 2.11 is an analytical approximation to the Saha equation, strictly valid if there are no other ionized elements, and if x_e itself is less than the element mass fraction a_K. At high temperatures $T \gtrsim 2500$ K, this approximation becomes less reliable; however, we checked that the results of Kumar et al., 2021, who solved the full Saha equation including a more diverse chemical composition, agree within a factor of a few maximum, in the hottest regions. Given that the conductivity varies by orders of magnitude across the domain here considered due to the density and temperature variations, we consider the potassium-only analytical approximation adequate for our purposes (see Appendix A for further details).

The third term represents the Hall effect, which arises from the fact that the electric current $\mathbf{J}$ is mainly carried by electrons, whose velocity differs from the bulk plasma velocity set by the ions. This relative motion produces a drift perpendicular to the magnetic field without directly dissipating energy. The Hall effect becomes relevant in weakly ionized or low-density plasmas and can promote the formation of small-scale magnetic structures. Note that from now on the prefactor will be denoted as $f_h := 1/(e\, n_e)$

Finally, the forth term corresponds to the ambipolar diffusion. This term arises from the drift between ions (whose velocity is v_i) and neutrals (whose velocity is v_n) in partially ionized plasmas and can be evaluated as:

$$v_i - v_n = \frac{\mathbf{J} \times \mathbf{B}}{\rho_i \nu_{in}}\,. \tag{2.14}$$

in this term ρ_i is the mass density of ions while ν_{in} the collision rate between ions and neutrals, which, for an ideal, classical gas, is given by (Pandey and Wardle, 2008; Draine, Roberge, and Dalgarno, 1983):

$$\nu_{in} = \rho_n \frac{\langle \sigma_c v_{in} \rangle}{\bar{m}_i + \bar{m}_n} \simeq \rho \frac{\langle \sigma_c v_{in} \rangle}{\bar{m}_i + \mu m_u}\,, \tag{2.15}$$

where ρ_n is the neutral particle density, $\langle \sigma_c v_{in} \rangle = 1.9 \times 10^{-9}$ cm^3 s^{-1} is the momentum transfer rate between ions and neutrals, $\bar{m}_i$ is the mean ion mass, for which we adopt the value $\bar{m}_i = 30\, m_p$, which is a representative value for the expectedly most abundant ions, K^+ and Na^+ and $\bar{m}_n$ is the mean neutral mass. It allows magnetic

fields to diffuse through the neutral component and can enhance dissipation in certain regions. The ambipolar term is expected to play an important role in partially ionized plasma, specially in the widely studied case of the solar photosphere and its overlying layers (e.g., Chitre and Krishan 2001; Popescu Braileanu and Keppens 2021). If we rewrite the ambipolar term as:

$$-\frac{1}{\nu_{in}\rho_i}(\mathbf{J}\times\mathbf{B})\times\mathbf{B} = \frac{1}{\nu_{in}\rho_i}[B^2\mathbf{J} - (\mathbf{J}\cdot\mathbf{B})\mathbf{B}] = \frac{1}{\nu_{in}\rho_i}B^2\mathbf{J}_\perp\,, \tag{2.16}$$

we can see the ambipolar term tends to dissipate the part of the currents $\mathbf{J}_\perp$ which are perpendicular to the magnetic field. In other words, it tend to align electrical currents and magnetic field, in order to minimize the Lorentz force and approach a so-called force-free configuration, $\mathbf{J}\times\mathbf{B} = 0$. In HJs, indeed, the winding term creates a configuration with an induced current $\mathbf{J}\perp\mathbf{B}$, i.e., a Lorentz force which, in the simplest axisymmetric, aligned case, go exactly against the wind direction (Batygin, Stanley, and Stevenson, 2013). Such a term enters in the ambipolar term in our local simulations, and represents a large drag term in the momentum equations in GCMs. Moreover, since the ambipolar effect scales with B^2, regions with larger winding-induced field will potentially undergo ambipolar dissipation more easily. Note that, hereafter, on the ambipolar prefactor will be denoted as $f_a := 1/(\nu_{in}\rho_i)$.

Compared to the two dominant terms (advection and Ohmic), the Hall and ambipolar effects are expected to be negligible in dense environments, but they could be relevant for the uppermost layers (Perna, Menou, and Rauscher 2010a), especially if the locally induced magnetic field is large enough, since their relative importance with respect to the Ohmic term scales as B and B^2, respectively. For this reason in Chapters 3 and 5 (Soriano-Guerrero et al., 2023; Soriano-Guerrero et al., 2025a) these two terms have not been considered in the induction equation, but we assess their relevance in Chapter 4, i.e. Soriano-Guerrero et al., 2025b.

It is relevant to note that in all the work we have neglected the terms proportional to the pressure gradient, which would give the Biermann battery effect and contribute further to the ambipolar diffusion. Such terms are safely negligible, since in our case the Álfven speed is much smaller than the sound speed (Pandey and Wardle, 2008). Note also that we are considering pressures $p \gtrsim$ mbar, for which eq. 2.7 applies, since the collision frequencies of both ions and electrons are larger than the electron plasma frequency. This implies that charged components are strongly coupled to the neutral one, so that we can neglect electron plasma waves and the anisotropic nature of the conductivity (we are in the M1 region of Koskinen et al. 2014).

2.2 Numerical setup

In the simulations computed in this thesis, the MHD equations, together with the hydrostatic equilibrium equation and the EOS presented earlier, are solved to obtain the full three-dimensional dynamics structure of the local atmospheric fluid.

The quantities corresponding to the density ρ, momentum density $\mathbf{S}$, magnetic field $\mathbf{B}$, and total energy density U are numerically evolved using spatially and temporally discretized equations. At each timestep of the simulation, the velocity field is recovered via $\mathbf{v} = \mathbf{S}/\rho$, and the pressure is computed by inverting eq. 2.8, resulting in:

$$p = (\gamma - 1)\left[U - \frac{1}{2}\left(\rho v^2 + \frac{B^2}{\mu_0}\right)\right]. \tag{2.17}$$

The other thermodynamical quantities (e.g., e, T) can be obtained via eq. 2.1. The recovered variables $\mathbf{v}$, p (or e or T, instead of p), together with ρ and $\mathbf{B}$, are commonly referred to as the primitive variables in MHD: they constitute the complete basic set of dynamical and thermodynamical fields that describe the system. The solution of the equations depends on the background profiles for the wind, pressure, density temperature and magnetic field as well as the domain size and the boundary conditions (BCs).

This section describes the numerical framework adopted, including the forcing term, the divergence cleaning scheme, the perturbed-background approach, the rescaled equations, the detailed domain and BCs, and the methods and software employed to perform the simulations presented in this work.

2.2.1 Divergence cleaning scheme

The magnetic field must satisfy the $\nabla \cdot \mathbf{B} = 0$. Since our numerical scheme does not conserve by construction the Maxwell divergence constraint a divergence cleaning scheme (Dedner et al., 2002), in the generalized Lagrange multiplier form, is implemented like in Palenzuela et al., 2018, to which we refer also for further details and references about the numerical scheme and benchmark tests of the code. The constraint is well maintained during the entire evolution in our simulations.

The method introduces an auxiliary scalar field φ that converts non-zero $\nabla \cdot \mathbf{B}$ contribution into waves travelling at speed c_h, and damps them at rate κ. When we include this term in the induction equation, eq. 2.7 it can be rewritten as:

$$\partial_t \mathbf{B} + \nabla \varphi = -\nabla \times \mathbf{E}, \tag{2.18}$$

$$\tag{2.19}$$

where φ evolves as:

$$\partial_t \varphi + c_h^2 \, \nabla \cdot \mathbf{B} = -\kappa \, \varphi \tag{2.20}$$

Taking the divergence of (2.18), deriving in time, and combining with (2.20), we obtain a damped wave equation for $\nabla \cdot \mathbf{B}$:

$$\partial_{tt}(\nabla \cdot \mathbf{B}) + \kappa \, \partial_t (\nabla \cdot \mathbf{B}) - c_h^2 \, \nabla^2 (\nabla \cdot \mathbf{B}) = 0, \tag{2.21}$$

so divergence errors are advected out of the domain at finite speed $c_h = c_{h*}$ while being damped at a rate $\kappa = \kappa_*$ (see below for a definition of the * variables), based on Palenzuela et al., 2018. The coefficients are tuned in such a way that the deviations from the physical constraints cannot grow to a significant level.

2.2.2 Rescaled equations

In the numerical implementation, the MHD equations have been rescaled so that the coordinates and all the fields, expressed in units of a reference value, become dimensionless as follows. Variables in the code are denoted with $\hat{\cdot}$, reference values with $\cdot_*$ (see Appendix B for a full derivation of these reference values):

$$\rho = \rho_* \hat{\rho},\ \ p = p_* \hat{p},\ \ v = c_* \hat{v},\ \ B = B_* \hat{B},\ \ T = T_0 \hat{T}, \tag{2.22}$$

$$x = H_* \hat{x} \ \Rightarrow\ \partial_x = \frac{1}{H_*} \partial_{\hat{x}}, \tag{2.23}$$

$$t = t_* \hat{t} \ \Rightarrow\ \partial_t = \frac{1}{t_*} \partial_{\hat{t}}, \tag{2.24}$$

$$\tag{2.25}$$

where x is representative of any spatial coordinate, and the reference values are defined as:

$$H_* := \frac{RT_0}{g} = 1.66 \times 10^6\, m \frac{T_{2000}}{\mu g_{10}}\,, \tag{2.26}$$

$$B_* := \sqrt{\mu_0 p_*} \simeq 0.354 \sqrt{p_{\text{bar}}}\,\text{T}\,, \tag{2.27}$$

$$\rho_* := \frac{p_*}{RT_0} \simeq 6.01 \cdot 10^{-3} \frac{\text{kg}}{\text{m}^3} \frac{p_{\text{bar}} \mu}{T_{2000}}\,, \tag{2.28}$$

$$c_* := \sqrt{\frac{p_*}{\rho_*}} = \sqrt{RT_0} \simeq 4.08 \times 10^3 \frac{\text{m}}{\text{s}} \sqrt{\frac{T_{2000}}{\mu}}\,, \tag{2.29}$$

$$t_* := \frac{H_*}{c_*} = \frac{RT_0}{g c_*} = \frac{c_*}{g} \simeq 408\ \text{s} \frac{\sqrt{T_{2000}}}{g_{10} \sqrt{\mu}}\,, \tag{2.30}$$

where $p_{\text{bar}} := p_*/(1\ \text{bar})$, $T_{2000} = T_0/(2000K)$, $g_{10} = g/(10\ m/s^2)$. Where T has been rescaled to 2000 K while g to 10 m/s^2, which is a representative value of the gravity for a gas giant.

Note that p_*, g, μ, T_0 are the variables which should be fix to determine all the reference variables for a given model. In the models presented $p_* = 1$ bar and g can be fixed using eq. 2.3. T_0 is fixed as described in the next paragraph.

Note that H_* is the pressure scale height, which is a natural vertical length-scale of the problem. However, it can be clearly defined only if the temperature is constant, as in the isothermal scenarios of Chapter 3. In the general, non-isothermal scenario, the choice of the lenghtscale is not trivial because the magnitude scales vary with z. Therefore, the reference value H_* is defined as described in Chapters 4.

With this convenient definition of the six reference values (H_*, p_*, ρ_*, c_*, B_* and t_*) the MHD equations 2.4-2.7 look the same, replacing the original variables with the dimensionless ones (i.e., the values used in the code), and reabsorbing μ_0 in the magnetic field:

$$\frac{\partial \hat{\rho}}{\partial \hat{t}} + \hat{\nabla} \cdot (\hat{\rho}\, \hat{\mathbf{v}}) = 0\,, \tag{2.31}$$

$$\frac{\partial \hat{\mathbf{S}}}{\partial \hat{t}} + \hat{\nabla} \cdot \left[\hat{\rho}\, \hat{\mathbf{v}}\, \hat{\mathbf{v}} + \left(\hat{p} + \frac{\hat{B}^2}{2} \right) \mathbf{I} - \hat{\mathbf{B}}\, \hat{\mathbf{B}} \right] = \hat{\rho}\, \hat{\mathbf{g}} + \hat{\mathbf{F}}, \tag{2.32}$$

$$\frac{\partial \hat{U}}{\partial \hat{t}} + \hat{\nabla} \cdot \left[\left(\hat{U} + \hat{p} + \frac{\hat{B}^2}{2} \right) \hat{\mathbf{v}} - (\hat{\mathbf{v}} \cdot \hat{\mathbf{B}}) \hat{\mathbf{B}} \right] = \hat{\rho}\, \hat{\mathbf{v}} \cdot \hat{\mathbf{g}} + \hat{\mathbf{v}} \cdot \hat{\mathbf{F}} - \frac{\hat{p}}{\tau_{\text{cool}}} + Q_j, \tag{2.33}$$

$$\frac{\partial \hat{\mathbf{B}}}{\partial \hat{t}} = -\hat{\nabla} \times \left(-\hat{\mathbf{v}} \times \hat{\mathbf{B}} + \frac{\hat{\mathbf{J}}}{\hat{\sigma}} + \hat{f}_h \left(\hat{\mathbf{J}} \times \hat{\mathbf{B}} \right) - \hat{f}_a \left((\hat{\mathbf{J}} \times \hat{\mathbf{B}}) \times \hat{\mathbf{B}} \right) \right), \tag{2.34}$$

where the rescaled definitions of gravity, total energy density, specific internal energy, forcing, pressure, current density, momentum density, electrical conductivity, Ohmic dissipation, and Hall and ambipolar prefactors are, respectively:

$$\hat{\mathbf{g}} = \frac{\mathbf{g}}{g} = (0,0,-1)\,, \tag{2.35}$$

$$\hat{U} = \frac{U}{p_*} = \hat{\rho}\,\hat{e} + \frac{1}{2}\left(\hat{\rho}\,\hat{\mathbf{v}}^2 + \hat{\mathbf{B}}^2\right)\,, \tag{2.36}$$

$$\hat{e} = \frac{e}{c_*^2}\,, \tag{2.37}$$

$$\hat{F} = \frac{F}{\rho_* g}\,, \tag{2.38}$$

$$\hat{p} = \hat{\rho}\,\hat{T} = (\gamma-1)\,\hat{\rho}\,\hat{e}\,, \tag{2.39}$$

$$\hat{\mathbf{J}} = \frac{\mathbf{J}}{J_*} = \hat{\boldsymbol{\nabla}} \times \hat{\mathbf{B}}, \qquad \text{with } J_* = \frac{B_*}{\mu_0 H_*}\,, \tag{2.40}$$

$$\hat{\mathbf{S}} = \frac{\mathbf{S}}{S_*} = \hat{\rho}\,\hat{\mathbf{v}}, \qquad \text{with } S_* = \rho_* c_*\,, \tag{2.41}$$

$$\hat{\eta} = \frac{\eta}{\eta_*} = \frac{\eta}{H_* c_*}, \qquad \text{with } \eta_* = H_* c_*\,, \tag{2.42}$$

$$\hat{\sigma} = \frac{\sigma}{\sigma_*} = \mu_0\, H_*\, c_*\, \sigma, \qquad \text{with } \sigma_* = \frac{1}{\mu_0 H_* c_*}\,, \tag{2.43}$$

$$\hat{Q}_j = \frac{Q_j}{Q_{j*}}, \qquad \text{with } Q_{j*} = J_*^2\, H_*\, c_*\, \mu_0\,, \tag{2.44}$$

$$\hat{f}_h = \frac{f_h}{f_{h*}}, \qquad \text{with } f_{h*} = \frac{c_*}{J_*}\,, \tag{2.45}$$

$$\hat{f}_a = \frac{f_a}{f_{a*}}, \qquad \text{with } f_{a*} = \frac{H_*}{c_*\,\rho_*}\,, \tag{2.46}$$

$$\hat{\kappa} = \frac{\kappa}{\kappa_*}, \qquad \text{with } \kappa_* = \frac{1}{t_*} \tag{2.47}$$

$$\hat{c}_h = \frac{c_h}{c_{h*}}, \qquad \text{with } c_{h*} = c_*\,, \tag{2.48}$$

$$\hat{\nu}_{\text{cool}} = \frac{\nu_{\text{cool}}}{\nu_{\text{cool}*}}, \qquad \text{with } \nu_{\text{cool}*} = \frac{1}{t_*}\,. \tag{2.49}$$

2.2.3 Perturbed-background approach

As common in numerical simulations of strongly stratified media, we decompose the field in a static background component, $\cdot_0$ (for which the time evolution is always zero), plus a perturbed one, $\cdot_1$, for instance:

$$\hat{p} = \hat{p_0} + \hat{p_1}\,, \tag{2.50}$$

$$\hat{\rho} = \hat{\rho_0} + \hat{\rho_1}\,. \tag{2.51}$$

It is worth noting that the background profiles ρ_0, p_0, as well as those of the other background quantities, will be explicitly specified in each chapter according to the setup employed for the corresponding simulations.

Since the time evolution of $\hat{\rho}_0$ is zero, the continuity equation (2.31), including the rescaled equations, becomes:

$$\frac{\partial \hat{\rho}_1}{\partial \hat{t}} + \hat{\nabla} \cdot [(\hat{\rho}_0 + \hat{\rho}_1)\, \hat{\mathbf{v}}] = 0\,. \tag{2.52}$$

and the perturbed pressure is calculated as:

$$\hat{p}_1 \;=\; (\gamma - 1)\left(\hat{E} - \frac{\hat{S}^2}{2\hat{\rho}} - \frac{\hat{B}^2}{2}\right) - \hat{p}_0\,, \tag{2.53}$$

which implies, via the EoS:

$$\hat{T}_1 \;=\; (\gamma - 1)\frac{\hat{U} - \frac{\hat{S}^2}{2\hat{\rho}} - \frac{\hat{B}^2}{2}}{\hat{\rho}} - \hat{T}_0\,, \tag{2.54}$$

$$\hat{e}_1 \;=\; \frac{\hat{E} - \frac{\hat{S}^2}{2\hat{\rho}} - \frac{\hat{B}^2}{2}}{\hat{\rho}} - \hat{e}_0\,. \tag{2.55}$$

This approach generally allows the numerical scheme to be more stable over a largely varying range of densities, since it avoids the numerical problems that arise from inaccurate numerical operations due to large numerical differences in the background fields between the extremes of the domain.

2.2.4 Domain and boundary conditions

Throughout our work, a parallelepiped mapped by Cartesian coordinates (x, y, z) is chosen to describe a small atmospheric column. The spherical coordinate components azimuthal, meridional, and radial directions locally correspond to the x-, y-, and z-components, respectively, see Fig. 2.1 for a schematic representation. Therefore, the y-z components are a representation of the poloidal fields, and the x component represents the toroidal field.[2] For the three coordinates we set the parallelepiped size to be $L_x \times L_y \times L_z = (L/2) \times (L/2) \times L$, where L is fixed to $10\,H_*$. We consider a vertical domain which extends from 10-100 bars up to 0.0005-0.01 bar, depending on the model computed. Physically, the horizontal domain corresponds to $\lesssim 1$ degree in latitude and azimuth, for typical values of planetary radius and H_*. Such domain hence represents a narrow column, and we will in particular consider steep wind profiles from GCM, corresponding to a region close to the dayside substellar point.

As initial conditions, we impose the hydrostatic background profiles, which have only vertical gradients: $p = p_0(z)$, $\rho = \rho_0(z)$, $v_x = w(z)$, together with an initial magnetic field that can be oriented along either the y or the z direction. A simple schematic representation of the simulation box, including the initial wind direction and magnetic field, is shown in Fig. 2.1.

The boundary conditions in $\hat{x}$ and $\hat{y}$ are periodic. The vertical boundary conditions are less trivial. They are designed to: (i) ensure hydrostatic stability of the static background, which is delicate especially at the top; (ii) let the upwards perturbations to propagate in the damping region, described before, where they are dissipated or

[2] In the poloidal-toroidal decomposition of a field, approximating the components as toroidal as exactly lying along the azimuthal direction and poloidal being contained in the meridional plane is exact only in axial symmetry. However, it is commonly done for simplicity, and we will stick to this terminology.

go out of the domain, without any artificial reflection. For the perturbed fields $\hat{\rho}_1, \hat{v}_i$ and $\hat{p}_1$, we impose a symmetric boundary condition over the ghost cells at the top and bottom layers, e.g., $\hat{\rho}_1(L) = \hat{\rho}_1(L - dz)$ (where dz is the spatial spacing), meaning that $\partial_z \hat{\rho}_1 = 0$ among the two last cells. The only exception is for $\hat{v}_z$, for which we impose instead a reflective boundary condition among the last two numerical points, i.e. $\hat{v}_z(L) = -\hat{v}_z(L - dz)$.[3] The boundary conditions on $(\hat{\rho}, \hat{S}_i, \hat{U})$ are consistently imposed automatically from the perturbed and background fields, using the previous relations.

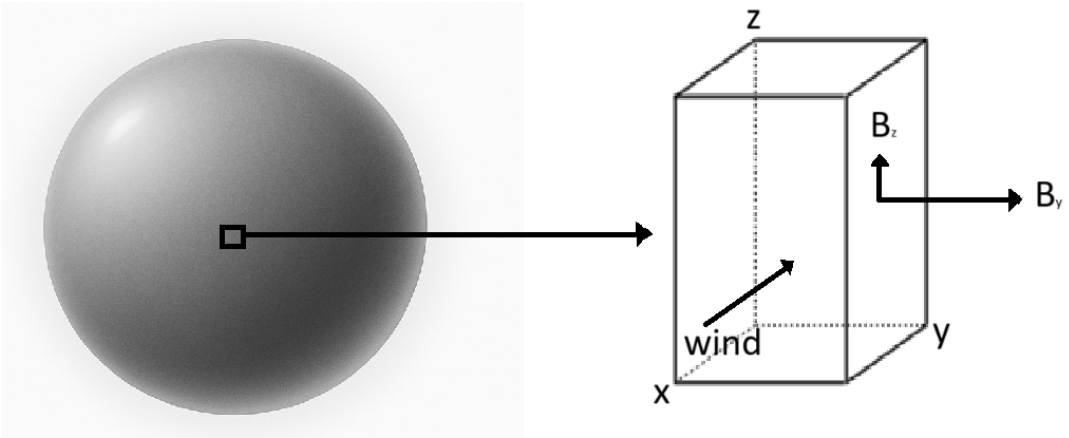

FIGURE 2.1: Schematic representation of the Cartesian coordinates used in this thesis: x (azimuthal), y (meridional) and z (vertical or radial). The directions of the background wind (w) and of a purely radial background magnetic field (B_z^{in}) have been represented.

2.2.5 Forcing: wind and perturbations

As mentioned before, GCMs predict transonic zonal winds of order km/s at pressures of a fraction of a bar (Showman and Guillot, 2002; Showman, Cho, and Menou, 2010; Heng, Menou, and Phillipps, 2011). Since we do not solve the global circulation here, we impose a local background wind in which, for simplicity, we retain only the dominant azimuthal (zonal) component, neglecting meridional and vertical contributions (see Fig. 2.1). On top of this, we superpose small-scale perturbations through the forcing described below.

The total forcing term used in the simulations, included in eqs. 2.5 and 2.6, and aimed at studying their combined effects on the atmospheric dynamics, is defined as:

$$\mathbf{F} = \frac{\rho_0}{\tau}(\mathbf{f}_{\text{wind}} + \delta\mathbf{v}(\mathbf{x})) - \mathbf{S_d}, \tag{2.56}$$

where ρ_0 is the background density (explained below), τ is the forcing timescale, $\mathbf{f}_{wind}$ corresponds to the wind-driven forcing, whose exact form varies across simulations and will be specified in the corresponding chapters. Notice that since we perform a local simulation with a prescribed external forcing, there is no effective feedback on the velocities from the magnetic drag. Finally, $\mathbf{S_d}$ is a damping term, and $\delta\mathbf{v}(\mathbf{x})$ represents spatially varying random deviations from the mainly zonal

[3] In the Simflowny user interface, they are called *Reflection positive* and *Reflection negative*, respectively.

flow $w(z)$, defined as:

$$\boldsymbol{\delta v} = \lambda \left(r_1 \mathbf{e}_x + r_2 \mathbf{e}_y + r_3 \mathbf{e}_z \right) w(z) \,, \tag{2.57}$$

where λ is a constant parameter regulating the average relative forcing amplitude $\delta v / w$, e_i indicates the unit vector along a direction i, and r_1, r_2 and r_3 are random numbers $\in [-1, 1]$ associated to each direction. The random variations are totally uncorrelated from point to point and from one timestep to another (meaning that, effectively, the perturbation are correlated over a time dt).

The introduction of the turbulent-like contribution to the forcing throughout the domain is a simple, effective way to consider at the same time the intrinsic time variability of the wind (e.g. Menou 2020), and the injection of small scale perturbations. This study takes this simple white spectrum-like forcing, leaving the study of other types of injection scales to future work.

Note that, in other studies of turbulence in box simulations they only apply an initial perturbation to $\mathbf{v}$ (Ryu, Zingale, and Perna, 2018), and study the properties of the slowly decaying turbulence. We choose instead to apply a continuous small-scale forcing, since we seek to achieve a stationary state (not a decaying one), sustained by the persistent climate-induced winds (including the small-scale variations) acting on our small column.

Finally, the damping term $\mathbf{S_d}$ is applied to the upper 20% region of the domain. The mathematical form of $\mathbf{S_d}$ will be given in each specific chapter, as its exact definition depends on the chosen domain. However, its purpose is common to all setups presented: to enhance numerical stability in the low-density part of the domain, where high velocities can more easily develop. It is designed to limit the velocities in the low-density regions and avoid numerical instabilities.

2.2.6 Numerical framework: Simflowny

In order to perform our simulations we use version 3.7.3 of SIMFLOWNY (Arbona et al., 2013; Arbona et al., 2018; Palenzuela et al., 2021), a user-friendly and highly flexible platform for the generation of scientific codes that solve systems of partial differential equations (PDEs) in a variety of physical contexts using finite differences and finite volumes. The platform is designed with a modular structure that separates the definition of the mathematical model (set of PDEs, in our case MHD equations, source terms and EOS) from the specification of the physical problem (BCs and initial conditions) and the numerical configuration (spatial and temporal schemes). This approach facilitates the reproducibility of scientific results and allows the user to focus on the physics of the problem rather than on the technical details of code implementation.

The generated code is compiled and executed on the local and HPC systems available at our institution as well as external HPC such as the Barcelona Supercomputing Center (BSC). Note that post-processing of the output is performed with custom Python routines, which read the raw data produced by Simflowny and compute the physical quantities and diagnostics discussed in later chapters.

Simflowny has been used to solve equations under different physical scenarios, including hydrodynamics, MHD, and relativistic MHD. For our purposes, we make use of the classical MHD equations, suitably modified to incorporate the specific rescaled formulation and source terms described in § 2.1.

The execution of Simflowny generated codes is supported by the SAMRAI infrastructure[4] (Hornung and Kohn, 2002; Gunney and Anderson, 2016). SAMRAI provides efficient parallelization through message passing interface (MPI)[5], as well as advanced features such as Adaptive Mesh Refinement (AMR), which dynamically increases resolution in selected regions of the computational domain where enhanced accuracy is required. In addition to AMR, the framework also supports Fixed Mesh Refinement (FMR), in which refinement levels and their positions are predefined at the start of the simulation, a feature particularly useful when the regions of interest are known a priori. Although neither AMR nor FMR are employed in this work (only FMR was used in some tests), this parallelization and mesh management framework ensures excellent scalability on high-performance computing (HPC) systems. For completeness, we note that Simflowny also offers AMReX[6] as an alternative to SAMRAI which can be faster for computationally expensive simulations; however, throughout this has not been used.

Numerical methods

For the spatial discretization we employ the high-resolution, 5^{th} order accurate monotonicity preserving scheme (MP5) (Suresh and Huynh, 1997), which provides fifth-order accuracy in smooth regions while preventing spurious oscillations near discontinuities. This balance between high-order accuracy and robustness makes MP5 especially suitable for MHD problems where both smooth flows and strong gradients (or shocks) may be present (Palenzuela et al., 2018). The scheme is implemented within a flux-splitting approach, in which the physical fluxes are decomposed into separate contributions that can be treated individually, improving both stability and accuracy for complex systems of equations.

Time integration is performed using an explicit 4^{th}-order Runge–Kutta (RK4) method, which offers a good compromise between computational cost and temporal accuracy. The RK4 scheme evaluates the system at four intermediate stages per timestep, reducing truncation errors and providing stable evolution as long as the Courant–Friedrichs–Lewy (CFL) condition is satisfied.

The timestep is restricted by the CFL condition, which for a characteristic velocity $c_{\max}$ reads:

$$\Delta t_{\rm CFL} \lesssim \frac{\Delta z}{\hat{c}_{\max}} \,, \tag{2.58}$$

where Δz is the grid spacing in the vertical direction and $\hat{c}_{\max}$ is the maximum dimensionless characteristic speed in the domain. In our setup, the largest velocities are typically of the order of the background sound speed, $c_{s,0}$ so that the Courant timestep becomes:

$$\Delta t_c \lesssim \frac{L}{\sqrt{\gamma}\, N_z} \,, \tag{2.59}$$

with $N_z = L/\Delta z$ the number of points in the vertical direction. For $\gamma = 7/5$ and $L = 10$, the RK4 scheme used here implies a maximum allowed timestep

$$\Delta t_{\max} = 0.4\, \Delta t_c \lesssim \frac{2.11}{N_z} \,, \tag{2.60}$$

[4] https://computing.llnl.gov/projects/samrai

[5] MPI is a standard for parallel programming that allows multiple processes to communicate by sending and receiving messages, commonly used in scientific simulations and high-performance computing.

[6] https://amrex-codes.github.io

which ensures numerical stability for all simulations presented in this work.

It is useful to compare this numerical timescale with relevant physical timescales of the problem. For instance, the vertical crossing time of the sound speed across the whole domain is

$$t_z(L) \sim \frac{L}{c_{s,0}} \approx 8.45\, t_* \approx 1 \text{ hour} , \tag{2.61}$$

which is much larger than the numerical timestep, ensuring that the simulations resolve adequately both fast and slow dynamical processes.

3

Ideal 3D MHD simulations: winding and turbulence in ultra HJs

3.1 Introduction and objectives

In this Chapter we present the results obtained in Soriano-Guerrero et al., 2023. We address the problem of local MHD simulations of a narrow atmospheric column on the dayside radiative layers of a HJ upper atmosphere ($\sim$ mbar–10 bar) through simplified simulations under the non-linear regime. Our aim is to have a first assessment of two key processes: the winding of magnetic fields driven by strong zonal winds, and the generation of small-scale turbulence. On one side, we simulate the generation of strong toroidal fields in the wind shear layer, as also pointed out by Dietrich et al. (2022) after we started this project. We include realistic, parametrized profiles for the wind velocity, qualitatively mimicking the steepest profiles of GCMs (Beltz et al., 2022). On the other side, we enforce turbulent perturbations in addition to the zonal wind, aiming to evaluate where electrical currents are induced and to quantify how the wind profile affects the generation of currents and local magnetic fields. To this end, we adopt an idealized setup appropriate for the very high temperatures ($T \gtrsim 3000$ K) of these uHJs, and make use of simplified prescriptions for the background state and resistivity, without the inclusion of further magnetic effects such as the Hall and ambipolar terms. This is a first step, since the resistivity is given here implicitly by the numerical scheme at a fixed resolution, rather than by the physical resistivity. This approach allows us to explore the combined effects of large-scale shear and turbulent motions in a controlled framework, providing a first step towards more complete models of magnetic induction in uHJs atmospheres under the non-linear regime.

3.2 Initial setup and conditions

In this section we present the initial setup and conditions adopted for this study where we set a Cartesian domain with $\hat{x}, \hat{y} \in [0, L/2]$, and the vertical direction $\hat{z} \in [0, L]$. In the following subsection we check the isothermal background profiles for density and pressure, $\rho_0(z)$ and $p_0(z)$, as well as the prescribed profiles $w(z)$ and $B_x^{\rm in}(z)$. In addition, we summarize the differences adopted in this simplified setup, compared to the standard MHD model presented in § 2.1.2 and we describe the computational domain and the boundary conditions for the magnetic field.

3.2.1 Background profiles and formulation of the atmospheric column equations for this setup

As an initial approach, the simulations presented in this Chapter consider a simplified model of a uHJ atmospheric column under the isothermal assumption.Below we detail the background profiles used to solve the physical equations of the problem as well as any difference in those equations compared to the reference model presented in Chapter 2.

Hydrostatic equilibrium under an isothermal scenario

Analytical and numerical studies (Guillot, 2010; Youdin and Mitchell, 2010) indicate that the outermost radiative layers of HJs, located well above the RCB, may be treated, to first order, as approximately isothermal. Accordingly, we adopt a uniform background temperature T_0 in this work. It should be emphasized, however, that this constitutes an approximation, as will be demonstrated in Chapter 4.

Under this assumption, the background pressure profile resulting from the hydrostatic equilibrium equation is

$$p_0(z) = p_b\, e^{-z/H_*}, \tag{3.1}$$

where p_b is the pressure at the bottom boundary ($z = 0$) and H_* can be calculated from eq. 2.26.

The pressure and density profiles are related through the ideal gas equation of state, eq. 2.1. Under the isothermal assumption ($T = T_0$), this relation implies that the density profile has the same exponential dependence:

$$\rho_0(z) = \rho_b\, e^{-z/H_*}, \tag{3.2}$$

Specific setup for MHD equations

The MHD equations introduced in eqs. 2.4-2.7 are adapted here to the specific setup of this Chapter. In this context, some terms in the momentum, energy, and induction equations are adjusted or suppressed to reflect the configuration considered here.

In this model, a key feature is the wind profile adopted. We prescribe an analytical zonal-wind profile $w(z)$ that enters all MHD equations. In the momentum and energy equations, this velocity also modifies the forcing term $\mathbf{F}$ (eq. 2.56); in particular, the wind contribution $\mathbf{f}_{\rm wind}$ which is defined consistently with $w(z)$, as described below.

In this simplified setup, as an effective approach, we assume a zonal wind that mimics the main features seen in GCMs (e.g. Fig. 4 of Beltz et al., 2022 or right panel

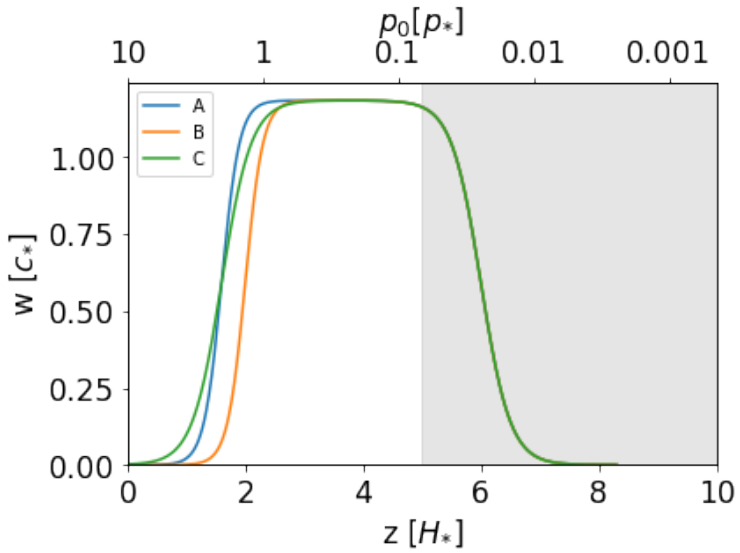

FIGURE 3.1: Wind profiles adopted in this work, as a function of height $\hat{z}$, and background pressure p_0 (in units p_*, which we take 1 bar by default), for the models A, B, C of Table 3.1. The damping region (see text) is shaded in grey.

of Fig. 2 of Rogers and Komacek, 2014), using the least possible parameters. For simplicity, we consider a zero zonal velocity at the bottom of the domain, since at those pressure (10 bar) the zonal velocity is one or two orders of magnitude smaller than at the top.[1] Additionally, in order to ensure stability in the top part, we prescribe a transition to zero velocity in the damping region. Cnsidering this, the implemented wind profile reads:

$$w(z) = w_0\sqrt{\gamma}\left(\frac{1+\mathcal{B}}{2}\right)\left(\frac{1+\mathcal{T}}{2}\right), \tag{3.3}$$

where

$$\mathcal{B} = \tanh\left(\frac{\hat{z}-z_b}{\alpha_b}\right) \tag{3.4}$$

$$\mathcal{T} = \tanh\left(\frac{z_t-\hat{z}}{\alpha_t}\right), \tag{3.5}$$

and w_0 corresponds to the amplitude of the wind, z_t, z_b correspond to the height of the shear layers at the top (which is fictitious) and at the bottom (the real one), respectively, and α_t, α_b the corresponding shear layer thickness. This implies that the middle region ($\hat{z} \sim (z_b{+}\alpha_b,\ z_t{-}\alpha_t)$) has a characteristic speed $w = \sqrt{\gamma}$, i.e. the speed of sound. Fig. 3.1 displays the different wind profiles that have been used in this project. We consider different parameters for the physical shear layer: depth, taking z_b=1.6 or $z_b = 2$, and thickness, taking $\alpha_b = 0.3$ or $\alpha_b = 0.5$. We fix $z_t = 6$ and $\alpha_t = 0.5$, a choice that, within a preliminary exploration of different values (in combination with the other numerical parameters as discussed in Appendix C.1), allows stability and minimize the influence of the artificial shear layer on the rest of the domain.

[1] Seen in another way, we choose the frame which is co-moving with the wind at the bottom of the layer; results are insensitive to the frame choice.

The effective forcing for the wind is consequently defined as:

$$\mathbf{f}_{wind} = f_0 \max\{w(z) - \langle v_x \rangle, 0\}\mathbf{e_x} \,. \quad (3.6)$$

where: $\langle v_x \rangle$ is a local average of v_x in the x-direction (across a few points) and f_0 corresponds to the amplitude of the forcing and it is fixed to f_0=1 here and in Chapters 4 and 5.

As shown, we prescribe the initial value of $v_x = w(z)$, and, with this forcing prescription (in either flavours), we keep v_x close to the wind profile (compensating the numerical dissipation). However, this choice lets v_x slowly vary in time and become locally slightly larger than $w(z)$, allowing positive deviations from the simple wind profile. Such deviations provide winds that slowly vary in time and lead to an increase of the total kinetic energy (see below). Although this arbitrary choice can be improved, this doesn't hamper the main conclusions.

As discussed in § 1.4.3, turbulence can arise through multiple mechanisms. In the configuration considered here, where we have a shear-layer, one of those possible mechanisms is KHI. A condition for developing turbulence via this method is that the Richardson number $\mathcal{R}i$ (ratio between buoyancy and flow shear terms) is below a critical value

$$\mathcal{R}i = \frac{g|\partial_z(\ln \rho)|}{(\partial_z v_x)^2} < 1/4 \,. \quad (3.7)$$

This critical value can be a bit higher (therefore, making turbulence easier) when thermal diffusivity is taken into account, as shown by Li and Goodman, 2010. However, it is important that the shear layer is smaller than the scale height. In our case, $\hat{g} = \partial_z \ln \hat{\rho}_0 = 1$ from eq. 3.3, so that $\partial_z \hat{v}_x \sim \alpha_b^{-1} \gtrsim 2$. We therefore test values $\alpha_b \lesssim 0.5$, indeed in line with the GCM wind profiles discussed above.

Moreover as seen in eq. 2.2.5, there exist the damping term, $\mathbf{S_d}$. Within this framework $\mathbf{S_d}$ follows:

$$\mathbf{S}_d = A_d \frac{(z - z_d)^2}{(L - z_d)^2} \mathbf{S} \quad (3.8)$$

where A_d is the amplitude of the damping factor, z_d the lower boundary of the damping region, and L the vertical size of the domain. $A_d = 10$ and $z_d = 0.8L$, see Appendix C.1 for a discussion of the selected values. As seen this terms acts in the upper part of the domain $z > z_d$ and is gradually increasing with height.

In our setup, the induction equation, eq. 2.7, is simplified by retaining only the advective term $\nabla \times (\mathbf{v} \times \mathbf{B})$ and removing the Ohmic, Hall and ambipolar diffusion contributions, which are estimated to be negligible for magnetic fields of the order of a few Gauss (Perna, Menou, and Rauscher, 2010a). Moreover, as our simulations explore the non-linear regime (as defined by Dietrich et al. 2022), where the winding effect is expected to generate a strong toroidal field, dynamically relevant and more intense than the background field, the physical resistivity is expected to be very low, allowing the field to wind up considerably and sustain localized currents. In this first work we use the ideal MHD equations, neglecting the explicit inclusion of thermal, viscous, or magnetic diffusivities; instead, all dissipative effects, including the effective magnetic dissipation, arise implicitly from the numerical diffusivity of the scheme. For very high temperatures ($T \gtrsim 3000$ K) and the resolution used here, the numerical and physical magnetic diffusivities are comparable (see below and Appendix C.3 for details), so the results presented here should not be far from those obtained in a non-ideal MHD case, which will be explored in a follow-up work. Nevertheless, magnetic field amplitudes could be slightly lower in such a case. The

corresponding Ohmic heating is computed a posteriori from the numerical current density **J** derived from the magnetic field output, and the Q_j term has consequently been suppressed from the energy equation (eq. 2.6).

Initial magnetic field

Under the presence of a large-scale vertical component of the magnetic field (generated in the interior of the HJ), the most relevant effect is its winding. As a matter of fact, if for simplicity we consider the azimuthal wind profile $w(z)$ and a purely uniform magnetic field along any direction, the ideal induction equation reads

$$\frac{\partial \mathbf{B}}{\partial t} = \nabla \times (\mathbf{v} \times \mathbf{B}) = B_z \frac{\partial w}{\partial z} \mathbf{e_x} \,, \tag{3.9}$$

since $\mathbf{v} \simeq w(z)\mathbf{e}_x$. This means that, provided a non-null value of B_z, there is at the beginning a continuous generation of the azimuthal (x) component of magnetic field, linear in time:

$$B_x = B_z \frac{\partial v_x}{\partial z} t \,, \tag{3.10}$$

which shows how the horizontal field grows in correspondence to the shear layers of the wind. This linear growth saturates when either the resistivity starts counteracting the field growth, or when the magnetic drag becomes important. In our case, however, the shear flow is time-independent due to the forcing, therefore the magnetic drag does not act. The only force stopping an indefinite growth of the field is then the numerical resistivity, which depends on the resolution (see §3.3.1). Since we do not have an explicit physical resistivity implemented, we initialize the magnetic field with an equipartition guess for the saturated field $B_x^2 \simeq \rho v_x^2$. Such guess should not be far from reality if we are considering the physically realistic values of the wind and the numerical resistivity (i.e., the resolution). Using such a prescription, together with the chosen profile $\frac{\partial v_x}{\partial z} \sim w/\alpha_b$, gives a saturation timescale (marking the end of the linear growth) of:

$$t = \sqrt{\rho} \frac{\alpha_b}{|B_z|} \,, \tag{3.11}$$

that we use in eq. 3.10 to set the initial magnetic field:

$$\begin{aligned} B_x^{in}(z) &= C_B \, \mathrm{sgn}(B_z^{in}) \, \sqrt{\rho_0(z)} \, \frac{\partial w}{\partial z}(z) \, \alpha_b = \\ &= C_B \, \mathrm{sgn}(B_z^{in}) \, \sqrt{\rho_0} \, w \left(1 - \mathcal{B} - \frac{\alpha_b}{\alpha_t}(1 - \mathcal{T}) \right) \,, \end{aligned} \tag{3.12}$$

where we have employed the wind velocity prescription, eq. 3.3. C_B is a parameter of order one that we vary to test different initial amplitudes, since our guess is not rigorous.

Additionally, we consider an initial small, uniform magnetic field in the vertical direction, B_z^{in}, representing the one generated inside. The initial field B_x^{in}, eq. 3.12, only depends on the direction of the planetary field, which sets the direction of the winding. Such induced field $B_x(z)$ is sustained by currents $J_y(z)$, which, as we will see, represent the dominant component. If we consider this local model part of a global, spherical one, these would be the latitudinal currents. They enclose a toroidal field in a this shearing shell, which can be extremely intense (see below), but completely screened outside.

Starting from the initial magnetic field, eq. 3.12, allows us to save computational time during the linear growth, entering directly in the non-linear dynamics. In particular, we start with $C_B = 1$, since lower or higher values imply a much longer time to approach the asymptotic winding-generated profile of B_x, as shown in the 1D tests (i.e., $\lambda = 0$) in Appendix C.2.

3.2.2 Domain and boundary conditions

Under the choice of $L = 10$, which defines the vertical domain as extending over ten atmospheric scale heights, both the reference pressure p_0 and density ρ_0 decrease exponentially with height, following $p, \rho \propto e^{-z/H}$. Therefore, across the domain, they vary by a factor $e^{-10} \approx 4.5 \times 10^{-5}$ between the bottom and the top boundary.

We consider a bottom pressure of 10 bar (i.e., $p_b = 10$, using $p_{\rm bar} = 1$ as code units), so that the pressure at the top of the domain is $\sim$ 0.45 mbar. Taking the fiducial values appearing in eq. 2.26 for T_0, μ and g, the chosen domain is $\mathcal{O}(10)\%$ of the typical radius of a HJ.

In the simulations presented in this Chapter we set $N_z = 100$, with the same spacing in the three direction, i.e. $N_x = N_y = N_z/2$. We typically run our simulations for several thousands t_*, that would correspond to days (by chance, of the same order of magnitude of the computational clock time using a few tens of processors in our local cluster). However, time units are pretty unimportant, since our simulations aim at finding a steady state, rather than evolving the system.

Most of the BCs have already been defined in § 2.2.4, however the elections of the BCs for **B** change among the chapters. In this case, for all the components $\hat{B}_i$, we impose a symmetric, i.e. $\partial_z B_i = 0$, boundary condition over the ghost cells at the top and bottom layers.

Note that the upper half of our domain presents an artificial setup: (i) the damping region for $z_d > 8$, with the term $\mathbf{S}_d$, eq. 3.8, included in forcing; (ii) a wind intensity that unphysically decreases upward, to zero, as described in the previous section. While these are unphysical features, we have verified that the amplitude of the magnetic field and currents generated here is much less than in the physical part, and, more importantly, the fluid dynamics propagate mostly upwards. No sign of artificially induced dynamics (e.g., spurious waves) is seen to appear at the top and propagate to the bottom, at least for the time over which we run most simulations ($t \sim 3000\ t_*$).

As a consequence of the existence of the previously described artificial setup, we will focus mostly on the analysis below $\hat{z} < 5$, the physical region (leaving shaded in gray the artificial ones $\hat{z} \gtrsim 5$ in all plots hereafter). In particular, we will focus on the volume-integrated energies and on the x-y plane-averaged and time-averaged values of the vector components. All the quantities are given in terms of the reference units defined in § 2.2.2, by which they can be translated into physical units by fixing p_*, g, μ, T_0. These magnitudes are assigned a posteriori to convert the dimensionless code units into physical quantities. However note that the value of T_0 is higher than T_{eq}, if we consider a column close to the substellar point, because the temperature varies with longitude (Rogers and Komacek, 2014), unless the thermal redistribution is unrealistically perfect.

In Appendix C.1 we provide more information about how we have tuned the size of the domain, the damping region parameters and the boundary conditions, by assessing the stability of the background hydrostatic profile alone.

3.3 Results

We have explored different initial configurations, in order to study the general behaviour and to quantitatively assess the magnetic field and current profiles. In Table 3.1 we present the models with the different initial parameters which are varied (varying only one compared to the reference model A). In particular, we study the dependence on the wind profiles shown in Fig. 3.1 (compare models A, B, C), and study the role of some forcing details: the perturbation amplitude (A0, A, Al, Ah), time correlation (Adt), and with/without the average over v_x (without for AS, AlS, AhS). In all simulations, we fix the same values of the numerical parameters ($\nu_{\rm cool}$, A_d, z_d, as discussed above) and for the other physical parameters: $\gamma = 1.4$, $C_B = 1$, $\hat{B}_z(t=0) = 0.0001$, $\hat{B}_y(t=0) = 0$, $w_0 = 1$.

Name	z_b	α_b	λ	$dt\ [t_*]$	$\mathcal{I}$	$\max(\langle B_x \rangle)[kG]$
A	1.6	0.3	0.01	0.0025	0.26	5.3
B	2	0.3	0.01	0.0025	0.096	5.6
C	1.6	0.5	0.01	0.0025	0.46	5.1
A0	1.6	0.3	0	0.0025	0.36	6.1
Al	1.6	0.3	0.001	0.0025	0.30	5.6
Ah	1.6	0.3	0.1	0.0025	0.28	5.9
Adt	1.6	0.3	0.01	0.01	0.18	1.5
AS	1.6	0.3	0.01	0.0025	0.30	5.4
AlS	1.6	0.3	0.001	0.0025	0.31	5.4
AhS	1.6	0.3	0.1	0.0025	0.24	5.3

TABLE 3.1: List of the parameters varied in the different models. In the first column we indicate the name of the simulation where A is the default simulation; B, C explore modifications of the wind profile (see the height z_b and thickness α_b of the shear layer, second and third columns); l and h refer to lower or higher values of perturbations λ (fourth column); dt refers to a change in the timestep (i.e., the time between random perturbations, fifth column); S to take the simple local velocity v_x without the local average in the forcing, eq. 3.6. The sixth column indicates the numerical integral $\mathcal{I} := \int_0^5 \hat{f}^2 \exp(-\hat{z}/2)\, d\hat{z}$, averaged in the $x-y$ plane and in time (i.e., over all the tens of 3D outputs available after $t \gtrsim 500\ t_*$), eq. 3.19. Such quantity is related to the a-posteriori Ohmic dissipation estimation, see § 3.4. The last column indicates the maximum value of the temporal and spatial average of $B_x(z)$ in kG (taking $p_{\rm bar} = 1$, i.e., a pressure at the bottom of $p_b = 10$ bar).

3.3.1 The role of resolution and numerical resistivity

The results presented here are valid as long as the physical magnetic diffusivity, η, neglected in this work, is not much larger than the numerical one, $\eta_{\rm num}$. If not, we underestimate the effect of the physical resistivity that limits the winding growth, and thus we overestimate the magnetic fields. Indeed, as a first indication, Fig. 3.2 shows the dependence of the winding-controlled shape of B_x and J_y on the resolution, for 1D models (i.e., with $\delta = 0$, so no x or y dependence is included). As we increase the resolution, the magnetic field gets larger and larger, with a difference in peak of a factor ~ 2 between $N_z = 50$ and 400. This is because increasing the resolution means having less numerical resistivity, which is the only term counter-acting the winding (recall that magnetic drag is not active due to the fixed velocity forcing). Therefore, this lack of numerical convergence is expected. Moreover, note that the order of magnitude of the quantities is the same (hundreds of gauss for the maximum value of B_x). The natural question is then which resolution we should adopt.

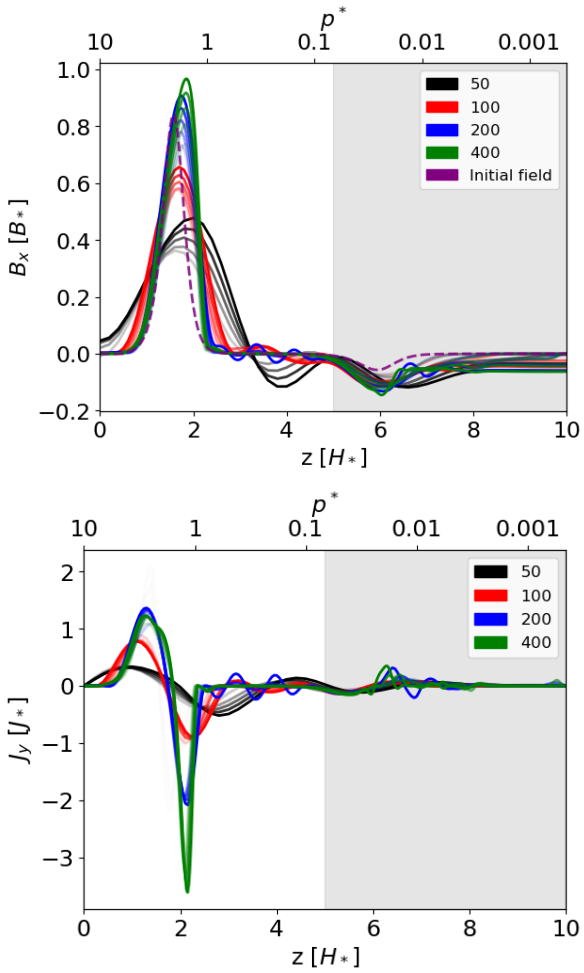

FIGURE 3.2: Comparison of the vertical profile evolution of B_x (top) and J_y (bottom) in the 1D problem, i.e., in the absence of perturbations, $\lambda = 0$ (model A0). The four colors indicate different values of the vertical resolution used, N_z (legend). The five shades (transparent to opaque) indicate different times: $t/t_* = 500, 1000, 1500, 2000, 2500$. For the top figure the initial magnetic field, i.e. $t/t_* = 0$, common for the four resolutions, has been plotted in a purple dashed line.

In Appendix C.3 we estimate the numerical resistivity and we show how very HJs ($\gtrsim$ 3000 K) have physical resistivities of the order of the numerical diffusivity with $N_z \sim 100$, which is the resolution we adopt hereafter. Such a resolution is enough to resolve the shear layer and to assess the turbulent motions. Higher resolutions would need the inclusion of the physical magnetic diffusivity.

We reserve the implementation of a realistic profile of the physical magnetic diffusivity, as well as higher resolutions, to the following chapters

3.3.2 General behaviour

We begin with a detailed analysis of the reference simulation A, which we ran for a very long time (6000 t_*), having $\lambda = 0.01$, $\alpha_b = 0.3$, $\hat{z}_b = 1.6$, $C_B = 1$, a conservative timestep $dt = 0.0025\ t_*$, and employs a local average $\langle v_x \rangle$ in the forcing, eq. 2.56. The general behaviour described here is common to all other simulations that we

have analyzed in this Chapter, though we follow them for shorter times, $t \sim 2000 - 3000\ t_*$.

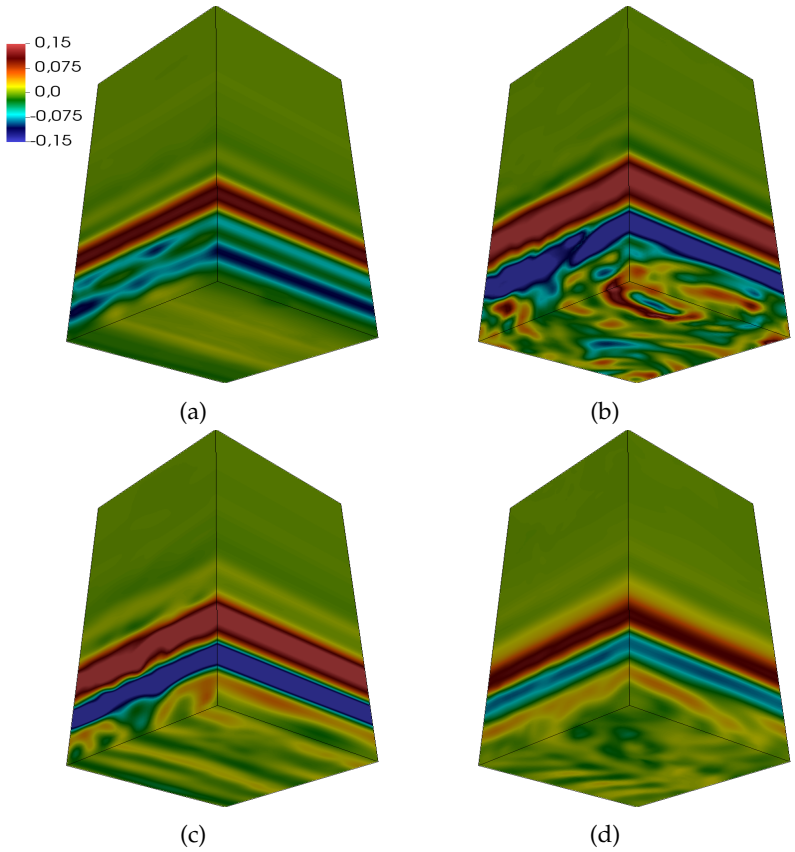

FIGURE 3.3: Vertical 3D snapshots of the perturbed density ρ_1 (scale color, in units ρ_*) for simulation A, at four different times $t/t_* = 500$ (a), 2000 (b), 3000 (c) and 6000 (d). The shear layer is centered at $z_b = 1.6$. The values related to the color scale are in units of ρ_*.

In Fig. 3.3 we show a 3D box of the density perturbation ρ_1, for four different timesteps of the simulation between t/t_*=500 and 6000. Such perturbations, generated by the turbulent state that quickly develops, are typically of the relative amplitude $\rho_1/\rho_0 \sim \mathcal{O}(0.01)$. The perturbations ρ_1 (and the corresponding p_1, not shown here), depend mostly on z. However, in the lower part of the domain some 3D structures appear due to the random perturbation enforced. These structures show a pseudo-oscillatory trend of increasing (e.g., second panel) and decreasing amplitudes (by a factor of a few) on timescales of roughly a thousand t_*. In the upper unphysical region there are no significant perturbations; only at very late times $t \gtrsim 4000\ t_*$, some perturbations pile up, but in any case they do not propagate downwards. Such piling up is probably due to the magnetic field easily induced in the uppermost regions, despite the damping in the velocities.

The upward propagation is explicitly seen in the corresponding v_z vertical 3D snapshot (first panel of Fig. 3.4): the fluid motion structure is dominated by positive values (red), although at mid latitude there are turbulent structures in the $y - z$ plane. The x-dependence is instead limited, due to the forcing. As for ρ_1, the v_z keeps fluctuating around small values. In general, the vertical motion is the result of the following three contributions:

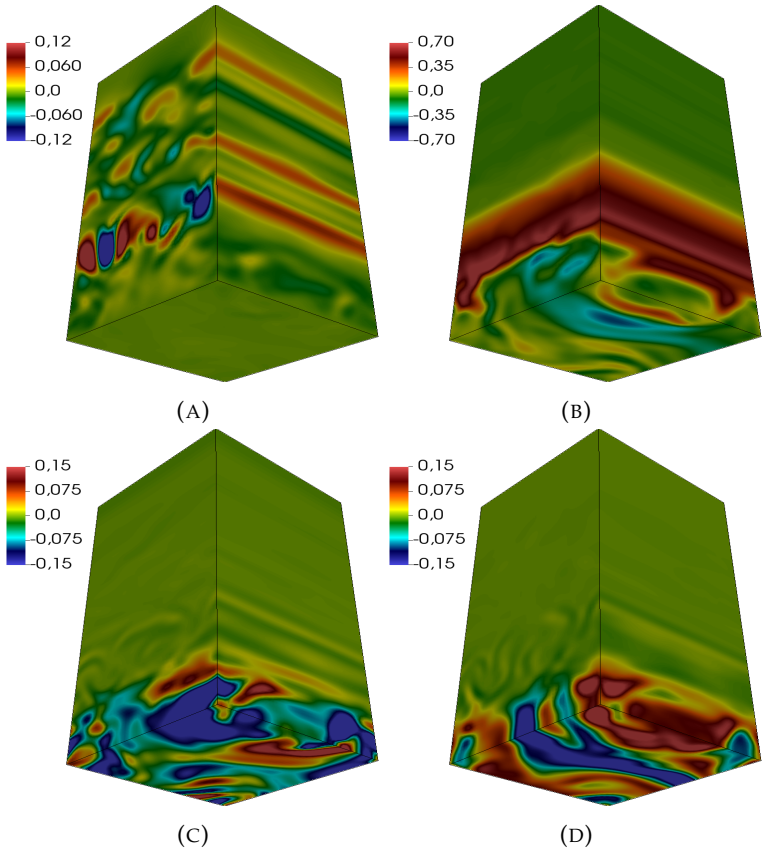

FIGURE 3.4: Vertical 3D snapshots of v_z $[c_*]$ (a), B_x $[B_*]$ (b), B_y $[B_*]$ (c) and B_z $[B_*]$ (d), for simulation A, at $t = 2000\, t_*$.

1. The main one comes from the presence of the magnetic pressure in the shear layers (the physical one around $z_b = 1.6$ and the artificial one around $z_t = 6$), with values of a few percent of the speed of sound. At later times, the upward motions dominate but they are efficiently absorbed by the damping region at $\hat{z} > 8$.

2. The second contribution comes from the turbulent motions, leading to the 3D vertical structures seen in both v_z and ρ_1 (especially at the time shown here).

3. Finally, a third source of vertical motion comes from the hydrostatic readjustment due to discretisation and is seen even in non-magnetic 1D tests for stability (i.e., without perturbation, hence no x or y dependencies, see Appendix C.1). However, this latter numerical contribution is orders of magnitude smaller compared to the other two physical sources.

Generally speaking, after a transitory phase from the initial conditions lasting $\lesssim$ 1000 t_* (a hundred crossing timescales), the system tends to reach a quasi-stationary state, where winding and numerical diffusivity reach a balance (see the 1D simulations with $\lambda = 0$ in Appendix C.2). This general behaviour is reflected by the kinetic and magnetic energies, integrated over the domain, as shown in Fig. 3.5, for models A and AS. Both the velocity and magnetic fields are dominated by the x (zonal) components since the beginning. The total magnetic energy stays within a factor of a few of its initial value, thanks to the educated guess on B_x, eq. 3.12. The total kinetic energy experiences a slight secular increase, due to the forcing function we assume,

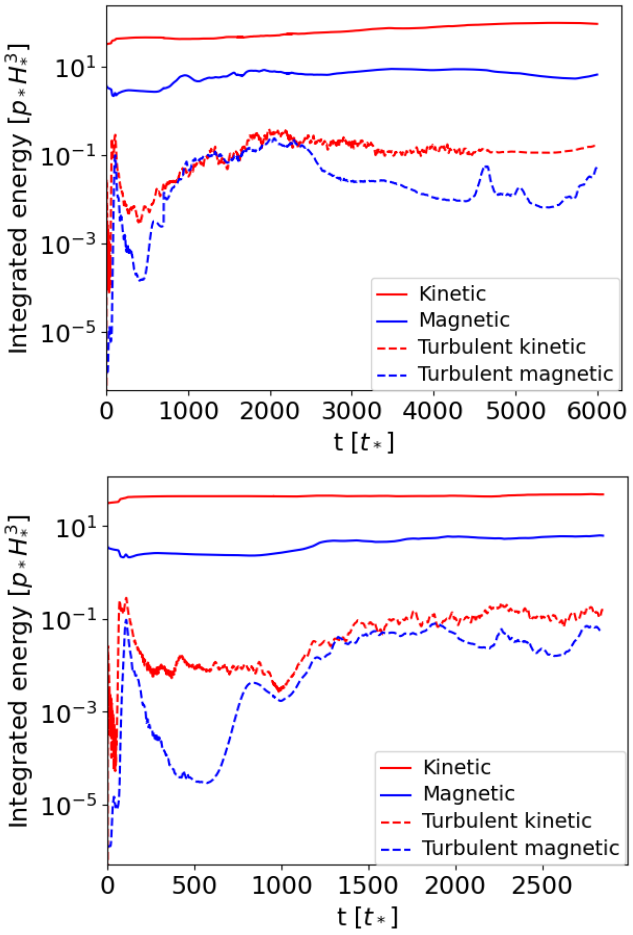

FIGURE 3.5: Volume-integrated kinetic (red) and magnetic (blue) energies, for the representative simulations A (top), followed for a very long time, and AS (bottom). Solid lines represent the total value, overwhelmingly dominated by the x component (zonal). Dashed lines represent the turbulent contributions (y and z components, i.e. meridional and vertical).

eq. 2.56. It is very useful to look at the turbulence-induced components, y and z. The turbulent magnetic energy sharply increases in the very early times, then stabilises around $0.01 - 0.1\ p_* H_*^3$. On the other hand, the turbulent kinetic energy shows less variations and is more stable. The AS model looks slightly more stable, especially in the total kinetic energy, due to the different prescription of the forcing.

3.3.3 Magnetic fields topology

We now focus on the properties of the magnetic fields at equilibrium. Fig. 3.6 is a representative snapshot of the magnetic fields (lines in blueish scale) and $\hat{\rho}_1$ (rainbow-like colors) for simulation A, at $t = 2000\ t_*$. Fig. 3.4, second, third and forth panels, also shows the snapshots of $\hat{B}_x$, $\hat{B}_y$ and $\hat{B}_z$ at the same time. The strongest magnetic field in the $\hat{x}$ direction is generated in the shear layer. The magnetic field is clearly composed by structures are elongated in the $\hat{x}$ direction, due to the winding. However, they show a certain complexity in the $\hat{y}$-$\hat{z}$ plane, reflecting the curling and twisting effect of MHD turbulence. Such structures tend to periodically become

more or less complex, similarly to what is seen for $\hat{\rho}_1$ (here we show a snapshot at $t = 2000\ t_*$ with a particularly rich topology, on average they are less visible).

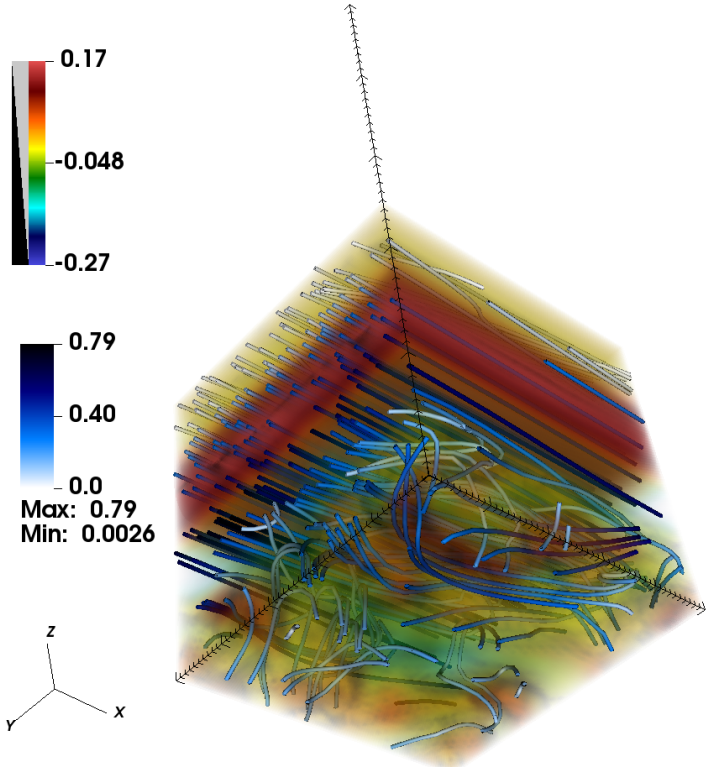

FIGURE 3.6: Representative 3D snapshot of simulation A, at $t = 2000\ t_*$. The rainbow color scale represents the value of ρ_1 in units ρ_*, while the magnetic field lines are colored with the intensity of the magnetic field. We focus here only on the physical part of the domain, $\hat{z} < 5$.

In Fig. 3.7, we show in a clearer way the evolution of the three magnetic field components, averaged over the $\hat{x}$-$\hat{y}$ plane. They represent time-averaged quantities for $t/t_* > 500$. Hereafter, the shaded area in any plot represents the unphysical region (see § 3.2.2), which anyway encloses a negligible fraction of the magnetic energy, currents and vorticity produced.

Let's start with the dominant component, $\langle \hat{B}_x \rangle(z)$. It readjusts from the initial profile, showing in particular an increase for $\hat{z} \in (2, 4)$. The average has been calculated for values $t_* > 500$ since after this time the profile keeps within the same order of magnitude with only some fluctuations due to the movement of the fluid, as the stationary equilibrium has been reached. At saturation, the maximum value $B_x \sim 0.5 B_*$ is slightly above the shear layer, $\hat{z} \sim 2$ (see Table 3.1). The magnetic field is negligible for $\hat{z} \gtrsim 5$. These values corresponds to local intensities up to a few $\sim$ kG in the shear layer (in the physical units discussed in § 2.2.2), while just outside that the field drops by one order of magnitude or more.

Note also that at the bottom of the the domain ($\hat{z} < 1$) there is a non-negligible value of $\hat{B}_x$. This is due mostly to the numerical diffusion, combined with the bottom boundary conditions that allow non-zero vales. The boundary conditions enforce zero tangential currents ($\hat{J}_x$, $\hat{J}_y$), while radial currents $\hat{J}_z$ can penetrate to deeper layers. This is interesting, since propagation to deeper levels has direct consequences for the inflation of the planetary radii. A more rigorous characterization of these

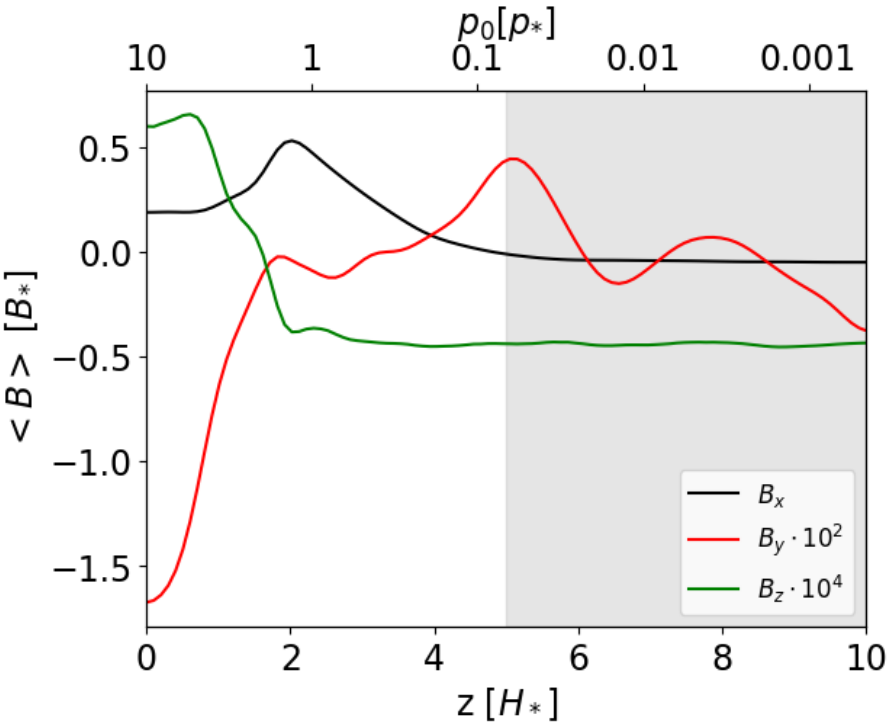

FIGURE 3.7: The vertical profiles $\langle \hat{B}_x \rangle(\hat{z})$, $\langle \hat{B}_y \rangle(\hat{z})$ and $\langle \hat{B}_z \rangle(\hat{z})$ averaged over the $\hat{x}$-$\hat{y}$ plane. The averaged value for all the times after $t/t_* > 500$ for all the components is shown. B_x is in black, B_y in red and B_z in green. We indicate the background value of the pressure, p_0, in units of $p_* = 1$ bar. The shaded area represents the unphysical region, which for numerical reasons includes an artificial shear and a damping layer.

details needs resistive MHD simulations, which will allow us to understand better what comes from physics and what is numerical.

Compared to $\langle \hat{B}_x \rangle$, the other two components (spatially averaged in the same way), $\langle \hat{B}_y \rangle(\hat{z})$ (middle panel) and $\langle \hat{B}_z \rangle(\hat{z})$ (bottom) are a few orders of magnitude smaller, with more fluctuations around zero. The fact that $\langle \hat{B}_z \rangle$ is substantially smaller than $\langle \hat{B}_y \rangle$ is a reflection of the stratification that makes fluid motions (and therefore, magnetic amplification by stretching) easier in the horizontal directions rather than vertical one. Importantly, the vertical field in the outer region has a pretty flat behaviour, with much smaller values, confirming that the atmospherically induced fields are screened outside the shear layer.

3.3.4 Currents

We now move to examine the sustaining atmospheric currents, showing the vertical profile, component by component, in Fig. 3.8, again averaged over the $\hat{x}$-$\hat{y}$ plane. Looking at the time-averages (again at times $\gtrsim 500\ t_*$), we note that the dominant component is $\langle \hat{J}_y \rangle(z)$ (in the plot, J_x and J_z are amplified by factors of 100 and 1000, respectively). It has a maximum value at around $\hat{z} \sim 1.8$, close to the shear layer center z_b. There is a readjustment from the initial value (given by the z-derivative of eq. 3.12). However, there is a change of sign across the shear layer, indicative of the two sides of the meridional loop of currents that enclose the generated toroidal field.

The peak in the deep side (low $\hat{z}$) is sharper than the spatially extended negative currents in the shallow side (high $\hat{z}$). Finally, the remaining two components oscillate instead around zero, with different amplitudes, reflecting again their stochastic turbulent behaviour.

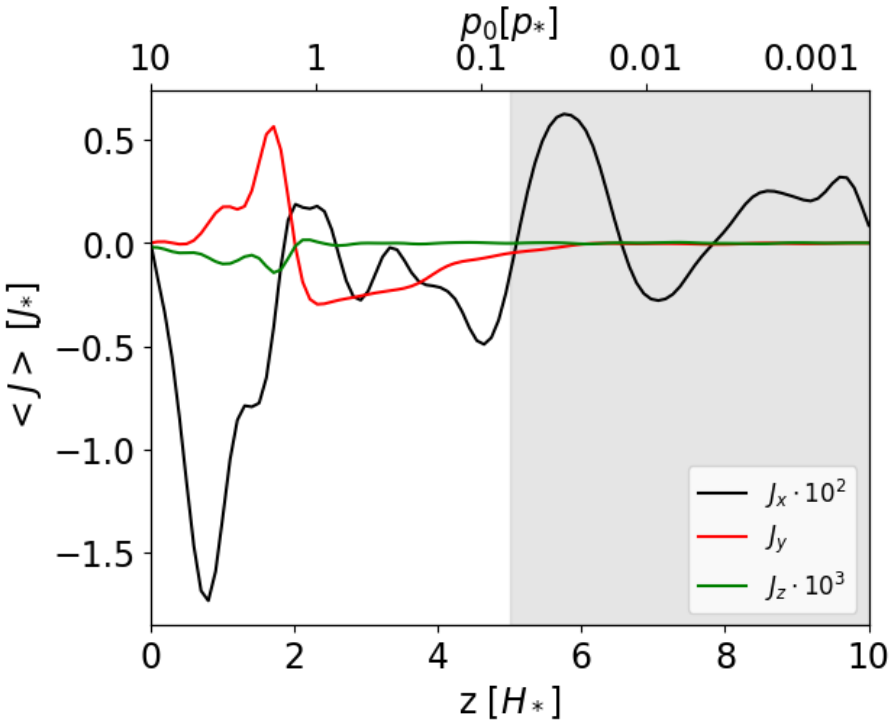

FIGURE 3.8: Same as Fig. 3.7, but for $\langle \hat{J}_x \rangle(\hat{z})$ (amplified by a factor of 100 for clarity), $\langle \hat{J}_y \rangle(\hat{z})$ (amplified by a factor of 1000), and $\langle \hat{J}_z \rangle(\hat{z})$.

3.3.5 Dependence on the wind profile

Let us now move to assess the dependence of the field configuration on the different wind profiles. The top panel of Fig. 3.9 compares $\langle \hat{B}_x \rangle(z)$ for simulations A, B, and C. Firstly, the maximum value for $\langle \hat{B}_x \rangle(z)$ for simulations A and C is relatively similar, while for simulation B, the peak is slightly smaller and displaced to the right due to the increase of z_b from 1.6 to 2. Furthermore, the deviations around the averaged profiles observed for simulations B and C are smaller compared to those in simulation A. Considering the standard deviations, the statistically significant differences are seen at the deepest side. Part of these deviations maybe to the different length of the simulations, with A lasting longer and experiencing a slow gradual rising of $\langle \hat{B}_x \rangle$ for $\hat{z} \lesssim 1$.

3.3.6 Dependence on the forcing

In the central panel of Fig. 3.9, we compare the magnetic profiles (as above), for models A0 (no perturbations), A, Al, Ah, and Adt, i.e. varying either λ (for the first three), or the timestep (At, which physically means a different time correlation between the random perturbations). The amplitude of the perturbation is not producing any substantial change in the average amplitude, meaning that the average state is not

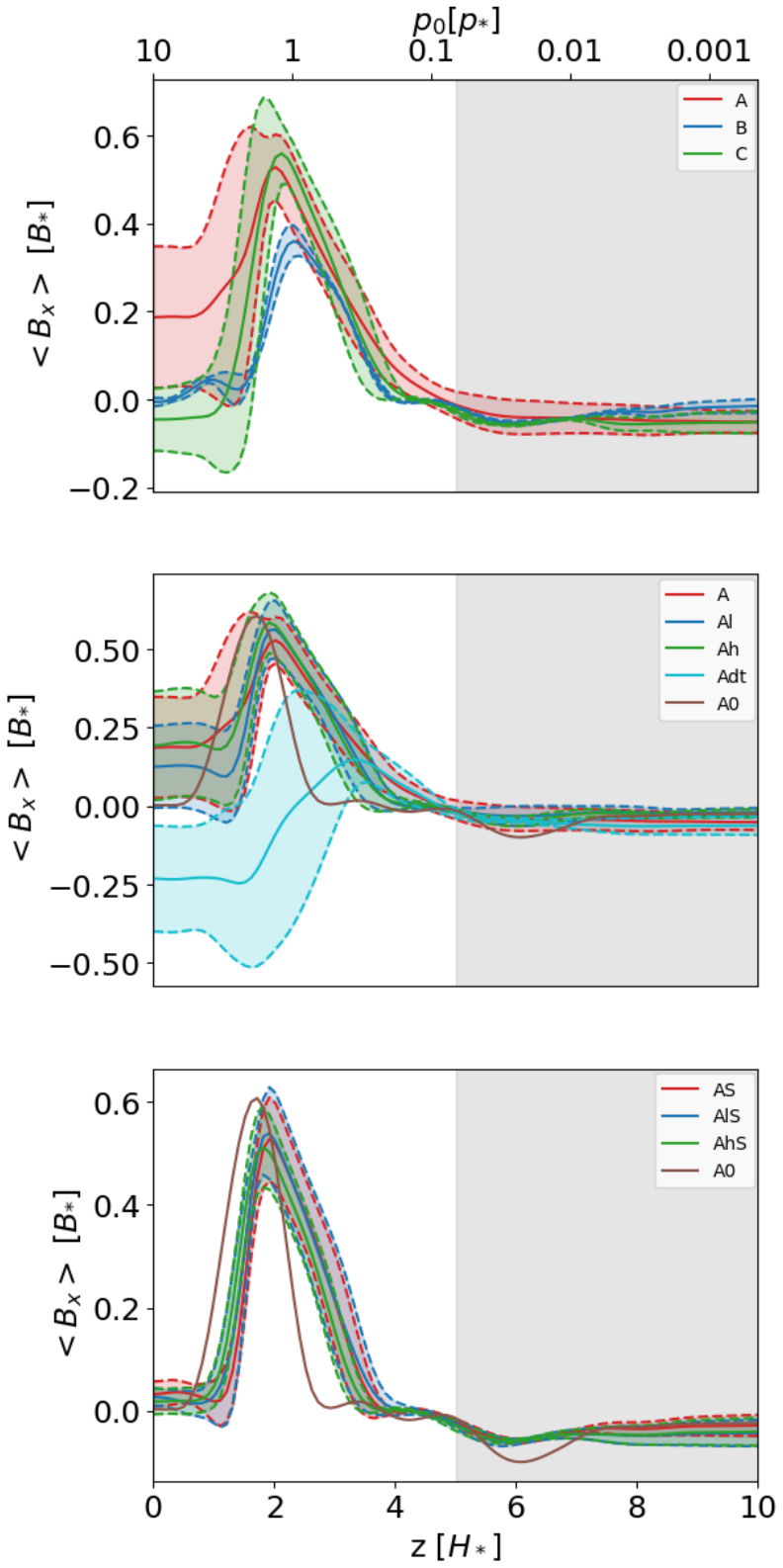

FIGURE 3.9: Comparison of the time-averaged vertical profiles $\langle \hat{B}_x \rangle (\hat{z})$ averaged over the $\hat{x}$-$\hat{y}$ plane, for different representative times. *Top panel:* simulations A, B and C. *Central panel:* simulations A0, A, Al, Ah and Adt. *Bottom panel*: A0, AS, AlS and AhS, which are all models without the local average of $\hat{v_x}$ in the forcing. The solid lines indicate the average, and the dashed, with the enclosed shades, the standard deviation (except for the 1D model A0 for which the solution does not present stochastic variations).

affected by the details of the turbulent motions. However, for the model Adt there is a much larger dispersion of values, with lower induced fields and currents.

In the bottom panel of Fig. 3.9 we show the same comparison for different λ, but in the case of the version of the forcing without the local averaging of $\hat{v}_x$, as discussed above. Such models have very similar average profiles of the models A0, A, Al and Ah, respectively. The differences among different perturbation amplitudes are negligible also in this case, as shown by the overlapping shaded regions. However, they present a much smaller dispersion of the values, reducing greatly the temporal changes, and giving a more constrained average profile as well. Considering also the model Adt, our interpretation is that rising the temporal correlation (lower dt) or spatial correlation (doing local average $\langle v_x \rangle$ in the forcing) of the induced perturbations makes the timescales of saturation longer, allowing stronger long-term pseudo-oscillatory changes in the configuration.

A comparison between A0 and the full 3D models shows that the presence of turbulence ($\lambda > 0$) slightly shifts the dominant component B_x in pressure (and the main component of the current, J_y), but the overall quantity (the peak of B_x) is of the same order. More importantly, turbulence adds a weaker, but non-zero, radial current component (which is otherwise zero), which might be relevant for the interaction with the deeper levels.

Summarizing, the details of the forcing employed can quantitatively (but not qualitatively) affect only to a minor extent the average profiles. Since the forcing is an effective way to mimic the effects of wind and turbulence, we can consider these model-to-model differences as fundamental model uncertainties, related to the nature of the perturbations.

3.4 Applicability of the simulations and estimate of the Ohmic dissipation

The local simulations we have performed here are scale-invariant and we employ a fixed (local) profile of the wind, over which temperature and magnetic fields have no feedback (in other words, we don't have the full global pattern of thermal winds like in GCMs). Instead, in order to convert to physical units, we assign a-posteriori the reference values of temperature T_0, pressure p_*, gravity g and average molecular weight μ (entering in the unit conversion factors, § 2.2.2, via their dimensionless values T_{2000}, p_{bar}, g_{10}, μ, respectively). While the latter two only modify the final physical units and can be assigned with the reasonable expected range, the pressure and temperature have to be chosen consistently with the choice of the wind profile and the isothermal assumption.

The reference pressure (i.e., the units of pressure p_*, which set its value at the bottom of our domain, p_b) is set to be consistent with the shear layer being located around $\sim$ 1 bar, according to most GCM studies (although they usually assume deeper RCBs than what HJs should have, Thorngren, Gao, and Fortney 2019). On the other hand, we know from GCMs that the vertical wind profile depends: (i) on the position (i.e. latitude and longitude), reaching the value of the speed of sound in the most irradiated (sub-stellar) outermost layers ($\lesssim 0.1$ bar); and (ii) on the temperature, because winds are powered by the thermal contrast via irradiation, and because magnetic dragging induced by strong thermal gradients can slow them down (Perna, Menou, and Rauscher, 2010a). The resulting heating efficiency ϵ, defined as the ratio of Ohmic heating to irradiation flux, peaks around $\sim 1500 - 1600$ K (e.g., Thorngren and Fortney 2018b).

Although we don't consider the wind-temperature relations in this work, we can put some physical constraints on the range of temperatures T_0 that we can consider without violating physical constraints. First of all, ideal MHD can be applied if $\mathcal{R}m \gg 1$. The higher the temperature, the greater the ionization, and therefore, the higher the conductivity. This is granted for $T \gtrsim 2000$ K, according to Dietrich et al., 2022.

Secondly, here we provide an additional self-consistency check for our local simulations. Seen from a macroscopic perspective, the amount of Ohmic dissipation should be much smaller than the irradiation flux. Previous works have considered a maximum global (i.e. integrated over the whole surface of the planet) conversion efficiency (ratio of Ohmic heating to irradiation) of about $\epsilon \lesssim 5\%$ (Batygin, Stevenson, and Bodenheimer, 2011), since larger values of ϵ might make the planet exponentially unstable via atmospheric losses. Thorngren and Fortney, 2018b used Bayesian statistics to infer the distribution of ϵ as a function of the incoming flux, obtaining typical values of $\lesssim 2-3\%$ at most (dropping fast for higher T).

We do not have a global simulation, but we can compare the two local fluxes (energy per surface per time) as

$$\int_z Q_j(z)dz < F_{irr} = \sigma_B T_0^4 \simeq 0.9\ T_{2000}^4 \frac{\mathrm{MW}}{\mathrm{m}^2}\ , \tag{3.13}$$

where the left-hand side is the heat flux released by Ohmic dissipation along the column, and F_{irr} is the irradiation over the column under consideration (the usual factor 4 in F_{irr} is not present since this is not the globally averaged irradiation).

The electrical conductivity, eq. 2.11, after a re-grouping of pre-coefficients and using the dimensionless value T_{2000}, that is writing x_e (eq. 2.13) and $\langle \sigma_c v_{en} \rangle$ (eq. 2.12) as:

$$\begin{aligned} x_e(T,p) &= 7.7\times10^{-4}\left(\frac{a_K}{10^{-7}}\right)^{1/2} T_{2000}^{3/4} \\ &\quad \times \left(\frac{n_{10}}{n_n(T,p)}\right)^{1/2} e^{-\alpha/T_{2000}} \end{aligned} \tag{3.14}$$

$$\begin{aligned} \langle \sigma_e v_{en} \rangle(T) &= 10^{-19}\left(\frac{128 k_\mathrm{B} T}{9\pi m_e}\right)^{1/2} \mathrm{m}^2 = \\ &= 3.7\times10^{-14}\ T_{2000}^{1/2}\ \mathrm{m}^3\mathrm{s}^{-1} \end{aligned} \tag{3.15}$$

where: $n_{10} = 3.62\times10^{25}\ \mathrm{m}^{-3}$ is the neutral number density at $p = 10$ bar and $T = 2000$ K and $\alpha = 12.594$ is a numerical factor. See specific details and applicability of these equations in § 2.1.2.

Keeping these expressions in mind, we can quantitatively estimate the local Ohmic dissipation a-posteriori, evaluating the physical conductivity and assuming that the results would not drastically change. Assuming an homogeneous composition in the domain considered, the only quantity of $\sigma(T)$ that depends on the height $\hat{z}$ (via pressure) is:

$$n_n(T, p(\hat{z})) = \frac{\rho(T,\hat{z})}{\mu m_u} \simeq \frac{p_b}{k_\mathrm{B} T_0} e^{-\hat{z}}\ , \tag{3.16}$$

where we have assumed the background state, i.e. $T \simeq T_0$ and $p_1 \ll p_0$. Then the $\hat{z}$-dependence in conductivity can be factorized by defining $\sigma(T) = \sigma_*(T)\ e^{\hat{z}/2}$ (see Appendix C.3 for plots), such that the a-posteriori estimated Ohmic dissipation is:

$$Q_j(T) = \zeta(T)\ \mathcal{I}\ , \tag{3.17}$$

where we have defined a function that combines all of the temperature-dependent terms and numerical factors in eqs. 2.11, 3.14, 3.15 and 3.16:

$$\zeta(T) = \frac{J_*^2 H_*}{\sigma_*(T)} \simeq 24 \left(\frac{e^{\frac{\alpha}{T_{2000}}}}{T_{2000}^{7/4}} \frac{\mu\, g_{10}}{a_{K,7}^{1/2}} \right) \frac{\mathrm{MW}}{\mathrm{m}^2}, \tag{3.18}$$

where $a_{K,7} := a_K / 10^{-7}$, we have used $p_b = 10$ bar, eq. (2.40) for J_* and eq. (2.26) for H_*. The dimensionless integral

$$\mathcal{I} := \int_0^L \langle \hat{J}^2 \rangle(\hat{z}) e^{-\hat{z}/2} d\hat{z} \tag{3.19}$$

is numerically computed by using the average vertical profiles $\langle \hat{J}^2 \rangle(z)$ shown above. In our numerical simulations, we typically obtain $\mathcal{I} \sim 0.1 - 0.3$ (see last column of Table 3.1). As said above, such integral physically depends on the temperature, since it determines the wind profile, which here we fix for a given simulation. When we use higher resolutions, as commented above, we obtain higher values of B_x, J_y, and, as a consequence, $\mathcal{I}$. In the 1D problem (A0), for $N_z = 50, 100, 200, 400$, we obtain the values of $\mathcal{I} = 0.11, 0.36, 0.85, 1.13$, respectively. This is consistent with the fact that higher resolutions correspond to lower numerical resistivities, which are representative of hotter Jupiters. The chosen resolution here ($N_z = 100$) corresponds to an implicit numerical resistivity comparable to a physical one for very high temperatures ($T_0 \gtrsim 3000$ K) at the pressures of the shear layer where most currents live (see Appendix C.3). In this range, local energy balance gives local efficiencies $Q_j / F_{irr} \lesssim 0.01$ (Fig. 3.10), which are reasonable values, comparable to the usual estimates of overall heating efficiencies (Thorngren, Gao, and Fortney, 2019). In a follow-up work, we will implement realistic profiles of the magnetic diffusivity for different temperatures. Since in most HJs ($T_{eq} \sim 1500 - 2500$ K) the diffusivity will be higher than the implicit one implemented here, we expect lower values of B_x and J_y.

Since Fig. 3.10 only takes into account the dependencies on temperature of the unit conversion and the conductivity $\sigma(T)$, and not the wind $w(T)$, the decrease of Ohmic heating with temperature is steeper than in reality. For low temperatures, the wind and induced magnetic fields (hence, $\mathcal{I}$) are much lower, hence the curve would bend down. At high temperatures, the intensity of the wind saturates due to magnetic drag, so the trend could be more realistic. In fact, Thorngren and Fortney, 2018b infer a strong decrease of efficiency (well below 1%) for very HJs.

Finally, note that here we are only considering the energetics that represent a column in the hotter part of the day-side atmosphere. Hence, the temperature here considered is higher than the the equilibrium temperature (which is the one entering in the global energy balance), $T_0 > T_{eq}$. This also means that the shear-induced currents are on average lower than what we infer here, so the total Ohmic deposition will be less. As a matter of fact, the velocity profile changes according to the longitude, and the ideal MHD including winding mechanism and turbulence apply only in the regions with high enough $\mathcal{R}m$, i.e., in the regions with the steepest shear layers (e.g., Rogers and Komacek 2014, Beltz et al. 2022). Therefore, Fig. 3.10 should not be taken as an indication of the global energetics (efficiency), although it provides important qualitative insights of what happens at high T (non-linear regimes).

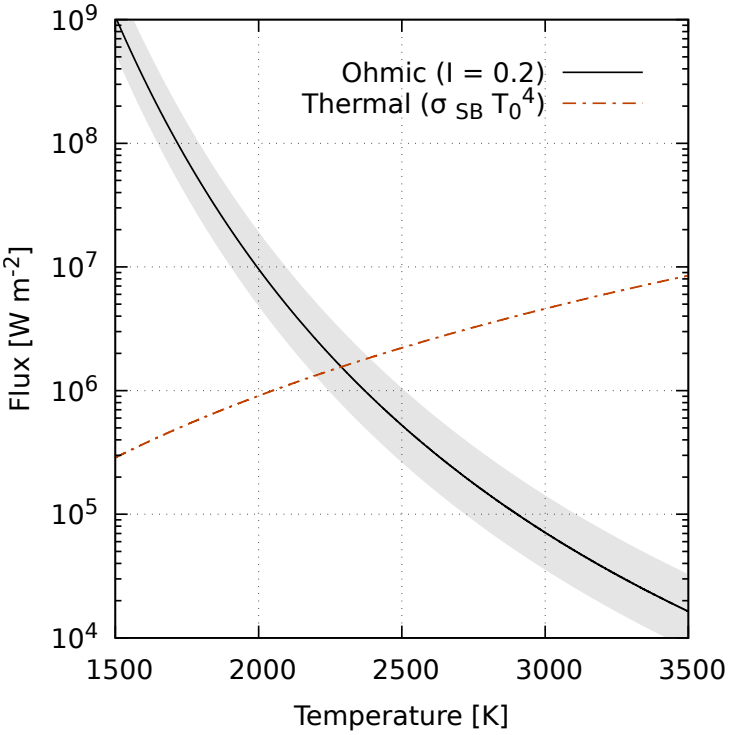

FIGURE 3.10: Applicability of our results: conversion to physical units as a function of T_0, the background temperature that we assign a-posteriori to a given simulation. We compare the estimated Ohmic heat over the column (black line, assuming $g_{10} = 1, \mu = 2$, $p_{bar} = 1$ and $a_k = 10^{-7}$) and the local irradiation flux (red dot-dashed line). The gray shaded area indicates a range of typical values of the dimensionless integral $\mathcal{I}$, evaluated from the numerical simulations: from 0.1 to 0.4, while the black line is for 0.2. Our estimate is self-consistent only if the Ohmic heating is approximately below the irradiation line. From the plot, this corresponds to $T_0 \gtrsim 2300$ K, for the parameters chosen. Note that this plot is not meant to display the dependence of Ohmic dissipation on temperature: here, with our local simulations, we consider a fixed wind profile and hence we do not account for the important global temperature-dependence on the wind (considered instead in GCMs).

3.5 Final remarks

In this Chapter we have performed ideal MHD simulations of a HJ's narrow atmospheric column. We have used a forcing to mimic a realistic model of zonal wind profile, on which we added random perturbations. The main conclusions obtained from this work are:

- The shear layer gives rise to an intense magnetic field winding, consistently with a semi-analytically estimate. At equilibrium, such a toroidal field can reach local values of up to a few kG, in a very small region.
- The huge magnetic field is sustained by meridional currents that close within a narrow vertical layer, corresponding to the shear region. These results are in qualitative agreement with the non-linear regime by Dietrich et al., 2022 and share common features with the dynamo in Jovian outer layers simulated by

Wicht, Gastine, and Duarte, 2019, scaled by orders of magnitude due to the higher energy budget.

- The turbulence induced by the random perturbations creates an additional magnetic field, which tends to acquire a small meridional component (of the order of tens of Gauss maximum). The stratification hampers the stretching of the lines in the vertical direction, and the turbulent field tends to be evident in the bottom of the box, possibly pointing to a penetration of currents to deeper levels, a fundamental premise to power the radii inflation.

- The results show an important stochastic variability in the plane-averaged vertical profiles of the different quantities, specially when the details of the imposed forcing are modified.

- The results, interpreted here in terms of a zonal wind and induced toroidal field, can apply also to a meridional wind: in that case the induced magnetic field would be mainly meridional, supported by local azimuthal currents.

- We neglected the physical resistivity and it only comes from the numerical scheme, for this reason the simulations are only valid high values of the conductivity $\sigma(z)$. As σ increases with temperature, considerations of local energy balance, numerical dissipations and magnetic Reynolds number gives us a bound on the minimum local temperature of about $T_0 \gtrsim 3000$ K, above which these simulations can be considered applicable.

- The rough estimate of the Ohmic dissipation can be used as a proxy for the deposited heat in the upper radiative layer. Although we cannot infer the global energetics from our local simulations, we find that the Ohmic heating efficiency decreases for increasing temperature, since the conductivity increases. Although here we do not consider the important dependence of wind on temperature such trends are probably real and compatible with other complementary studies (Thorngren and Fortney, 2018b), since the wind velocity stops increasing with T due to magnetic drag (Perna, Menou, and Rauscher, 2010a). Therefore, the results reported here should be regarded as an upper limit on the amount of Ohmic dissipation in the outer parts of the atmosphere (but not far from reality for very large T).

- The confinement of the magnetic field implies that they cannot unfortunately power detectable $\lesssim$ GHz coherent magnetospheric radio emission, expected via electron cyclotron maser mechanism at frequencies ν [MHz]=2.8 B [G] (Zarka, 1998). In our case, the magnetic field amplified in the atmospheric layers is predominantly toroidal and remains confined within the planetary envelope, lacking a significant radial component that would allow the emission to escape into space. However, the interaction between such shallow magnetic field and the one generated in the convective dynamo region, possibly reaching $\lesssim 100$ G (Cauley et al., 2019), is an interesting point to be explored further.

Our aim is to extend this framework beyond the present isothermal, analytically forced column. In the following chapters, we address some of these aspects by introducing more realistic wind and thermodynamic profiles, exploring non-ideal MHD effects, and disentangling the roles of forcing and perturbations.

4

Non-ideal MHD simulations of hot Jupiter atmospheres

4.1 Introduction and objectives

In this Chapter, largely corresponding to the work presented in Soriano-Guerrero et al., 2025b, we investigate the outermost, radiative layers of a HJ atmospheric column, building upon our previous work in Chapter 3. A key caveat in that chapter was the use of ideal MHD, with numerical resistivity as the only limiting factor to the otherwise unbounded winding, which restricted applicability to uHJs only. Here, we extend the study to HJs of any temperature by incorporating the three main non-ideal MHD terms, Ohmic, Hall, and ambipolar, into the analysis. As a first step, we solve the general 1D induction equation in a plane-parallel approximation, considering only vertical variations, and adopt as inputs the thermodynamic and wind profiles from GCM simulations by Rauscher and Menou, 2013, Beltz et al., 2022 and Coulombe et al., 2023. For all GCM outputs, we focus on the substellar point, which is expected to be the most extreme in terms of local induction, due to its higher T_{eq} and, consequently, higher conductivity and stronger induced currents. The profiles of conductivity, electron density, and ion density entering the non-ideal terms are computed self-consistently from the imposed thermodynamical profiles. We evolve the MHD equations, including forcing terms to maintain the background wind and temperature profiles, until a stationary solution is reached. Note that, compared to the previous Chapter, we increase the numerical resolution of the simulations to $N = 400$. We then evaluate the induced magnetic field components and the deviations of thermodynamical quantities from the original background state. Although intrinsically local and not a substitute for GCMs, this approach allows us to characterise the main features of non-ideal atmospheric induction, inform Ohmic dissipation models, enable a more realistic inclusion of magnetic drag in hydrodynamical GCMs, and provide a basis for future 3D turbulence studies.

4.2 Initial conditions and setup

4.2.1 Background profiles and formulation of the atmospheric column equations for this setup

In this Chapter, the background profiles and the atmospheric column equations become more complex, compared to Chapter 3. The atmospheric column is no longer assumed to be isothermal; instead, the background information for the temperature (T_0) as well as for pressure (p_0) and wind (w) are obtained directly from the output of a GCM at the substellar point. This approach replaces the simplified isothermal setup and the approximate wind profiles used previously, as we now rely on GCM ouptuts. Below we detail those background profiles used to solve the physical equations of the problem as well as any difference in those equations compared to the reference model presented in Chapter 2.

GCM data, initial and background profiles

In order to prescribe a column profile for $p_0(z)$, $\rho_0(z)$ and $w(z)$, we make use of profiles calculated from GCM models of specific planets. We consider profiles at the sub-stellar point of each setup, covering a significant fraction of the HJ parameter space, described in Table 4.1.

Model	M_p $[M_J]$	R_p $[R_J]$	$T_{\rm eq}$ [K]	$F_{\rm irr}$ [MW/m^2]	$B_{\rm d}$ [G]
WASP 76b-d0	0.92	1.83	2160	4.9	0
WASP 76b	0.92	1.83	2160	4.9	3
HD 189733b	1.13	1.13	1191	0.32	3
HD 209458b	0.73	1.36	1484	1.1	3
WASP 18b	10.2	1.24	2413	7.7	20
WASP 121b	1.16	1.75	2358	7.0	3

TABLE 4.1: List of the main properties of the input profiles used in this work. For each planet modelled by the GCM, labelled as in the first column, we indicate: the observed values (retrieved from the NASA Exoplanet Archive) of mass M_p, radius R_p (in units of Jupiter mass and radius, respectively), equilibrium temperature $T_{\rm eq}$ and irradiation $F_{\rm irr}$, and the background magnetic field value B_d used in the drag term in the GCM.

A summary of these inputs can be found in Fig. 4.1, where we show the $p(T)$ and $w(z)$ profiles for the different cases considered. Such profiles are output from previous works, including Coulombe et al., 2023 for the WASP 18b model, and Beltz et al., 2022 for the models of WASP 76b. The models for HD 209458b and HD 189733b are equivalent to those published in Rauscher and Menou, 2013. Each model was calculated at a resolution of T32 (corresponding to roughly 3 degrees separation at the equator) and ran until a steady state was reached, corresponding to at least 1000 planetary orbits. Those works make use of the Rauscher and Menou (RM)-GCM[1] (Rauscher and Menou, 2013), incorporating an updated radiative transfer scheme from Roman and Rauscher, 2017, which is based on Toon, 1989. The set of models used in this paper fall under two categories for radiative transfer: double gray and correlated-K. The models for HD 209458b and HD 189733b use a *double-gray* approach, employing two absorption coefficients: one for the visible wavelength range to account for the absorption of the host star's radiation, and another for the infrared

[1] https://github.com/emily-rauscher/RM-GCM

range to represent the planet's thermal emission; for further details see Rauscher and Menou, 2013. The remaining GCM models use a *picket fence* radiative transfer scheme, which uses 5 absorption bands compared to the two used by the double-gray method. For more details on the picket fence radiative transfer, see Malsky et al., 2024.

Additionally, all the GCM input models, except WASP 76b-d0, make use of a spatially varying drag timescale that approximates the Lorentz force felt by charged atmospheric species. The background magnetic field strength, B_d is shown in the last column of Table 4.1. The inclusion of this active drag reduces circulation efficiencies and increases the day-night contrast. This magnetic drag is calculated based on local atmospheric conditions and applied in a geometrically and energetically consistent way using the expression (Perna, Menou, and Rauscher, 2010a):

$$\tau_{\rm drag} \sim \frac{\rho c}{B_d^2 \sigma |\cos(\theta)|}\,, \tag{4.1}$$

where θ is the latitude, c the vacuum light speed, and the background field B_d is a free parameter of the model, taken as constant in depth. This expression is a good approximation of the drag timescales if: (i) the induced field is only a perturbation of the background field (i.e it does not include the atmospherically induced field which can be much larger than the background one); (ii) the magnetic field is approximated as a pure dipole (which gives the $\cos\theta$ dependence), aligned with the axis of rotation; (iii) the background field strength does not vary much as a function of radius.

With these assumptions, at the sub-stellar point, which lies on the equator, the magnetic field is expected to be purely meridional, with a zero radial component. However, misaligned magnetic fields, composed by a combination of multipoles, are seen both observationally from e.g. the Jovian magnetic spectrum inferred directly from Juno low-orbit measurements (Connerney et al., 2022), and theoretically through dynamo simulations of gas giants, e.g. the state-of-the-art simulations by Gastine and Wicht, 2021. Both features (misalignment and non-trivial multipolarity) would result in a non-zero radial component of the magnetic field at the equator. Future GCM works will explore the effects of tilted dipoles or more complex geometries. For this reason, we introduce a small but non-zero initial radial component, that we fix by default as $B_z^{\rm in} = 0.1\, B_y^{\rm in}$ (if not indicated otherwise), which acts as a necessary seed to trigger the winding mechanism in our 1D setup. Note that, by default, we set $B_y^{\rm in} = B_d$, so $B_y^{\rm in}$ is fixed to the same value of the background field used in the GCM drag timescale. However, note that we also explore different values of $B_y^{\rm in}$ and $B_z^{\rm in}$ for WASP 76b, which we use a reference model. We list in Table 4.2 the different setups shown in the paper. The azimuthal component is initially vanishing, $B_x^{\rm in} = 0$ in order to obtain at the stationary state a B_x that would be purely the result of the winding effect. See also § 4.2.2 for boundary conditions.

The profiles employed in this study (Fig. 4.1) span a range of pressures of $\sim$ 0.005-100 bars for all models. A wide range of temperatures $\sim$ 1500-3500 K can be observed (top panel), depending on the pressure and the planetary model. In particular, for those models with higher equilibrium temperatures, there is a characteristic temperature inversion region where temperature decreases as p decreases. This feature only occurs in the hottest models: WASP 76b, WASP 76b-d0, WASP 18b, and WASP 121b, and is not found in the models for HD 20958b or HD 189733b.

In the bottom panel of Fig. 4.1, we show the profiles of the azimuthal (east-west)

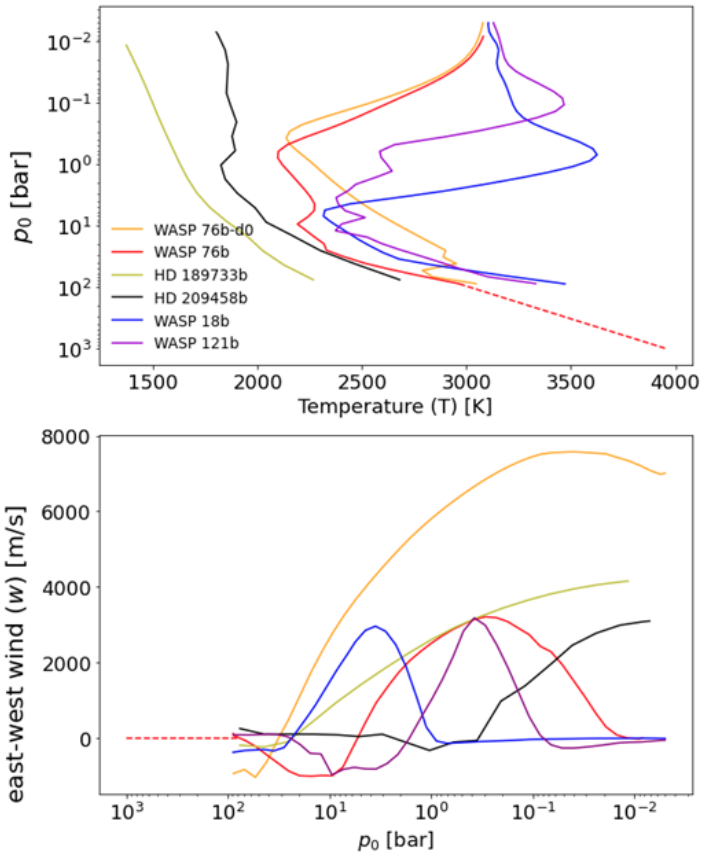

FIGURE 4.1: Substellar profiles for the different models shown in Table 4.1: $p(T)$ (top) and zonal winds $w(z)$ (bottom). We show the extension to deeper pressures for WASP 76b with a dashed line.

wind. The meridional components (north-south) of the winds are 1-2 orders of magnitude lower than the dominant east-west winds. This is primarily due to the influence of thermal tides induced by stellar radiation, which generate a super-rotational eastward jet at the equator (Showman and Guillot, 2002; Showman, Menou, and Cho, 2008; Menou, 2019).

Among the modelled planets, WASP 18b-20 is the one with the highest equilibrium temperature and gravity. The high gravity of this planet results in a much thinner domain (see L values in Table 4.1), compared to the other models. Moreover, this model also used the strongest background magnetic field strength, $B_d = 20$ G (chosen based on fitting the *JWST* light curve of the planet, Coulombe et al. 2023) causing the resulting east-west winds to be slower for a larger faction of the modeled domain than in other planets. For the other planets, the GCMs adopted instead a value of $B_d = 3$ G. For comparison, we also consider the profile for a WASP 76b GCM model without magnetic drag, $B_d = 0$ G.

Using the $p(T)$ profiles from the GCM models, we recover the hydrostatic equilibrium profiles $(p_0(z), \rho_0(z), T(z))$ by solving eq. 2.2 for the different cases.[2] The $p(z)$ and $T(z)$ profiles are shown in the top and middle panels of Fig. 4.2. There, $z = 0$, with the corresponding pressured defined as p_{top}, corresponds to the values in the range $p_{\rm top} \in (5 \times 10^{-3}, 10^{-2})$, depending on the simulation. Using these

[2]In order to minimize the discretization errors when solving the hydrostatic solution, we have interpolated on a much finer grid the GCM output $p(T)$, which has typically only 30-100 points.

profiles, we compute the conductivity, σ, based on eq. 2.11 and shown in the bottom panel of Fig. 4.2 as a function of pressure p_0. Planets with higher equilibrium temperatures display higher conductivity over the modelled domain. Moreover, if we carefully analyze individual profiles, especially those with higher temperatures, we can appreciate that higher conductivity values are reached near the top of the domain as both the higher temperatures and the lower pressures enhance the conductivity (see eq. 2.11). At deeper layers, we encounter regions of temperature inversions (decreasing temperature) followed by a region of increasing temperature. Correspondingly the conductivity, after a decline, increases again, albeit to a lesser extent due to the higher density of the deeper levels. HD 1898733b and HD 209458b, being colder than the other planets, have much lower conductivities. The former in particular do not show temperature inversion.

Extension of the WASP 76b model to deeper layers

In order to test the influence of considering deeper layers in our simulations we extend the temperature, wind, and conductivity profiles of our representative case, WASP 76b. This is displayed in Fig. 4.1 and 4.2 with dashed lines. We extend the model up to 1000 bar, i.e. connecting to the convective region, which, for HJ, can be between $\sim 10^2$ and 10^3 bar, depending on the amount of irradiation and internal heating (Komacek and Youdin, 2017; Thorngren, Gao, and Fortney, 2019). Specifically, we impose an adiabat $p \propto T^{\frac{\gamma-1}{\gamma}}$, with a euristically chosen index $\gamma = 1.12$ which enables us to smoothly connects with the GCM $p(T)$ profile (the precise value of the slope is a second-order effect, for our general purposes).

Regarding the extrapolation of the wind profile, we note that in regions of higher pressure, $p \gtrsim 10$ bar, the wind speeds tend to greatly decrease (Fig. 4.1). As a matter of fact, the azimuthal temperature gradients present in these layers can still drive significant winds, but the increased density and pressure tend to drastically moderate the speeds. For this reason, we assume $v_w = 0$ for the extended range of pressure, $p \gtrsim 100$ bar.

We note, however, that this downward extrapolation is a simplified approach and should be interpreted with caution. At higher pressures, both the equation of state and the thermodynamic properties of the gas may vary significantly, potentially altering the temperature and wind structure. Therefore, our adiabatic extension provides only a first-order approximation of the deep atmosphere. More realistic interior–atmosphere coupling models, such as those presented (Sainsbury-Martinez et al., 2023), show that the deep temperature–pressure profiles deviate from a linear or simple adiabatic slope. While our assumption enables a smooth connection with the GCM domain, it does not capture these non-linear effects and should be considered an idealized continuation for the purpose of testing the influence of deeper layers.

Specific setup for MHD equations and 1D approach

With these background profiles, we solve the compressible MHD equations in a column, using Cartesian coordinates, as presented in Chapter 2. However, unlike the 3D study in Chapter 3, here we consider a 1D problem, with a purely vertical domain ($z \in [-L, 0]$). The bottom boundary is characterized by a pressure ranging from 76.44 to 1000 bar. The pressure at the top boundary is the minimum value which differ from model to model but lies in the range $p_{\rm top} \sim 0.002 - 0.02$ bar. The upper fifth of the domain, in which we artificially damp the vertical momentum for

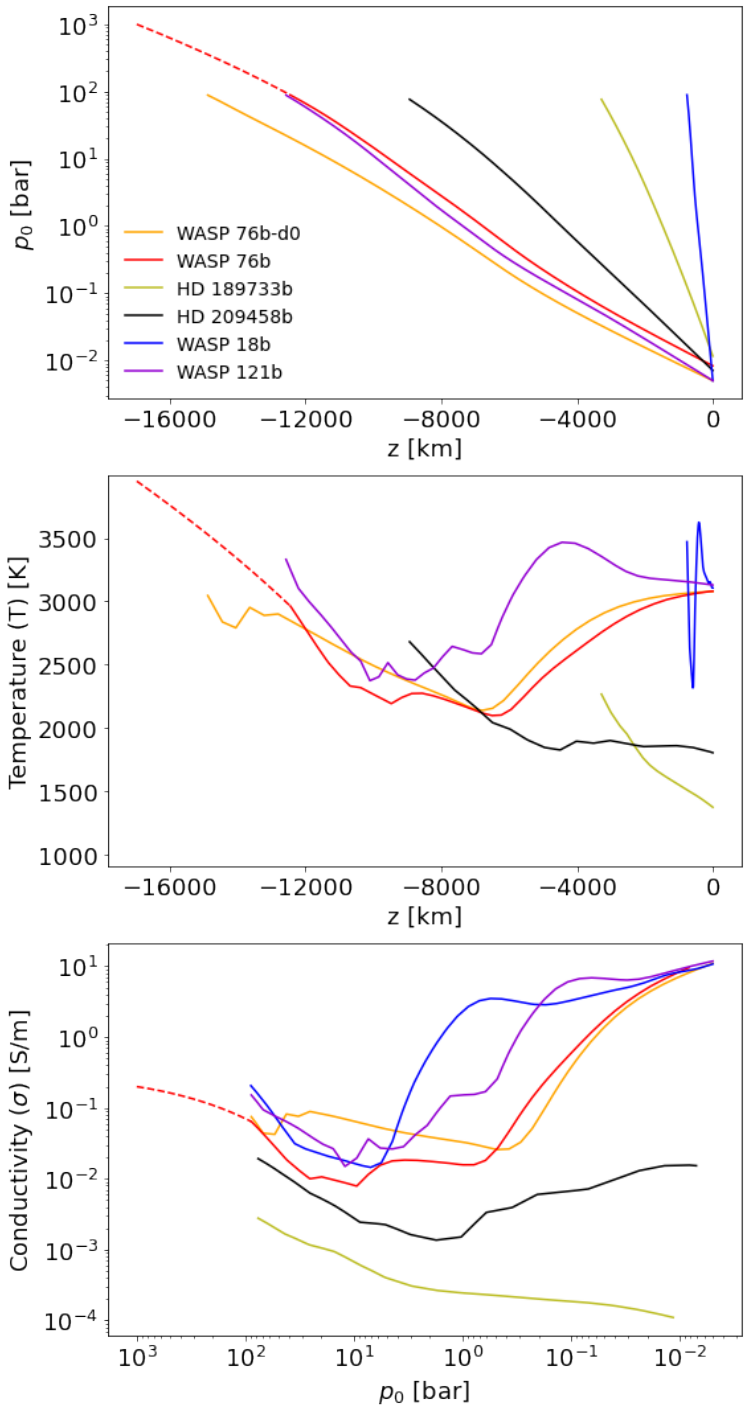

FIGURE 4.2: Vertical profiles at hydrostatic equilibrium, for the different models shown in Table 4.1, of: pressure $p_0(z)$ (top), temperature $T(z)$ (center) and the corresponding electrical conductivity $\sigma(p)$ (bottom). The layer $z = 0$ corresponds to the top boundary of the numerical domain, p_{top}.

stability purposes (see § 2.1), corresponds to pressures $p \lesssim 0.01 - 0.09$ bar, with the specific value depending on the planet.

Note that we only consider vertical dependences since we are interested in the main magnetic effects caused by the dominant, vertical gradients set by the background state and wind profile. Practically, we set up a 1D, plane-parallel problem and evolve the deviations of density ρ_1, the components of the momentum density, $\mathbf{S} = \rho\mathbf{v}$ of the magnetic field, and the total energy density U, keeping in mind that the gradient, divergence, and curl operators reduce to non-zero ∂_z derivatives only.

It is worth noting some aspects of the MHD equations (§ 2.1.2). Compared to the previous Chapter 3, in the present setup, in addition to the advective term, the induction equation, eq. 2.7 includes Ohmic dissipation, Hall drift, and ambipolar diffusion. Note that since the Ohmic term has been explicitly included in the induction equation, the corresponding Ohmic heating term Q_j has also been incorporated into the energy density evolution equation.

It may be instructive to show the dependence of the evolution of the magnetic field components as a function of the electric field terms in order to explicitly identify which components of velocity, magnetic field, and current directly affect the evolution of each magnetic field component. This evolution can be written as:

$$\frac{\partial \mathbf{B}}{\partial t} = -\nabla \times \mathbf{E} \quad \Rightarrow \quad \begin{aligned} \frac{\partial B_x}{\partial t} &= -\left(\frac{\partial E_z}{\partial y} - \frac{\partial E_y}{\partial z}\right), \\ \frac{\partial B_y}{\partial t} &= -\left(\frac{\partial E_x}{\partial z} - \frac{\partial E_z}{\partial x}\right), \\ \frac{\partial B_z}{\partial t} &= -\left(\frac{\partial E_y}{\partial x} - \frac{\partial E_x}{\partial y}\right). \end{aligned} \tag{4.2}$$

For brevity, we can rewrite the electric, eq. 2.9, field as:

$$\mathbf{E} = -\mathbf{v} \times \mathbf{B} + \frac{\mathbf{J}}{\sigma} + f_h\,(\mathbf{J} \times \mathbf{B}) - f_a\left[(\mathbf{J} \times \mathbf{B}) \times \mathbf{B}\right], \tag{4.3}$$

Writing each vector product in Cartesian components:

$$\mathbf{v} \times \mathbf{B} = \begin{pmatrix} v_y B_z - v_z B_y \\ v_z B_x - v_x B_z \\ v_x B_y - v_y B_x \end{pmatrix}, \quad \mathbf{J} \times \mathbf{B} = \begin{pmatrix} J_y B_z - J_z B_y \\ J_z B_x - J_x B_z \\ J_x B_y - J_y B_x \end{pmatrix}, \tag{4.4}$$

$$(\mathbf{J} \times \mathbf{B}) \times \mathbf{B} = \begin{pmatrix} B_x(J_z B_z + J_y B_y) - J_x(B_z^2 + B_y^2) \\ B_y(J_x B_x + J_z B_z) - J_y(B_x^2 + B_z^2) \\ B_z(J_y B_y + J_x B_x) - J_z(B_y^2 + B_x^2) \end{pmatrix}. \tag{4.5}$$

Since we consider only vertical gradients, the partial gradients in x and y can be omitted, resulting in:

$$
\begin{aligned}
\partial_t B_x = & -\partial_z(v_z B_x - v_x B_z) + \partial_z\left(\frac{J_y}{\sigma}\right) \\
& + \partial_z\Big[f_h\left(J_z B_x - J_x B_z\right)\Big] \\
& - \partial_z\Big\{f_a\left[(J_x B_y - J_y B_x)B_x - (J_y B_z - J_z B_y)B_z\right]\Big\}, \qquad (4.6)\\
\partial_t B_y = & \ \partial_z(v_y B_z - v_z B_y) - \partial_z\left(\frac{J_x}{\sigma}\right) \\
& - \partial_z\Big[f_h\left(J_y B_z - J_z B_y\right)\Big] \\
& + \partial_z\Big\{f_a\left[(J_z B_x - J_x B_z)B_z - (J_x B_y - J_y B_x)B_y\right]\Big\} \qquad (4.7)
\end{aligned}
$$

Overall, at first order, the dominant contributions are expected to come from the winding mechanism (advective term, $\partial_z(v_x B_z)$), and Ohmic dissipation, $\partial_z(J_y/\sigma)$, especially for deep enough layers. Depending on the relative weight of the advective to resistive terms, the induced field can be just a perturbation of the background field (Ohmic-dominated regime), or be locally comparable to or even larger than it (advection-dominated regime), see Dietrich et al., 2022 for an in-depth discussion. Note that the winding mechanism is intrinsically linear: the induced field grows linearly with the component of the magnetic field which is perpendicular to the flow. However, the advection-dominated regime is sometimes called non-linear, in the sense that, in a full 3D GCM, the induced field can have a non-trivial feedback on the flow, which in turn modifies the direction and intensity of the induced field, so that considering the background field alone in the $(\mathbf{v} \times \mathbf{B})$ term is not valid anymore (see e.g. the analytical and numerical study by Batygin, Stanley, and Stevenson 2013), unless one considers a very idealized case (axial symmetry, purely azimuthal wind, alignment between rotational axis and magnetic moment).

On the other hand, it is important to note that the expression for $\mathbf{F}$ is slightly different from that in eq. 3.6. First, under the present 1D scenario there are no perturbations in the forcing, this means $\lambda = 0$. In addition, a small adjustment is made to the wind forcing term, compared to Chapter 3 which leads to rewriting eq. 2.2.5 as

$$\mathbf{F} = \frac{\rho_0}{\tau}\mathbf{f}_{\text{wind}} - \mathbf{S_d} = \frac{\rho_0}{\tau} f_0\left(v_x - w(z)\right)\mathbf{e_x} - \mathbf{S_d}. \qquad (4.8)$$

although the $\mathbf{f}_{wind}$ slightly changes from previous chapter, the practical aim is the same, to keep the azimuthal velocity v_x very close to the imposed wind profile $w(z)$.[3]

Finally note that, since the domain is limited to the vertical direction, the damping term $\mathbf{S}_d$ is applied only in the vertical (z) direction, resulting in:

$$\mathbf{S_d} = A_d\left(\frac{z_d - z}{z_d}\right)^2 S_z \mathbf{e_z} \qquad (4.9)$$

where $z_d = -0.2L$. Note that the prefactor slightly changes compared to Chapter 3 as it has redefined according to the new domain.

[3] In this study the x-component of the forcing, $\propto (v_x - v_w(z))$, is used to keep the flow symmetrically close to the wind profile. In our previous study, Chapter 3, inspired by the decaying turbulent study of Ryu, Zingale, and Perna, 2018, the azimuthal forcing was applied only if v_x (or a local average of it) was larger than $v_w(z)$, i.e. potentially allowing v_x to locally grow to larger intensities, limited only by the numerical dissipation, leading more easily to numerical instabilities.

Finally, we should specify how the election of the reference values has been done. As mentioned, p_*, μ, T_0 and g have to be fixed in order to define the physical units of the system. However the selection of T_0, which determines the characteristic length scale of the problem, in a non-isothermal domain, is not obviously determined. In this case we defined the $H_* = L/10$. In this way the relation between T_0 and g is univocally determined and can be resolved using the gravitational law, according the the mass and radii data in Table 4.1. Note that in Chapter 5 we have followed the same procedure presented here.

By using our hybrid approach, i.e. a full MHD system of equations plus a forcing on the vertical profiles of p (i.e., T and ρ) and v_x, we can partially evaluate the vertical distribution of density/pressure perturbations and the magnetic feedback on the vertical and meridional fluid velocity, which in turn enters in the induction equation. In general, the thermodynamic deviations are much smaller than the background values, being non-negligible only in some particular ranges, usually in correspondence of low density or high shear (i.e., high induced field). Therefore, although our local box simulations with given input profiles cannot consistently include the global feedback of magnetic effects on the flow and on the $p(T)$ profiles, we can roughly assess at which depths and by how much the induced magnetic fields are expected to change the considered thermodynamic profiles, if they were fully included in GCM models.

4.2.2 Resolution and boundary conditions

In the simulations presented in this Chapter the bottom domain is characterized by a pressure ranging from 76.44 to 1000 bar. The pressure at the top boundary is the minimum value which differ from model to model but lies in the range $p_{\rm top} \sim 0.002 - 0.02$ bar. The upper fifth of the domain, in which we artificially damp the vertical momentum for stability purposes (see § 2.1), corresponds to pressures $p \lesssim 0.01 - 0.09$ bar, with the specific value depending on the planet.

We employ a discretization of $N_z = 400$ grid points in all the simulations presented, except where specified otherwise. This resolution has been chosen to balance computational efficiency with the need of numerical convergence of the solution, which may be demanding in the uppermost, highly conductive layers of the hottest models. Said in another way, the chosen resolution is enough to ensure that the physical resistivity is higher than the numerical one almost everywhere in all cases, see Appendix D.2.

For the magnetic field, we fix all components B_x, B_y and B_z to their background, initial values, both at the top and the bottom boundaries. In other words, we are confining the atmospheric induction only to the considered domain. This is a conservative choice and neglects the extension of induced currents at deeper layers (Liu, Goldreich, and Stevenson, 2008; Batygin and Stevenson, 2010; Wu and Lithwick, 2013; Ginzburg and Sari, 2016; Knierim, Batygin, and Bitsch, 2022). This assumption is in part dictated by the need to have a numerically convergent solution (see Appendix D.1). We will discuss the caveats and implications of this assumption in § 4.3.5, showing how the results change when we consider deeper layers, for the extended setup of WASP 76b explained in § 4.2.1.

Finally note that for consistency with the continuity equation at equilibrium, we impose $\partial_z S_z = 0$,[4] and consequently $v_z = S_z/\rho$.

[4]The presence of a non-zero v_z and the necessity of a damping term in the uppermost layers don't allow a perfectly constant S_z at equilibrium: however, if we remove the damping term, the velocity grows uncontrollably, for large enough domains (Soriano-Guerrero et al., 2023).

4.3 Results

Model	$B_z^{\rm in}$ [G]	$B_y^{\rm in}$ [G]	$p_{\rm top}$ [bar]	$p_{\rm bot}$ [bar]	L [km]	$\lvert B_x\rvert_{\rm max}$ [G]	$\int_D Q_j dz$ [MW/m^2]	ϵ
WASP 76b	0.3	3	0.002	88.34	18762	180	8.0×10^{-4}	1.6×10^{-4}
HD 189733b	0.3	3	0.02	76.44	2830	0.39	2.9×10^{-6}	9.1×10^{-6}
HD 209458b	0.3	3	0.007	76.44	8190	14	8.5×10^{-5}	7.7×10^{-5}
WASP 18b	2	20	0.004	89.13	770	260	7.5×10^{-3}	9.7×10^{-4}
WASP 121b	0.3	3	0.003	88.34	13230	1550	8.0×10^{-3}	1.1×10^{-3}
WASP 76b-p300*	0.3	3	0.005	300	19249	210	8.1×10^{-4}	1.7×10^{-4}
WASP 76b-p500*	0.3	3	0.005	500	20367	275	7.8×10^{-4}	1.6×10^{-4}
WASP 76b-p1000*	0.3	3	0.005	1000	21979	390	7.8×10^{-4}	1.6×10^{-4}
WASP 76b-d0-Bz0.3*	0.3	0	0.005	88.34	17220	870	3.5×10^{-3}	7.1×10^{-4}
WASP 76b-d0-Bz0.03*	0.03	0	0.005	88.34	17220	80	3.1×10^{-5}	6.3×10^{-6}
WASP 76b-d0-Bz0.003*	0.003	0	0.005	88.34	17220	8	3.1×10^{-7}	6.3×10^{-8}

TABLE 4.2: Input properties of the models considered in this work. In each column, we indicate: the model, the initial value of radial ($B_z^{\rm in}$) and meridional ($B_y^{\rm in}$, taken equal to the background field B_d assumed in the GCM models on which we base our profiles), the pressure at the top and bottom of the domain, the corresponding size D of the numerical domain, the maximum absolute value of the main induced component B_x, the integrated Ohmic dissipation rate, and the corresponding heating efficiency ϵ, eq. 4.11. The asterisk indicates purely winding+Ohmic cases (i.e., without Hall and ambipolar terms), for which the solution is completely independent of $B_y^{\rm in}$.

4.3.1 General behaviour

We let the system evolve until all terms in the electric fields find a balance and a stationary solution is reached, i.e., spatially uniform electric field components E_x, E_y. In all the simulations, at the beginning, the main effect is the creation of the initially inexistent azimuthal field, B_x, via winding, as long as there is a non-zero vertical component (B_z). At first order, the induced field grows linearly until the Ohmic term associated with the induced meridional currents, J_y, grows enough to limit it:

$$\frac{\partial B_x}{\partial t} \simeq \frac{\partial v_x}{\partial z} B_z + \frac{1}{\sigma}\frac{\partial J_y}{\partial z} \simeq 0\,. \tag{4.10}$$

The resulting magnetic field lines are highly wound up. At the same time, the B_y component can deviate from the initial, background value only due to the Hall and ambipolar terms, which in turn highly depend on the winding-induced component B_x and its associated current component J_y. Note that there is no induced B_z, by construction, in our 1D approach.

We begin with a detailed analysis of the simulation WASP 76b, which we will take as the reference case. In Fig. 4.3 we show, the 1D evolution (marked by increasing color shades) of the vertical profiles B_x (top left), B_y (bottom left), J_y (top right), and J_x (bottom right). The solution converges at a time $t/t_* \sim 7\times10^3$.

Let us start by examining $B_x(z)$, which is initially zero. It quickly increases until convergence, when, at first order, the advection and the Ohmic terms balance each other. At such equilibrium solution, $B_x(z)$ has a maximum value $B_x \sim 80$ G at $p \sim 1$ bar, and a minimum value of $B_x \sim -180$ G at $p \sim 0.04$ bar, corresponding to the shear regions, i.e., where the wind profile presents the strongest vertical variations (see Fig. 4.1). There is a change of sign in the magnetic field at $p \sim 0.1$ bar, due to the combination of the change of sign the shear term and the relative flattening of $\sigma(z)$, both at $p \gtrsim 0.3$ bar.

Note that the locally induced field is ∼1-2 orders of magnitude larger than the background field, in line with the non-linear regime expectations in the presence of high temperature (Dietrich et al., 2022). The winding effect is supported by the meridional current profile, J_y. As shown in the third panel, it has a minimum of around $p \sim 0.1$ bar and a maximum at $p \sim 0.01$ bar. The change of sign and steep profile of $J_y(z)$ is related to the meridional loop which support the meridional induced field. A comparison between the equilibrium solution with (red darkest line) or without (blue dashed line) the Hall and ambipolar terms shows that the azimuthal component of the magnetic field is mostly set by the winding-Ohmic balance alone, with only slight corrections by the non-linear terms (a few %).

However, an interesting result is that, at equilibrium, the B_y profile strongly deviates from its initial, constant value $B_y^{\rm in} = B_d = 3$ G, as seen in Fig. 4.3 (bottom left) if the non-linear terms are activated (otherwise, it cannot change by construction). Note that, due to the outer BCs, B_y in the upper part of the domain is forced to its initial value. However, the overall trend is towards a constant B_y approaching zero in the outer layers just beneath the outer boundary. Correspondingly to the induced B_y, there is an azimuthal induced current component, J_x, shown in the bottom panel of Fig. 4.3, which is significantly smaller compared to J_y throughout the entire domain. For $p \gtrsim 0.5$ bar, its contribution is practically negligible in comparison to J_y. However, it shows a positive peak at $p \sim 0.08$ bar. This increase is caused by the strong local variation of B_y. In order to understand this behaviour, it is important to notice that the induced Lorentz force triggers non-zero meridional (v_y) and vertical (v_z) velocities (on the azimuthal one there is no feedback since we force it to remain equal to its input value), via the momentum equation. Both components, which can reach peaks of $\lesssim 10$ m/s, are much smaller than the $w \sim$ km/s values, which is consistent with the small but non-zero vertical velocities found in GCMs (e.g., Rauscher and Menou 2010). While v_z appears due to the winding-dominating $J_y B_x$ term, a non-zero v_y appears solely as an indirect consequence of the Hall drift, i.e. if $J_x \neq 0$, through the $B_z J_x$ term in the momentum equation. Such velocities play an important role, since they enter as further advective terms in the induction equation, as we will see below.

Therefore, even though the direct Hall contribution to the induction equation (the term $\propto \partial_z(B_z J_y)$) is never dominant, its presence triggers a meridional field and a Lorentz force which has a feedback on the fluid and renders the system non-linear.

This is very important, since previous studies (Perna, Menou, and Rauscher, 2010a) were considering the relevance of Hall and ambipolar terms using only the background field to estimate the magnitudes, under the implicit assumption of a perturbative regime (induced field much smaller than the background one). In our simulations, where the winding grows the field to a strongly non-linear regime, the induced field in the meridional direction, B_y, is comparable to the background field, because the winding-induced current component J_y, which enters as $J_y B_z$ in the y-component of the induction equation, is locally very strong.

We further calculated the Ohmic heating rate Q_j, associated with the induced currents. In Fig. 4.4 (top) it can be observed that most of the Ohmic dissipation occurs for pressures higher than 0.1 bar. Moreover, the highest values are located at pressures higher than 5 bar, which is relevant as it indicates that Q_j has the highest contribution in the deepest regions. As a result, more dissipated energy will be available near the RCB; if this energy penetrates into the convective region, it could be redistributed throughout the planet and inflate it more efficiently. The vertically-integrated Ohmic dissipation (per unit surface) is $\int_D Q_j \, dz = 0.0008$ MW/m^2, which

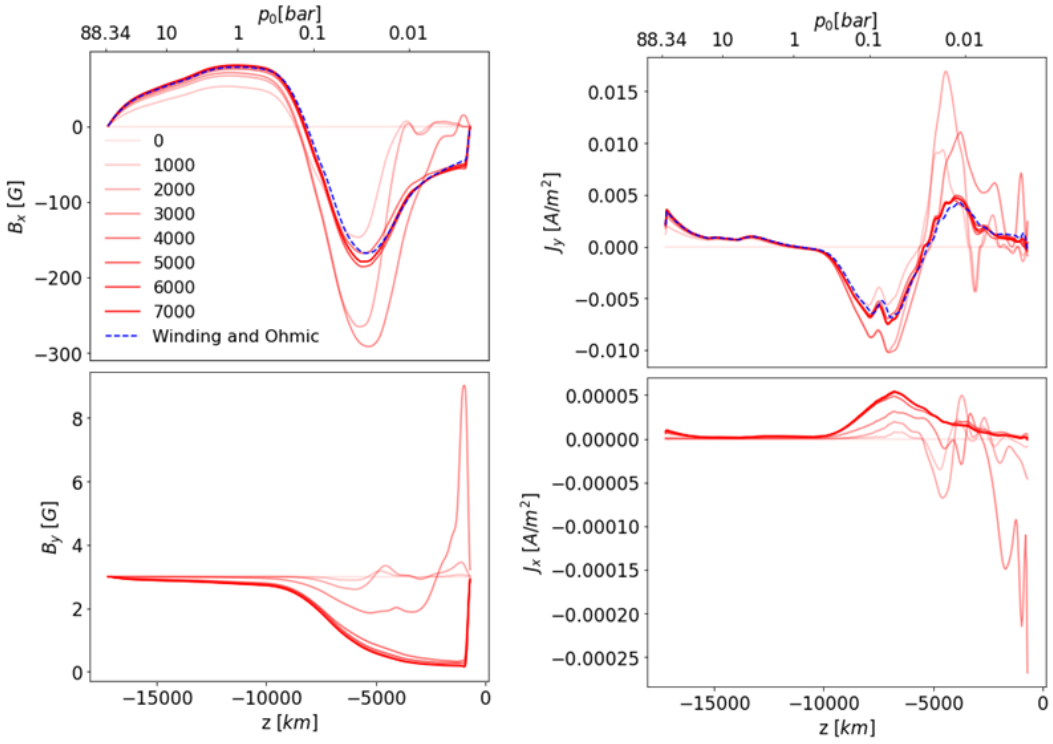

FIGURE 4.3: The vertical profiles of $B_x(z)$ (top left), $B_y(z)$ (bottom left), $J_y(z)$ (top right) and $J_x(z)$ (bottom right) for WASP 76b. The different intensities of red for B_x indicate the magnitudes at each time as indicated in the legend, until $t/t_* \sim 7000$. The blue dashed line corresponds to the solution found in case of winding and Ohmic only, without the Hall and ambipolar terms (in which case, by construction, there is no y component in the induction equation, i.e., $B_y = B_y^{\rm in} = B_d$ and $J_x = 0$). Note that at the outer boundary there is a sharp discontinuity in both magnetic field components, corresponding to a tangential current sheet (here cut out for visualization purposes). This is due to the (conservative) boundary conditions at the top; it only affects the very last points and should be regarded as a numerical artifact rather than a physical current sheet.

compared with the flux irradiating it, $F_{\rm irr} = 4\sigma_{\rm sb}T_{\rm eq}^4$, we obtain the local heating efficiency [5]:

$$\epsilon = \frac{\int_D Q_j(z)dz}{F_{\rm irr}} \,. \tag{4.11}$$

which in this case corresponds to $\epsilon \simeq 0.016\%$ of the stellar irradiation $F_{\rm irr}$.

[5]Note that this is a local definition (fluxes are defined per unit surface) apt for our local simulation, while normally the heating efficiency is defined at a global level, i.e., integrating over the entire planet and considering deeper, convective layers (well outside our numerical domain), where heat deposition has a pronounced impact on inflation (e.g., Batygin and Stevenson 2010; Wu and Lithwick 2013; Ginzburg and Sari 2015; Komacek and Youdin 2017; Thorngren and Fortney 2018b).

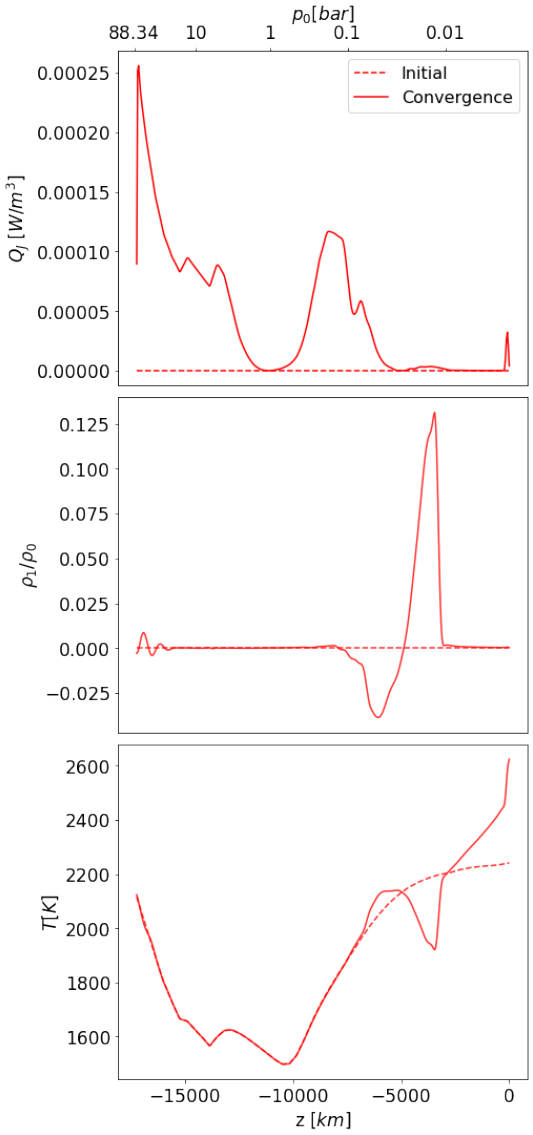

FIGURE 4.4: The vertical profiles of $Q_j(z)$ (top), $\rho_1/\rho_0(z)$ (centre) and $T(z)$ (bottom). The dashed line corresponds to the background profile at the beginning of the simulations and the continuous line at the convergence at $t/t_* \sim 7000$.

We also examined the influence of magnetic terms on the density and temperature within the region of interest, looking at the deviations from the background profile. The center panel in Fig. 4.4 illustrates the ratio ρ_1/ρ_0, i.e. the perturbed density over the background density. It shows that magnetic terms induce slight, but non-negligible modifications, to the background density profile. For $p \gtrsim 0.5$ bar, these variations are at maximum $\sim 2\%$, becoming more pronounced at lower pressures, where the density is inherently lower. In these regions, changes can reach up to $\sim$ 5–12%. On the other hand the initial profile of T, shown in Fig. 4.4 (bottom), maintains the same shape for $p \gtrsim 0.1$ bar. However, due to the low density in the upper layers and the ease of energetically modifying these regions, significant variations between the initial and evolved profiles can be observed for $p \lesssim 0.1$ bar. These variations lead to temperature changes locally exceeding 200 K. Looking at the contributions to the energy equation, the forcing and cooling term balance each other

everywhere, except in the outer regions where the buoyancy-related term ($\rho g v_z$) becomes significant and causes thermodynamic deviations from the background profiles, at equilibrium. The Ohmic rate is never dominant, and therefore its heating is not reflected. Due to the sensitivity of the results on the forcing, the cooling term, and the profile of v_z (i.e., on the damping term in the S_z evolution equation in the outer region, see above), the T profile should be taken with much caution.

Finally, we have calculated the magnetic Reynolds number, R_m, and Hall parameter to understand the relative contributions of the advective and Hall terms compared to the Ohmic term. There is however a subtle point which is important to discuss. Since we are looking for exactly stationary solutions, $\partial_t \mathbf{B} = 0$, which is a balance largely dominated by the advective and Ohmic terms, the formal ratio of the contributions to the induction equation (see e.g. eq. 4 of Dietrich et al. 2022):

$$R_m = \frac{|\nabla \times (\mathbf{v} \times \mathbf{B})|}{|\nabla \times (\mathbf{J}/\sigma)|} \tag{4.12}$$

by definition is ~ 1 at equilibrium, regardless of the velocity and of ratio between the background and induced magnetic fields. This may appear puzzling, but it is reconciled with the expected non-unity values of R_m by noticing that the usually definition simplifies the ingredients to:

$$R_m \simeq \frac{v B_{bkg}}{L_{v\times B}} \frac{L_\eta L_B}{\eta B_{ind}} \simeq \frac{vL}{\eta}\,, \tag{4.13}$$

This definition assumes that $B_{ind} \simeq B_{bkg}$, which is not the case when $B_{ind} \gg B_{bkg}$ (reminding that $B_{ind} \perp v$ so $v \times B \sim v \times B_{bkg}$, and $J \sim B_{ind}/L_B$), so that $v \times B \sim vB_{bkg} \ll vB_{ind}$. This means that the standard approximation, eq. 4.13, results in R_m being an order-of-magnitude estimate for the ratio between the induced and background fields. However, even neglecting this subtlety (i.e., assuming $B_{ind} = B_{bkg}$ in the definition of R_m), the calculation of the Reynolds number presents the ambiguity of the definition of the lengthscale L: the velocity, the magnetic diffusivity, and the magnetic field vary non-trivially, and the local associated length scales are in general comparable and oscillating, as seen in the top panel of Fig. 4.5. None of them is negligible in all the domain. In any case, in order to have a useful quantification of R_m in the standard way, the central panel of Fig. 4.5 shows R_m using $L(z)$ =min(L_v,L_η,L_B), as done by Dietrich et al., 2022. We observe that R_m remains greater than 1 in practically the entire domain, a characteristic of the advection-dominated (non-linear) regime studied in this paper.

We can also evaluate the Hall parameter (defined as $\omega_e \tau_e$, where ω_e is the electron gyrofrequency and τ_e the electron collision time), by showing directly the ratio between the Hall and Ohmic contributions,

$$\omega_e \tau_e = \frac{\left|\nabla \times \left(\frac{\mathbf{J}\times\mathbf{B}}{e n_e}\right)\right|}{|\nabla \times (\mathbf{J}/\sigma)|}\,. \tag{4.14}$$

In the bottom panel of Fig. 4.5, we can see that the Hall parameter remains between 10^{-6} and 10^{-2}, which is indicative of the dominance of the Ohmic term over the Hall term. However, note that as the pressure decreases, the Hall parameter increases, indicating the growing relevance of the Hall effect in the outermost layers. Again, it is important to note that the analytical estimate of the Hall parameter is also affected by specific choices of length scales and velocities. In any case, the Hall parameter (or magnetization) remains much smaller than one, which is expected, see

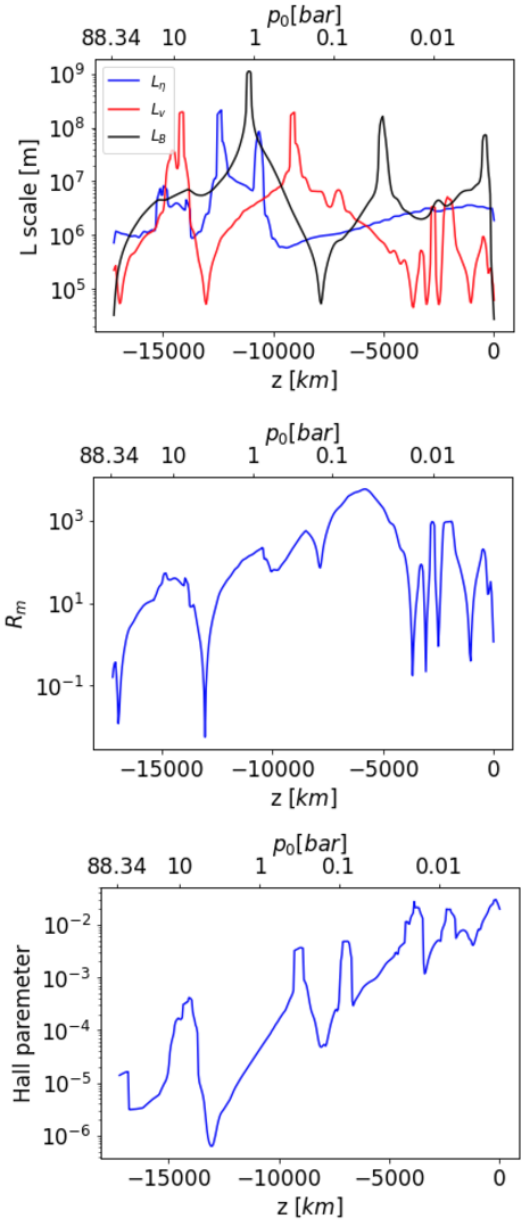

FIGURE 4.5: *Top:* Local lengthscales calculated with the local vertical gradients of magnetic diffusivity (blue), velocity (red) and induced magnetic field (black) for WASP 76b, at convergence. *Center:* magnetic Reynolds number, calculated using L as the local minimum of the three lengthscales shown on the left. *Bottom:* Hall parameter (see text for definition employed) in the studied domain for the default simulation WASP 76b at convergence.

e.g. the small magnetization parameters in the M1 region in Koskinen et al., 2014.

4.3.2 Comparison between modelled Hot Jupiters

Let's now compare the solutions for the different planets, shown in Fig. 4.6 and Table 4.2. In general, there are two competing temperature-dependent effects for sustaining the magnetic field. On one hand, we expect that a hotter planet will have stronger temperature gradients and hence faster zonal winds to amplify the magnetic field, and higher values of σ, thus higher induced fields. On the other hand, there is a larger counteracting magnetic drag expected, which will slow down the wind. In this study, we can only evaluate the first effect, since the second one requires, as already mentioned, a fully consistent MHD treatment in GCMs.

A close inspection of the simulation results for the five planets shows that the one presenting the highest induced field is WASP 121b, with a maximum absolute value of the main field component $|B_x|_{\max} \sim 1550$ G. Although we might have expected WASP 18b to have a higher magnetic field compared to the previous one based on its T_{eq} and the highest initial field, we rather find that it is lower than WASP 121b, with a maximum of $|B_x|_{\max} \sim 260$ G. This is because the magnetic drag present in the winds used as input from the GCM is based on a field strength of $B_d = 20$ G, higher than the $B_d = 3$ G of the other planets, which substantially damps any wind at pressures p $\lesssim 1$ bar (Fig. 4.1). Following the two aforementioned planets, we have WASP 76b, with a maximum $|B_x|_{\max} \sim 180$ G. The colder HJs HD 209458b and HD 189733b show much lower induced fields: $|B_x|_{\max} \sim 14$ G and only ~ 0.4 G, respectively. Note that, even in these cases, the locally induced field is of the same order of magnitude of the background field (at least at the sub-stellar point), making the linear regime assumption $|B_x| \ll B_d$ inadequate.

Fig. 4.6 also shows a comparison of the results including only the Ohmic and winding terms, excluding the Hall and ambipolar contributions (dashed lines, to be compared with the full solution with solid lines). Minor differences in B_x can be seen for the hottest planets, WASP 76b and WASP 121b, where there is a slight correction introduced by the non-linear terms (Hall and ambipolar), as previously discussed for WASP 76b. These differences are noticeable in the upper part of the domain due to the increase of the contribution of the ambipolar and Hall terms in the region. However, for the cooler planets, the contribution of the Hall and ambipolar terms is significantly smaller, as will be further discussed in the next section, and they produce virtually no differences in the B_x profile.

On the other hand, the Hall and ambipolar terms also affect the evolution of B_y. This component evolves over time, deviating from its initial value as it reaches equilibrium, particularly in cases where the Lorentz force varies steeply with altitude, as seen in the central panel of Fig. 4.6. Typically, B_y reaches peak values of the order of $\sim$ G, as shown in detail for WASP 76b. For the other two hot planets, WASP 121b and WASP 18b, B_y reaches similar or even slightly higher values compared to WASP 76b. In contrast, for the colder planets HD 209458b and HD 189733b, B_y remains nearly unchanged from its initial value of 3 G. This is due to the much weaker Hall and ambipolar effects, resulting in minimal evolution of the magnetic field. In these cases, B_y remains practically constant throughout the entire domain.

If we now examine the corresponding accumulated dissipated energy, $\int_z^0 Q_j(z')\,dz'$ (bottom panel of Fig. 4.6), we observe that the planet with the highest dissipation are WASP 18b, WASP 121b and WASP 76b. These hot planets exhibit Ohmic dissipation rates that are approximately 1 to 3 orders of magnitude higher than those of the

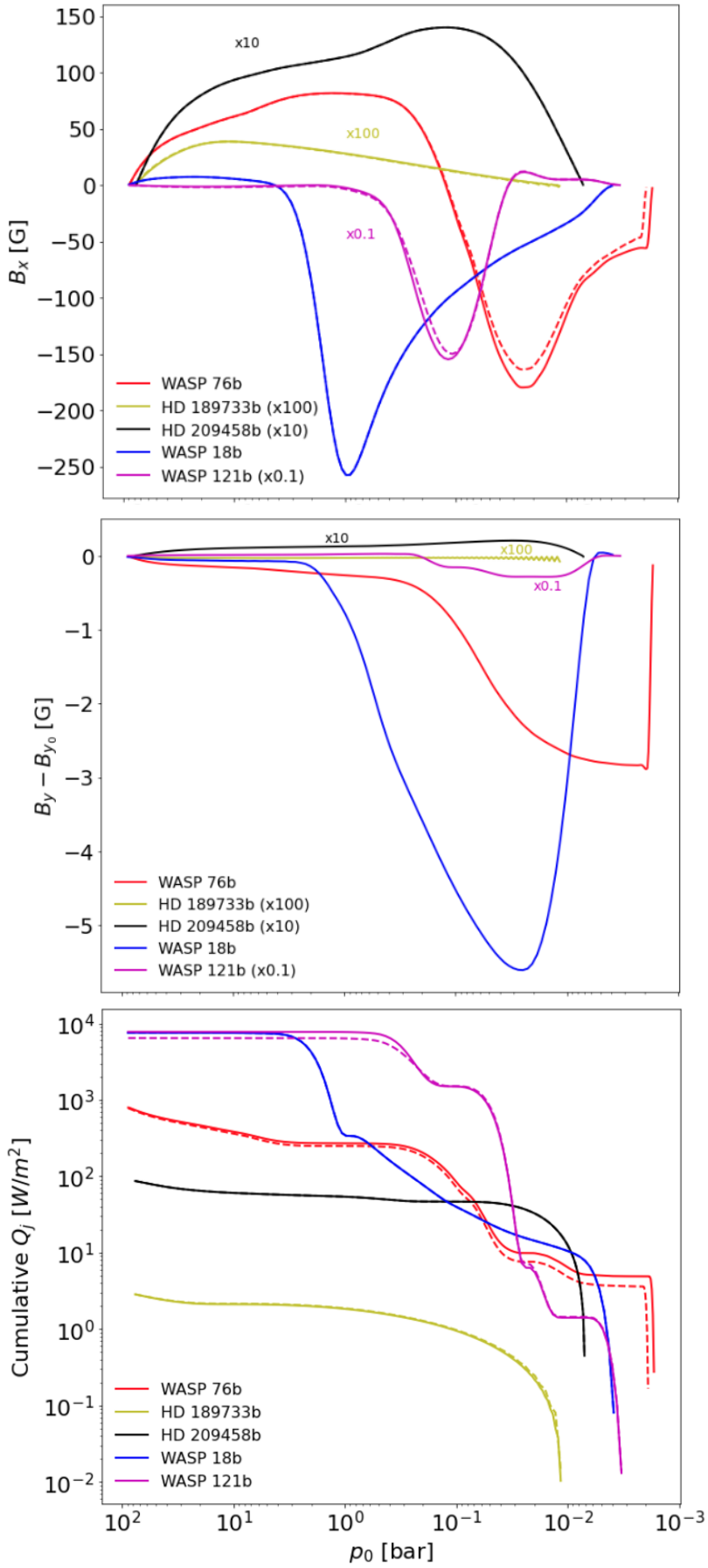

FIGURE 4.6: Comparison of the vertical profiles (from top to bottom) $B_x(z)$, $B_y(z)$, and cumulative Ohmic heating, $\int_z^0 Q_j(z')\,dz'$, for the different models. The dashed lines correspond to the purely winding+Ohmic cases, with no Hall and ambipolar terms included.

colder planets HD 209458b and HD 189733b, respectively. When comparing the cumulative Q_j profiles for each planet, with and without the inclusion of the Hall and ambipolar terms, we find that the differences between the two cases are minimal. However for those simulations with higher contribution of the Hall and ambipolar terms, WASP 121b and WASP 76b, the cumulative Q_j is slighlty higher compared to the models with just advection and Ohmic terms.

In all cases, most of the energy is dissipated around the shear layer, so that the cumulative energy saturates at a pressure $\sim 0.1-$few bars, depending on the planet. If we compare this local efficiency for the different planets (eq. 4.11), which is we can see that the highest value is reached for WASP 121b, $\epsilon = 0.1\%$, compared to the deposited energy from the star, while the lowest is HD 189733b, $\epsilon = 0.0009\%$. Compared with the statistical study by Thorngren and Fortney, 2018b which infers a maximum heating efficiency for $T_{\rm eq} \sim 1600$ K, after which the efficiency quickly drops, here we see a more monotonic trend $\epsilon(T_{\rm eq})$ for two main reasons: (i) our local simulations only allow an estimate of the local efficiency at the substellar point which is substantially hotter than the average, so that the local estimate is highly overestimating the global efficiency; (ii) since the induction is non-linear and $B_x \gg B_d$ especially at high $T_{\rm eq}$, the magnetic drag GCM is probably largely underestimating the real effects that slow down the winds. Moreover, Thorngren and Fortney, 2018b and similar works consider only the heat deposited below the radiative-convective boundary, therefore our results, confined to the uppermost, radiative layers, are not directly comparable to theirs (see e.g. Batygin, Stevenson, and Bodenheimer 2011; Wu and Lithwick 2013 for the expected radial profiles of Ohmic heating rate across all planetary layers).

4.3.3 Contributions to the electric components

In order to properly quantify the relative effect of the advective, Ohmic, Hall, and ambipolar terms in our simulations, in this section we present an analysis of their contribution to the electric field components which govern the induction equation.

The analysis of the representative cases WASP 76b and HD 209458b is presented in Fig. 4.7 (top and bottom panels, respectively), showing the different contributions to the electric field components E_x (left) and E_y (right). These contributions depend on the velocity, magnetic and current fields and on the prefactors, as shown in eq. 2.7, which are determined by the local density and temperature. Note that E_x and E_y are flat in all the domain (except for the very last points, a boundary artifact), indicative of the stationary state. In general, several dips appear in the magnitude of most contributions, corresponding to changes of sign in the dominant components of each term. Both the Hall and ambipolar contributions increase in altitude, especially at the high pressures of the domain, due to their density dependence.

For WASP 76b, the analysis of the E_y component (top right), which is primarily linked to the induced magnetic field B_x, shows that the dominant contributions arise from the Ohmic and advective terms (i.e., magnetic winding). As expected, the Hall and ambipolar contributions are several orders of magnitude smaller throughout the entire domain. Their contributions increase at lower pressures due to the decreasing density; however, they remain significantly smaller than the dominant terms, with the exception of the ambipolar term $\propto B_x B_x J_y$, which can locally reach values comparable to the advective term $B_z v_x$ for $p < 0.01$ bar. However, at these layers, the vertical advective term $B_x v_z$ is the one balancing out the Ohmic dissipation. For the E_x component (top left), the Ohmic term is apparently flat above $p \gtrsim 0.04$ bar, and its small derivative is balanced by the $(B_y v_z)$ and Hall $(J_y B_z/(en_e))$ components. At

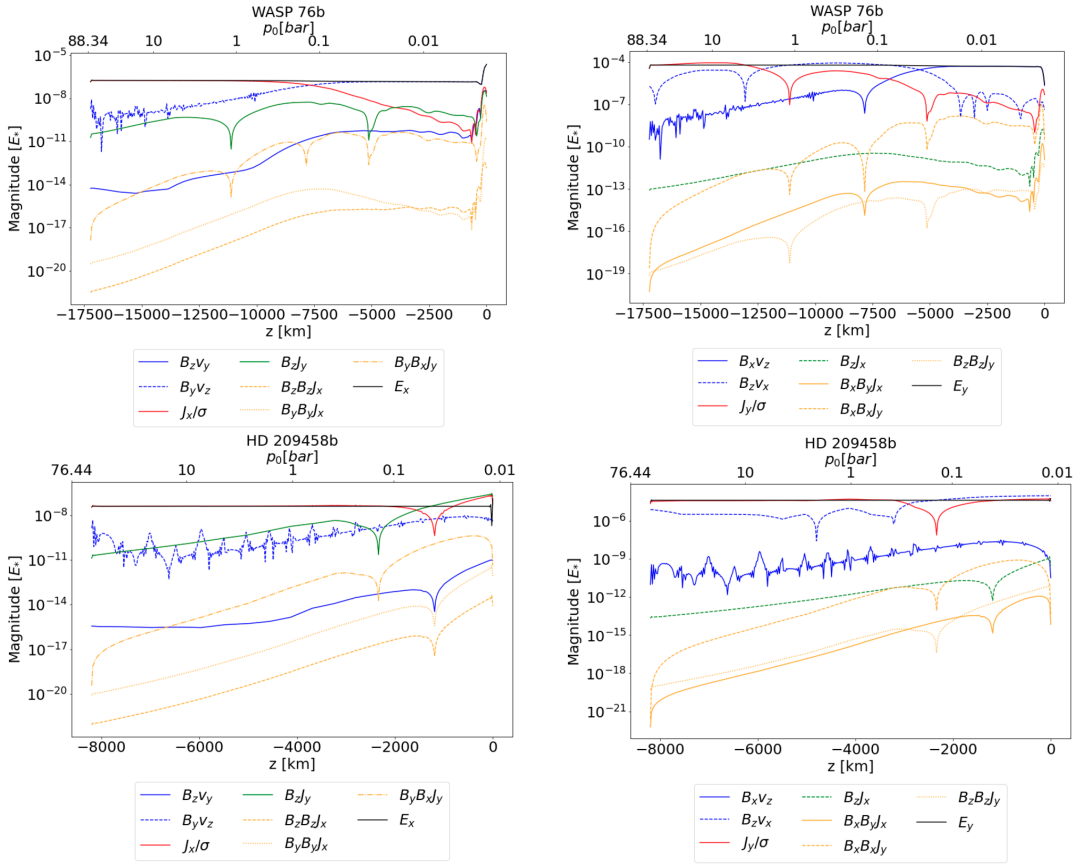

FIGURE 4.7: Evaluation of the different contributions to the electric field components: E_x (left) and E_y (right) for WASP 76b (top) and HD 209458b (bottom) across the entire domain. Advective terms are shown in blue, Ohmic in red, Hall in green, ambipolar in yellow, and the total electric field (E_x and E_y) in black. The continuous, dashed, and dash-dot lines represent the non-zero different components of each contribution, as in the legend (which omits for brevity the Hall and ambipolar pre-factors).

shallower layers, the derivative of the Ohmic and the Hall terms dictate the equilibrium, because the absolute value of the $v_z B_y$ contribution is larger, but constant.

For HD 209458b, E_x represents a balance between the Ohmic, the advective $v_y B_z$ and the Hall terms, with the advective $B_z v_y$ term always playing a minor role. Since the largest, Ohmic term is practically constant, the advective and Hall terms also play an important role in the evolution of the B_y component. However, the order of magnitude of the terms is slightly smaller compared to WASP 76b, thus almost no significant variations of B_y are expected, as seen in the previous section for the cooler planets. Regarding the component E_y, we observe that, for all the domain, the main contributions come from the advective term ($B_z v_x$) and the Ohmic term. Although the Hall and ambipolar terms increase as pressure decreases, they remain several orders of magnitude smaller than the Ohmic and advection terms, and smaller by one order of magnitude compared to the same contributions for WASP 76b. The analysis of HD 209458b is representative of the cooler HJ models, and shows the general behaviour of the different components that play a role in the magnetic field evolution equation.

4.3.4 Ion-neutral relative velocity and its detectability

Our results on the ambipolar term can be connected to the recent work by Savel et al., 2024. They proposed a novel method to constrain the magnetic field in hot gas giants by comparing the velocities of heavy ions and neutral gas using high-resolution spectroscopy. Ideally, if one measured the ambipolar velocity, eq. 2.14, in the photospheric region, the magnetic field of the planet could be constrained.

In Fig. 4.8, we plot the profiles of the relative velocity, inferred from our simulations. Note that our domain is much deeper than the photosphere, $p \lesssim 10^{-4}$ bar, which is where one could observationally test predictions. We observe a common trend for all planets. First, for the highest pressures achieved in our simulations, the relative velocity difference is negligible, but grows by several orders of magnitude outward, due to the decrease of both n_p and ν_{in}. In the bulk of our domain ($p \gtrsim 0.01$ bar), the values of the relative velocities are still very small, but our results, at these depths, are roughly in line with the calculations by Savel et al., 2024 (see their Fig. 1, especially in the 150 G magnetic field line, a value which is the same order of magnitude of the induced magnetic field in our simulations).

However, there are important differences, compared to the smooth, monotonically growing outward profiles by Savel et al., 2024. First, the noticeable drops in the intensity of the velocity difference, at specific pressure values, correspond to the changes of sign in the ambipolar term. Secondly, and more importantly, we observe either a decrease in the relative velocity for WASP 121b, WASP 76b, WASP 18b and even HD 209458b, or a reduction in its rate of increase (i.e., a flattening of the slope) for HD 189733b, at the lowest pressure levels. This is mainly due to the increasing relative importance of the ambipolar diffusion itself compared to the winding term, as seen in Fig. 4.7, which increases exponentially with pressure and their effect is visible in WASP 121b and WASP 76b. The ambipolar term tends to minimize the Lorentz forces and limits the growth of the currents perpendicular to the magnetic field, which are mostly induced by winding (J_y and B_x). However, our enforcement of no induced field at the boundaries (see Appendix D.1) could also have an effect, so that one should ideally extend outwards the domain to have a better assessment (which is numerically unfeasible due to the too large top/bottom density contrast and low values of density and pressure, see Appendix A of Soriano-Guerrero et al. 2023). Moreover, we are employing values of background magnetic field much lower than those used in Savel et al., 2024: higher values of B_d could enhance the relative velocities.

Although, for the reasons just discussed, we cannot give a clear quantitive confirmation of the potential spectroscopical detectability of the ion-neutral relative velocity in the photosphere (needed to be $\gtrsim$ km/s, Savel et al. 2024), we confirm that the ambipolar diffusion is not negligible in the uppermost layers, and it is intimately related to the other terms and the configuration of the background and induced magnetic fields.

4.3.5 Sensitivity on the maximum depth considered

The depth at which most of the energy is deposited is relevant for the inflation of the planet. The deeper the energy is dissipated, the less energy is needed to inflate the planet (Guillot, 2010), with dissipation below the radiative-convective boundary being optimal. Inflation efficiency reaches its maximum if the energy is deposited in the convective region, allowing the energy to be redistributed throughout the entire planet (Ginzburg and Sari, 2016). Since in our approach, by construction, we confine

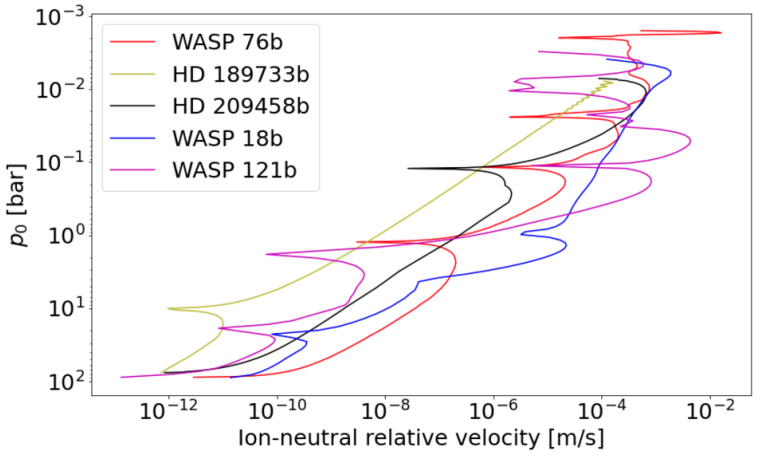

FIGURE 4.8: Relative velocity between ions and neutrals inferred from the solutions of the different models.

the induction to the numerical domain only, in the following we analyse the effect of extending the domain to deeper regions for the reference case of WASP 76b (see § 4.2.1). Three different extensions have been studied, with $p_{\rm max} = 300$, 500 and 1000 bar respectively; see Table 4.2. Also, note that the top pressure has been kept fixed at $p_{\rm top} = 0.005$ bar.

For simplicity, we focus on the dominant induced components B_x and J_y, and consider cases without the Hall and ambipolar diffusion, which, in any case, are completely negligible in the extended deep regions. When analysing differences in the magnitudes of the relevant simulated variables for various values of the maximum pressure, we observe the following trends. First, as the maximum pressure increases, the generated magnetic field strength also increases (see Fig. 4.9 top). This is essentially due to the chosen boundary conditions, which tie B_x at both extremes, allowing to reach higher peaks if the domain is more extended. The highest field strength is observed close to the shear layer, e.g. at $p \simeq 1$ bar for the most extended simulation ($p_{\rm max} = 1000$ bar), corresponding to approximately 390 G. Notably, the vertical variability of the magnetic field is similar across the four simulations, with the maximum values for B_x consistently around 1 bar, as explained in § 4.3.1.

Examining the amount of currents generated, J_y (see middle panel of Fig. 4.9), we note that, despite the shifts in pressure across different simulations, the overall behaviour remains consistent with the patterns described in § 4.3.1. The currents exhibit positive values below 1 bar, negative values between $\sim$ 0.05 and $\sim$ 1 bar, and positive values below $\sim$ 0.01 bar. Moreover, the deeper is the lowest boundary of the simulation, the highest is the absolute value of the minimum of J_y, since there is a steeper increase of magnetic field in the shear region.

Finally, we study the cumulative Ohmic dissipation Q_j for the different cases (see Fig. 4.9, bottom). We note that the main contribution to dissipation appears to be largely concentrated around a few bars. As a matter of fact, in the outermost region, as the pressure increases, the amount of accumulated Ohmic rate rises rapidly until it reaches a constant value, which is similar for all simulations. On the other hand, after this constant value is achieved, there is another significant increase in $\int_z^0 Q_j(z')dz'$ for all cases until the four simulations gradually converge to a nearly identical total deposited energy of $7.8 - 8.1 \times 10^{-4}$ MW/m^2. Even for the most extended case, the maximum cumulative energy is reached at pressures around $\sim$ 50 bars. Therefore, extending the domain does not contribute to a higher cumulative

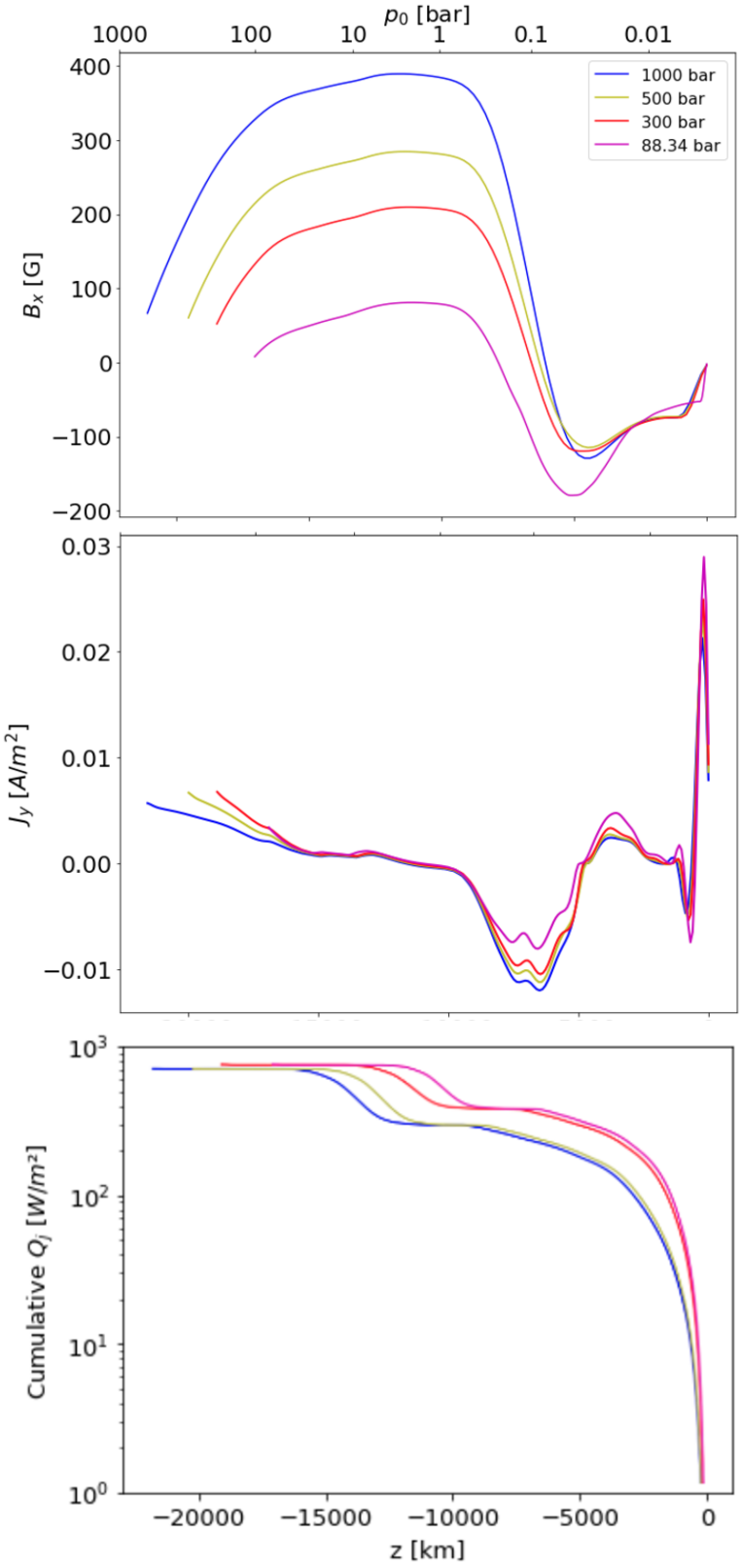

FIGURE 4.9: The vertical profiles for B_x(z) (top), J_y(z) (center) and cumulative Ohmic heating $\int_z^0 Q_j(z')dz'$ (bottom) at convergence, corresponding to $t/t_* \sim 10000$ for four simulations with different maximum pressures: 1000 bar (blue), 500 bar (yellow), 300 bar (red) and 88.34 bar (pink) for WASP 76b. The minimum pressure is the same at the top of the four simulations, 0.005 bar. In these simulations, we only considered winding and Ohmic dissipation.

energy.

This convergence with the domain size might be an effect of fixing $B_x = 0$ at $p_{\rm bot}$. When this condition is relaxed, and a global solution is retrieved, the induced field and currents, and the associated Ohmic dissipation, partially spread to deeper layers, as long as the conductivity is non-zero (Batygin and Stevenson, 2010; Batygin, Stevenson, and Bodenheimer, 2011; Wu and Lithwick, 2013; Knierim, Batygin, and Bitsch, 2022). In this sense, in our study, we cannot quantifying the global Ohmic dissipation, also because, as said above, we have a local setup at the sub-stellar point, and not a fully-consistent GCM with the magnetic feedback on the fluid.

4.3.6 Sensitivity on the internal magnetic field

In this section, we explore the effect that the strength of the radial background magnetic field component B_z has on the induced field, since the growth due to winding is proportional to it. Variations in the magnitude of the B_z component can be either due to a different overall strength of the magnetic field of the planet, to a different alignment, or different multipolar contributions

It is important to highlight that these runs have been performed using the input from GCM models of WASP 76b but without any magnetic drag, and therefore with higher wind speeds. We prefer this choice since inputs from GCM models with drag would implicitly fix a background magnetic field. As a consequence, the induced fields are likely overestimated; however, we are interested in relative comparisons. Furthermore, for this test, we include only the dominant winding and Ohmic terms (therefore, the value of $B_y^{\rm in}$ is irrelevant since it doesn't enter in our setup, i.e. the plane-parallel advective+Ohmic induction equation).

In Fig. 4.10 we show $B_x(z)$, $Q_j(z)$, and the cumulative $Q_j(z)$ exploring three different values of the internal field. In the top panel, we see that the induced magnetic field B_x roughly scales with B_z (as expected in the linear regime), varying between $B_x \simeq 8$ G for $B_z = 0.003$ G, and 870 G for $B_z = 0.3$ G. The maximum values of the induced fields are much higher than the background ones as expected for all cases, typically increasing the initial field by about three orders of magnitude, due to the non-linear regime caused by the high conductivity.

We clearly note the linearity of the dominant winding effect: the profile perfectly scales with B_z, for the three simulations without drag. Consequently, the dissipated heat Q_j and its cumulative value (middle and bottom panels), and the heating efficiency, scale quadratically with $B_z^{\rm in}$. In all the cases, the Ohmic dissipation occurs almost entirely at levels $p \gtrsim 0.1$ bar, with the bulk of it mainly at $p \gtrsim 1$ bar, since the value of the currents is higher in deeper regions.

It is important to highlight that the local efficiency values are likely overestimated for the high magnetic field cases, since the strong induced magnetic field would slow down the wind to speeds lower than the GCM profiles assumed here, which would result in a less pronounced shear layer, and consequently, a lower induced magnetic field.

In the same Fig. 4.10, we compare the results with the simulations that include profiles with the drag models (black line), to be compared with the case with the same $B_z^{\rm in}$ (red). For the magnetic field, B_x it can be seen that, in the case where magnetic drag is not present, the field B_x can increase up to $|B_x|_{\rm max} \sim 870$ G compared to $|B_x|_{\rm max} \sim 180$ G that is reached when the drag is present in the GCM model. This further implies a higher amount of Ohmic dissipation, which accumulated, results in one order of magnitude higher in the case without drag. Correspondingly, this also

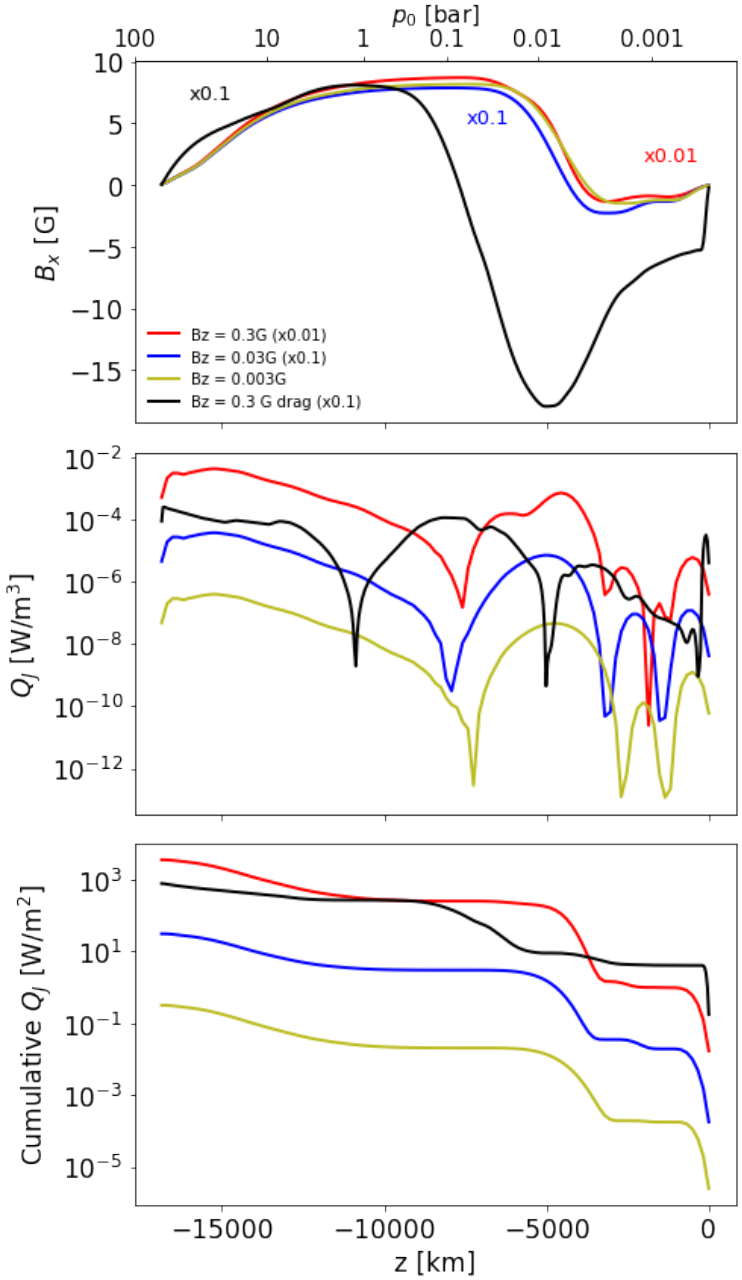

FIGURE 4.10: Comparison of the $B_x(z)$ (top), the Ohmic dissipation per unit volume $Q_j(z)$ and the cumulative one, $\int_z^0 Q_j(z')\,dz'$, for different values $B_z^{\rm in} = 0.3$ G (red), 0.03 G (blue) and 0.003 (yellow) for WASP 76b. As a reference, the default case with GCM inputs that consider a drag of $B_d = 3$ G is shown in black, for which $B_z^{\rm in} = 0.3$ G. Note that some B_x profiles have been rescaled as mentioned in the legend, for the sake of clarity. In these simulations we only focus on the dominant winding and Ohmic effects, neglecting the Hall and ambipolar terms.

implies a more efficient heat deposition for the non-drag case, of about $\epsilon \sim 0.71\%$, compared with the 0.16% for the case with drag.

4.4 Final remarks

In this study, we have performed 1D MHD simulations of HJs atmosphere columns to investigate the impact of the non-ideal MHD effects. We have employed wind and $p(T)$ profiles obtained from GCM of several specific planets, spanning a range of equilibrium temperatures. The assumed background magnetic field has been parametrized by two constants, the meridional and the radial components. We have solved the MHD equations in their perturbative form, where the velocity and the pressure (i.e., temperature) are forced to keep very close to the prescribed profiles; keeping the full MHD set allows us to include part of the feedback on the fluid (on the meridional and vertical velocities, initially set to zero), and, to a lesser extent, to evaluate the location and magnitude of expected relative deviation from the background profiles. However, the system substantially reduces to the evolution of the induction equation, until it converges to a solution. The main conclusions are:

- The main and common behaviour is the generation of a strong ($\sim 10^1$-10^2 G), localized azimuthal magnetic field (B_x), supported by meridional currents (J_y). This is due to the balance between the winding mechanism and the Ohmic term. The induction is most effective close to the shear region, which is the main one contributing to the total Ohmic dissipation along the column, which is typically a fraction 10^{-6}-10^{-3} of the irradiation.

- The Hall and ambipolar terms are generally smaller than the dominant winding and Ohmic terms. However, at second order, the Hall effect modifies the solution, contributing to an additional component of the magnetic field in the meridional direction. Moreover, although the contribution of the Hall term to E_y is not dominant, its variation may introduce non-linear effects in the evolution of B_x that combined with the ambipolar contribution modifies the B_x profile. Note that this effect is relevant for considerations on the spectroscopic detectability of ion-neutral relative velocity (Savel et al., 2024), and for a proper evaluation of the widely used magnetic drag in GCMs.

- We found that extending the simulation domain to deeper levels, up to 1000 bar, increased the vertical range where the magnetic field can amplify, leading to higher magnetic field strengths.

- Another critical factor affecting the magnitude of the magnetic field growth due to winding is the planetary internal magnetic field, with a roughly linear relation, as expected from the induction equation x component.

- The GCM models produce larger velocities for hotter planets; moreover, the conductivity, dominated by the thermal ionization of alkali metals, is much larger and leads to a much stronger winding effect.

- We stress that the GCM models which use an effective magnetic drag term should ideally incorporate the complexity of the solution that we found. Although here we have modeled only the sub-stellar point, and elsewhere the effects could be less dramatic, the main features are clear.

In an Chapter 5, we will use these equilibrium 1D solutions to study the 3D turbulence induced by small, forced perturbations in the shear layers, extending the ideal MHD turbulent simulations with isothermal background by Soriano-Guerrero et al., 2023 to the non-ideal regime with the more realistic $p(T)$ profiles used here.

5

Influence of turbulent perturbations in the magnetised atmospheres of Hot Jupiters

5.1 Introduction and objectives

In this Chapter, largely corresponding to Soriano-Guerrero et al., 2025a, we focus on modeling the outermost radiative layers of HJs. The core of the code is the same as in Chapter 3, later extended in Chapter 4 with more realistic atmospheric profiles and non-ideal MHD effects. Here, we further build on that framework by performing fully 3D cartesian box MHD simulations that incorporate both large-scale wind shear and small-scale perturbations, in order to quantify their combined role in magnetic induction and Ohmic dissipation. By comparing these results with one-dimensional winding-dominated models lacking turbulence, we quantify the relative contribution of perturbative effects to magnetic induction and Ohmic dissipation in HJ atmospheres. Each new component of the model is described in detail in the following sections, with the main modifications relative to earlier versions highlighted, while referring the reader to Chapter 2 and the aforementioned studies for a full description of the original implementation and methodology.

5.2 Initial setup and conditions

5.2.1 Background profile and atmospheric column equations

The background profiles and column setup follow the same methodology described in Chapter 4, with the governing MHD equations introduced in Chapter 2.1.2. Only the specific modifications relevant to this work are outlined below.

GCM data and background profiles

In order to prescribe a column profile for the background various $p(T)$ and $w(z)$ profiles are obtained and used from GCM. Specifically we have selected WASP 76b, WASP 18b, HD 209458b and HD 189733b, which is a good representative selection of the HJs population. We refer the reader to § 4.2.1 for a summary of these inputs and a full of the GCM framework and the extension of these profiled to study MHD effects in deeper atmospheric regions. However for clarity the $w(z)$ and $p(T)$ profiles have been represented again for the selected planets, in Fig. 5.1 and the main characteristics of the background models are summarized in Table 5.1.

Specific setup for MHD equations

With these background profiles, we solve the compressible MHD equations, incorporating gravity and forcing as presented in § 2.1.2. The model follows the framework developed in Chapter 3 and 4. The local Cartesian box is designed to capture the interactions between magnetic fields, atmospheric turbulence, and wind shear under a statistically steady regime. Note, however, that our local setup forces the bulk of the velocity to closely stick to the prescribed background profile of the wind, and therefore does not allow for the full non-linear feedback between flow and field.

Nonetheless, it is relevant to highlight that there are some modifications of the general MHD setup presented in § 2.1.2, to adapt the simulations to the aim of the paper. First, in this study, the electric field $\mathbf{E}$ is expressed as the sum of the advective and Ohmic contributions:

$$\mathbf{E} = -\mathbf{v} \times \mathbf{B} + \frac{\mathbf{J}}{\sigma}, \tag{5.1}$$

where we neglect the Hall and ambipolar terms. This decision comes from the results seen in Chapter 4 in which the Hall and ambipolar terms are typically subdominant compared to the winding and Ohmic ones, and their influence is confined to the outermost layers of the hottest planets, where they introduce only minor corrections to the magnetic field, typically of a few percent. Given their negligible impact, omitting them allows for a simpler and more tractable formulation without a significant loss of accuracy.

For our setup, both the wind profile and its random perturbations, whose effect on the atmosphere we aim to study, are introduced through the forcing term, specifically here it reads as:

$$\mathbf{F} = \frac{\rho_0}{\tau}[f_0(v_x - v_w)\mathbf{e}_x + \boldsymbol{\delta v}] - \mathbf{S_d} \tag{5.2}$$

where f_0 is the amplitude of the forcing in the x-direction. The x-component forces the azimuthal velocity, v_x, to remain close to the imposed wind profile $w(z)$. Note that in this setup there can be non-zero average induced meridional and vertical components which can in turn advect the field lines, as shown in Chapter 4. On the other hand, the damping term $\mathbf{S_d}$ is redefined as:

$$\mathbf{S_d} = A_d \left(\frac{z_d - z}{z_d}\right)^2 (\mathbf{S} - \mathbf{S_{in}}) \tag{5.3}$$

Note that it acts on all components of the momentum vector, damping any deviation from the initial, background state, $\mathbf{S}_{\rm in}$: in the y and z directions, it reduces ρv_y and ρv_z toward zero, while in the x-direction, it enforces relaxation toward the background flow $\rho_0 w$. Remember that this term is non-zero only for $z > z_d$. In all the

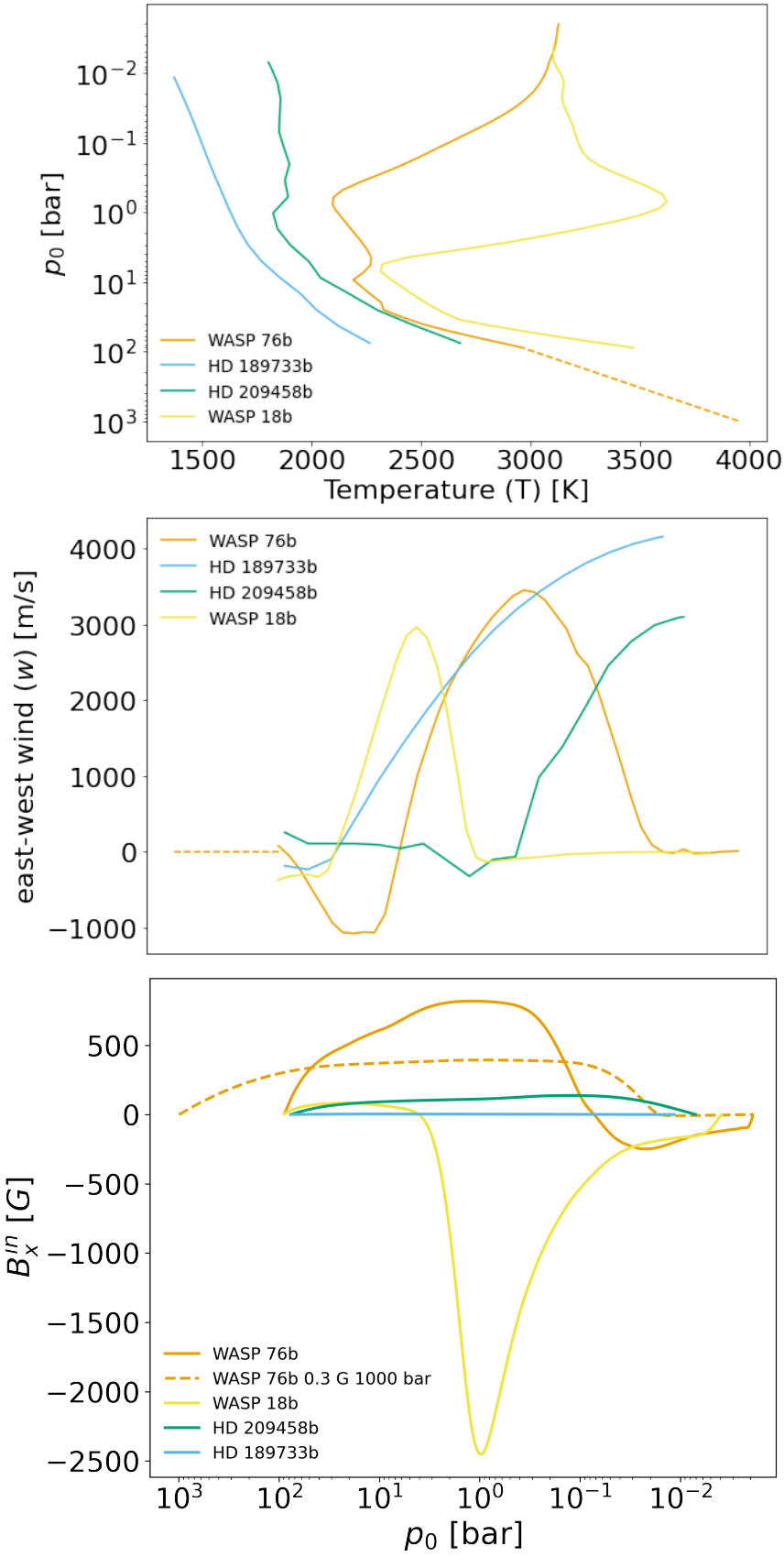

FIGURE 5.1: Background input quantities for the different models. Pressure (top) and zonal wind (middle) profiles at the substellar profiles for the different planets listed in Table 5.1. We show the extension to deeper pressures for WASP 76b with a dashed line. B_x (bottom) used in the simulations as obtained from the convergence of 1D simulations from Chapter 4.

simulations presented here, we adopt $z_d = -0.2\,L$ (see below for domain definition). The corresponding pressure of the damping layer bottom, $p_{\rm damp} := p_0(z = z_d)$, ranges between 0.01 and 0.09 bar, depending on the specific atmospheric profile of each model (see Table 5.1).

5.2.2 Domain and initial and boundary conditions

We adopt a 3D Cartesian domain with vertical coordinate $z \in [-L, 0]$ and horizontal extents $x, y \in [0, L/2]$. Depending on the planetary model, the values of L span between 770 and $\sim$ 22000 km, the pressure at the lower boundary ranges from $p_{\rm bottom} \simeq 76.4$ to 1000 bar, while the upper boundaries lie within the range $p_{\rm top} \sim 0.002$–0.02 bar (see Table 5.1).

In all cases, the resolution is set to $N_z = 200$ grid points in the vertical direction, and $N_x = N_y = N_z/2$ horizontally. This resolution is sufficient to ensure that the physical magnetic diffusivity remains larger than the numerical one, i.e., that the dominant 1D solution dictated by the balance between winding and Ohmic terms (see below), numerically converges, as discussed in Chapter 4.

At the top and bottom boundaries, we apply different treatments depending on the variable: we impose zero vertical derivative to the magnetic field components B_y and B_z, while B_x is enforced to be zero. As discussed in Chapter 4, these conservative choices limit the growth of the average B_x (which could be uncontrolled if, e.g., a flat BC $dB_x/dz = 0$ was adopted instead). Therefore, box simulations have intrinsic limitations, i.e., simplified BCs and lack of self-consistent feedback on zonal winds, which should be kept in mind when looking at the quantities obtained.

Moreover, to minimize the computational time required to reach the quasi-steady state dominated by magnetic winding, we initialize our 3D local simulations using converged, unperturbed 1D MHD solutions for each atmospheric model with a given initial vertical uniform field $B_z^{\rm in}$, using the same methodology as Chapter 4, but neglecting the ambipolar and Hall terms for the reasons explained above. In one dimension, the evolution of the azimuthal magnetic field B_x is governed by a balance between the winding term, induced by the effect of the large-scale shear dv_w/dz on B_z, and the Ohmic dissipation of the associated currents. This leads to an exact balance, $\partial B_x/\partial t = 0$. The induced magnetic field linear growth saturates when the rate of field amplification by shear is compensated by resistive diffusion. This background solution can be quickly computed efficiently in 1D, and we import such steady-state profiles $B_x^{\rm in}(z)$ (shown in the bottom panel of Fig. 5.1), as well as the corresponding perturbations in density $\rho_1(z)$ and pressure $p_1(z)$, to initialize our 3D simulations.

This strategy ensures that the local 3D simulations start from an idealized 1D MHD equilibrium configuration, significantly accelerating convergence toward the quasi-steady state. The full 3D setup can then focus solely on the role of the forced perturbations. We let each local 3D simulation to run for a time $t_{\rm max}$ which is typically a few thousand timescales (t_*), where the latter are the estimated sound-crossing time over one scale height, defined by a representative background temperature (see Chapter 3 for more details). With the values of t_* of $\sim$ minutes (see Table 5.1), our simulations run for a physical timescales of a few days, sufficient to reach a statistically steady state.

Note that a part from the damping term, $\mathbf{S_d}$, previously described, here we also added an artificial resistivity term that increases the magnetic diffusivity in the

Model	$B_z^{\rm in}$ (G)	$p_{\rm bottom}$ (bar)	$p_{\rm damp}$ (bar)	D (km)	λ	t_* (s)	$t_{\rm max}$ (t_*)
WASP 76b-3-88	3	88.34	1.23×10^{-2}	18762	0.01	454	3500
WASP 76b-0.3-1000-0.01	0.3	1000	7.5×10^{-2}	21979	0.01	495	4000
WASP 76b-0.3-1000-0.1	0.3	1000	7.5×10^{-2}	21979	0.1	495	9000
WASP 18b	20	89.13	2.73×10^{-2}	770	0.01	22	900
HD 189733b	3	89.13	9.20×10^{-2}	2830	0.01	123	55
HD 209458b	3	76.44	5.20×10^{-2}	8190	0.01	309	1250

TABLE 5.1: Input properties of the models. Columns: (1) model identifier; (2) initial vertical, homogeneous magnetic field, $B_z^{\rm in}$; (3) pressure at the bottom of the domain, $p_{\rm bottom}$; (4) pressure at the bottom of the damping region, $p_{\rm damp}$; (5) vertical size of the domain, D; (6) amplitude of the initial perturbation, λ; (7) physical timescale, t_*; (8) total simulated time, $t_{\rm max}$, in units of t_*.

Ohmic term $\eta(z) = (\sigma\mu_0)^{-1}$ in the damping layer only:

$$\eta(z) \rightarrow \eta(z) + \eta_{\rm damp} \left(\frac{z - z_d}{z_d} \right)^2 \qquad \text{if} \quad z > z_d \, . \tag{5.4}$$

Following stability tests similar to what described in Soriano-Guerrero et al., 2023, we heuristically fix the damping pre-coefficients A_d, as in that work, and $\eta_{\rm damp} = 0.05\, H_*^2/t_*$.

While necessary for numerical stability, these two extra terms affect the physical reliability of the solution in the uppermost region of the domain, but not in the lower, dense part of the domain, since the stratification mostly hampers vertical motions, and the induction is guided mostly by the 1D winding- and Ohmic-dominated background MHD profiles. As such, all physical interpretations in this work are restricted to layers where the total diffusivity is dominated by the physical component. We note that this damping region overlaps with the atmospheric layers where non-ideal effects such as Hall and ambipolar diffusion may become relevant. However, since the magnetic diffusivity is artificially enhanced there, any minor contributions from these non-ideal terms are effectively suppressed, further justifying their omission in the present model.

5.3 Results

All the simulations analysed in this section, along with their associated parameters, are summarized in Table 5.1.

5.3.1 Analysis of WASP 76b

Let's first focus on the WASP 76b model, taken as the reference case, to investigate whether any of the induced perturbations affects the magnetic field components, in addition to the pre-existing field produced via winding.

First, Fig. 5.2 shows the time evolution of several quantities averaged over the volume V of the physical part of the domain, $p < p_{\rm damp}$, excluding the damping layer described above. We look at the following indicators of deviations from the background state, which consist of the input velocity $v_x = w$, $v_y = v_z = 0$, a uniform $B_z^{\rm in}$, and the 1D-saturated state $B_x^{\rm in}$:

- The contribution to the kinetic energy from the meridional and vertical velocity components,

$$E'_{\rm kin} = \frac{1}{V}\int_V \frac{1}{2}\rho\left(v_y^2 + v_z^2\right)\, dV\,; \tag{5.5}$$

- The contribution to the root mean square (rms) deviations from the 1D background magnetic fields B_y and B_z:

$$B_{y,rms} = \sqrt{\frac{1}{V}\int_V B_y^2\, dV}\,, \quad B_{z,rms} = \sqrt{\frac{1}{V}\int_{\rm vol}(B_z - B_z^{in})^2\, dV}\,, \tag{5.6}$$

- The contribution to the average enstrophy density from the squared vorticity components ω_x^2 and ω_z^2, where the vorticity is $\boldsymbol{\omega} = \nabla \times \mathbf{v}$, as proxies of the rotational features in turbulent flows (Brandenburg and Subramanian, 2005):

$$\mathcal{E}_x = \frac{1}{V}\int_{\rm vol}\omega_x^2\, dV, \quad \mathcal{E}_z = \frac{1}{V}\int_{\rm vol}\omega_z^2\, dV\,. \tag{5.7}$$

The choice of the specific components in these indicators is motivated by the setup. In particular, the dominant components v_x and B_x are substantially tied to their background values due to the dominant zonal wind forcing term $\propto (v_x - w)$ in eq. 5.2. Analogously, ω_y and J_y are the only non-zero background components of the vorticity and current density, and they dominate over the other components in all the cases. On the other hand, the components v_y, v_z, B_y, and B_z are free to deviate from their initial conditions and are connected to the growth of turbulence, if any. The z-components of vorticity, ω_z, and current density, J_z, are particularly important, since they depend on the horizontal derivatives of the background flow and field horizontal components, respectively, and they do not depend on vertical derivatives, which are expected to be partially hampered by stratification.

Fig. 5.2 shows the time evolution of these quantities, denoted by a tilde, e.g., $\tilde{B}_{y,rms}$, to indicate that they are normalized to reference background values. Specifically, the turbulent kinetic energy $E'_{\rm kin}$ is normalized to the total initial kinetic energy, $E_{\rm kin} = \frac{1}{V}\int_{vol}\frac{1}{2}\rho v_w^2$. Similarly, the enstrophy density components $\mathcal{E}_x$ and $\mathcal{E}_z$ are normalized to the initial value of background component, $\mathcal{E}_y = (1/V)\int_V (dv_w/dz)^2 dV$. The rms of the induced magnetic energies $B_{y,rms}$ and $B_{z,rms}$ are instead normalised to $B_z^{\rm in}$.

All these indicators, which are initially zero by construction, show a fast growth and saturate to a quasi-steady state after some hundreds of t_*, with stochastic fluctuations typical of turbulent states. Such a state is characterized by values of perturbed kinetic energy and enstrophy components much smaller ($\sim 10^{-3}$) than the background shear, and by induced perturbed magnetic field components much smaller than the dominant B_x, but comparable to $B_z^{\rm in}$. Moreover, the enstrophy components are the first ones to saturate, and the magnetic field components take longer. This is possibly indicative of a (failed) attempt to trigger a vorticity dynamo (e.g., Elias-López, Del Sordo, and Viganò 2024), i.e., amplification of magnetic fields by advection of small-scale flows.

Looking in more detail, note that $\tilde{B}_{y,rms}$, after the initial growth during the first $t \sim 200\, t_*$ is followed by a slower but persistent increase over the rest of the simulation. This is caused by the slight continued growth of B_y due to the boundary conditions imposed on v_y, which fix its vertical derivatives to zero at the top and bottom boundaries. As a result, v_y does not fully converge and slowly increases with time. Therefore, the advection term of the magnetic field lines in the y-direction produces

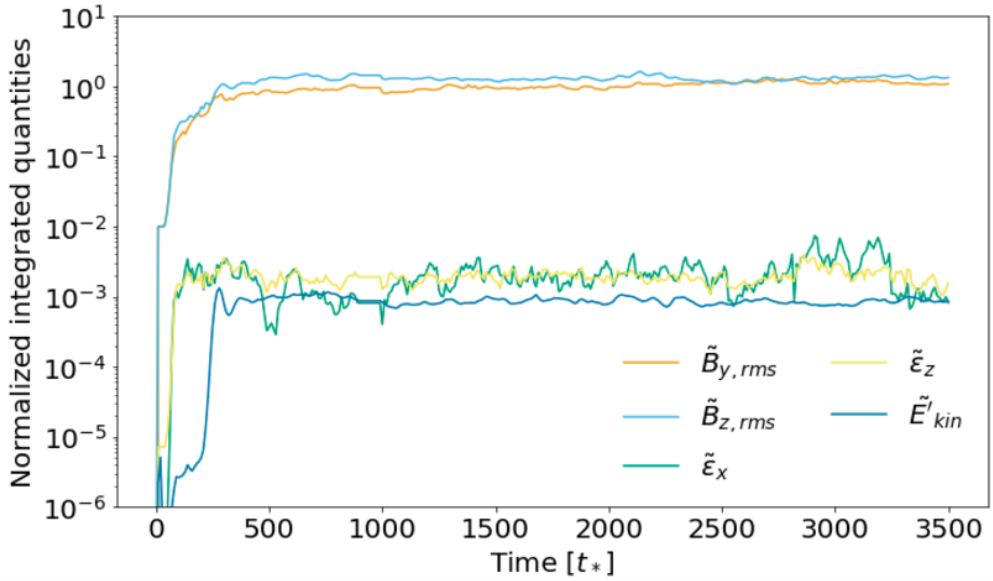

FIGURE 5.2: Evolution of the average quantities: $\tilde{B}_{y,rms}$ (orange), $\tilde{B}_{z,rms}$ (light blue), $\tilde{\mathcal{E}}_x$ (green), $\tilde{\mathcal{E}}_z$ (yellow) and $\tilde{E}'_{\rm kin}$ (dark blue) for WASP 76b (see text for their definition). Note that the integration has been computed up to p_{damp}=1.23 $\times$ 10^{-2} bar.

a gradual build-up of B_y. Physically, this reflects a slow increase of meridional flows which cause an induced meridional magnetic field component, which remains weak but increases over time.

This behaviour of v_y and its effect on B_y is qualitatively similar to the feedback observed in Chapter 4, but the physical origin is different. In Chapter 4 it arose because of the inclusion of the non-ideal terms, specifically the Hall effect. However, in the present case, the amplitude of v_y remains significantly smaller, and its evolution is not driven by a non-ideal term, but rather emerges from the interaction between the induced magnetic field and the flow, producing an advective effect. Despite the soft persistent growth of $\tilde{B}_{y,rms}$, its increase is sufficiently slow that it does not affect the statistical properties of the quasi-steady regime reached by the other quantities. For the purposes of this work, this drift in B_y can be considered negligible in terms of the assessment of small-scale relevant deviations from the background fields.

To better visualize the development of large-scale deviations, Fig. 5.3 shows the vertical profile of the B_y (top) and B_z (bottom) components, averaged over the x-y plane. To investigate how these components fluctuate at a given depth, we plot their initial values (orange), the time-averaged values and associated standard deviation after convergence (for $t \gtrsim 1000\ t_*$, blue lines and bands).

The average profile B_y shows that its mean is not zero, i.e., that there is the creation of a non-zero large-scale meridional component. The dispersion around the average profile corresponds to fluctuations in both space and time, while the drift in time is caused by the slow increase of the meridional flow. The largest deviations are seen in the upper layers, but this region is not of interest for our analysis, as it includes the damping layer. At deeper layers, we observe that B_y has an average value of a few Gauss, indicating that magnetic field generation via advection for this component can reach amplitudes comparable to the initial $B_z^{\rm in}$ field coming from the dynamo region, and much smaller than the dominant winding-generated component $B_x^{\rm in}$.

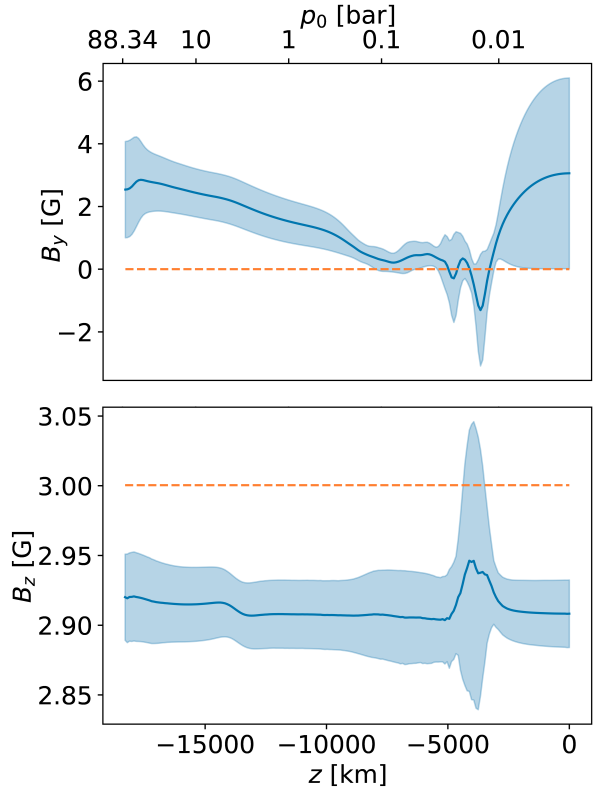

FIGURE 5.3: The vertical profiles $\langle B_y \rangle_{x,y}(z)$ and $\langle B_z \rangle_{x,y}(z)$ averaged over the x-y plane for the initial setup, and the averaged value over t>1000 t_* with the associated dispersion (blue band) for WASP 76b.

In contrast, the B_z profile, which is initially set to $B_z^{\text{in}} = 3$ G, is more uniform (with a peak caused by the start of the damping layer), with the mean value adjusting by only a few %. The difference with B_y arises from the vertical boundary conditions $v_z = 0$ and the damping layer, implying a convergence of the average profile of B_z. The dominant contributions to the dispersion are from small-scale fluctuations across the horizontal directions of the domain. These are driven by the turbulent perturbations and are among the best indicators of turbulence. Nevertheless, the amplitude of these fluctuations remains relatively small, on the order of $\sim 1\%$ B_z^{in}, highlighting that deviations are small-scale and have a second-order effect on B_z.

In order to further distinguish between large-scale and small-scale induced components, we continue analysing the evolution of the spectral kinetic and magnetic energy distribution for WASP 76b as a function of the wavenumber, k, calculated in the lower cube, far from the damping layer. For a full description of the spectra calculation, see Appendix E. In Fig. 5.4, we show the magnetic and kinetic energy spectra split into the x, y, and z components at three different times during the simulation, with the most intense colour resenting the latest stage. Note that, for large wavenumbers, the spectrum exhibits a slope typical of the dissipative range, reflecting the effect of the numerical diffusion of our finite difference/volume schemes, which is usually evident at values of k corresponding to several times the grid spacing (e.g., Viganò, Aguilera-Miret, and Palenzuela 2019). Therefore, hereafter we will neglect the tails of the spectra, and focus on the large and intermediate parts of them.

First, we observe that the contribution to the kinetic energy from each component is significantly higher than the corresponding magnetic one at all scales. This

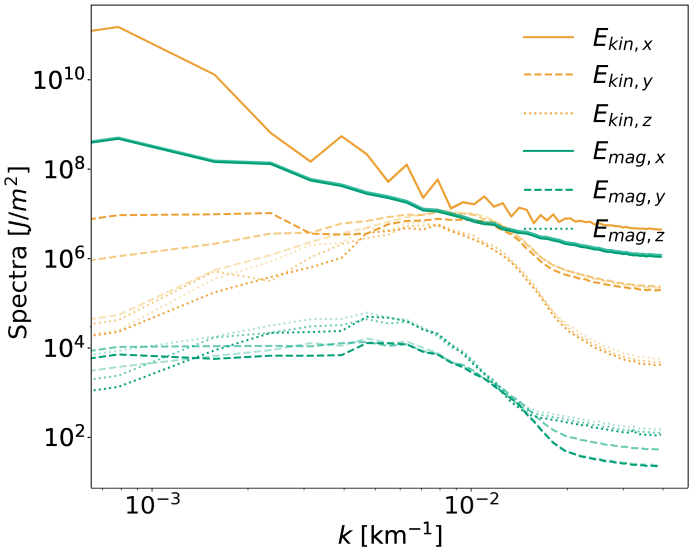

FIGURE 5.4: Contributions to the magnetic (blue) and kinetic (gold) energy density spectra by the x (solid lines), y (dashed lines), and z (dotted lines) components, for WASP-76b, at three different times: 500 t_*, 1500 t_*, and 3000 t_* (from lighter to more intense colours).

indicates that we are far from equipartition, and that there is no fully developed turbulence, even considering only the small scales of the perturbed components y and z. The contributions from B_x and v_x to the magnetic and kinetic spectra are essentially constant in time and are dominant by several orders of magnitude over their respective y and z components. This strong anisotropy reflects the fact that the system is kinematically governed by strong zonal winds which are kept stable by forcing, and magnetically dominated by the fully developed winding-generated $B_x(z)$, resulting in a strongly anisotropic configuration.

The most relevant components for this study are the perturbed ones, i.e., those associated with the meridional and vertical directions (y and z), which are generated by variations in the magnetic field and velocity. Focusing first on the kinetic perturbed components, we observe that $E_{\mathrm{kin,y}}$ is slightly larger than $E_{\mathrm{kin,z}}$, which indicates that the velocities in the y-direction might be generally larger. In addition, their temporal evolution is different. While for $E_{\mathrm{kin,y}}$ there is a noticeable increase in energy over time, especially at large and intermediate length-scales, approximately in the range 2000-9000 km (where hereafter we calculate length-scales L corresponding to a given k as $L = 2\pi/k$), for $E_{\mathrm{kin,z}}$, there is a slight decrease in energy at the largest spatial scales (i.e., low k). Both behaviours are related to the aforementioned slow increase of non-zero average v_y profiles, with the average profile v_z being more stable and better converging. In terms of spatial distribution, both $E_{\mathrm{kin,y}}$ and $E_{\mathrm{kin,z}}$ exhibit a clear bump in their spectra, with most of the energy concentrated at intermediate length scales corresponding to spatial scales, between 300 and 1000 km.

Among the perturbed magnetic components, $E_{\mathrm{mag,y}}$ and $E_{\mathrm{mag,z}}$ are significantly weaker than the x-component or any of the kinetic components. Nonetheless, $E_{\mathrm{mag,z}}$ is slightly stronger than $E_{\mathrm{mag,y}}$, especially at intermediate and small scales. Both show slight evolution over time, with variations of less than one order of magnitude, in most of the k domain. A broad bump is also visible for y and z magnetic spectral components which correspond to length-scales between, approximately, 700-1500 km.

When examining the B_y and B_z components in the x–y plane of the planet (see Fig. 5.5), coherent magnetic structures are indeed observed at such spatial scales. This bump could represent an attempt at an inverse cascade, but it does not fully develop, as the spectra for both components remain flat at low k values. The absence of a consistently negative slope across a large inertial range suggests that there is no effective redistribution of energy across spatial scales. Instead, large-scale components (i.e., the average vertical profiles) co-exist with intermediate structures, which, however, are not strong enough to dominate the dynamics.

Moreover, it is relevant to note that the spectra of the y-components are quite constant at low wavenumbers, while the ones of the z-components show a decrease at the smallest k. This behaviour is due to the stratification of the medium along the z-direction (and the different boundary conditions on v_y and v_z), which in turn hampers the presence of coherent vertical flows able to partially advect the dominant azimuthal lines and produce vertically extended perturbations of B_z.

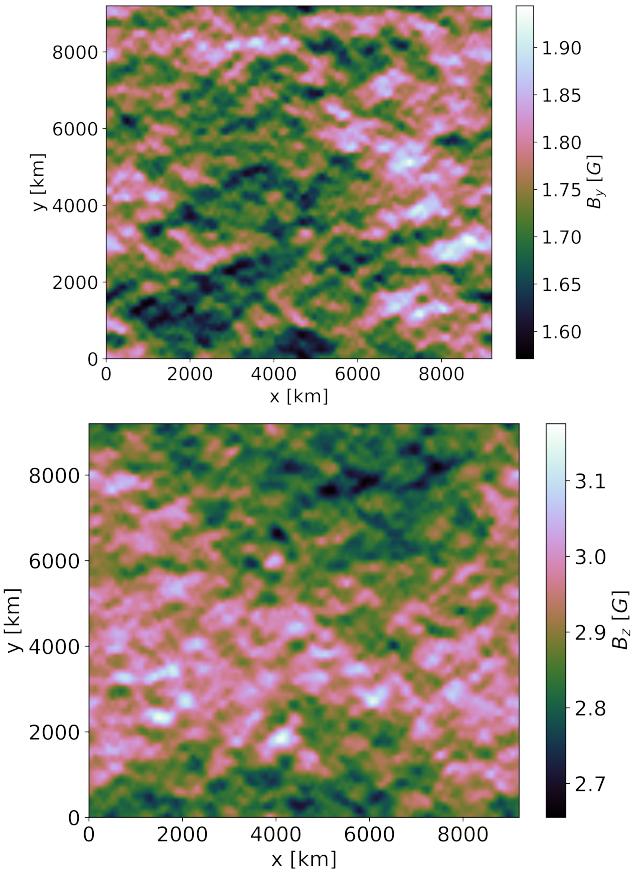

FIGURE 5.5: B_y (top) and B_z (bottom) slices for WASP 76b at $p = 0.5$ bar in the x-y plane, at the representative time $t = 3500\ t_*$.

5.3.2 Development of perturbations in different planetary models

Having examined in detail the reference case of WASP 76b, we now extend our analysis to the full set of simulated planetary models. The goal is to assess if the observed trends, such as the development of perturbed magnetic components and turbulent vorticity, are features across different atmospheric conditions.

We start by analysing the energy density spectra for the different models. Although the exact wavenumber scale k depends on the size of the physical domain

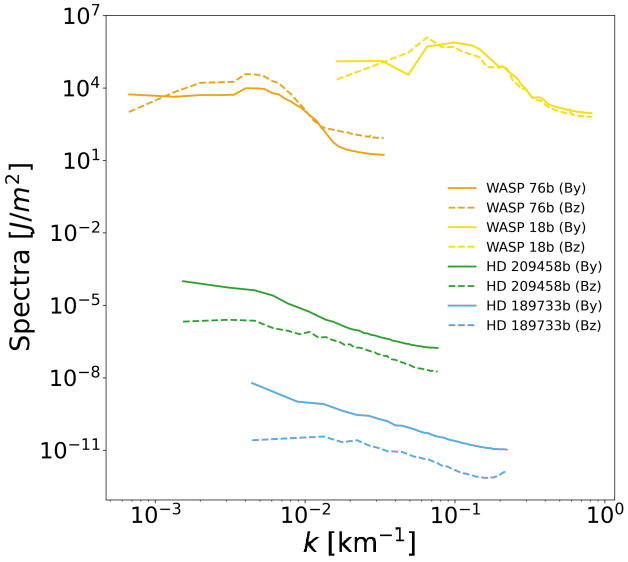

FIGURE 5.6: Magnetic energy density spectra (i.e., normalised for each simulation volume) contributions from B_y (continuous line) and B_z (dashed line), at $t = t_{max}$ for WASP 76, WASP 18b, HD 209458b, and HD 189733b.

considered for the calculation of the spectra, the range of pressures over which the simulations are performed is similar across all models, as previously stated. In Fig. 5.6, we show the B_y and B_z contributions to the magnetic energy density spectra (i.e., normalized to the volume of each simulation domain), for the four different models, at the final time available for each model. First, we observe that the highest values of magnetic energy are for WASP 18b and WASP 76b. In the coldest models, HD 209458b and HD 189733b, the magnetic energy density stored in the B_y and B_z components is negligible, being $\sim 12 - 15$ orders of magnitude lower.

Additionally, a closer inspection reveals that the hot models, WASP 76b and WASP 18b, present noticeable energy bumps in the spectra for intermediate k of each simulation corresponding to structures of size around 600 km and 60 km, respectively. These bumps, previously discussed for WASP 76b, are not present in the colder HJs.

In Fig. 5.7 we have a visual look at the WASP 18b model. In the left panel, the B_x component in a representative y–z plane and given time is shown. It illustrates the emergence of perturbative structures around $p_0 = 1$ bar, on top of the large scale winding-generated vertical profile $B_x^{\rm in}$. Although not shown here, compared to the WASP 18b model, similar B_x perturbations are visible but much slighter in WASP 76b, and they are not observed in the colder models. In the right panel, we observe that the B_z slice for WASP 18b shows structures of similar size to those seen in Fig. 5.5 for WASP 76b, with variations between maximum and minimum values on the order of a few Gauss. In contrast, these structures are not present for the coldest planets, HD 209458b and HD 189733b, which display only negligible variations visible on small scales, close to the numerical resolution and to the scale of energy injection via forcing. This further confirms that our cold models do not develop structures and, therefore, do not show the spectral bump associated with them.

In order to assess the local variability of the meridional and radial magnetic field components B_y and B_z at each atmospheric layer, Fig. 5.8 (top) shows the relative

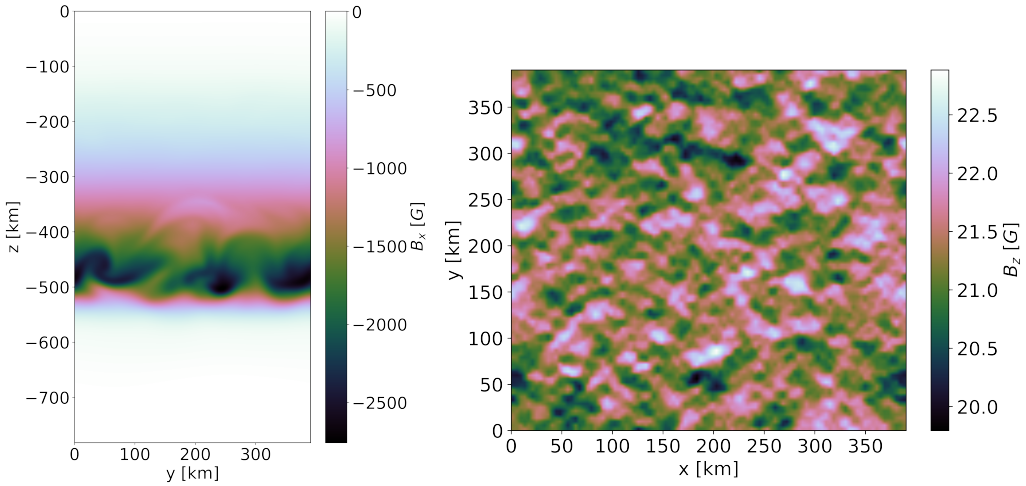

FIGURE 5.7: B_x in a $y-z$ plane (left) and B_z in the $x-y$ plane at $p_0 = 0.3$ bar (right), for WASP 18b, at a time 900 t_*, representative of the saturated state.

average fluctuation amplitude $\Delta_{B_i}(z)$, defined as:

$$\Delta_{B_i}(z) = \left\langle \frac{\sqrt{\left\langle (B_i')^2(z,t) \right\rangle_{xy}}}{\left| \langle B_i \rangle_{xy}(z,t) \right|} \right\rangle_{t>0.3\,t_{\max}} , \tag{5.8}$$

where

$$B_i'(x,y,z,t) = B_i(x,y,z,t) - \langle B_i \rangle_{xy}(z,t) , \tag{5.9}$$

with $i = y$ or z; $B_i(x,y,z,t)$ is the magnetic field component at each spatial location and time, and hereafter the brackets $\langle \cdot \rangle_{xy}$ denote the average over the horizontal x-y plane at a given height z and time t. The numerator corresponds to the rms of the local deviations in the x–y plane, and the full expression is then averaged over time, considering only around the last 70% of the simulation ($t \gtrsim 0.3\,t_{\max}$). This quantity measures the relative amplitude of spatial fluctuations of B_i with respect to its mean at each height. Values larger than one indicate that the fluctuations dominate over the mean profile, suggesting small-scale variability, while values below one correspond to more homogeneous profiles. Comparing the profiles across different planets reveals how the degree of horizontal inhomogeneity in B_y and B_z varies with depth.

Analysing the profiles of Δ_{B_y}, all models show a common pattern: the relative fluctuation decreases for pressures $p \lesssim 50$ bar, except for HD 189733b which already starts with low Δ_{B_y} due to the weak perturbations in the bottom. It subsequently rises again to values of order unity or higher at intermediate pressures (in a variable range for each model), which approximately corresponds to the shear layer in the wind profile, and finally drops at lower pressures, indicating increasing horizontal uniformity caused by the damping layer. Moreover, it can be seen that Δ_{B_z} remains around 10^{-1} and 10 for WASP 18b and WASP 76b, respectively, throughout the entire domain. This indicates that the fluctuations dominate or are of the same order as the background field in all layers. In contrast, for HD 209458b and HD 189733b, the ratio remains below 10^{-4} across the domain, suggesting a highly homogeneous magnetic field with negligible fluctuations in the plane for this component.

In order to quantify the impact of small-scale perturbations on the generation

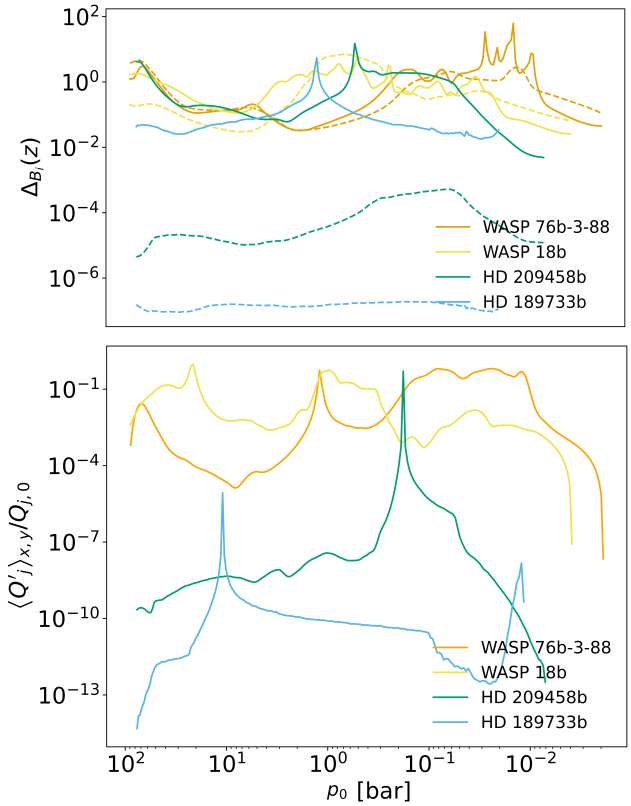

FIGURE 5.8: Top: Δ_{B_y} (solid lines) and Δ_{B_z} (dashed lines), as defined in eq. 5.8, as a function of pressure p_0 for WASP 76b, WASP 18b, HD 209548b and HD 189733b. This ratio has been averaged over the final, approximately 70% time, of each simulation. Bottom: The vertical profiles of the ratio $\left\langle Q'_j \right\rangle_{x,y}(z)/Q_{j,0}(z)$ at the final time of the simulations as a function of p_0.

Model	$B_{y,\mathrm{rms}}$ (G)	$B_{z,\mathrm{rms}}$ (G)	$\mathcal{E}_x$ (s^{-2})	$\mathcal{E}_z$ (s^{-2})	X_{pert}
WASP 76b-3-88	6.2×10^{-1}	4.9×10^{-1}	5.5×10^{-10}	1.1×10^{-9}	2.5×10^{-2}
WASP 76b-0.3-1000-0.01	7.0×10^{-3}	7.0×10^{-4}	2.1×10^{-18}	3.4×10^{-12}	3.3×10^{-5}
WASP 76b-0.3-1000-0.1	2.4×10^{-1}	8.0×10^{-3}	3.8×10^{-14}	3.6×10^{-10}	3.1×10^{-3}
WASP 18b	1.9	8.0×10^{-1}	4.2×10^{-6}	8.6×10^{-6}	3.2×10^{-2}
HD 189733b	9.1×10^{-7}	4.5×10^{-8}	1.6×10^{-20}	2.3×10^{-12}	1.9×10^{-10}
HD 209458b	2.4×10^{-4}	1.0×10^{-4}	9.9×10^{-20}	9.0×10^{-13}	1.3×10^{-7}

TABLE 5.2: Properties of the models at saturation. Columns: (1) model identifier; (2)–(3) root-mean-square perturbed magnetic-field components, $B_{y,\mathrm{rms}}$ and $B_{z,\mathrm{rms}}$; (4)–(5) normalised final enstrophy indicators for the x- and z-components, $\mathcal{E}_x$ and $\mathcal{E}_z$, evaluated at the final time. All magnitudes are integrated up to p_{damp} for each simulation. (6) Ratio of the estimated perturbative to background contributions to the volume-integrated Ohmic dissipation rates, X_{pert}.

of ohmic dissipation, $Q_j(z,t) = J^2(z,t)/\sigma(z)$, we compare at t_{max} the contributions from the turbulent and background fields, estimated as:

$$Q_{j,0}(z) = \frac{J_{y,0}^2(z)}{\sigma}, \qquad \left\langle Q_j' \right\rangle_{x,y}(z) = \left\langle \frac{J_z^2(x,y,z)}{\sigma(z)} \right\rangle_{x,y} \tag{5.10}$$

where $Q_{j,0}(z)$ represents the Ohmic dissipation arising solely from the background currents, $J_{y,0} = (dB_x^{\text{in}}/dz)/\mu_0$, and $\left\langle Q_j' \right\rangle_{x,y}(z)$ is a proxy for the contribution from turbulent structures at each depth, and is estimated from the vertical component of the current, J_z, an indicator of small-scale magnetic variations, as explained above.

The ratios between these two contributions are presented in the bottom panel of Fig. 5.8. Looking at the vertical profiles, the ratio tends to increase at high and intermediate pressures, likely due to the presence of vertical shear and a more active development of the perturbations. At lower pressures, however, the ratio drops significantly, which can be interpreted as the result of the artificial damping effects which reduce the turbulent fluctuations in the upper atmosphere. It is also relevant to note that the peaks present for the different planets are caused by changes of sign of the generated J_y as described in Chapter 4.

The local profiles reveal that, among the models analysed, WASP 18b presents the highest ratios, followed by WASP 76b, HD 209458b, and HD 189733b. This is consistent with the trends observed in other turbulence indicators. Moreover, in the most extreme cases, such as WASP 18b, the ratio can reach values between 10^{-2} and 1, particularly in the deeper atmospheric layers. This suggests that turbulent perturbations might play a significant role in some regions of the hottest atmospheres. In contrast, for the two coldest cases, the contribution from perturbations is negligible throughout almost the entire domain.

Finally, Table 5.2 shows several indicators of the deviations from the background state: $B_{y,\text{rms}}$, $B_{z,\text{rms}}$, $\mathcal{E}_x$, $\mathcal{E}_z$, and X_{pert} defined as:

$$X_{pert} = \frac{\int_{-D}^{0} \left\langle Q_j' \right\rangle_{x,y} dz}{\int_{-D}^{0} Q_{j,0} dz}. \tag{5.11}$$

The latter shows that the contributions of the deviations from the background, when integrated over the domain, are still only $\lesssim 3\%$ even for the hottest planets. All indicators show clear differences between cold and hot cases. Both $B_{y,\text{rms}}$ and $B_{z,\text{rms}}$ increase significantly in hotter models, reflecting the growth of perturbed magnetic components and the formation of non-negligible magnetic structures. The average enstrophy density components, $\mathcal{E}_x$ and $\mathcal{E}_z$, follow a similar trend, indicating enhanced turbulent activity and rotational motions for the hottest cases, for which both components are of the same order. In hot atmospheres, the v_y profile grows, indicating the triggering of a large-scale meridional circulation, an important contribution to $\mathcal{E}_x$, while small-scale deviations define $\mathcal{E}_z$. Overall, these indicators consistently show that hotter atmospheres favour both stronger magnetic perturbations and more vigorous turbulence.

5.3.3 Dependence on the depth and perturbation strength

Next we explore whether going deeper into the atmosphere, or increasing the strength of the perturbation, allows the perturbation to develop more easily. We begin by

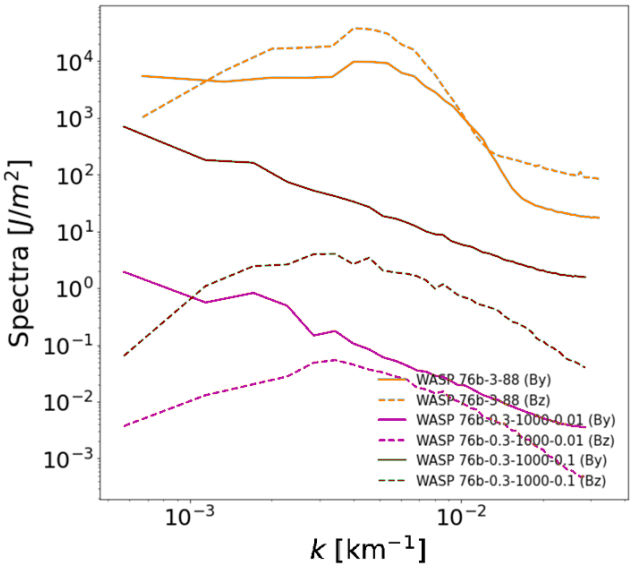

FIGURE 5.9: Magnetic energy density spectra for the B_y (solid line) and B_z (dashed line) components at the final time of each simulation, shown in Table 5.1 as a representative steady-state case, for three WASP 76b simulations: the default case, the same planet with an extended domain down to 1000 bar, and the extended-domain case with $\lambda = 0.1$. Note that the simulations with an extended domain assume an initial background field $B_z = 0.3$ G.

first extending the bottom boundary of WASP 76b atmosphere down to 1000 bar, while keeping the rest of the variables constant (see Chapter 4 for details about the methodology for the extension and the 1D winding-ohmic solutions). We consider two cases, with $\lambda = 0.01$ (as above) and $\lambda = 0.1$. In both cases, the initial background field $B_z^{\rm in}$ is taken to be 0.3 G.

In Fig. 5.9 we show the magnetic spectra normalised for the final time in the y and z directions for the default case, as well as for the two extended models. When comparing WASP 76b with a perturbation amplitude of $\lambda = 0.01$ and $p_{bottom} = 1000$ bar and with a perturbation amplitude one order of magnitude higher, we observe that both the B_y and B_z contribution to the magnetic energy increase, by approximately one order of magnitude for the contribution from B_z and two for B_y. This suggests, not surprinsingly, that stronger perturbations enhance magnetic field development.

We note that the bumps previously seen in the magnetic spectra of WASP 76b for both B_y and B_z behave differently when using the extended domain. While the bump in the B_z contribution persists, corresponding to sizes around 1000 km and with reduced intensity, the previously prominent bump in B_y is no longer clearly visible. This is indicative that there is no dominance of a particular size structures over the domain for B_y. However, it is important to emphasize that the spectra in the two setups are computed over different vertical domains. In particular, the extended case includes deeper and denser atmospheric layers, which are generally less turbulent and may therefore suppress the development of mid-k magnetic features. This change in the integration region could explain the smoother spectra in B_y, especially if the previously dominant structures were confined to the upper layers, whose contribution is now diluted by averaging over a larger, more stable region.

Fig. 5.10 shows the horizontal x–y slices of the magnetic field component B_y at 1 bar for the two extended simulations, to be qualitatively compared with Fig. 5.5.

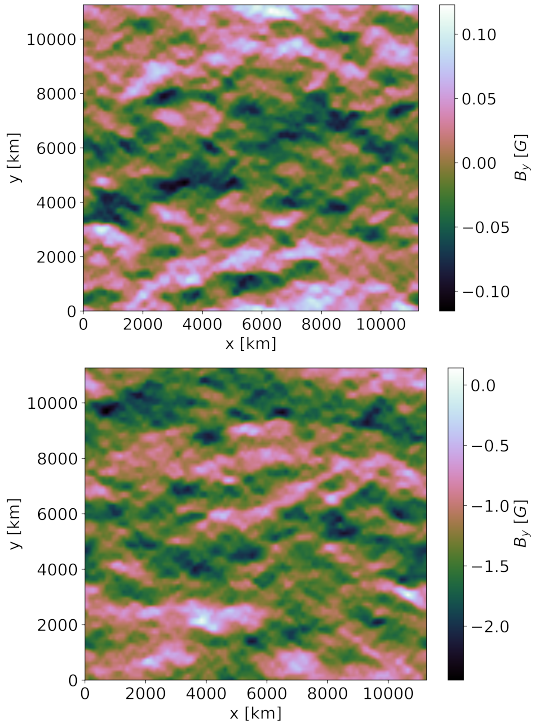

FIGURE 5.10: B_y slices in the x–y plane for WASP 76b extended model (up to 1000 bar), at $p = 1$ bar. We show the final time as a representative case of the steady-state, with $\lambda = 0.01$ (left) and $\lambda = 0.1$ (right).

The previously described patterns are clearly visible and appear more intense in the more perturbed case. We further confirmed the presence of these features of various sizes throughout the domain for B_y. Although not shown here, we verified the existence of structures of different size formed for B_y, as expected from the spectra. However, for B_z, large-scale coherent structures are practically absent, which is consistent with the drop in magnetic energy density at low k values observed in the corresponding spectra.

In order to study the local variability of the magnetic field components B_y and B_z at each atmospheric layer, Fig. 5.11 (top) shows the rms of the magnetic field fluctuations B'_y and B'_z, previously defined in section eq. 5.9. Comparing the rms of B'_y between the $\lambda = 0.1$ and $\lambda = 0.01$ cases, we observe that both rms follow the same general shape: higher values at the bottom due to boundary condition effects, followed by an increase at intermediate pressure levels, and finally a decrease in the outer layers. This trend is identical for both models; the only difference is that the rms values are higher in the case with stronger perturbations. This result is consistent with the expectation that a stronger perturbation parameter λ induces more intense atmospheric dynamics, leading to larger magnetic field fluctuations. In particular, the simulation with $\lambda = 0.1$ exhibits significantly higher rms values in the intermediate and upper layers, reflecting enhanced variability in these regions. This behaviour supports the interpretation that stronger perturbations trigger more turbulent or fine-scale magnetic structures. For the rms of B'_z, both the qualitative and quantitative behaviours are similar to those of the rms of B'_y, with the only difference being the lower values of of the rms of B'_z at high pressures, which result from the aforementioned boundary conditions differences between v_y and v_z.

Finally, to quantify the impact of small-scale perturbations and evaluate how their amplitude influences the amount of ohmic dissipation, we analyse the vertical profile of the ratio $\frac{\langle Q'j\rangle_{x,y}(z)}{Q_{j,0}}$, shown in Fig. 5.11 (bottom). Both extended cases display a similar qualitative trend as a function of pressure, with the ratio increasing at intermediate pressures, where turbulence is more active, and decreasing again in both the deepest and outermost layers. This indicates that the relative contribution of perturbations to ohmic heating is strongly pressure-dependent, peaking in the mid-atmosphere. Importantly, this trend may also depend on the boundary conditions and the presence of the damping layer in the outermost regions of the atmosphere, which can artificially reduce magnetic activity near the top of the domain.

Quantitatively, the case with stronger perturbations ($\lambda = 0.1$) shows values approximately two orders of magnitude higher than the weaker perturbation case ($\lambda = 0.01$). At low pressures, the two cases tend to converge and the ratio drops sharply due to the presence of the damping layer, which effectively suppresses any turbulent component. As shown in Table 5.2, the X_{pert} value 3.1×10^{-3} and 3.5×10^{-5} for the more and less perturbed cases, respectively, which is translated in a low impact of the perturbations on the total dissipation.

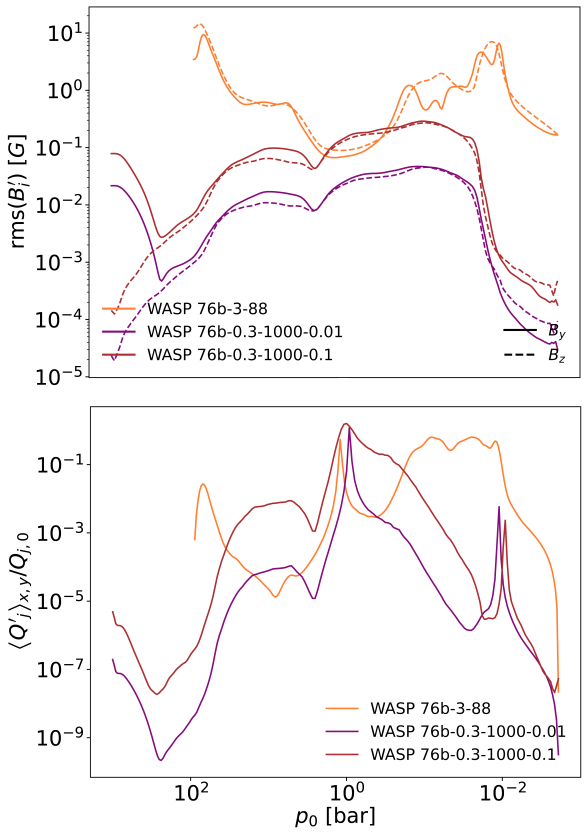

FIGURE 5.11: Top: rms of the magnetic field fluctuations B'_y as a function of pressure p_0 for WASP 76b with p_{bottom}=88.34 bar and $\lambda = 0.01$ (red) and p_{bottom}=1000 bar using λ=0.01 (olive) and λ=0.1 (blue). This ratio has been averaged over the final, approximately 70% time, of each simulation. Bottom: The vertical profiles of the ratio $\left\langle Q'_j \right\rangle_{x,y}(z)/Q_{j,0}(z)$ at the final time of the simulations as a function of p_0 for the three cases.

Importantly, this behaviour may also be influenced by the choice of boundary conditions and the implementation of the damping layer in the outermost regions of the atmosphere, which can artificially reduce magnetic activity near the top of the domain. Finally, from Table 5.2 we can observe that both $B_{y,\mathrm{rms}}$ and $B_{z,\mathrm{rms}}$ are smaller in the extended cases compared to the default setup, with the lowest values found in the $\lambda = 0.01$ case. For the enstrophy indicators $\mathcal{E}_x$ and $\mathcal{E}_z$, the latter remains dominant, as discussed in § 5.3.2. However, the magnitude of both $\mathcal{E}_x$ and $\mathcal{E}_z$ is reduced compared to the default case, reflecting that the resulting structures are both weaker and less spatially extended. In contrast, in the more perturbed case, both vorticity components are larger than in the $\lambda = 0.01$ simulation, consistent with the stronger and more developed structures observed.

5.4 Discussion and final remarks

In this work, we have presented a set of non-ideal MHD simulations in 3D Cartesian box aimed at exploring the influence of small-scale perturbations in atmospheric columns representative of sub-stellar outermost layers of HJs. We enforced small-scale perturbation on top of a 1D static solution, dominated by strong winds and azimuthal field as in Chpater 4. From the previous results we conclude:

- Since the wind velocity profile acts as a shear layer, a potential mechanism that could be triggered is the KHI. A key diagnostic used to assess whether the minimum conditions for the onset of the KHI are met is the $\mathcal{R}i$. Give our setup this can be calculated as:

$$\mathcal{R}i = \frac{g}{\rho_0} \frac{\partial \rho_0 / \partial z}{\left(\partial v_w / \partial z\right)^2} \,. \tag{5.12}$$

  We found that $\mathcal{R}i$ remains above the critical threshold throughout the entire domain in all the cases, with the lowest local values between 3 and 10 depending on the model, but always much larger than the threshold. Therefore, the Richardson number suggests that large-scale turbulence driven by the KHI is not possible for the profiles considered here.

- The analysis of our simulations finds that the induced turbulent-like contributions remain weak, as the random forcing typically introduces only minor perturbations in the magnetic field. While there is no fully developed turbulence, small-scale perturbative structures can still emerge, especially in hotter planets, at scale larger than the injection scale.

- The simulations show that such perturbations can induce non-negligible components of the magnetic field in the meridional and vertical directions. In particular, the generation of a non-zero meridional field component B_y, from an initially null configuration, demonstrates that perturbative effects alone can produce the development of magnetic structures.

- However, when considering the entire column, even in the hottest models, and in cases where stronger external perturbations are present, turbulence only adds no more than a few % of extra Ohmic dissipation to what associated to the winding-dominated field, at least with the setup presented here.

6

Conclusions

While the impact of magnetic processes on the long-term evolution of HJs, especially through Ohmic heating and radius inflation, has been studied extensively (Huang and Cumming, 2012; Ginzburg and Sari, 2016; Komacek and Youdin, 2017; Viganò et al., 2025), their influence on atmospheric circulation and wind dynamics has been investigated far less. Only a few works have explored these effects (Rogers and Komacek, 2014; Rogers and Showman, 2014; Rogers and McElwaine, 2017), while most GCMs reduce magnetic feedback to simplified drag prescriptions (Rauscher and Menou, 2013; Beltz et al., 2022). Studying magnetic effects in HJs is particularly important because these planets have been predicted to sustain large-scale magnetic fields, generated in the deep interior via dynamo, significantly stronger than those of the solar system giants (Yadav and Thorngren, 2017; Kilmetis et al., 2024), although we have recently obtained more moderate fields considering realistic internal heating models (Elias-López et al., 2025; Viganò et al., 2025), not shown in this thesis. In addition, their upper atmospheres contain partially ionized particles, making them natural sites for magnetic induction and dissipation. Moreover, the turbulence in HJs atmospheres may also be affected by the magnetic effects. While previous hydrodynamic studies of turbulence in HJs have reported instabilities driven by baroclinic modes, inertial waves, or strong thermal forcing (Fromang, Leconte, and Heng, 2016; Lian and Showman, 2010; Li and Goodman, 2010; Skinner and Cho, 2025), they typically neglect magnetic feedback. This thesis aims to go a step further by exploring magnetic induction in irradiated gas giant atmospheres under the non-linear regime and non-ideal MHD conditions, exploring how strong winds and small-scale perturbations combine to shape the local atmoshperic magnetism.

First, I have confirmed that intense shear layers in the upper radiative atmosphere naturally lead to the winding of the background field into strong azimuthal fields, supported by narrow meridional currents. This behaviour persists regardless of the specific perturbation amplitude or the position and width of the shear, as long as the shear layer is sufficiently steep. The resulting localized magnetic fields can typically reach hundreds of gauss (or kG levels in the most extreme cases), albeit locally confined to thin layers, which has important implications for the efficiency

of magnetic drag. Moreover, considering the small-scale perturbations, additional magnetic fields tend to acquire a component perpendicular to the wind (of the order of a few Gauss).

Second, the inclusion of non-ideal MHD effects (Ohmic, Hall, and ambipolar diffusion) adds an additional level of complexity to the resolution of the MHD equations. While the main outcome remains the generation of a strong localized azimuthal magnetic field, the Ohmic term now regulates the balance between winding and dissipation. Quantifying the efficiency of Ohmic dissipation allowed us to place upper limits on the amount of heat that can be deposited in the radiative layers. Although this does not directly constrain radius inflation, which requires heat deposited in deeper interior regions, our results provide input conditions that could be coupled in the future with long-term evolutionary models. The Hall and ambipolar terms are generally smaller than the dominant winding and Ohmic contributions, but at second order, specially for the upper regions and for those HJs with higher temperatures, the Hall effect modifies the MHD solutions, contributing to an additional meridional component of the magnetic field. Combined with the ambipolar effect, which tends to dissipate currents perpendicular to the magnetic field, this results in modifications to the B_x profile. These effects are not negligible: they are relevant for the spectroscopic detectability of ion–neutral velocity drifts (Savel et al., 2024), and for a more accurate evaluation of the widely used magnetic drag in GCMs.

Third, through the first fully local 3D non-ideal simulations of HJ atmospheric columns, I have quantified the relative contributions of small-scale perturbations to magnetic amplification and dissipation. While turbulent-like behaviour was found to remain weak in most cases, it can still introduce non-negligible additional magnetic components in the meridional and vertical directions. However, even in the hottest models, and in those cases where stronger external perturbations are present, turbulence contributes no more than a few percent of extra Ohmic dissipation compared to that associated with the winding-dominated field. Furthermore, the magnetic field evolution depends sensitively on model parameters such as the temperature–pressure profile, the vertical extent of the simulation domain, and the strength of the imposed perturbations. These first simulations demonstrate how small-scale perturbations can interact with the imposed large-scale shear, highlighting the limits of one-dimensional approaches and providing guidance on where turbulence may become relevant in future models.

Overall, this thesis contributes to the still unclear magnetism in HJs, by providing an in-depth study of non-ideal MHD effects in their atmospheres, identifying the contributions to local magnetic field amplification from winding and perturbative effects, for a variety of background and boundary conditions. Finally, it also helps to estimate Ohmic dissipation enhancement in environments where the local magnetic field can be up to two orders of magnitude stronger than the background field. The results highlight that GCM models using an effective magnetic drag term should ideally incorporate the complexity of the solutions we found.

Although only the substellar point background profiles from GCMs were modelled in this study, and elsewhere the effects could be less dramatic, the main features are clear: the shear layer should host a very intense, magnetic field in the direction of the wind. The Hall and ambipolar terms can induce the field in all three directions, with frequent changes of sign in the induced components.

The work presented in this thesis naturally opens the way to further developments, both within the same local simulation scenario, and in its broader applicability. Several directions are particularly relevant:

- **Instabilities, turbulence, and forcing:** A natural improvement would be to impose different kinds of perturbations (i.e., forcing), corresponding to plausible instability sources (e.g. Kelvin–Helmholtz, vertical shear, gravity wave breaking, or magnetic instabilities), rather than using the simple purely random forcing here presented. Particularly, we also aim to identifying the local shear conditions that favour the onset of such instabilities. This will help determining the regimes (if any) for which turbulence can develop and where enhanced Ohmic dissipation is more likely.

- **Improved treatment of energy and conductivity:** A more realistic approach to the energy equation and conductivity is required. In the present models, magnetic resistivity is assumed to be time-independent, which is a reasonable simplification given the limited temperature variations obtained under the Newtonian cooling scheme. However, in the outer regions of the atmosphere, stronger gradients are expected, which would affect both thermal evolution and magnetic diffusivity (Menou, 2012; Hardy, Cumming, and Charbonneau, 2022). Future work will therefore focus on coupling a more consistent energy transport prescription with detailed conductivity tables (including additional species), as well as revisiting the role of Ohmic heating as a possible source term in the local energy balance.

- **Sensitivity with background profiles:** Within the local 3D framework I aim to explore a wider range of temperature–pressure profiles, including those representative of different longitudes and latitudes. In particular, extending the simulations towards lower pressures, before the hydrostatic limit brakes, will make it possible to assess Hall and ambipolar terms in the regions where they are most relevant. This will also help to re-evaluate ion–neutral velocity differences within a region that is accessible to high-resolution spectroscopy, but that are still under the hydrostatic equilibrium.

- **Connection with GCMs:** Beyond model refinement, the results of this thesis also have important implications for their implementation in global models. The simulations carried out here provide a characterization of the main non-ideal atmospheric effects, which are usually neglected in GCMs but can and should be incorporated. This would directly impact the parametrization of magnetic drag, which in most GCMs is currently reduced to a simplified Rayleigh-type term and assumes a linear regime in which the induced field remains much weaker than the background dipole and under the assumption of a dipolar field aligned with the spin axis. Future efforts could therefore follow two complementary paths. One option would be that of directly incorporating the full non-ideal MHD formulation into GCM simulations, while another of producing systematic sets of local 3D MHD simulations at different planetary points to construct global interpolations. The latter approach would allow the derivation of effective parametrizations that could be implemented in GCMs, thus bridging local non-ideal MHD processes with large-scale atmospheric modelling.

- **Connection with observations:** Finally, an essential step is to establish a closer link between simulations and observations. On one hand, improved characterization of atmospheric temperature profiles, circulation patterns, and wind velocities from HR spectroscopy will provide real data which could be used as input for the models presented here. On the other hand, possible indirect hints

of magnetism in HJs, such as detections of low-frequency coherent radio emission or signatures of star-planet interaction (Cauley et al., 2019), could help constrain one of the main free parameters in our models. Combining observational constraints with non-ideal MHD simulations will thus be key to assess the role of magnetic effects in HJs atmospheres.

A

On the atmospheric electrical conductivity

This appendix justifies the use of the analytical approximation based on the thermal ionization of potassium to estimate the electrical conductivity in the outer radiative layers of HJs. This discussion is based in § 4.1 Viganò et al., 2025, where we reconstructed conductivity profiles $\sigma(\rho, T)$ by combining two physical regimes: (i) thermal ionization of alkali metals in shallow layers and (ii) pressure ionization of H/He in deeper layers. In the following lines we summarize those results, explain the interpolation procedure, and compare them to the K-only approximation (Balbus and Hawley, 2000), concluding that the latter is sufficient for our purposes.

Following Viganò et al. (2025), three main density–temperature domains are identified to calculate the conductivity:

- **Shallow layers** ($\rho \lesssim 10^{-2}\,\mathrm{g\,cm^{-3}}$, i.e. $p \lesssim$ kbar at Gyr ages): conductivity is dominated by thermal ionization of alkali metals. In this range we adopt the tables of Kumar et al. (2021). These include partially ionised plasma composed of hydrogen, helium, and a small fraction of metals (Li, Na, Ca, Fe, K, Rb, and Cs), typical for atmospheres of HJs.

- **Deep layers** ($\rho \gtrsim 10^{-2}\mathrm{g\,cm^{-3}}$): electrons start becoming degenerate and the ions are strongly coupled (Redmer, 1997; Ramakrishna, Lokamani, and Cangi, 2024). Therefore, the contributions of ionised hydrogen and helium, increase significantly. Their ionization is caused by the pressure and this produces a sudden increase of the conductivity with density. For the calculation of the conductivity in this range we adopt the reference values compiled in Fig. 42 of Bonitz et al. (2024), which summarize the state-of-the art calculations, based on density functional theory and molecular dynamics (DFT-MD). Note that at $\rho \gtrsim 1\,\mathrm{g\,cm^{-3}}$ the curves converge towards the Jovian adiabat of French et al. (2012), with values typically differing by a factor of a few from one model to another. However this region is very far from the atmospheric regions which is of interest in this thesis.

- **Intermediate regime** ($10^{-2} \lesssim \rho \lesssim 1\,\mathrm{g\,cm^{-3}}$): there is a rapid and strongly temperature-dependent transition (especially for $T \lesssim 10^4$ K) ((Holst, French, and Redmer, 2011)).

The interpolation procedure used to calculate the conductivity across the full range of densities presented above is the following. Let $\sigma_{\mathrm{alk}}(\rho, T)$ denote the values from Kumar et al. (2021), and $\sigma_{\mathrm{DFT}}(\rho, T)$ the DFT–MD values from Bonitz et al. (2024). Since both ρ and σ span several orders of magnitude and are strictly positive, the interpolation is performed in logarithmic space. The prescription is:

1. If $\rho \leq 10^{-2}\,\mathrm{g\,cm^{-3}}$: use $\sigma = \sigma_{\mathrm{alk}}$. This is the only regime relevant for the work here presented.
2. If $\rho \geq 10^{-1}\,\mathrm{g\,cm^{-3}}$: use $\sigma = \sigma_{\mathrm{DFT}}$. This regime is relevant for the deep interior, where the planetary fields are generated (e.g., Elias-López et al., 2025).
3. If $10^{-2} < \rho < 10^{-1}\,\mathrm{g\,cm^{-3}}$: it is the region least explored by simulations, thus we simply linearly interpolate $\log(\sigma)$ in the $\log(\rho)$-$\log(T)$ plane between the closest extremes of the two tables.

This conductivity, shown in Fig. A.1, is calculated for a planet of 1 M_J while varying the age, the equilibrium temperature T_{eq}, and considering models with and without the inclusion of Ohmic heating (parametrized by the average wind speed v_{avg}; we refer the reader to Viganò et al., 2025 for further details). In the same figure, we also show the widely used K^+-only approximation from Balbus and Hawley (2000), evaluated for planets with $T_{\mathrm{eq}} = 1500$ and 2000 K. A closer inspection of the conductivity curves shows that the K^+-*only* formula reproduces the correct trend of σ in the outer atmosphere, but starts to deviate significantly from our interpolated values beyond $p \gtrsim 10^3$ bar. At even higher pressures, $p \gtrsim 10^5$ bar, the interpolated conductivity profiles converge towards very high σ values that are largely insensitive to T, in agreement with the Jovian adiabat reported by French et al. (2012).

Within the pressure range relevant to this thesis, $p \sim 0.01 - 1000$ bar, the K^+-only approximation provides sufficiently accurate conductivity estimate, also considering that composition variations will give at least conductivity difference which are at least as large as the discrepancies here shown.

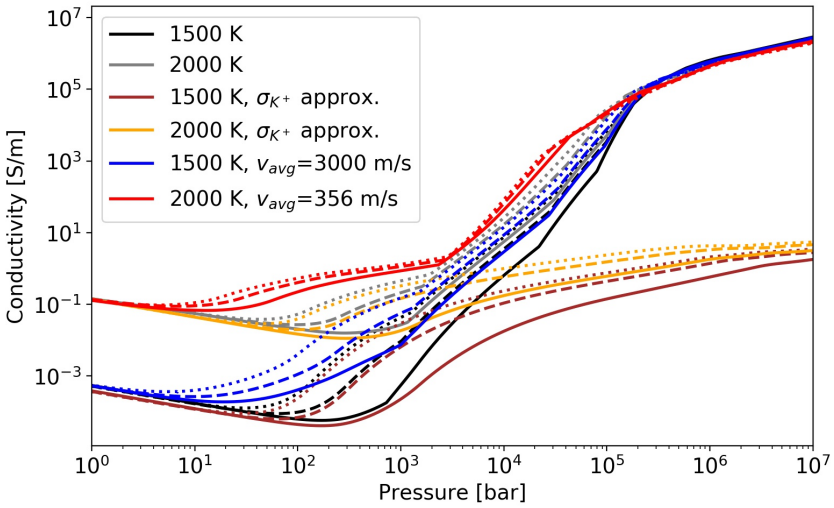

FIGURE A.1: Electrical conductivity σ as a function of pressure for different planetary models evolved with the evolutionary code MESA. We show ages of $t \simeq 0.4$ (dots), 1.1 (dashes), and 5 Gyr (solid lines), for a planet with $M = 1$, showing two cases $T_{\rm eq} = 1500, 2000$ K, without (black, grey) and with internal Ohmic heating (blue, red). We also show (brown and gold lines), for comparison, the simplified K^+-only thermal ionization formula, which neglects pressure ionization, for the cases without Ohmic heating. From Viganò et al., 2025, to which we refer for more details.

B

Reference values for rescaled MHD equations

In this appendix we derive the expressions of the reference quantities used in the non-dimensional formulation of the hydrostatic equilibrium and MHD equations equations. These reference scales (H_*, B_*, ρ_*, c_*, t_*) are introduced in order to write dimensionless quantities in the equations.

Pressure scale height H_*

Starting from the hydrostatic balance (eq. 2.2) and the ideal gas law (eq. 2.1),

$$\frac{dp}{dz} = -\rho g, \qquad p = \rho RT, \tag{B.1}$$

we obtain

$$\frac{1}{p}\frac{dp}{dz} = -\frac{g}{RT(z)}. \tag{B.2}$$

The pressure scale height is defined as the inverse magnitude of the logarithmic pressure gradient,

$$H(z) := -\left(\frac{d\ln p}{dz}\right)^{-1} = \frac{RT(z)}{g}. \tag{B.3}$$

In the special case of an isothermal atmosphere, where $T(z) = T_0$ is constant, this reduces to a constant value:

$$H_* = \frac{RT_0}{g}. \tag{B.4}$$

Reference density ρ_*

The reference density follows directly from the ideal gas equation of state (eq. 2.1) for a chosen reference pressure p_* and temperature T_0:

$$\rho_* := \frac{p_*}{RT_0}. \tag{B.5}$$

This quantity serves as the normalization for the density field.

Characteristic velocity c_*

The characteristic velocity is naturally associated with the sound speed in an ideal gas. Starting from the definition,

$$c_* := \sqrt{\frac{p_*}{\rho_*}}, \tag{B.6}$$

and substituting the expression for ρ_*, we obtain

$$c_* = \sqrt{RT_0}. \tag{B.7}$$

Thus, c_* corresponds to the sound speed at the reference temperature.

Characteristic magnetic field B_*

The characteristic magnetic field is defined by equating the magnetic pressure

$$\frac{B^2}{2\mu_0} \tag{B.8}$$

to a reference gas pressure p_*. This yields

$$\frac{B_*^2}{2\mu_0} = p_*, \tag{B.9}$$

and therefore

$$B_* = \sqrt{2\mu_0 p_*}. \tag{B.10}$$

In some conventions the factor of 2 is omitted, leading to

$$B_* = \sqrt{\mu_0 p_*}. \tag{B.11}$$

For $p_* = 1\,\text{bar}$, this evaluates to approximately

$$B_* \simeq 0.354\,\sqrt{p_{\text{bar}}}\ \text{T}, \tag{B.12}$$

where p_{bar} is the pressure expressed in bar. This provides an order-of-magnitude estimate of the magnetic field strength balancing a bar-level pressure.

Characteristic time scale t_*

A natural time scale can be defined as the ratio between the pressure scale height and the characteristic velocity:

$$t_* = \frac{H_*}{c_*}. \tag{B.13}$$

Substituting the previously derived expressions gives

$$t_* = \frac{RT_0}{g\, c_*}. \tag{B.14}$$

Using $c_* = \sqrt{RT_0}$, we obtain

$$t_* = \frac{c_*}{g}. \tag{B.15}$$

This represents the characteristic timescale for a sound wave to travel a scale height.

Connection with the adiabatic sound speed

The adiabatic sound speed is defined as

$$c_{s,0} = \sqrt{\gamma \frac{p}{\rho}} = \sqrt{\gamma}\, c_*, \tag{B.16}$$

where γ is the adiabatic index of the gas. The corresponding crossing time for one scale height is therefore

$$t_{x,0} = \frac{H_*}{c_{s,0}} = \frac{t_*}{\sqrt{\gamma}}. \tag{B.17}$$

Relation with the acoustic cut-off frequency

In a vertically stratified atmosphere, acoustic waves are subject to a cut-off frequency. Following e.g. **tobias_thesis** (eq. 2.66), this is given by

$$\nu_{c,0} = \frac{\gamma g}{2c_{s,0}}. \tag{B.18}$$

It is useful to note that the fundamental reference timescale introduced above is directly related to this frequency:

$$\frac{1}{t_*} = \frac{\sqrt{\gamma}}{2}\, \nu_{c,0}. \tag{B.19}$$

Hence the acoustic cut-off provides a physical interpretation for the inverse of the nondimensional reference timescale.

Isothermal vs. non-isothermal cases

The above definitions assume a reference temperature T_0. If the atmosphere is not isothermal, the election of the reference magnitudes is not trivial as they become function of altitude, see Chapter 4 and 5 for details. The main differences are summarized below:

- **Pressure scale height:**
  Isothermal: $H_* = \dfrac{RT_0}{g}$ (constant).
  Non-isothermal: $H(z) = \dfrac{RT(z)}{g}$.

- **Reference density:**
  Isothermal: $\rho_* = \dfrac{p_*}{RT_0}$.
  Non-isothermal: $\rho_*(z) = \dfrac{p_*}{RT(z)}$.
- **Characteristic velocity (sound speed):**
  Isothermal: $c_* = \sqrt{RT_0}$.
  Non-isothermal: $c_*(z) = \sqrt{RT(z)}$.
- **Magnetic field scale:**
  If p_* is taken as a fixed reference (e.g. 1 bar), then B_* is constant.
  If instead the local pressure $p(z)$ is used, then $B_*(z) = \sqrt{\mu_0 p(z)}$.
- **Time scale:**
  Isothermal: $t_* = \dfrac{c_*}{g}$ (constant).
  Non-isothermal: $t_*(z) = \dfrac{\sqrt{RT(z)}}{g}$.

In summary, in the isothermal case the characteristic quantities are constants, while in the non-isothermal case they inherit the vertical dependence. In practice, many studies such as Chapters 4 and 5 adopt mean values of T in the region of interest to define the reference scales.

C

Details about ideal MHD simulations in Chapter 3

C.1 Hydrostatic stability

In this appendix we present the tests for the hydrostatic stability of the atmospheric column represented by our domain. It is important to note that these tests were performed under the setup presented in the first work (Chapter 3), but the verification of hydrostatic stability applies to all subsequent chapters. The problem is typical of different astrophysical scenarios, where one needs to simulate fast dynamics over a much longer timescale. Specific solutions have been studied (e.g., Zingale et al. 2002), depending on the numerical scheme employed. In our case, the total timescale is the one needed to reach a stationary state, which under our conditions is typically hundreds time the sound crossing time.

The basic test is then to study the numerical stability of the vertical background profile described in § 3.2.2. We run simulations with no forcing and no initial velocity perturbations or magnetic fields, $\vec{v}(t=0) = \vec{B}(t=0) = \vec{F}_{\rm src} = 0$. Such tests are 1D, since the only spatial dependence in the initial fields is on z. We then analyse the results computing the domain-integrated L2-norm of $\hat{v}_z$, i.e. the ambient vertical velocities that depart from the analytical equilibrium ($\hat{v}_z = \hat{\rho}_1 = \hat{p}_1 = 0$).

In all cases, tiny vertical velocities arise from the boundaries and from the readjustment due to discretisation. Part of it is due to the huge differences in the magnitudes of the fields, an issue that is greatly mitigated by evolving the perturbed density ρ_1 instead of the total one ρ. In order to find the numerical setup that minimizes such spurious velocities, we explore the influence of the following numerical parameters: (i) $\nu_{\rm cool}$; (ii) vertical size of the domain (L); (iii) parameters of the artificial damping region: lower boundary (z_d) and amplitude (A_d); (iv) resolution.

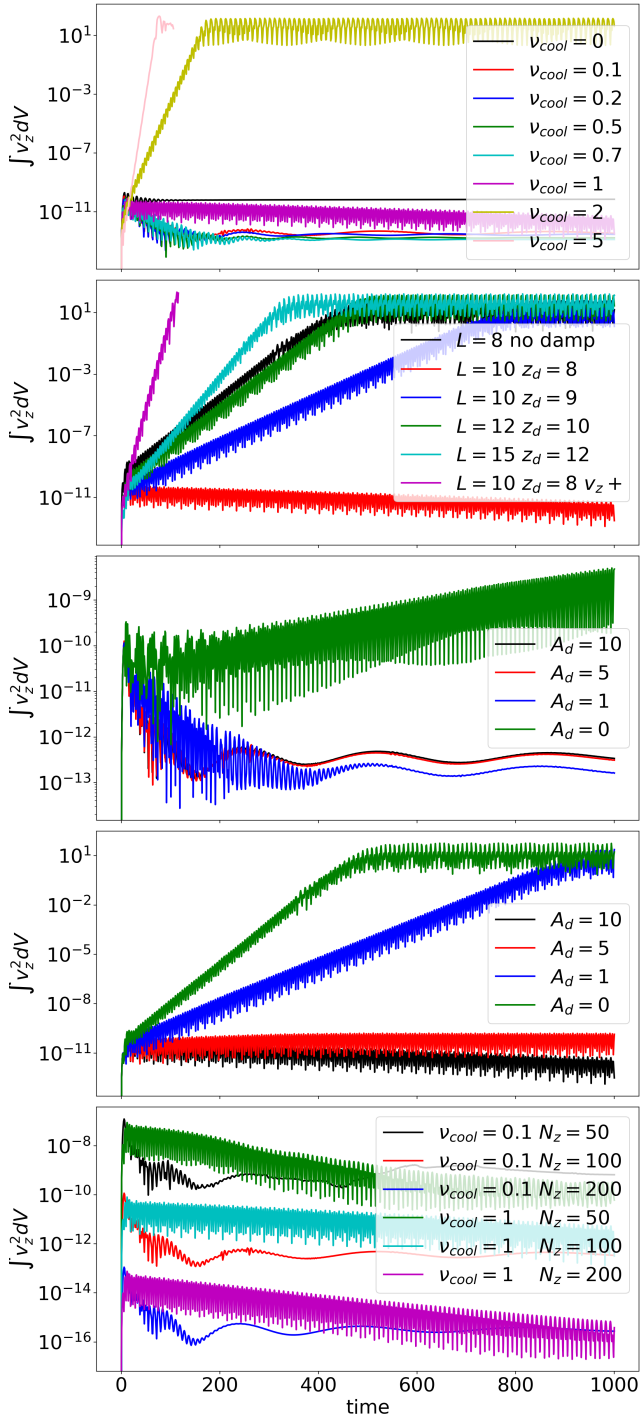

FIGURE C.1: Hydrostatic stability tests for variations of different parameters over the standard set $\nu_{\rm cool} = 0.1$, $A_d = 10$, $L = 10$, $z_d = 8$, $N_z = 100$. From top to bottom, such variations are over (see legends for their values): $\nu_{\rm cool}$; combinations of domain size $\hat{L}$ and damping region position z_d and symmetric radial boundary conditions on v_z (purple) for $\nu_{\rm cool} = 1$; A_d with $\nu_{\rm cool} = 0.1$; A_d with $\nu_{\rm cool} = 1$; resolution for two different $\nu_{\rm cool}$. We show the integrated L2 norm of v_z, which is the proxy to the discretisation error in case of no forcing (wind or perturbations) and no initial magnetic fields. The integral over the volume $V = (5 \times 5 \times 10)\ H_*^3$ in units of $c_*^2 H_*^3$; time in units t_*.

In Fig. C.1 we show the evolution of $\int \hat{v}_z^2 dV$ over 1000 t_*, showing the variation of the different parameters. In the top panel, we see that any choice $\nu_{\rm cool} \lesssim 1$ provides similar and acceptable results, with velocities much lower than the $\nu_{\rm cool} = 0$ case (which is low, but experiences a slow rise in T). Larger values of $\nu_{\rm cool} \gtrsim 2$ provide instead a persistent growth, that is unrelated to the timestep adopted. In all cases, some oscillations are seen, reflecting some waves that are triggered by the initial readjustment. Such waves are damped more efficiently for intermediate values of $\nu_{\rm cool}$. The value $\nu_{\rm cool} = 0.1$ adopted in the main text allows a damping in a few hundreds t_*.

In the second, third and fourth panels, we can see that cases with no damping ($L = 8$, $A_d = 0$) provide a continuous rise of the perturbation, which makes indeed the simulation unstable if we choose non-optimal values of other parameters (in particular, $\nu_{\rm cool} = 1$, fourth panel). The oscillations are damped effectively and quickly for $A_d \gtrsim 5$. Using larger domains (cyan and green line in second panel), or shallower damping regions (blue) also produce the effect of keeping the oscillations longer and usually stronger (which again is more evident if we use other non-optimal values of $\nu_{\rm cool} = 1$, as in the third panel). In the second panel we also show in purple the unstable case of other boundary conditions for $\hat{v}_z$ (i.e., $\hat{v}_z$ being flat close to the radial boundaries, instead of being zero): it makes any simulation highly unstable after few hundreds t_* typically, causing inflows and outflows of matter regardless of the damping region.

These trends are valid for the other resolutions (see bottom panel), among which we see the expected scaling of the discretization error. These tests highlight the need of a damping region and to limit the size of the domain, due to the exponential background profile. After comparing tens of runs, we consider as optimal and standard the following set of parameters: $\nu_{\rm cool} = 0.1$, $L = 10$, $z_d = 8$, $A_d = 10$.

C.2 1D runs for winding only: initial magnetic field dependence

In Fig. C.2 we show the comparison of the B_x evolution between different 1D runs, i.e., without any perturbations, $\lambda = 0$. Different colors mark different initial amplitudes of B_x (eq. 3.12), while the shades mark the evolution over long times ($t/t_* = 0, 500, 1000, 1500, 2000, 2500$). The initial profile (the most transparent lines) rapidly changes to a shape that resembles the asymptotic ones (the most opaque lines, at 2500 t_*), which is indeed similar to the full 3D cases discussed in the text, e.g. Fig. 3.7. Starting with low values of magnetic fields (black or red, $C_B = 0, 0.1$), the winding makes the field to grow, but it will take several thousands t_* to approach the asymptotic profile. On the contrary, starting with a large value of C_B (purple, $C_B = 2$), the numerical dissipation damps the peaks and on average the field decreases. Moreover, in the latter case such value seems to be higher than in the other cases. The cases with $C_B = 0.5, 1$ (blue, green) reach instead much faster a similar asymptotic profile, which is also similar to the one approached by $C_B = 0.1$. We also verified the same trends in the 3D: too small or too large values of C_B hampers the ability of reach a quasi-asymptotic profile of the winding-generated B_x profile. Therefore, we fix $C_B = 1$ in our 3D simulations, keeping in mind that it can take up to $\sim 1000\ t_*$ to approach the asymptotic profile.

Note that such asymptotic profile depends on the wind profile and on the numerical diffusivity (see below).

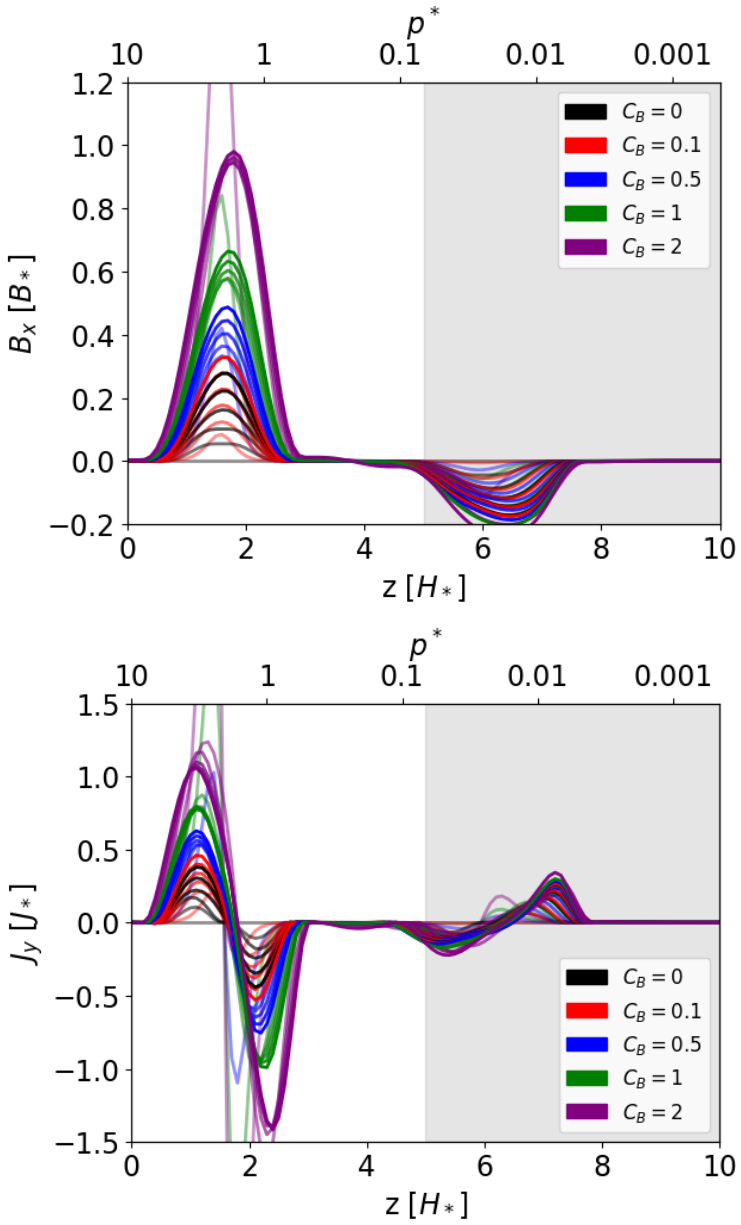

FIGURE C.2: Comparison of the vertical profile evolution of B_x (top) and J_y (bottom) in the 1D problem, i.e., in the absence of perturbations, $\lambda = 0$. The four colors indicate different values of the initial magnetic field amplitude $C_B = \{0, 0.1, 0.5, 1, 2\}$, in the eq. 3.12. The five shades (transparent to opaque) indicate different times: $t/t_* = 0, 500, 1000, 1500, 2000, 2500$.

C.3 Numerical vs. physical diffusivity

In Fig. C.3 we compare the physical conductivity $\sigma(T, p)$, given by eq. 2.11, with the numerical conductivity $\sigma_{\rm num}(T) := 1/(\eta_{\rm num}\mu_0)$. From this figure, we can determine the applicable region where $\sigma_{\rm num}$ is not much larger than σ. This is important especially in the region of the shear, $p \sim 1$ bar. Therefore, we conclude that: (i) the simulations presented here are valid for temperatures approaching $T \gtrsim 3800K$ (for which σ and $\sigma_{\rm num}$ are comparable in the shear layer region), and should give results not too far from the ones expected if resistivity is included, if $T \gtrsim 3000$ K (for which

the difference between σ at 1 bar and $\sigma_{\rm num}$ is less than one order of magnitude); (ii) higher resolutions would give numerical diffusivities that are too low, making the results unreliable.

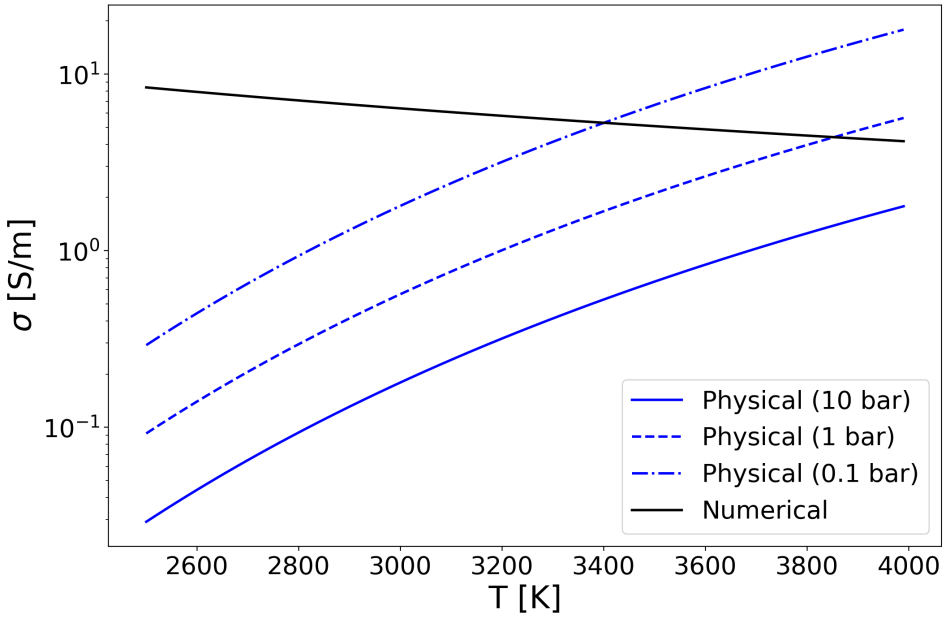

FIGURE C.3: Comparison between the physical conductivity $\sigma(T, p)$ as in eq. 2.11 (blue lines, for $p = 0.1, 1, 10$ bar) and numerical conductivity $\sigma_{\rm num}$ (estimated for $N_z = 100$, black), for $g_{10} = \mu = 1$, as a function of temperature. The results of this study are applicable if $\sigma_{\rm num}$ is not much larger than σ.

D

Details about 1D non-ideal MHD simulations in Chapter 4

D.1 Effect of different boundary conditions

Here we present a discussion on relaxing the different boundary conditions for the B_x component in the upper and lower limits for the simulations. The winding effect will directly depend on the magnetic field present in the domain and at the borders, i.e., the magnetic field in the inner and outer regions. For simplicity, we here restrain to the case of winding+Ohmic only. In Fig. D.1 (top), we can see the solutions for WASP 76b corresponding to different boundary conditions (BCs), using either a fixed value for B_x, or no induced current (i.e., $J_y = 0$, meaning $dB_x/dz = 0$).

When the induced magnetic field is fixed at $B_x = 0$ G at the borders, which is the choice used in the main text, the equilibrium B_x profile reaches approximately 100 G at its peak and -200 G at its minimum. Choosing a non-zero, large value (35 G in this case) of B_x at the lower boundary (i.e., not confining the induction to the considered domain), results in a slightly larger induced field. If we instead consider cases for which the inner boundary or both boundaries have $dB_x/dz = 0$ the magnetic field grows significantly larger and in many cases it doesn't converge: it tends to have a flat profile (i.e., current-free), but with a very large value.

If we analyze the effect of the different B_x boundary conditions (BCs) on the generated $Q_j(z)$, as shown in Fig. D.1 (bottom), we can observe that for high pressures ($p > 5$), there is a slight increase in Q_j when B_x is fixed to a certain value (purple and red lines). However, when the derivative of B_x is set to 0, this effect is not visible. For intermediate pressures ($1 < p < 0.05$), all cases show an increase in Q_j. As discussed, this increase is proportional to the magnetic field generated, and it converges for simulations with fixed B_x in the lower BCs, while it does not converge and continues to increase for those with the derivative of B_x set to 0 (blue and olive lines).

Therefore, to ensure convergence and avoid an artificial unrealistic growing of the field, we choose to be conservative and we apply boundary conditions of $B_x = 0$ on both sides.

D.2 Resolution and magnetic diffusivity

In this section, we aim to test that the numerical resistivity does not dominate over the analytical one. In Chapter 3, the only magnetic diffusivity considered arose from numerical effects. In this paper, as discussed, the physical magnetic diffusivity has been taken into account. If we compare it with the numerical diffusivity from Appendix C.3 in Chapter 3 the physical one should dominate. Thus, a change in the resolution of the simulations should not have any effect as long as the physical magnetic diffusivity is much larger than the numerical one. In Fig. D.2 we report three simulations in which the vertical resolution was changed to 100, 200, and 400 vertical points respectively.

It can be appreciated that an increase in the resolution under the same conditions does not affect the amplification of the magnetic field, since the numerical diffusivity is much smaller than the physical one, and the magnetic field throughout the domain does not practically change. If we examine the currents, J_y, the same trend can be observed. However, some slightly more significant variations among the various resolutions compared to B_x can be appreciated. This is especially so in the outermost region, where the physical resistivity drops and the numerical resistivity can be comparable to it; for this reason, the most external part of the domain, for $p \lesssim 0.01$ bar, should be considered with care.

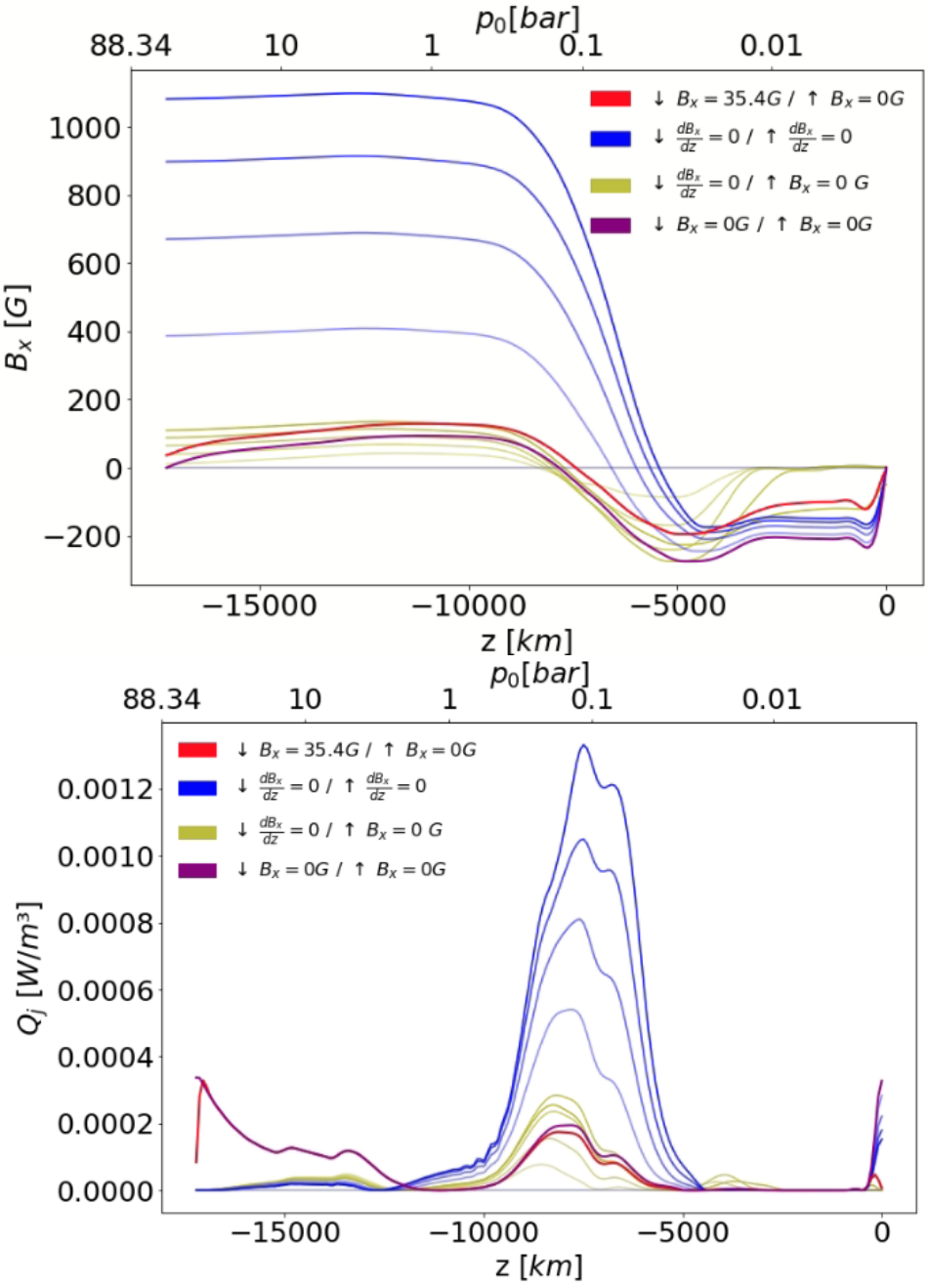

FIGURE D.1: Comparison of the vertical profiles $B_x(z)$ (top) and $Q_j(z)$ (bottom) for WASP 76b-d3, for different BC at different times (indicated with increasingly darker shades): B_x= 35 G in the lower border and $B_x = 0$ G in the upper border (red), dB_x/dz=0 in the upper and lower border (blue), $dB_x/dz = 0$ in the lower border and $B_x = 0$ G in the upper border (blue) and $B_x = 0$ G in the lower and upper border (purple).

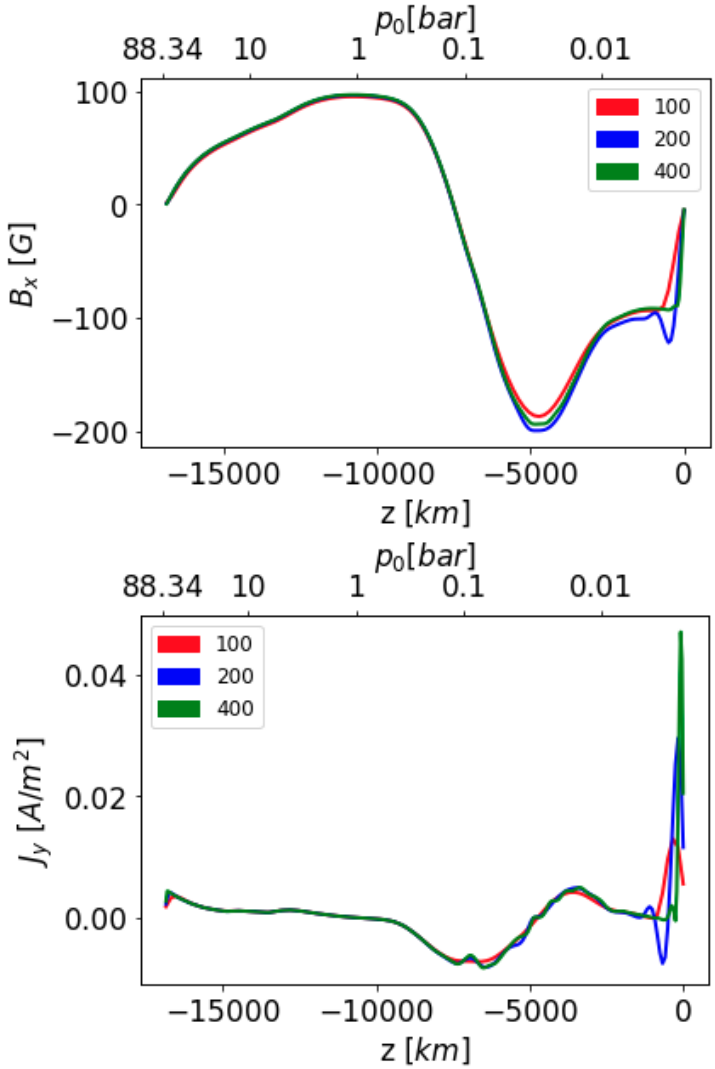

FIGURE D.2: Comparison of B_x (top) and J_y (bottom) at convergence for three different cases for WASP 76b: 100 (red), 200 (blue) and 400 (green) points in the vertical direction.

E

Calculation of the energy spectra

The energy spectra shown in this work are computed following the method described in Appendix A of Viganò, Aguilera-Miret, and Palenzuela (2019), adapted to our simulation domain. We consider the lower cube of the simulation box ($x \in [0, D/2]$, $y \in [0, D/2]$, $z \in [-D, D/2]$). This is because of two reasons. First, the upper half includes artificial diffusivity and a damping layer, which would contribute to the spectra, without being physical reliable. Secondly, we aim to evaluate the level of turbulence in the deepest regions of the domain, as these layers are the most significant contributors to additional Ohmic dissipation, especially due to their proximity to the convective zone, which could redistribute the heat throughout the planet if the dissipation reaches that region.

We compute the discrete 3D Fourier transform of the physical field of interest (velocity and magnetic field components), using a standard Fast Fourier Transform `python` algorithm. The wavenumber components along each direction i are defined on a discrete grid:

$$k_i = \frac{2\pi n_i}{L}, \quad n_i = 0, 1, ..., N/2, \quad i = x, y, z, \tag{E.1}$$

where $L = D/2$ is the box size, and N is the number of grid points per spatial dimension. We then consider the modulus of the wavenumber vector,

$$k = \sqrt{k_x^2 + k_y^2 + k_z^2}\,. \tag{E.2}$$

The power spectrum $E(k)$ of a scalar field f is computed by binning all Fourier modes whose modulus k falls within a given interval centered at each k_p, a set of values numerically defined as k_i. Within each bin, the following expression is evaluated:

$$E(k_p) = \frac{4\pi}{V \Delta k^3 N^6} \left\langle k^2 \cdot |\hat{f}(\mathbf{k})|^2 \right\rangle_{|\mathbf{k}| \in [k_p - \Delta k/2,\, k_p + \Delta k/2)}, \tag{E.3}$$

where $\Delta k = 2\pi/L$ is the bin size, the brackets indicate averaging over all modes $\mathbf{k}$ within the bin, and V corresponds to the total volume. The latter is added so that we can compare the spectral distribution of the energy density between models with different domain sizes. The field f depends on the type of spectrum being computed: for kinetic energy, we use $f = \sqrt{\rho} \cdot v_i$ and for magnetic energy, $f = B_i$. Given the intrinsic anisotropy (due to azimuthal winds) and inhomogeneity (due to stratification) of the magnetised HJ atmospheric columns considered in this work, we plot the components separately, rather than showing the total spectra, i.e. their sum.

Bibliography

Albrecht, S., Winn, J. N., Johnson, J. A., Howard, A. W., Marcy, G. W., Butler, R. P., Arriagada, P., Crane, J. D., Shectman, S. A., Thompson, I. B., Hirano, T., Bakos, G., and Hartman, J. D. (2012). "Obliquities of Hot Jupiter Host Stars: Evidence for Tidal Interactions and Primordial Misalignments"., 757(1): 18. DOI: 10.1088/0004-637X/757/1/18.

Alderson, L. et al. (2023). "Early Release Science of the exoplanet WASP-39b with JWST NIRSpec G395H"., 614(7949): 664–669. DOI: 10.1038/s41586-022-05591-3.

Arbona, A., Artigues, A., Bona-Casas, C., Massó, J., Miñano, B., Rigo, A., Trias, M., and Bona, C. (2013). "Simflowny: A general-purpose platform for the management of physical models and simulation problems". *Computer Physics Communications*, 184: 2321–2331. DOI: 10.1016/j.cpc.2013.04.012.

Arbona, A., Miñano, B., Rigo, A., Bona, C., Palenzuela, C., Artigues, A., Bona-Casas, C., and Massó, J. (2018). "Simflowny 2: An upgraded platform for scientific modelling and simulation". *Computer Physics Communications*, 229: 170–181. DOI: 10.1016/j.cpc.2018.03.015.

Arcangeli, J., Désert, J.-M., Parmentier, V., Stevenson, K. B., Bean, J. L., Line, M. R., Kreidberg, L., Fortney, J. J., and Showman, A. P. (2019). "Spectroscopic phase curve of WASP-18b with HST/WFC3". *Astronomy Astrophysics*, 625: A136. DOI: 10.1051/0004-6361/201834891.

Arcangeli, J., Desert, J.-M., Line, M. R., Bean, J. L., Parmentier, V., Stevenson, K. B., Kreidberg, L., Fortney, J. J., Mansfield, M., and Showman, A. P. (2018). "H^- Opacity and Water Dissociation in the Dayside Atmosphere of the Very Hot Gas Giant WASP-18b". *The Astrophysical Journal Letters*, 855(2): L30. DOI: 10.3847/2041-8213/aab272.

Arras, P. and Socrates, A. (2010). "Thermal tides in fluid extrasolar planets". *The Astrophysical Journal*, 714(1): 1–12. DOI: 10.1088/0004-637X/714/1/1.

Arras, P. and Bildsten, L. (2006). "Thermal Stability of Tidally Heated Giant Planets". *The Astrophysical Journal*, 650: 394–407. DOI: 10.1086/506011.

Baeyens, R., Désert, J.-M., Petrignani, A., Carone, L., and Schneider, A. D. (2024). "Photodissociation and induced chemical asymmetries on ultra-hot gas giants. A case study of HCN on WASP-76 b"., 686: A24. DOI: 10.1051/0004-6361/202348022.

Balbus, S. A. and Hawley, J. F. (2000). "Solar Nebula Magnetohydrodynamics". *Space Science Reviews*, 92(1): 39–54. DOI: 10.1023/A:1005293132737.

Baruteau, C., Crida, A., Paardekooper, S. J., Masset, F., Guilet, J., Bitsch, B., Nelson, R., Kley, W., and Papaloizou, J. (Jan. 2014). "Planet-Disk Interactions and Early Evolution of Planetary Systems". In: *Protostars and Planets VI*. Ed. by H. Beuther, R. S. Klessen, C. P. Dullemond, and T. Henning. (Jan. 2014), 667–689. DOI: 10.2458/azu_uapress_9780816531240-ch029. arXiv: 1312.4293 [astro-ph.EP].

Batalha, N. M., Rowe, J. F., Bryson, S. T., Barclay, T., Burke, C. J., Caldwell, D. A., and Jenkins, J. M. (2013). "Planetary Candidates Observed by Kepler. III. Analysis of the First 16 Months of Data". *The Astrophysical Journal Supplement Series*, 204: 24. DOI: 10.1088/0067-0049/204/2/24.

Batygin, K. (2012). "A primordial origin for misalignments between stellar spin axes and planetary orbits". *Nature*, 491: 418–420. DOI: 10.1038/nature11560.

Batygin, K., Bodenheimer, P. H., and Laughlin, G. P. (2016). "In Situ Formation and Dynamical Evolution of Hot Jupiter Systems"., 829(2): 114. DOI: 10.3847/0004-637X/829/2/114.

Batygin, K., Stanley, S., and Stevenson, D. J. (2013). "Magnetically controlled circulation on hot extrasolar planets". *The Astrophysical Journal*, 776: 53. DOI: 10.1088/0004-637X/776/1/53.

Batygin, K. and Stevenson, D. J. (2010). "Inflating Hot Jupiters with Ohmic Dissipation". *The Astrophysical Journal Letters*, 714: L238. DOI: 10.1088/2041-8205/714/2/L238.

Batygin, K., Stevenson, D. J., and Bodenheimer, P. H. (2011). "Evolution of Ohmically Heated Hot Jupiters". *The Astrophysical Journal*, 738: 1. DOI: 10.1088/0004-637X/738/1/1.

Becker, J. C., Vanderburg, A., Adams, F. C., Rappaport, S. A., and Schwengeler, H. M. (2015). "WASP-47: A Hot Jupiter System with Two Additional Planets Discovered by K2"., 812(2): L18. DOI: 10.1088/2041-8205/812/2/L18.

Bell, T. J. and Cowan, N. B. (2018). "Increased Heat Transport in Ultra-hot Jupiters through H_2 Dissociation and Recombination". *The Astrophysical Journal Letters*, 857: L20. DOI: 10.3847/2041-8213/aabcc8.

Bell, T. J., Welbanks, L., Schlawin, E., Line, M. R., Fortney, J. J., Greene, T. P., Ohno, K., Parmentier, V., Rauscher, E., Beatty, T. G., Mukherjee, S., Wiser, L. S., Boyer, M. L., Rieke, M. J., and Stansberry, J. A. (2023). "Methane throughout the atmosphere of the warm exoplanet WASP-80b"., 623(7988): 709–712. DOI: 10.1038/s41586-023-06687-0.

Beltz, H., Rauscher, E., Kempton, E. M.-R., Malsky, I., Ochs, G., Arora, M., and Savel, A. (2022). "Magnetic Drag and 3D Effects in Theoretical High-resolution Emission Spectra of Ultrahot Jupiters: the Case of WASP-76b". *The Astronomical Journal*, 164: 140. DOI: 10.3847/1538-3881/ac897b.

Benavides, S. J., Burns, K. J., Gallet, B., and Flierl, G. R. (2022). "Effective Drag in Rotating, Poorly Conducting Plasma Turbulence". *The Astrophysical Journal*, 938(2): 92. DOI: 10.3847/1538-4357/ac9137.

Benz, W. et al. (2020). "The CHEOPS mission". *Experimental Astronomy*, 51: 109–151. DOI: 10.1007/s10686-020-09679-4.

Bodenheimer, P., Laughlin, G., and Lin, D. N. C. (2003). "On the Radii of Extrasolar Giant Planets". *The Astrophysical Journal*, 592(1): 555–563. DOI: 10.1086/375565.

Bodenheimer, P., Lin, D. N. C., and Mardling, R. A. (2001). "On the Tidal Inflation of Short-Period Extrasolar Planets". *The Astrophysical Journal*, 548: 466–472. DOI: 10.1086/318667.

Bonitz, M., Vorberger, J., Bethkenhagen, M., Böhme, M. P., Ceperley, D. M., Filinov, A., Gawne, T., Graziani, F., Gregori, G., Hamann, P., Hansen, S. B., Holzmann, M., Hu, S., Kählert, H., Karasiev, V. V., Kleinschmidt, U., Kordts, L., Makait, C., Militzer, B., Moldabekov, Z. A., Pierleoni, C., Preising, M., Ramakrishna, K., Redmer, R., Schwalbe, S., Svensson, P., and Dornheim, T. (2024). "Toward first principles-based simulations of dense hydrogen". *Physics of Plasmas*, 31(110501). DOI: 10.1063/5.0219405.

Borchert, S. and Zängl, G. (2022). "Three-Dimensional Static Instability of Gravity Waves and a Possible Parameterization of the Associated Wave Breaking". *Journal of the Atmospheric Sciences*, 79(12): –.

Borucki, W. J. et al. (2010). "Kepler Planet-Detection Mission: Introduction and First Results". *Science*, 327(5968): 977–980. DOI: 10.1126/science.1185402.

Boss, A. P. (1997). "Giant planet formation by gravitational instability." *Science*, 276: 1836–1839. DOI: 10.1126/science.276.5320.1836.

Brandenburg, A. and Subramanian, K. (2005). "Astrophysical magnetic fields and nonlinear dynamo theory". *Physics Reports*, 417: 1–209. DOI: 10.1016/j.physrep.2005.06.005.

Brice-Olivier, D. and Seagers, S. S. (2011). "Lack of inflated radii for Kepler giant planet candidates receiving modest stellar irradiation". *The Astrophysical Journal Supplement Series*, 197. DOI: 10.1088/0067-0049/197/1/12.

Brogi, M., Kok, R. J. d., Albrecht, S., Snellen, I. A. G., Birkby, J. L., and Schwarz, H. (2016). "Rotation and winds of exoplanet HD 189733 b measured with high-dispersion transmission spectroscopy". *The Astrophysical Journal*, 817(2): 106. DOI: 10.3847/0004-637X/817/2/106.

Brown, T. M. (2001). "Transmission Spectra as Diagnostics of Extrasolar Giant Planet Atmospheres". *The Astrophysical Journal*, 553: 1006. DOI: 10.1086/320950.

Bryan, M. L., Knutson, H. A., Howard, A. W., Ngo, H., Batygin, K., Crepp, J. R., Fulton, B. J., Hinkley, S., Isaacson, H., Johnson, J. A., Marcy, G. W., and Wright, J. T. (2016). "Statistics of Long Period Gas Giant Planets in Known Planetary Systems"., 821(2): 89. DOI: 10.3847/0004-637X/821/2/89.

Buchhave, L. A., Bizzarro, M., Latham, D. W., Sasselov, D. D., Cochran, W. D., Endl, M., Isaacson, H., Juncher, D., and Marcy, G. W. (2014). "Three regimes of extrasolar planet radius inferred from host star metallicities". *Nature*, 509(7502): 593–595. DOI: 10.1038/nature13254.

Burrows, A., Marley, M., Hubbard, W. B., Lunine, J. I., Guillot, T., Saumon, D., Freedman, R., Sudarsky, D., and Sharp, C. (1997). "A Nongray Theory of Extrasolar Giant Planets and Brown Dwarfs". *The Astrophysical Journal*, 491: 856–875. DOI: 10.1086/305002.

Burrows, A., Hubeny, I., Budaj, J., and Hubbard, W. B. (2007). "Possible Solutions to the Radius Anomalies of Transiting Giant Planets". *The Astrophysical Journal*, 661: 502. DOI: 10.1086/514326.

Butler, R. P., Marcy, G. W., Williams, E., Hauser, H., and Shirts, P. (1997). "Three New "51 Pegasi-Type" Planets". *The Astrophysical Journal*, 474: L115. DOI: 10.1086/310444.

Carone, C., Baeyens, R., Mollière, P., Barth, P., Vazan, A., Decin, L., Sarkis, P., Venot, O., and Henning, T. (2020). "Equatorial retrograde flow in WASP-43b elicited by deep wind jets?" *Monthly Notices of the Royal Astronomical Society*, 496: 3582–3614. DOI: https://doi.org/10.1093/mnras/staa1733.

Cauley, P. W., Shkolnik, E. L., Llama, J., and Lanza, A. (2019). "Magnetic fields of hot Jupiters calculated from star-planet interactions". *Nature Astronomy*, 3: 1128–1134. DOI: 10.1038/s41550-019-0840-x.

Chabrier, G. and Baraffe, I. (2007). "Heat transport in giant (exo)planets: A new perspective". *The Astrophysical Journal*, 661: L81. DOI: 10.1086/518473.

Chang, S. H., Gu, P. G., and Bodenheimer, P. H. (2010). "Tidal and Magnetic Interactions Between a Hot Jupiter and its Host Star in the Magnetospheric Cavity of a Protoplanetary Disk"., 708(2): 1692–1702. DOI: 10.1088/0004-637X/708/2/1692.

Charbonneau, D., Allen, L. E., Megeath, S. T., Torres, G., Alonso, R., Brown, T. M., Gilliland, R. L., Latham, D. W., Mandushev, G., O'Donovan, F. T., and Sozzetti, A. (2005). "Detection of Thermal Emission from an Extrasolar Planet". *The Astrophysical Journal*, 626: 523. DOI: 10.1086/429991.

Charbonneau, D., Brown, T. M., Noyes, R. W., and Gilliland, R. L. (2002). "Detection of an Extrasolar Planet Atmosphere". *The Astrophysical Journal*, 568: 377. DOI: 10.1086/338770.

Chatterjee, S., Ford, E. B., Matsumura, S., and Rasio, F. A. (2008). "Dynamical Outcomes of Planet-Planet Scattering"., 686(1): 580–602. DOI: 10.1086/590227.

Chitre, S. M. and Krishan, V. (2001). "Ambipolar diffusion in the solar atmosphere". *Monthly Notices of the Royal Astronomical Society*, 323: L23. DOI: 10.1046/j.1365-8711.2001.04461.x.

Cho, J. Y.-K., Menou, K., Hansen, B. M. S., and Seager, S. (2008). "Atmospheric circulation of close-in extrasolar giant planets: I. Global, barotropic, adiabatic simulations". *The Astrophysical Journal*, 675: 817. DOI: 10.1086/524718.

Christensen, U. R. and Aubert, J. (2006). "Scaling properties of convection-driven dynamos in rotating spherical shells and application to planetary magnetic fields". *Geophysical Journal International*, 166(1): 97–114. DOI: 10.1111/j.1365-246X.2006.03009.x.

Christensen, U. R., Holzwarth, V., and Reiners, A. (2009). "Energy flux determines magnetic field strength of planets and stars". *Nature*, 457: 167–169. DOI: 10.1038/nature07626.

Connerney, J. E. P., Timmins, S., Oliversen, R. J., Espley, J. R., Joergensen, J. L., Kotsiaros, S., Joergensen, P. S., Merayo, J. M. G., Herceg, M., Bloxham, J., Moore, K. M., Mura, A., Moirano, A., Bolton, S. J., and Levin, S. M. (2022). "A New Model of Jupiter's Magnetic Field at the Completion of Juno's Prime Mission". *Journal of Geophysical Research: Planets*, 127: e2021JE007055. DOI: https://doi.org/10.1029/2021JE007055.

Cont, D., Yan, F., Reiners, A., Nortmann, L., Molaverdikhani, K., Pallé, E., Henning, T., Ribas, I., Quirrenbach, A., Caballero, J. A., Amado, P. J., Czesla, S., Lesjak, F., López-Puertas, M., Mollière, P., Montes, D., Morello, G., Nagel, E., Pedraz, S., and Sánchez-López, A. (2022). "Atmospheric characterization of the ultra-hot Jupiter WASP-33 b: Detection of Ti and V emission lines and retrieval of a broadened line profile". *Astronomy & Astrophysics*, 668: A53. DOI: 10.1051/0004-6361/202244277.

Cooper, C. S. and Showman, A. P. (2005). "Dynamic Meteorology at the Photosphere of HD 209458b". *The Astrophysical Journal*, 629: L45. DOI: 10.1086/444354.

Costa Silva, A. R., Demangeon, O. D. S., Santos, N. C., Ehrenreich, D., Lovis, C., Chakraborty, H., Lendl, M., Pepe, F., Cristiani, S., Rebolo, R., Zapatero-Osorio, M. R., Adibekyan, V., Alibert, Y., Allart, R., Allende Prieto, C., Azevedo Silva, T., Borsa, F., Bourrier, V., Cristo, E., Di Marcantonio, P., Esparza-Borges, E., Figueira, P., González Hernández, J. I., Herrero-Cisneros, E., Lo Curto, G., Martins, C. J. A. P., Mehner, A., Nunes, N. J., Palle, E., Pelletier, S., Seidel, J. V., Silva, A. M., Sousa, S. G., Sozzetti, A., Steiner, M., Suárez Mascareño, A., and Udry, S. (2024). "ESPRESSO reveals blueshifted neutral iron emission lines on the dayside of WASP-76 b". *Astronomy & Astrophysics*, 689: A8. DOI: 10.1051/0004-6361/202449935.

Coulombe, L.-P. et al. (2023). "A broadband thermal emission spectrum of the ultra-hot Jupiter WASP-18b". *Nature*, 620: 292–298. DOI: 10.1038/s41586-023-06230-1.

Cowan, N. B., Agol, E., and Charbonneau, D. (2007). "Hot nights on extrasolar planets: mid-infrared phase variations of hot Jupiters". *Monthly Notices of the Royal Astronomical Society*, 379(2): 641–646. DOI: 10.1111/j.1365-2966.2007.11897.x.

Cridland, A. J., Eistrup, C., and van Dishoeck, E. F. (2019). "Connecting planet formation and astrochemistry. Refractory carbon depletion leading to super-stellar C/O in giant planetary atmospheres"., 627: A127. DOI: 10.1051/0004-6361/201834378.

Crossfield, I. J. M. (2015). "Observations of Exoplanet Atmospheres". *Publications of the Astronomical Society of the Pacific*, 127: 941. DOI: 10.1086/683115.

Crouzet, N., McCullough, P. R., Deming, D., and Madhusudhan, N. (2014). "Water Vapor in the Spectrum of the Extrasolar Planet HD 189733b. II. The Eclipse"., 795(2): 166. DOI: 10.1088/0004-637X/795/2/166.

Cumming, A., Butler, R. P., Marcy, G. W., Vogt, S. S., Wright, J. T., and Fischer, D. A. (2008). "The Keck Planet Search: Detectability and the Minimum Mass and Orbital Period Distribution of Extrasolar Planets". *Publications of the Astronomical Society of the Pacific*, 120(867): 531–534. DOI: 10.1086/588487.

Dawson, R. I. and Johnson, J. A. (2018). "Origins of Hot Jupiters". *Annual Review of Astronomy and Astrophysics*, 56: 175–221. DOI: 10.1146/annurev-astro-081817-051853.

Debras, F. and Chabrier, G. (2019). "New Models of Jupiter in the Context of Juno and Galileo"., 872(1): 100. DOI: 10.3847/1538-4357/aaff65.

Dedner, A., Kemm, F., Kröner, D., Munz, C.-D., Schnitzer, T., and Wesenberg, M. (2002). "Hyperbolic Divergence Cleaning for the MHD Equations". *Journal of Computational Physics*, 175(2): 645–673. DOI: 10.1006/jcph.2001.6961.

Deming, D., Seager, S., Richardson, L. J., and Harrington, J. (2005). "Infrared radiation from an extrasolar planet". *Nature*, 434: 740–743. DOI: 10.1038/nature03507.

Deming, D., Wilkins, A., McCullough, P., Burrows, A., Fortney, J. J., Agol, E., Dobbs-Dixon, I., Madhusudhan, N., Crouzet, N., Desert, J.-M., Gilliland, R. L., Haynes, K., Knutson, H. A., Line, M., Magic, Z., Mandell, A. M., Ranjan, S., Charbonneau, D., Clampin, M., Seager, S., and Showman, A. P. (2013). "Infrared Transmission Spectroscopy of the Exoplanets HD 209458b and XO-1b Using the Wide Field Camera-3 on the Hubble Space Telescope". *The Astrophysical Journal*, 774: 95. DOI: 10.1088/0004-637X/774/2/95.

Dietrich, W., Kumar, S., Poser, A. J., French, M., Nettelmann, N., Redmer, R., and Wicht, J. (2022). "Magnetic induction processes in Hot Jupiters, application to KELT-9b". *Monthly Notices of the Royal Astronomical Society*, 517(3): 3113–3128. DOI: 10.1093/mnras/stac2849.

Dobbs-Dixon, I. and Agol, E. (2013). "Three-dimensional radiative-hydrodynamical simulations of the highly irradiated short-period exoplanet HD 189733b". *The Astrophysical Journal*, 435: 3159–3168. DOI: 10.1093/mnras/stt1509.

Draine, B., Roberge, and Dalgarno, A. (1983). "Magnetohydrodynamic shock waves in molecular clouds". *The Astrophysical Journal*, 264: 485. DOI: 10.1086/160617.

Duffell, P. C., Haiman, Z., MacFadyen, A. I., D'Orazio, D. J., and Farris, B. D. (2014). "The Migration of Gap-opening Planets is Not Locked to Viscous Disk Evolution"., 792(1): L10. DOI: 10.1088/2041-8205/792/1/L10.

Eggleton, P. P., Kiseleva, L. G., and Hut, P. (1998). "The Equilibrium Tide Model for Tidal Friction"., 499(2): 853–870. DOI: 10.1086/305670.

Ehrenreich, D. et al. (2020). "Nightside condensation of iron in an ultrahot giant exoplanet". *Nature*, 580(7805): 597–601. DOI: 10.1038/s41586-020-2107-1.

Elias-López, A., Cantiello, M., Viganò, D., Del Sordo, F., Kaur, S., and Soriano-Guerrero, C. (2025). "Rossby number regime, convection suppression, and dynamo-generated magnetism in inflated hot Jupiters". *The Astrophysical Journal*. DOI: 10.48550/arXiv.2507.05202.

Elias-López, A., Del Sordo, F., and Viganò, D. (2024). "Vorticity and magnetic dynamo from subsonic expansion waves II: Dependence on the magnetic Prandtl number, forcing scale, and cooling time". *Astronomy & Astrophysics*, 690: A77. DOI: 10.1051/0004-6361/202450398.

Enoch, B., Cameron, A. C., and Horne, K. (2012). "Factors affecting the radii of close-in transiting exoplanets". *Astronomy & Astrophysics*, 540: A99. DOI: 10.1051/0004-6361/201117317.

Etangs, A. Lecavelier des, Ehrenreich, D., Vidal-Madjar, A., Ballester, G. E., Désert, J.-M., Ferlet, R., Hébrard, G., Sing, D. K., Tchakoumegni, A. C., and Udry, S. (2010). "Evaporation of the planet HD 189733b observed in H I Lyman-α". *Astronomy & Astrophysics*, 514: A72. DOI: 10.1051/0004-6361/200913347.

Evans, T. M., Sing, D. K., Kataria, T., Goyal, J., Nikolov, N., Wakeford, H. R., Deming, D., Marley, M. S., Amundsen, D. S., Ballester, G. E., Barstow, J. K., Ben-Jaffel, L., Bourrier, V., Buchhave, L. A., Cohen, O., Ehrenreich, D., García Muñoz, A., Henry, G. W., Knutson, H., Lavvas, P., Lecavelier Des Etangs, A., Lewis, N. K., López-Morales, M., Mandell, A. M., Sanz-Forcada, J., Tremblin, P., and Lupu, R. (2017). "An ultrahot gas-giant exoplanet with a stratosphere"., 548(7665): 58–61. DOI: 10.1038/nature23266.

Evans, T. M., Sing, D. K., Wakeford, H. R., Nikolov, N., Ballester, G. E., Drummond, B., Kataria, T., Gibson, N. P., Amundsen, D. S., and Spake, J. (2016). "Detection of H_2O and Evidence for TiO/VO in the Atmosphere of the Hot-Jupiter WASP-121b". *The Astrophysical Journal Letters*, 822(1): L4. DOI: 10.3847/2041-8205/822/1/L4.

Fabrycky, D. and Tremaine, S. (2007). "Shrinking Binary and Planetary Orbits by Kozai Cycles with Tidal Friction"., 669(2): 1298–1315. DOI: 10.1086/521702.

Fischer, D. A. and Valenti, J. (2005). "The Planet-Metallicity Correlation"., 622(2): 1102–1117. DOI: 10.1086/428383.

Fortney, J. J., Lodders, K., Marley, M. S., and Freedman, R. S. (2008). "A Unified Theory for the Atmospheres of the Hot and Very Hot Jupiters: Two Classes of Irradiated Atmospheres". *The Astrophysical Journal*, 678: 1419–1435. DOI: 10.1086/528370.

Fortney, J. J., Marley, M. S., and Barnes, J. W. (2007). "Planetary Radii across Five Orders of Magnitude in Mass and Stellar Insolation: Application to Transits". *The Astrophysical Journal*, 659: 1661–1672. DOI: 10.1086/512120.

Fortney, J. and Nettelmann, N. (2010). "The Interior Structure, Composition, and Evolution of Giant Planets". *Space Science Reviews*, 152: 423–447. DOI: 10.1007/s11214-009-9582-x.

Fortney, J. J., Dawson, R. I., and Komacek, T. D. (2021). "Hot Jupiters: Origins, Structure, Atmospheres". *Journal of Geophysical Research: Planets*, 126: e06629. DOI: 10.1029/2020JE006629.

French, M., Becker, A., Lorenzen, W., Nettelmann, N., Bethkenhagen, M., Wicht, J., and Redmer, R. (2012). "Ab Initio Simulations for Material Properties along the Jupiter Adiabat". *The Astrophysical Journal Supplement Series*, 202: 5. DOI: 10.1088/0067-0049/202/1/5.

Fressin, F., Torres, G., Charbonneau, D., Bryson, S. T., Christiansen, J., Dressing, C. D., Jenkins, J. M., Walkowicz, L. M., and Batalha, N. M. (2013). "The False Positive Rate of Kepler and the Occurrence of Planets"., 766(2): 81. DOI: 10.1088/0004-637X/766/2/81.

Freytag, B., Allard, F., Ludwig, H.-G., Homeier, D., and Steffen, M. (2010). "The role of convection, overshoot, and gravity waves for the transport of dust in M dwarf and brown dwarf atmospheres". *Astronomy & Astrophysics*, 513(4): A19. DOI: 10.1051/0004-6361/200913354.

Fromang, S., Leconte, J., and Heng, K. (2016). "Shear-driven instabilities and shocks in the atmospheres of hot Jupiters". *Astronomy & Astrophysics*, 591: A144. DOI: 10.1051/0004-6361/201527600.

Gan, T., Wang, S. X., Wang, S., Mao, S., Huang, C. X., Collins, K. A., Stassun, K. G., Shporer, A., Zhu, W., Ricker, G. R., Vanderspek, R., Latham, D. W., Seager, S., Winn, J. N., Jenkins, J. M., Barkaoui, K., Belinski, A. A., Ciardi, D. R., Evans, P.,

Girardin, E., Maslennikova, N. A., Mazeh, T., Panahi, A., Pozuelos, F. J., Radford, D. J., Schwarz, R. P., Twicken, J. D., Wünsche, A., and Zucker, S. (2023). "Occurrence rate of hot Jupiters around early-type M dwarfs based on TESS data". *The Astronomical Journal*, 165: 17. DOI: 10.3847/1538-3881/ac9b12.

Gastine, T. and Wicht, J. (2021). "Stable stratification promotes multiple zonal jets in a turbulent Jovian dynamo model". *Icarus*, 368: 114514. DOI: 10.1016/j.icarus.2021.114514.

Ginzburg, S. and Sari, R. (2015). "Hot-Jupiter Inflation due to Deep Energy Deposition". *The Astrophysical Journal*, 803: 111. DOI: 10.1088/0004-637X/803/2/111.

Ginzburg, S. and Sari, R. (2016). "Extended Heat Deposition in Hot Jupiters: Application to Ohmic Heating". *The Astrophysical Journal*, 819(2): 116. DOI: 10.3847/0004-637X/819/2/116.

Gonzalez, G. (1997). "The stellar metallicity-giant planet connection"., 285(2): 403–412. DOI: 10.1093/mnras/285.2.403.

Grant, D., Lewis, N. K., Wakeford, H. R., Batalha, N. E., Glidden, A., Goyal, J., Mullens, E., MacDonald, R. J., May, E. M., Seager, S., Stevenson, K. B., Valenti, J. A., Visscher, C., Alderson, L., Allen, N. H., Cañas, C. I., Colón, K., Clampin, M., Espinoza, N., Gressier, A., Huang, J., Lin, Z., Long, D., Louie, D. R., Peña-Guerrero, M., Ranjan, S., Sotzen, K. S., Valentine, D., Anderson, J., Balmer, W. O., Bellini, A., Hoch, K. K. W., Kammerer, J., Libralato, M., Mountain, C. M., Perrin, M. D., Pueyo, L., Rickman, E., Rebollido, I., Sohn, S. T., van der Marel, R. P., and Watkins, L. L. (2023). "JWST-TST DREAMS: Quartz Clouds in the Atmosphere of WASP-17b"., 956(2): L32. DOI: 10.3847/2041-8213/acfc3b10.3847/2041-8213/acfdab.

Gu, P.-G., Bodenheimer, P. H., and Lin, D. N. C. (2004). "The Internal Structural Adjustment Due to Tidal Heating of Short-Period Inflated Giant Planets". *The Astrophysical Journal*, 608(2): 1076–1094. DOI: 10.1086/420867.

Gu, P.-G., Peng, D.-K., and Yen, C.-C. (2019). "Modeling the Thermal Bulge of a Hot Jupiter with the Two-Stream Approximation". *The Astrophysical Journal*, 887(2): 228. DOI: 10.3847/1538-4357/ab5a81.

Guillot, T. (1999). "Interior of Giant Planets Inside and Outside the Solar System". *Science*, 286(5437): 72–77. DOI: 10.1126/science.286.5437.72.

Guillot, T. (2005). "The interiors of giant planets: Models and outstanding questions". *Annual Review of Earth and Planetary Sciences*, 33: 493–530. DOI: 10.1146/annurev.earth.32.101802.120325.

Guillot, T. (2010). "On the radiative equilibrium of irradiated planetary atmospheres". *Astronomy & Astrophysics*, 520: A27. DOI: 10.1051/0004-6361/200913396.

Guillot, T. and Showman, A. P. (2002). "Evolution of '51 Pegasus b-like' planets". *Astronomy & Astrophysics*, 385: 156–165. DOI: 10.1051/0004-6361:20011624.

Gunney, B. T. and Anderson, R. W. (2016). "Advances in patch-based adaptive mesh refinement scalability". *Journal of Parallel and Distributed Computing*, 89: 65 –84. DOI: https://doi.org/10.1016/j.jpdc.2015.11.005.

Harada, C. K., Kempton, E. M.-R., Rauscher, E., Roman, M., Malsky, I., Brinjikji, M., and diTomasso, V. (2021). "Signatures of Clouds in Hot Jupiter Atmospheres: Modeled High-Resolution Emission Spectra from 3D General Circulation Models". *The Astrophysical Journal*, 909(1): 85. DOI: 10.3847/1538-4357/abdc22.

Hardy, R., Cumming, A., and Charbonneau, P. (2022). "Variability from Thermoresistive Instability in the Atmospheres of Hot Jupiters". *The Astrophysical Journal*, 940. DOI: 10.3847/1538-4357/ac9bfc.

Hatzes, A. P. and Rauer, H. (2015). "A Definition for Giant Planets Based on the Mass–Density Relationship". *Astrophysical Journal Letters*, 810(2): L25. DOI: 10.1088/2041-8205/810/2/L25.

Helled, R. and Stevenson, D. J. (2024). "The Fuzzy Cores of Jupiter and Saturn". *AGU Advances*, 5: e2024AV001171. DOI: 10.1029/2024AV001171.

Helled, R., Stevenson, D. J., Lunine, J. I., Bolton, S. J., Nettelmann, N., Atreya, S., Guillot, T., Militzer, B., Miguel, Y., and Hubbard, W. B. (2022). "Revelations on Jupiter's Formation, Evolution and Interior: Challenges from Juno Results". *Icarus*, 378: 114937. DOI: 10.1016/j.icarus.2022.114937.

Heller, R., Williams, D., Kipping, D., Limbach, M. A., Turner, E., Greenberg, R., Sasaki, T., Bolmont, E., Grasset, O., Lewis, K., Barnes, R., and Zuluaga, J. I. (2014). "Formation, Habitability, and Detection of Extrasolar Moons". *Astrobiology*, 14: 798–835. DOI: 10.1089/ast.2014.1147.

Helling, C., Iro, N., Corrales, L., Samra, D., Ohno, K., Alam, M. K., Steinrueck, M., Lew, B., Molaverdikhani, K., MacDonald, R. J., Herbort, O., Woitke, P., and Parmentier, V. (2019). "Understanding the atmospheric properties and chemical composition of the ultra-hot Jupiter HAT-P-7b: I. Cloud and chemistry mapping". *Astronomy & Astrophysics*, 631: A79. DOI: 10.1051/0004-6361/201935771.

Heng, K. (2012). "On the Existence of Shocks in Irradiated Exoplanetary Atmospheres". *The Astrophysical Journal Letters*, 761(1): L1. DOI: 10.1088/2041-8205/761/1/L1.

Heng, K. (2017). *Exoplanetary Atmospheres: Theoretical Concepts and Foundations*. Princeton Series in Astrophysics. Princeton University Press, (2017). DOI: 10.1515/9781400883073.

Heng, K., Menou, K., and Phillipps, P. J. (2011). "Atmospheric circulation of tidally locked exoplanets: a suite of benchmark tests for dynamical solvers". *Monthly Notices of the Royal Astronomical Society*, 413(4): 2380–2402. DOI: 10.1111/j.1365-2966.2011.18315.x.

Heng, K. and Showman, A. P. (2015). "Atmospheric Dynamics of Hot Exoplanets". *Annual Review of Earth and Planetary Sciences*, 43(1): 509–540. DOI: 10.1146/annurev-earth-060614-105146.

Hindle, A. W., Bushby, P. J., and Rogers, T. M. (2021). "The Magnetic Mechanism for Hotspot Reversals in Hot Jupiter Atmospheres". *The Astrophysical Journal*, 922: 176. DOI: 10.3847/1538-4357/ac0e2e.

Hoeijmakers, H. J., Ehrenreich, D., Heng, K., Kitzmann, D., Grimm, S. L., Allart, R., Deitrick, R., Wyttenbach, A., Oreshenko, M., Pino, L., Rimmer, P. B., Molinari, E., and Di Fabrizio, L. (2018). "Atomic iron and titanium in the atmosphere of the exoplanet KELT-9b". *Nature*, 560(7716): 453–456. DOI: 10.1038/s41586-018-0401-y.

Holmberg, M. and Madhusudhan, N. (2022). "A First Look at CRIRES+: Performance Assessment and Exoplanet Spectroscopy"., 164(3): 79. DOI: 10.3847/1538-3881/ac77eb.

Holst, B., French, M., and Redmer, R. (2011). "Electronic transport coefficients from ab initio simulations and application to dense liquid hydrogen". *Physical Review B*, 83(23): 235120. DOI: 10.1103/PhysRevB.83.235120.

Hornung, R. D. and Kohn, S. R. (2002). "Managing application complexity in the SAMRAI object-oriented framework". *Concurrency and Computation: Practice and Experience*, 14(5): 347–368. DOI: 10.1002/cpe.652.

Huang, X. and Cumming, A. (2012). "Ohmic Dissipation in the Interiors of Hot Jupiters". *The Astrophysical Journal*, 757(1): 47. DOI: 10.1088/0004-637X/757/1/47.

Hubbard, W. B., Fortney, J. J., Lunine, J. I., Burrows, A., Sudarsky, D., and Pinto, P. A. (2001). "Theory of Extrasolar Giant Planet Transits". *The Astrophysical Journal*, 560: 413–419. DOI: 10.1086/322490.

Hubeny, I., Burrows, A., and Sudarsky, D. (2003). "A Possible Bifurcation in Atmospheres of Strongly Irradiated Stars and Planets". *The Astrophysical Journal*, 594: 1011–1018. DOI: 10.1086/377080.

Hut, P. (1981). "Tidal evolution in close binary systems.", 99: 126–140.

Ibgui, L. and Burrows, A. (2009). "Coupled evolution with tides of the radious and orbit of transiting giant planets: general results". *The Astrophysical Journal*, 700: 1921–1931. DOI: 10.1088/0004-637X/700/2/1921.

Ikoma, M., Guillot, T., Genda, H., Tanigawa, T., and Ida, S. (2006). "On the origin of HD 149026b". *The Astrophysical Journal*, 650(2): 1150–1159. DOI: 10.1086/507088.

Ingersoll, A. P., Dowling, T. E., Gierasch, P. J., Orton, G. S., Read, P. L., Sánchez-Lavega, A., Showman, A. P., Simon-Miller, A., and Vasavada, A. R. (2004). "Dynamics of Jupiter's Atmosphere". In: *Jupiter: The Planet, Satellites and Magnetosphere*. Ed. by F. Bagenal, T. E. Dowling, and W. B. McKinnon. Cambridge: Cambridge University Press, (2004), 105–128.

Jackson, B., Greenberg, R., and Barnes, R. (2008). "Tidal Heating of Extrasolar Planets". *The Astrophysical Journal*, 681: 1631–1638. DOI: 10.1086/587641.

Jenkins, J. S., Jones, H. R. A., Tuomi, M., Díaz, M., Cordero, J. P., Aguayo, A., Pantoja, B., Arriagada, P., Mahu, R., Brahm, R., Rojo, P., Soto, M. G., Ivanyuk, O., Becerra Yoma, N., Day-Jones, A. C., Ruiz, M. T., Pavlenko, Y. V., Barnes, J. R., Murgas, F., Pinfield, D. J., Jones, M. I., López-Morales, M., Shectman, S., Butler, R. P., and Minniti, D. (2017). "New planetary systems from the Calan-Hertfordshire Extrasolar Planet Search"., 466(1): 443–473. DOI: 10.1093/mnras/stw2811.

Jiang, H., Wang, Y., Ormel, C. W., Krijt, S., and Dong, R. (2023). "Chemical footprints of giant planet formation. Role of planet accretion in shaping the C/O ratio of protoplanetary disks"., 678: A33. DOI: 10.1051/0004-6361/202346637.

Johansen, A. and Lambrechts, M. (2017). "Forming Planets via Pebble Accretion". *Annual Review of Earth and Planetary Sciences*, 45(1): 359–387. DOI: 10.1146/annurev-earth-063016-020226.

Kataria, T., Showman, A. P., Fortney, J. J., Stevenson, K. B., Line, M. R., Kreidberg, L., Bean, J. L., and Désert, J.-M. (2015). "The Atmospheric Circulation of the Hot Jupiter WASP-43b". *The Astrophysical Journal*, 801(2): 86. DOI: 10.1088/0004-637X/801/2/86.

Kilmetis, K., Vidotto, A. A., Allan, A., and Kubyshkina, D. (2024). "Magnetic field evolution of hot exoplanets". *Monthly Notices of the Royal Astronomical Society*, 535(4): 3646–3660. DOI: 10.1093/mnras/stae2505.

Kipping, D. M., Bakos, G. Á., Buchhave, L., Nesvorný, D., and Schmitt, A. R. (2012). "The Hunt for Exomoons with Kepler (HEK). I. Description of a New Observational Project". *The Astrophysical Journal*, 750: 115. DOI: 10.1088/0004-637X/750/2/115.

Kipping, D. M., Forgan, D., Hartman, J., Nesvorný, D., Bakos, G. Á., Schmitt, A. R., and Buchhave, L. A. (2013). "The Hunt for Exomoons with Kepler (HEK). III. The First Search for an Exomoon around a Habitable-zone Planet". *The Astrophysical Journal*, 777: 134. DOI: 10.1088/0004-637X/777/2/134.

Knierim, H., Batygin, K., and Bitsch, B. (2022). "Shallowness of circulation in hot Jupiters: Advancing the Ohmic dissipation model". *Astronomy & Astrophysics*, 658: L7. DOI: 10.1051/0004-6361/202142588.

Knutson, H. A., Charbonneau, D., Allen, L. E., Burrows, A., and Megeath, S. T. (2008). "The 3.6–8.0 Micron Broadband Emission Spectrum of HD 209458b: Evidence for

an Atmospheric Temperature Inversion". *The Astrophysical Journal*, 673(1): 526–531. DOI: 10.1086/523894.

Knutson, H. A., Charbonneau, D., Allen, L. E., Fortney, J. J., Agol, E., Cowan, N. B., Showman, A. P., Cooper, C. S., and Megeath, S. T. (2007). "A map of the day–night contrast of the extrasolar planet HD 189733b". *Nature*, 447: 183–186. DOI: 10.1038/nature05782.

Knutson, H. A., Fulton, B. J., Montet, B. T., Kao, M., Ngo, H., Howard, A. W., Crepp, J. R., Hinkley, S., Bakos, G. Á., Batygin, K., Johnson, J. A., Morton, T. D., and Muirhead, P. S. (2014). "Friends of Hot Jupiters. I. A Radial Velocity Search for Massive, Long-period Companions to Close-in Gas Giant Planets"., 785(2): 126. DOI: 10.1088/0004-637X/785/2/126.

Knutson, H. A., Lewis, N., and Fortney, J. J. (2012). "3.6 and 4.5 m Phase Curves and Evidence for Non-Zero Heat Redistribution in the Atmosphere of HD 189733 b". *The Astrophysical Journal*, 754(1): 22. DOI: 10.1088/0004-637X/754/1/22.

Kok, Brogi, M., Snellen, I.A.G., Birkby, J., Albrecht, S., and de Mooij, E.J.W. (2013). "Detection of carbon monoxide in the high-resolution day-side spectrum of the exoplanet HD 189733b". *AA*, 554: A82. DOI: 10.1051/0004-6361/201321381.

Koll, D. D. B. and Komacek, T. D. (2018). "Atmospheric Circulations of Hot Jupiters as Planetary Heat Engines". *The Astrophysical Journal*, 853(2): 133. DOI: 10.3847/1538-4357/aaa3de.

Komacek, T. D., Gao P., X., and Fortney, J. J. (2022). "The Intrinsic Temperature and Radiative–Convective Boundary Depth in the Atmospheres of Hot Jupiters". *The Astrophysical Journal Letters*, 884: L6. DOI: 10.3847/2041-8213/ab43d0.

Komacek, T. D. and Showman, A. P. (2016). "Atmospheric Circulation of Hot Jupiters: Dayside–Nightside Temperature Differences". *The Astrophysical Journal*, 821: 16–29. DOI: 10.3847/0004-637X/821/1/16.

Komacek, T. D., Thorngren, D. P., Lopez, E. D., and Ginzburg, S. (2020). "Reinflation of Warm and Hot Jupiters". *The Astrophysical Journal*, 893(1): 36. DOI: 10.3847/1538-4357/ab7eb4.

Komacek, T. D. and Youdin, A. N. (2017). "Structure and Evolution of Internally Heated Hot Jupiters". *The Astrophysical Journal*, 844: 94. DOI: 10.3847/1538-4357/aa7b75.

Koskinen, T. T., Lavvas, P., Harris, M. J., and Yelle, R. V. (2014). "Thermal escape from extrasolar giant planets". *Philosophical Transactions of the Royal Society A: Mathematical, Physical and Engineering Sciences*, 372(2014): 20130089. DOI: 10.1098/rsta.2013.0089.

Kozai, Y. (1962). "Secular perturbations of asteroids with high inclination and eccentricity"., 67: 591–598. DOI: 10.1086/108790.

Kumar, S., Poser, A. J., Schöttler, M., Kleinschmidt, U., Dietrich, W., Wicht, J., French, M., and Redmer, R. (2021). "Ionization and transport in partially ionized multicomponent plasmas: Application to atmospheres of hot Jupiters". *Physical Review E*, 103(6): 063203. DOI: 10.1103/PhysRevE.103.063203.

Kunimoto, M. and Matthews, J. M. (2020). "Searching the Entirety of Kepler Data. II. Occurrence Rate Estimates for FGK Stars"., 159(6): 248. DOI: 10.3847/1538-3881/ab88b0.

Kurokawa, H. and Inutsuka, S. ichiro. (2015). "On the radius anomaly of hot Jupiters: reexamination of the possibility and impact of layered convection". *The Astrophysical Journal*, 815: 78. DOI: 10.1088/0004-637X/815/1/78.

Lammer, H., Selsis, F., Ribas, I., Guinan, E. F., Bauer, S. J., and Weiss, W. W. (2003). "Atmospheric Loss of Exoplanets Resulting from Stellar X-Ray and Extreme-Ultraviolet Heating". *The Astrophysical Journal*, 598: L121. DOI: 10.1086/380815.

Laughlin, G., Crismani, M., and Adams, F. C. (2011). "On the Anomalous Radii of the Transiting Extrasolar Planets". *The Astrophysical Journal*, 729: L7. DOI: 10.1088/2041-8205/729/1/L7.

Leconte, J., Chabrier, G., Baraffe, I., and Levrard, B. (2010). "Is tidal heating sufficient to explain bloated exoplanets? Consistent calculations accounting for finite initial eccentricity". *Astronomy & Astrophysics*, 516: A64. DOI: 10.1051/0004-6361/201014337.

Lee, E. J. and Chiang, E. (2016). "Breeding Super-Earths and Birthing Super-puffs in Transitional Disks"., 817(2): 90. DOI: 10.3847/0004-637X/817/2/90.

Lee, E. J., Chiang, E., and Ormel, C. W. (2014). "Make Super-Earths, Not Jupiters: Accreting Nebular Gas onto Solid Cores at 0.1 AU and Beyond"., 797(2): 95. DOI: 10.1088/0004-637X/797/2/95.

Li, C. and Goodman, J. (2010). "Circulation and dissipation on hot Jupiters". *The Astrophysical Journal*, 725: 1146. DOI: 10.1088/0004-637X/725/1/1146.

Lian, Y. and Showman, A. P. (2010). "Generation of equatorial jets by large-scale latent heating on the giant planets". *Icarus*, 207: 373–393. DOI: https://doi.org/10.1016/j.icarus.2009.10.006.

Lidov, M. L. (1962). "The evolution of orbits of artificial satellites of planets under the action of gravitational perturbations of external bodies"., 9(10): 719–759. DOI: 10.1016/0032-0633(62)90129-0.

Lin, D. N. C. and Papaloizou, J. (1986). "On the Tidal Interaction between Protoplanets and the Protoplanetary Disk. III. Orbital Migration of Protoplanets"., 309: 846. DOI: 10.1086/164653.

Line, M. R., Stevenson, K. B., Bean, J. L., Desert, J.-M., Fortney, J. J., Kreidberg, L., Madhusudhan, N., Showman, A. P., and Diamond-Lowe, H. (2016). "No Thermal Inversion and a Solar Water Abundance for the Hot Jupiter HD 209458b from HST/WFC3 Spectroscopy". *The Astronomical Journal*, 152(6): 203. DOI: 10.3847/0004-6256/152/6/203.

Liu, J., Goldreich, P. M., and Stevenson, D. J. (2008). "Constraints on deep-seated zonal winds inside Jupiter and Saturn". *Icarus*, 196: 653–664. DOI: 10.1016/j.icarus.2007.11.036.

Lopez, E. D. and Fortney, J. J. (2016). "Re-inflated Warm Jupiters around Red Giants". *The Astrophysical Journal*, 818(1): 4. DOI: 10.3847/0004-637X/818/1/4.

Louden, T. and Wheatley, P. J. (2015). "Spatially Resolved Eastward Winds and Rotation of HD 189733 b". *The Astrophysical Journal Letters*, 814: L24–L29. DOI: 10.1088/2041-8205/814/2/L24.

Lubow, S. H., Tout, C. A., and Livio, M. (1997). "Resonant Tides in Close Orbiting Planets". *Astrophysical Journal*, 484: 866–874. DOI: 10.1086/304369.

Léger, A. et al. (2009). "Transiting exoplanets from the CoRoT space mission VIII: CoRoT-7b: the first super-Earth with measured radius". *Astronomy & Astrophysics*, 506: 287–302. DOI: 10.1051/0004-6361/200911933.

Madhusudhan, N., Amin, M. A., and Kennedy, G. M. (2014). "Toward Chemical Constraints on Hot Jupiter Migration". *The Astrophysical Journal Letters*, 794(1): L12. DOI: 10.1088/2041-8205/794/1/L12.

Madhusudhan, N., Mousis, O., Johnson, T. V., and Lunine, J. I. (2011). "Carbon-rich Giant Planets: Atmospheric Chemistry, Thermal Inversions, Spectra, and Formation Conditions". *The Astrophysical Journal*, 743(2): 191. DOI: 10.1088/0004-637X/743/2/191.

Madhusudhan, N. and Seager, S. (2010). "On the Inference of Thermal Inversions in Hot Jupiter Atmospheres". *The Astrophysical Journal*, 725(1): 261–274. DOI: 10.1088/0004-637X/725/1/261.

Maguire, C., Gibson, N. P., Nugroho, S. K., Fortune, M., Ramkumar, S., Gandhi, S., and de Mooij, E. (2024). "High resolution atmospheric retrievals of WASP-76b transmission spectroscopy with ESPRESSO: Monitoring limb asymmetries across multiple transits"., 687: A49. DOI: 10.1051/0004-6361/202449449.

Malhotra, R. (1993). "The origin of Pluto's peculiar orbit". *Nature*, 365: 819–821. DOI: 10.1038/365819a0.

Malsky, I., Rauscher, E., Roman, M. T., Lee, E. K., Beltz, H., and Savel, A. (2024). "A Direct Comparison between the Use of Double Gray and Multiwavelength Radiative Transfer in a General Circulation Model with and without Radiatively Active Clouds". *The Astrophysical Journal*, 961: 66. DOI: 10.3847/1538-4357/ad0b70.

Mayor, M., Pepe, F., Queloz, D., Bouchy, F., Rupprecht, G., Lo Curto, G., Avila, G., Benz, W., Bertaux, J. L., Bonfils, X., Dall, T., Dekker, H., Delabre, B., Eckert, W., Fleury, M., Gilliotte, A., Gojak, D., Guzman, J. C., Kohler, D., Lizon, J. L., Longinotti, A., Lovis, C., Megevand, D., Pasquini, L., Reyes, J., Sivan, J. P., Sosnowska, D., Soto, R., Udry, S., van Kesteren, A., Weber, L., and Weilenmann, U. (2003). "Setting New Standards with HARPS". *The Messenger*, 114: 20–24.

Mayor, M. and Queloz, D. (1995). "A Jupiter-mass companion to a solar-type star". *Nature*, 378: 355–359. DOI: 10.1038/378355a0.

Medvedev, A. S. and Yiğit, E. (2019). "Gravity Waves in Planetary Atmospheres: Their Effects and Parameterization in Global Circulation Models". *Atmosphere*, 10(9): 531. DOI: 10.3390/atmos10090531.

Menou, K. (2012). "Magnetic Scaling Laws for the Atmospheres of Hot Giant Exoplanets". *The Astrophysical Journal*, 745: 138. DOI: 10.1088/0004-637X/745/2/138.

Menou, K. (2019). "Turbulent vertical mixing in hot exoplanet atmospheres". *Monthly Notices of the Royal Astronomical Society: Letters*, 485: L98–L103. DOI: 10.1093/mnrasl/slz041.

Menou, K. (2020). "Hot Jupiter atmospheric flows at high resolution". *Monthly Notices of the Royal Astronomical Society*, 493(4): 5038–5044. DOI: https://doi.org/10.1093/mnras/staa532.

Menou, K. and Rauscher, E. (2009). "Atmospheric Circulation of Hot Jupiters: A Shallow Three-Dimensional Model". *The Astrophysical Journal*, 700: 887–897. DOI: 10.1088/0004-637X/700/1/887.

Miguel, Y., Bazot, M., Guillot, T., Howard, S., Galanti, E., Kaspi, Y., Hubbard, W. B., Militzer, B., Helled, R., Atreya, S. K., Connerney, J. E. P., Durante, D., Kulowski, L., Lunine, J. I., Stevenson, D., and Bolton, S. (2022). "Jupiter's inhomogeneous envelope". *Astronomy & Astrophysics*, 662: A18. DOI: 10.1051/0004-6361/202243207.

Miguel, Y. and Vazan, A. (2023). "Interior and Evolution of the Giant Planets". *Remote Sensing*, 15(3): 681. DOI: 10.3390/rs15030681.

Militzer, B., Hubbard, W. B., Wahl, S., Lunine, J. I., Galanti, E., Kaspi, Y., Miguel, Y., Guillot, T., Moore, K. M., Parisi, M., Connerney, J. E. P., Helled, R., Cao, H., Mankovich, C., Stevenson, D. J., Park, R. S., Wong, M., Atreya, S. K., Anderson, J., and Bolton, S. J. (2022). "Juno Spacecraft Measurements of Jupiter's Gravity Imply a Dilute Core"., 3(8): 185. DOI: 10.3847/PSJ/ac7ec8.

Miller, N., Fortney, J. J., and Jackson, B. (2009). "Inflating and Deflating Hot Jupiters: Coupled Tidal and Thermal Evolution of Known Transiting Planets". *The Astrophysical Journal*, 702(2): 1413–1427. DOI: 10.1088/0004-637X/702/2/1413.

Miller, N. and Fortney, J. J. (2011). "The Heavy-element Masses of Extrasolar Giant Planets, Revealed". *The Astrophysical Journal Letters*, 736: L29. DOI: 10.1088/2041-8205/736/2/L29.

Müller, S., Baron, J., Helled, R., Bouchy, F., and Parc, L. (2024). "The mass–radius relation of exoplanets revisited". *Astronomy & Astrophysics*, 686: A296. DOI: 10.1051/0004-6361/202348690.

Murray-Clay, R. A., Chiang, E. I., and Murray, N. (2009). "Atmospheric Escape From Hot Jupiters". *The Astrophysical Journal*, 693: 23–42. DOI: 10.1088/0004-637X/693/1/23.

Muñoz, A. G. (2007). "Physical and chemical aeronomy of HD 209458b". *Planetary and Space Science*, 55: 1426–1455. DOI: 10.1016/j.pss.2007.03.007.

Mâlin, Boccaletti, Anthony, Perrot, Clément, Baudoz, Pierre, Rouan, Daniel, Lagage, Pierre-Olivier, Waters, Rens, Güdel, Manuel, Henning, Thomas, Vandenbussche, Bart, Absil, Olivier, Barrado, David, Charnay, Benjamin, Choquet, Elodie, Cossou, Christophe, Danielski, Camilla, Decin, Leen, Glauser, Adrian M., Pye, John, Olofsson, Goran, Glasse, Alistair, Patapis, Polychronis, Royer, Pierre, Scheithauer, Silvia, Serabyn, Eugene, Tremblin, Pascal, Whiteford, Niall, van Dishoeck, Ewine F., Ostlin, Göran, Ray, Tom P., and Wright, Gillian. (2025). "First unambiguous detection of ammonia in the atmosphere of a planetary mass companion with JWST/MIRI coronagraphs". *AA*, 693: A315. DOI: 10.1051/0004-6361/202452695.

Nettelmann, N., Holst, B., Kietzmann, A., French, M., Redmer, R., and Blaschke, D. (2008). "Ab initio Equation of State Data for Hydrogen, Helium, and Water and the Internal Structure of Jupiter". *The Astrophysical Journal*, 683: 1217–1228. DOI: 10.1086/589806.

Nikolov, N., Sing, D. K., Burrows, A. S., Fortney, J. J., Henry, G. W., Pont, F., Ballester, G. E., Aigrain, S., Wilson, P. A., Huitson, C. M., Gibson, N. P., Désert, J.-M., Etangs, A. Lecavelier des, Showman, A. P., Vidal-Madjar, A., Wakeford, H. R., and Zahnle, K. (2015). "HST hot-Jupiter transmission spectral survey: Haze in the atmosphere of WASP-6b". *Monthly Notices of the Royal Astronomical Society*, 447(1): 463–478. DOI: 10.1093/mnras/stu2433.

Öberg, K. I., Murray-Clay, R., and Bergin, E. A. (2011). "The Effects of Snowlines on C/O in Planetary Atmospheres"., 743(1): L16. DOI: 10.1088/2041-8205/743/1/L16.

Ogilvie, G. I. and Gu, P. (2003). "Tidal dissipation in rotating solar-type stars". *The Astrophysical Journal*, 661: 1180. DOI: 10.1086/515435.

Oklopčić, A. and Hirata, C. M. (2018). "A New Window into Escaping Exoplanet Atmospheres: 10830 Å Line of Helium". *The Astrophysical Journal Letters*, 855(1): L11. DOI: 10.3847/2041-8213/aaada9.

Orton, G. S., Tabataba-Vakili, F., Eichstädt, G., Rogers, J., Hansen, C. J., Momary, T. W., Ingersoll, A. P., Brueshaber, S., Wong, M. H., Simon, A. A., Fletcher, L. N., Ravine, M., Caplinger, M., Smith, D., Bolton, S. J., Levin, S. M., Sinclair, J. A., Thepenier, C., Nicholson, H., and Anthony, A. (2020). "A Survey of Small-Scale Waves and Wave-Like Phenomena in Jupiter's Atmosphere Detected by JunoCam". *Journal of Geophysical Research: Planets*, 125(7): e2019JE006369. DOI: 10.1029/2019JE006369.

Owen, J. E. (2019). "Atmospheric Escape and the Evolution of Close-In Exoplanets". *Annual Review of Earth and Planetary Sciences*, 47: 67–90. DOI: 10.1146/annurev-earth-053018-060246.

Paardekooper, S. J. and Mellema, G. (2006). "Halting type I planet migration in non-isothermal disks"., 459(1): L17–L20. DOI: 10.1051/0004-6361:20066304.

Pacetti, E., Turrini, D., Schisano, E., and Molinari, S. (July 2022). "Chemical diversity in protoplanetary discs and its impact on the formation history of giant planets". In: *44th COSPAR Scientific Assembly. Held 16-24 July*. Vol. 44. (July 2022), 267.

Palenzuela, C., Miñano, B., Arbona, A., Bona-Casas, C., Bona, C., and Massó, J. (2021). "Simflowny 3: An upgraded platform for scientific modeling and simulation". *Computer Physics Communications*, 259: 107675. DOI: 10.1016/j.cpc.2020.107675.

Palenzuela, C., Miñano, B., Viganò, D., Arbona, A., Bona-Casas, C., Rigo, A., Bezares, M., Bona, C., and Massó, J. (2018). "A Simflowny-based finite-difference code for high-performance computing in numerical relativity". *Classical and Quantum Gravity*, 35(18): 185007. DOI: 10.1088/1361-6382/aad7f6.

Pandey, B. P. and Wardle, M. (2008). "Hall magnetohydrodynamics of partially ionized plasmas". *Monthly Notices of the Royal Astronomical Society*, 385(4): 2269–2278. DOI: 10.1111/j.1365-2966.2008.12998.x.

Parmentier, V., Fortney, J. J., Showman, A. P., Morley, C., and Marley, M. S. (2016). "Transitions in the Cloud Composition of Hot Jupiters"., 828(1): 22. DOI: 10.3847/0004-637X/828/1/22.

Parmentier, V., Komacek, Showman, A. P., and Fortney, J. (2021). "The Cloudy Shape of Hot Jupiter Thermal Phase Curves". *Monthly Noticies of the Royal Astronomical Society*, 501: 78–108. DOI: 10.1093/mnras/staa3418.

Parmentier, V., Line, M. R., Bean, J. L., Mansfield, M., Kreidberg, L., Lupu, R. E., Visscher, C., Désert, J.-M., Fortney, J. J., Showman, A. P., and Marley, M. S. (2018). "From thermal dissociation to condensation in the atmospheres of ultra hot Jupiters: WASP-121b in context". *Astronomy & Astrophysics*, 617: A110. DOI: 10.1051/0004-6361/201833059.

Parmentier, V., Showman, A. P., and Lian, Y. (2013). "3D mixing in hot Jupiters atmospheres. I. Application to the day/night cold trap in HD 209458b". *Astronomy & Astrophysics*, 558: A91. DOI: 10.1051/0004-6361/201321132.

Pepe, F. et al. (2021). "ESPRESSO at VLT. On-sky performance and first results"., 645: A96. DOI: 10.1051/0004-6361/202038306.

Pérez-Becker, D. and Showman, A. P. (2013). "Atmospheric Heat Redistribution on Hot Jupiters". *The Astrophysical Journal*, 776(2): 134. DOI: 10.1088/0004-637X/776/2/134.

Perna, R., Heng, K., and Pont, F. (2012). "The Effects of Irradiation on Hot Jovian Atmospheres: Heat Redistribution and Energy Dissipation". *The Astrophysical Journal*, 751: 59–70. DOI: 10.1088/0004-637X/751/1/59.

Perna, R., Menou, K., and Rauscher, E. (2010). "Magnetic Drag on Hot Jupiter Atmospheric Winds". *The Astrophysical Journal*, 719(2): 1421–1427. DOI: 10.1088/0004-637X/719/2/1421.

Perna, R., Menou, K., and Rauscher, E. (2010). "Ohmic Dissipation in the Atmospheres of Hot Jupiters". *The Astrophysical Journal*, 724(1): 313–317. DOI: 10.1088/0004-637X/724/1/313.

Perryman, M. A. C., Lindegren, L., Kovalevsky, J., Hoeg, E., Bastian, U., Bernacca, P. L., Crézé, M., Donati, F., Grenon, M., Grewing, M., Leeuwen, F. van, Marel, H. van der, Mignard, F., Murray, C. A., Le Poole, R. S., Schrijver, H., Turon, C., Arenou, F., Froeschlé, M., and Petersen, C. S. (1997). "The Hipparcos Catalogue". *Astronomy & Astrophysics*, 323: L49–L52.

Pluriel, W. (2023). "Hot Exoplanetary Atmospheres in 3D". *Remote Sensing*, 15(3): 635. DOI: 10.3390/rs15030635.

Polichtchouk, I. and Cho, J. Y.-K. (2011). "Baroclinic Instability on Hot Gas Giant Planets". In: *EPSC Abstracts*. EPSC-DPS Joint Meeting 2011. Vol. 6. (2011), EPSC-DPS2011-319.

Pollack, J. B., Hubickyj, O., Bodenheimer, P., Lissauer, J. J., Podolak, M., and Greenzweig, Y. (1996). "Formation of the Giant Planets by Concurrent Accretion of

Solids and Gas". *Icarus*, 124(1): 62–85. DOI: https://doi.org/10.1006/icar.1996.0190.

Popescu Braileanu, B. and Keppens, R. (2021). "Effects of ambipolar diffusion on waves in the solar chromosphere". *Astronomy & Astrophysics*, 653: A131. DOI: 10.1051/0004-6361/202140872.

Prinoth, B., Hoeijmakers, H. J., Kitzmann, D., Sandvik, E., Seidel, J. V., Lendl, M., Borsato, N. W., Thorsbro, B., Anderson, D. R., Barrado, D., Kravchenko, K., Allart, R., Bourrier, V., Cegla, H. M., Ehrenreich, D., Fisher, C., Lovis, C., Guzmán-Mesa, A., Grimm, S., Hooton, M., Morris, B. M., Oreshenko, M., Pino, L., and Heng, K. (2022). "Titanium oxide and chemical inhomogeneity in the atmosphere of the exoplanet WASP-189 b". *Nature Astronomy*, 6: 449–457. DOI: 10.1038/s41550-021-01581-z.

Quirrenbach, A. et al. (July 2018). "CARMENES: high-resolution spectra and precise radial velocities in the red and infrared". In: *Ground-based and Airborne Instrumentation for Astronomy VII*. Ed. by C. J. Evans, L. Simard, and H. Takami. Vol. 10702. Society of Photo-Optical Instrumentation Engineers (SPIE) Conference Series. (July 2018), 107020W, 107020W. DOI: 10.1117/12.2313689.

Ramakrishna, K., Lokamani, M., and Cangi, A. (2024). "Electrical conductivity of dense hydrogen and helium from density functional theory". *Electronic Structure*, 6(4): 045008. DOI: 10.1088/2516-1075/ad912b.

Ramkumar, S., Gibson, N. P., Nugroho, S. K., Maguire, C., and Fortune, M. (2023). "High-resolution emission spectroscopy retrievals of MASCARA-1b with CRIRES+: strong detections of CO, H_2O, and Fe emission lines and a C/O consistent with solar". *Monthly Notices of the Royal Astronomical Society*, 525(2): 2985–3005. DOI: 10.1093/mnras/stad2476.

Rasio, F. A., Tout, C. A., Lubow, S. H., and Livio, M. (1996). "Tidal Decay of Close Planetary Orbits". *The Astrophysical Journal*, 470: 1187–1191. DOI: 10.1086/177941.

Rauscher, E. and Menou, K. (2010). "Three-dimensional Atmospheric Circulation Models of hot Jupiter atmospheric flow". *The Astrophysical Journal*, 714(2): 1334–1342. DOI: 10.1088/0004-637X/714/2/1334.

Rauscher, E. and Menou, K. (2013). "Three-Dimensional Atmospheric Circulation Models of HD 189733 b and HD 209458 b with Consistent Magnetic Drag and Ohmic Dissipation". *The Astrophysical Journal*, 764: 103. DOI: 10.1088/0004-637X/764/1/103.

Redfield, S., Endl, M., Cochran, W. D., and Koesterke, L. (2008). "Sodium Absorption from the Exoplanetary Atmosphere of HD 189733b Detected in the Optical Transmission Spectrum". *The Astrophysical Journal Letters*, 673(1): L87–L90. DOI: 10.1086/527475.

Redmer, R. (1997). "Physical properties of dense, low-temperature plasmas". *Physics Reports*, 282(2): 35–157. DOI: 10.1016/S0370-1573(96)00033-6.

Reffert, S. and Quirrenbach, A. (2011). "Mass constraints on substellar companion candidates from the re-reduced Hipparcos intermediate astrometric data: nine confirmed planets and two confirmed brown dwarfs". *Astronomy & Astrophysics*, 527: A140. DOI: 10.1051/0004-6361/201015861.

Reiners, A. and Christensen, U. R. (2010). "A magnetic field evolution scenario for brown dwarfs and giant planets". *Astronomy & Astrophysics*, 522: A13. DOI: https://doi.org/10.1051/0004-6361/201014251.

Ribas, I., Guinan, E. F., Güdel, M., and Audard, M. (2005). "Evolution of the Solar Activity over Time and Effects on Planetary Atmospheres. I. High-Energy Irradiances (1–1700 Å)". *The Astrophysical Journal*, 622(1): 680–694. DOI: 10.1086/427977.

Rice, W. K. M., Armitage, P. J., and Hogg, D. F. (2008). "Why are there so few hot Jupiters?", 384(3): 1242–1248. DOI: 10.1111/j.1365-2966.2007.12817.x.

Ricker, G. R. et al. (2015). "Transiting Exoplanet Survey Satellite (TESS)". *Journal of Astronomical Telescopes, Instruments, and Systems*, 1(1): 014003. DOI: 10.1117/1.JATIS.1.1.014003.

Rogers, L. A., Bodenheimer, P., Lissauer, J. J., and Seager, S. (2011). "Formation and Structure of Low-Density Exo-Neptunes". *The Astrophysical Journal*, 738(1): 59. DOI: 10.1088/0004-637X/738/1/59.

Rogers, T. M., Lin, D. N. C., and Lau, H. H. B. (2012). "Internal Gravity Waves Modulate the Apparent Misalignment of Exoplanets Around Hot Stars". *The Astrophysical Journal Letters*, 758(1): L6. DOI: 10.1088/2041-8205/758/1/L6.

Rogers, T. M. and Showman, A. P. (2014). "Magnetohydrodynamic Simulations of the Atmosphere of HD 209458b". *The Astrophysical Journal Letters*, 782(1): L4. DOI: 10.1088/2041-8205/782/1/L4.

Rogers, T. M. and Komacek, T. D. (2014). "Magnetic effects in hot Jupiter atmospheres". *The Astrophysical Journal*, 794: 132. DOI: 10.1088/0004-637X/794/2/132.

Rogers, T. M. and McElwaine, J. N. (2017). "The hottest hot Jupiters may host atmospheric dynamos". *The Astrophysical Journal Letters*, 841: L26. DOI: 10.3847/2041-8213/aa72da.

Roman, M. and Rauscher, E. (2017). "Modeling the Effects of Inhomogeneous Aerosols on the Hot Jupiter Kepler-7b's Atmospheric Circulation". *The Astrophysical Journal*, 850: 17. DOI: 10.3847/1538-4357/aa8ee4.

Roman, M. T., Kempton, E. M.-R., Rauscher, E., Harada, C. K., Bean, J. L., and Stevenson, K. B. (2021). "Clouds in Three-Dimensional Models of Hot Jupiters over a Wide Range of Temperatures: I. Thermal Structures and Broadband Phase Curve Predictions". *The Astrophysical Journal*, 908(2): 101. DOI: 10.3847/1538-4357/abd549.

Ryu, T., Zingale, M., and Perna, R. (2018). "Turbulence-driven thermal and kinetic energy fluxes in hot Jupiter atmospheres". *Monthly Notices of the Royal Astronomical Society*, 481: 5517–5530. DOI: 10.1093/mnras/sty2638.

Sainsbury-Martinez, F., Wang, P., Fromang, S., Tremblin, P., Dubos, T., Meurdesoif, Y., Spiga, A., Leconte, J., Baraffe, I., Chabrier, G., Mayne, N., Drummond, B., and Debras, F. (2019). "Idealised Simulations of the Deep Atmosphere of Hot Jupiters: Deep, Hot Adiabats as a Robust Solution to the Radius Inflation Problem". *Astronomy & Astrophysics*, 632: A114. DOI: 10.1051/0004-6361/201936445.

Sainsbury-Martinez, F., Tremblin, P., Schneider, A. D., Carone, L., Baraffe, I., Chabrier, G., Helling, C., Decin, L., and Jørgensen, U. G. (2023). "Evidence of radius inflation in radiative GCM models of WASP-76b due to the advection of potential temperature"., 524(1): 1316–1325. DOI: 10.1093/mnras/stad1905.

Sarkis, P., Mollière, P., and Mordasini, C. (2021). "Evidence of three mechanisms explaining the radius anomaly of hot Jupiters". *Astronomy & Astrophysics*, 645: A79. DOI: 10.1051/0004-6361/202038361.

Saumon, D. and Chabrier, G. (1991). "Fluid hydrogen at high density: Pressure dissociation". *Phys. Rev. A*, 44: 5122–5141. DOI: 10.1103/PhysRevA.44.5122.

Savel, A. B., Beltz, H., Komacek, T. D., Tsai, S.-M., and Kempton, E. M.-R. (2024). "A New Lever on Exoplanetary B Fields: Measuring Heavy Ion Velocities". *The Astrophysical Journal Letters*, 969(2): L27. DOI: 10.3847/2041-8213/ad5a0a.

Scharf, C. A. (2010). "Possible Constraints on Exoplanet Magnetic Field Strengths from Planet-star Interaction". *Astrophysical Journal*, 722(2): 1547–1555. DOI: 10.1088/0004-637X/722/2/1547.

Schlichting, H. E. (2014). "Formation of Close in Super-Earths and Mini-Neptunes: Required Disk Masses and their Implications"., 795(1): L15. DOI: 10.1088/2041-8205/795/1/L15.

Seager, S. and Sasselov, D. D. (2000). "Theoretical Transmission Spectra during Extrasolar Giant Planet Transits". *The Astrophysical Journal*, 537: 916–921. DOI: 10.1086/309088.

Seager, S. (2013). "Exoplanet habitability". *Science*, 340(6132): 577–581. DOI: 10.1126/science.1232226.

Seager, S. and Deming, D. (2010). "Exoplanet Atmospheres". *Annual Review of Astronomy and Astrophysics*, 48: 631–672. DOI: 10.1146/annurev-astro-081309-130837.

Seidel, J. V., Ehrenreich, D., Allart, R., Hoeijmakers, H. J., Lovis, C., Bourrier, V., Pino, L., Wyttenbach, A., Adibekyan, V., Alibert, Y., Borsa, F., Casasayas-Barris, N., Cristiani, S., Demangeon, O. D. S., Di Marcantonio, P., Figueira, P., González Hernández, J. I., Lillo-Box, J., Martins, C. J. A. P., Mehner, A., Molaro, P., Nunes, N. J., Palle, E., Pepe, F., Santos, N. C., Sousa, S. G., Sozzetti, A., Tabernero, H. M., and Zapatero Osorio, M. R. (2021). "Into the storm: diving into the winds of the ultra-hot Jupiter WASP-76 b with HARPS and ESPRESSO"., 653: A73. DOI: 10.1051/0004-6361/202140569.

Seidel, J. V., Ehrenreich, D., Pino, L., Bourrier, V., Lavie, B., Allart, R., Wyttenbach, A., and Lovis, C. (2020). "Wind of change: retrieving exoplanet atmospheric winds from high-resolution spectroscopy". *Astronomy & Astrophysics*, 633: A86. DOI: 10.1051/0004-6361/201936892.

Seifahrt, A., Bean, J. L., Kasper, D., Stürmer, J., Brady, M., Liu, R., Zechmeister, M., Stefánsson, G. K., Montet, B., White, J., Tapia, E., Mocnik, T., Xu, S., and Schwab, C. (Aug. 2022). "MAROON-X: the first two years of EPRVs from Gemini North". In: *Ground-based and Airborne Instrumentation for Astronomy IX*. Ed. by C. J. Evans, J. J. Bryant, and K. Motohara. Vol. 12184. Society of Photo-Optical Instrumentation Engineers (SPIE) Conference Series. (Aug. 2022), 121841G, 121841G. DOI: 10.1117/12.2629428. arXiv: 2210.06563 [astro-ph.IM].

Sestović, M., Demory, B.-O., and Queloz, D. (2018). "Investigating hot-Jupiter inflated radii with hierarchical Bayesian modelling". *Astronomy & Astrophysics*, 616: A76. DOI: 10.1051/0004-6361/201731454.

Showman, A. P. and Guillot, T. (2002). "Atmospheric Circulation and Tides of '51 Pegasus b-like' Planets". *Astronomy & Astrophysics*, 385: 166–180. DOI: 10.1051/0004-6361:20020101.

Showman, A. P., Lewis, N. K., and Fortney, J. J. (2015). "Three-dimensional Atmospheric Circulation of Warm and Hot Jupiters: Effects of Orbital Distance, Rotation Period, and Non-Synchronous Rotation". *The Astrophysical Journal*, 801: 95. DOI: 10.1088/0004-637X/801/2/95.

Showman, A. P., Cho, J. Y.-K., and Menou, K. (2010). "Atmospheric Circulation of Exoplanets". In: *Exoplanets*. Ed. by S. Seager. University of Arizona Press, (2010), 471–516. DOI: 10.48550/arXiv.0911.3170. URL: https://doi.org/10.48550/arXiv.0911.3170.

Showman, A. P., Fortney, J. J., Lian, Y., Marley, M. S., Freedman, R. S., Knutson, H. A., and Charbonneau, D. (2009). "Atmospheric Circulation of Hot Jupiters: Coupled Radiative-Dynamical General Circulation Model Simulations of HD 189733b and HD 209458b". *The Astrophysical Journal*, 699(1): 564–584. DOI: 10.1088/0004-637X/699/1/564.

Showman, A. P., Menou, K., and Cho, J. Y.-K. (2008). "Atmospheric Circulation of Hot Jupiters: A Review of Current Understanding". In: *Extreme Solar Systems*.

Ed. by D. Fischer, F. A. Rasio, S. E. Thorsett, and A. Wolszczan. Vol. 398. ASP Conference Series. (2008), 419–439. DOI: 10.48550/arXiv.0710.2930.

Showman, A. P. and Polvani, L. M. (2011). "Equatorial superrotation on tidally locked exoplanets". *The Astrophysical Journal*, 738: 71. DOI: 10.1088/0004-637X/738/1/71.

Showman, A. P., Tan, X., and Parmentier, V. (2020). "Atmospheric Dynamics of Hot Giant Planets and Brown Dwarfs". *Space Science Reviews*, 216(8): 139. DOI: 10.1007/s11214-020-00758-8.

Simon, A. A., Wong, M. H., and Orton, G. S. (2015). "First Results from the Hubble OPAL Program: Jupiter in 2015". *The Astrophysical Journal*, 812(1): 55. DOI: 10.1088/0004-637X/812/1/55.

Simonnin, A., Parmentier, V., Wardenier, J. P., Chauvin, G., Chiavassa, A., N'Diaye, M., Tan, X., Heidari, N., Prinoth, B., Bean, J., Hébrard, G., Line, M., Kitzmann, D., Kasper, D., Pelletier, S., Seidel, J. V., Seifhart, A., Benneke, B., Bonfils, X., Brogi, M., Désert, J. M., Gandhi, S., Hammond, M., Lee, E. K. H., Moutou, C., Palma-Bifani, P., Pino, L., Rauscher, E., Weiner Mansfield, M., Serrano Bell, J., and Smith, P. (2025). "Time-resolved absorption of six chemical species with MAROON-X points to a strong drag in the ultra-hot Jupiter TOI-1518 b"., 698: A314. DOI: 10.1051/0004-6361/202453241.

Sing, D. K., Wakeford, H. R., Showman, A. P., Nikolov, N., Fortney, J. J., Burrows, A. S., Ballester, G. E., Deming, D., Aigrain, S., Désert, J.-M., Gibson, N. P., Henry, G. W., Knutson, H., Etangs, A. Lecavelier des, Pont, F., Vidal-Madjar, A., Williamson, M. W., and Wilson, P. A. (2015). "HST hot-Jupiter transmission spectral survey: detection of potassium in WASP-31 b along with a cloud deck and Rayleigh scattering". *Monthly Notices of the Royal Astronomical Society*, 446(3): 2428–2443. DOI: 10.1093/mnras/stu2279.

Sing, D. K., Fortney, J. J., Nikolov, N., Wakeford, H. R., Kataria, T., Evans, T. M., Aigrain, S., Ballester, G. E., Burrows, A. S., Deming, D., Désert, J.-M., Gibson, N. P., Henry, G. W., Huitson, C. M., Knutson, H. A., Etangs, A. Lecavelier des, Pont, F., Showman, A. P., Vidal-Madjar, A., Williamson, M. H., and Wilson, P. A. (2016). "A continuum from clear to cloudy hot-Jupiter exoplanets without primordial water depletion". *Nature*, 529: 59–62. DOI: 10.1038/nature16068.

Skinner, J. W. and Cho, J. Y.-K. (2025). "Early Time Small-scale Structures in Hot-Exoplanet Atmosphere Simulations". *The Astrophysical Journal*, 982(1): 64. DOI: 10.3847/1538-4357/adb0ce.

Snellen, I. A. G., Kok, R. J. de, Mooij, E. J. W. de, and Albrecht, S. (2010). "The Orbital Motion, Absolute Mass and High-Altitude Winds of Exoplanet HD 209458 b". *Nature*, 465: 1049–1051. DOI: 10.1038/nature09111.

Socrates, A. (2013). "Relationship Between Thermal Tides and Radius Excess". DOI: https://arxiv.org/abs/1304.4121v1.

Soriano-Guerrero, C., Viganò, D., Perna, R., Elias-López, A., and Beltz, H. (2025). "Influence of turbulent perturbations in the magnetised atmospheres of Hot Jupiters". *Astronomy & Astrophysics (under review)*.

Soriano-Guerrero, C., Viganò, D., Perna, R., Elias-López, A., and Beltz, H. (2025). "Non-ideal MHD simulations of hot Jupiter atmospheres". *Monthly Notices of the Royal Astronomical Society*, 540: 1827. DOI: 10.1093/mnras/staf842.

Soriano-Guerrero, C., Viganò, D., Perna, R., Akgün, T., and Palenzuela, C. (2023). "Magnetic winding and turbulence in ultra-hot Jupiters". *Monthly Notices of the Royal Astronomical Society*. DOI: 10.1093/mnras/stad2311.

Spake, J. J., Sing, D. K., Evans, T. M., Oklopčić, A., Bourrier, V., Kreidberg, L., Rackham, B. V., J. Irwin, D. E., Wyttenbach, A., Wakeford, H. R., Zhou, Y., Chubb,

K. L., Nikolov, N., Goyal, J. M., Henry, G. W., Williamson, M. H., Blumenthal, S., Anderson, D. R., Hellier, C., Charbonneau, D., Udry, S., and Madhusudhan, N. (2018). "Helium in the eroding atmosphere of an exoplanet". *Nature*, 557: 68–70. DOI: 10.1038/s41586-018-0067-5.

Spiegel, D. S. and Burrows, A. (2013). "Thermal processes governing hot-Jupiter radii". *The Astrophysical Journal*, 772(1): 76. DOI: 10.1088/0004-637X/772/1/76.

Steffen, J. H., Ragozzine, D., Fabrycky, D. C., Carter, J. A., Ford, E. B., Holman, M. J., Rowe, J. F., Welsh, W. F., Borucki, W. J., Boss, A. P., Ciardi, D. R., and Quinn, S. N. (2012). "Kepler constraints on planets near hot Jupiters". *Proceedings of the National Academy of Science*, 109(21): 7982–7987. DOI: 10.1073/pnas.1120970109.

Stevenson, D. J. (1983). "Planetary magnetic fields". *Reports on Progress in Physics*, 46(5): 555. DOI: 10.1088/0034-4885/46/5/001.

Stevenson, D. J. (2010). "Planetary Magnetic Fields: Achievements and Prospects". *Space Science Reviews*, 152: 651–664. DOI: 10.1007/s11214-009-9572-z.

Stevenson, K. B., Line, M. R., Bean, J. L., Désert, J.-M., Fortney, J. J., Showman, A. P., Kataria, T., Kreidberg, L., and Feng, Y. K. (2017). "Spitzer phase curve constraints for WASP-43b at 3.6 and 4.5 m". *The Astronomical Journal*, 153(2): 68. DOI: 10.3847/1538-3881/153/2/68.

Storch, N. I., Anderson, K. R., and Lai, D. (2014). "Chaotic dynamics of stellar spin in binaries and the production of misaligned hot Jupiters". *Science*, 345(6202): 1317–1321. DOI: 10.1126/science.1254358.

Suresh, A. and Huynh, H. T. (1997). *Accurate Monotonicity-Preserving Schemes with Runge-Kutta Time Stepping*. Tech. rep. NASA-TM-107367 (AIAA-97-2037). NASA Lewis Research Center, (1997). DOI: 10.1006/jcph.1997.5745.

Tan, X. and Komacek, T. D. (2019). "The atmospheric circulation of ultra-hot Jupiters". *The Astrophysical Journal*, 886(1): 26. DOI: 10.3847/1538-4357/ab4a76.

Tan, X. and Showman, A. P. (2020). "Atmospheric Circulation of Tidally Locked Gas Giants with Increasing Rotation and Implications for White-Dwarf–Brown-Dwarf Systems". *Astrophysical Journal*, 902(1): 27. DOI: 10.3847/1538-4357/abb3d4.

Temmink, P. and Snellen, I. A. G. (2023). "The occurrence rate of hot Jupiters orbiting evolved stars from TESS". *Astronomy & Astrophysics*, 670: A26. DOI: 10.1051/0004-6361/202244180.

Thommes, E. W., Duncan, M. J., and Levison, H. F. (1999). "The formation of Uranus and Neptune in the Jupiter–Saturn region of the Solar System". *Nature*, 402: 635–638. DOI: 10.1038/45185.

Thorngren, D. P. (2024). "The Hot Jupiter Radius Anomaly and Stellar Connections". *arXiv preprint*. DOI: arXiv:2405.05307.

Thorngren, D. P. and Fortney, J. J. (2018). "Bayesian Analysis of Hot-Jupiter Radius Anomalies: Evidence for Ohmic Dissipation?" *The Astronomical Journal*, 155: 214. DOI: 10.3847/1538-3881/aaba13.

Thorngren, D. P. and Fortney, J. J. (2018). "Connecting Giant Planet Atmosphere and Interior Modeling: Constraints on Atmospheric Metal Enrichment". *The Astrophysical Journal*, 874(1): L31. DOI: 10.3847/2041-8213/ab1137.

Thorngren, D. P., Fortney, J. J., Murray-Clay, R. A., and Lopez, E. D. (2016). "The giant planet mass–metallicity relation". *The Astrophysical Journal*, 831: 64. DOI: 10.3847/0004-637X/831/1/64.

Thorngren, D. P., Gao, P., and Fortney, J. J. (2019). "The Intrinsic Temperature and Radiative-Convective Boundary Depth in the Atmospheres of Hot Jupiters". *The Astrophysical Journal Letters*, 884: L6. DOI: 10.3847/2041-8213/ab43d0.

Tinetti, G., Vidal-Madjar, A., Liang, M.-C., Beaulieu, J.-P., Yung, Y., Carey, S., Barber, R. J., Tennyson, J., Ribas, I., Allard, N., Ballester, G. E., Sing, D. K., and Selsis, F. (2007). "Water vapour in the atmosphere of a transiting extrasolar planet"., 448(7150): 169–171. DOI: 10.1038/nature06002.

Tinetti, G. et al. (2018). "A chemical survey of exoplanets with ARIEL". *Experimental Astronomy*, 46: 135–209. DOI: 10.1007/s10686-018-9598-x.

Toon, O. B. (1989). "Rapid Calculation of Radiative Heating Rates and Photodissociation Rates in Inhomogeneous Multiple Scattering Atmospheres". *Journal of Geophysical Research: Atmospheres*, 94: 16287–16301. DOI: 10.1029/JD094iD13p16287.

Tremblin, P., Chabrier, G., Mayne, N., Amundsen, D., Baraffe, I., Debras, F., Drummond, B., Hébrard, E., Venot, O., and Fromang, S. (2017). "Advection of Potential Temperature in the Atmosphere of Irradiated Exoplanets: A Robust Mechanism to Explain Radius Inflation". *The Astrophysical Journal*, 841(1): 30. DOI: 10.3847/1538-4357/aa6e57.

Trilling, D. E., Benz, W., Guillot, T., Lunine, J. I., Hubbard, W. B., and Burrows, A. (1998). "Orbital Evolution and Migration of Giant Planets: Modeling Extrasolar Planets"., 500(1): 428–439. DOI: 10.1086/305711.

Turner, J. D., Grießmeier, J.-M., Zarka, P., Zhang, X., and Mauduit, E. (2024). "Follow-up LOFAR observations of the τ Boötis exoplanetary system"., 688: A66. DOI: 10.1051/0004-6361/202450095.

Turner, J. D., Zarka, P., Grießmeier, J.-M., Lazio, J., Cecconi, B., Enriquez, J. E., Girard, J. N., Jayawardhana, R., Lamy, L., Nichols, J. D., and Pater, I. de. (2021). "The search for radio emission from the exoplanetary systems 55 Cancri, And Andromedae, and Tau Boötis using LOFAR beam-formed observations". *Astronomy & Astrophysics*, 645: A59. DOI: 10.1051/0004-6361/201937201.

Valencia, D., Sasselov, D. D., and O'Connell, R. J. (2007). "Detailed Models of Super-Earths: How Well Can We Infer Bulk Properties?" *The Astrophysical Journal*, 665: 1413–1420. DOI: 10.1086/519554.

Valsecchi, F., Rasio, F. A., and Steffen, J. H. (2014). "From Hot Jupiters to Super-Earths via Roche Lobe Overflow". *The Astrophysical Journal Letters*, 793(1): L3. DOI: 10.1088/2041-8205/793/1/L3.

Vidal-Madjar, A., Etangs, A. Lecavelier des, Désert, J.-M., Ballester, G. E., Ferlet, R., Hébrard, G., and Mayor, M. (2003). "An extended upper atmosphere around the extrasolar planet HD209458b". *Nature*, 422: 143–146. DOI: 10.1038/nature01448.

Viganò, D., Aguilera-Miret, R., and Palenzuela, C. (2019). "Extension of the sub-grid-scale gradient model for compressible magnetohydrodynamics turbulent instabilities". *Physics of Fluids*, 31(10): 105102. DOI: 10.1063/1.5121546.

Viganò, D., Sengupta, S., Soriano-Guerrero, C., Perna, R., Elias-López, A., Kumar, S., and Akgün, T. (2025). "Inflated hot Jupiters: Inferring average atmospheric velocity via Ohmic models coupled with internal dynamo evolution". *Astronomy & Astrophysics*. DOI: 10.1051/0004-6361/202555219.

Walsh, K. J., Morbidelli, A., Raymond, S. N., O'Brien, D. P., and Mandell, A. M. (2011). "A low mass for Mars from Jupiter's early gas-driven migration". *Nature*, 475(7355): 206–209. DOI: 10.1038/nature10201.

Weidenschilling, S. J. and Marzari, F. (1996). "Gravitational scattering as a possible origin for giant planets at small stellar distances"., 384(6610): 619–621. DOI: 10.1038/384619a0.

Wicht, J., Gastine, T., and Duarte, L. D. V. (2019). "Dynamo Action in the Steeply Decaying Conductivity Region of Jupiter-Like Dynamo Models". *Journal of Geophysical Research: Planets*, 124(3): 837–855. DOI: 10.1029/2018JE005759.

Winn, J. N. and Fabrycky, D. C. (2015). "The occurrence and architecture of exoplanetary systems". *Annual Review of Astronomy and Astrophysics*, 53(1): 409–447. DOI: 10.1146/annurev-astro-082214-122246.

Wolszczan, A. and Frail, D. A. (1992). "A planetary system around the millisecond pulsar PSR1257 + 12". *Nature*, 355: 145–147. DOI: 10.1038/355145a0.

Wright, J. T., Marcy, G. W., Howard, A. W., Johnson, J. A., Morton, T. D., and Fischer, D. A. (2012). "The Frequency of Hot Jupiters Orbiting nearby Solar-type Stars". *The Astrophysical Journal*, 753(2): 160. DOI: 10.1088/0004-637X/753/2/160.

Wu, Y. and Murray, N. (2003). "Planet Migration and Binary Companions: The Case of HD 80606b"., 589(1): 605–614. DOI: 10.1086/374598.

Wu, Y. and Lithwick, Y. (2011). "Secular Chaos and the Production of Hot Jupiters"., 735(2): 109. DOI: 10.1088/0004-637X/735/2/109.

Wu, Y. and Lithwick, Y. (2013). "Ohmic Heating Suspends, not Reverses, the Cooling Contraction of Hot Jupiters". *The Astrophysical Journal*, 763: 13. DOI: 10.1088/0004-637X/763/1/13.

Wyttenbach, A., Ehrenreich, D., Lovis, C., Udry, S., and Pepe, F. (2015). "Spectrally resolved detection of sodium in the atmosphere of HD 189733b with the HARPS spectrograph". *Astronomy & Astrophysics*, 577: A62. DOI: 10.1051/0004-6361/201525729.

Yadav, R. K., Gastine, T., Christensen, U. R., and Duarte, L. D. V. (2013). "Consistent scaling laws in anelastic spherical shell dynamos". *The Astrophysical Journal*, 774(1): 6. DOI: 10.1088/0004-637X/774/1/6.

Yadav, R. K. and Thorngren, D. P. (2017). "Estimating the Magnetic Field Strength in Hot Jupiters". *The Astrophysical Journal Letters*, 849: L12. DOI: 10.3847/2041-8213/aa93fd.

Youdin, A. N. and Mitchell, J. L. (2010). "The mechanical greenhouse: burial of heat by turbulence in hot Juptie atmospheres". *The Astrophysical Journal*, 721(2): 1113–1126. DOI: 10.1088/0004-637X/721/2/1113.

Young, R. M. B. and Read, P. L. (2017). "Forward and inverse kinetic energy cascades in Jupiter's turbulent weather layer". *Nature Physics*, 13: 1135–1140. DOI: 10.1038/nphys4227.

Zarka, P. (1998). "Auroral radio emissions at the outer planets: Observations and theories". *Journal of Geophysical Research: Space Physics*, 103(A9): 20159–20194. DOI: 10.1029/98JE01323.

Zhang, X. and Showman, A. P. (2017). "Effects of Bulk Composition on the Atmospheric Circulation and Climate of Giant Planets". *The Astrophysical Journal*, 836(1): 73. DOI: 10.3847/1538-4357/836/1/73.

Zhou, G. et al. (2019). "Two New HATNet Hot Jupiters around A Stars, and the First Glimpse at the Occurrence Rate of Hot Jupiters from TESS". *The Astronomical Journal*, 158: 141. DOI: 10.3847/1538-3881/ab36b5.

Zhu, W., Petrovich, C., Wu, Y., Dong, S., and Xie, J. (2018). "About 30% of Sun-like Stars Have Kepler-like Planetary Systems: A Study of Their Intrinsic Architecture"., 860(2): 101. DOI: 10.3847/1538-4357/aac6d5.

Zingale, M., Dursi, L. J., ZuHone, J., Calder, A. C., Fryxell, B., Olson, K., MacNeice, P., Robinson, A. C., Fisher, R. T., Klein, R. I., Calder, A. M. C., Almgren, A. S., and Woosley, S. E. (2002). "Mapping Initial Hydrostatic Models in Godunov Codes". *The Astrophysical Journal Supplement Series*, 143(2): 539–565. DOI: 10.1086/342754.